VARIATION OF LOCAL PRESSURES DURING ICE-STRUCTURE INTERACTION

MICHELLE JOHNSTON

Variation of Local Pressures During Ice-Structure Interaction

by

Michelle Johnston, B. Eng.

A thesis submitted to the School of Graduate Studies
in partial fulfillment of the requirements of the degree of
Master of Engineering

Faculty of Engineering and Applied Science
Memorial University of Newfoundland
March, 1994

St. John's Newfoundland Canada

Abstract

Ice-structure interaction is characterized by a nonuniform distribution of pressure across the impact zone. The interface between the structure and the parent ice consists of a matrix of crushed and sintered ice, throughout which regions of intense pressure are randomly dispersed.

The variation of localized pressures generated during ice-structure interaction was examined for several sets of data. Ice indentation tests conducted at Hobson's Choice Ice Island (1989), ship ramming trials of the Louis S. St. Laurent and the CanMar Kigoriak, and one ice event which involved the offshore drilling structure 'Molikpaq' each exhibited rapid fluctuations of pressure in space and in time.

Small regions of intense pressure are termed **critical zones** and are identified as important elements in the crushing process. Fundamental properties of the high pressure zones such as the average size, force and spatial density are quantified. Critical zones are of the order of $0.10 m^2$ and may experience forces ranging from 0.1-4MN. The analyzed data exhibited a reduction in the average pressure of a critical zone with increasing area of instrumentation. A decrease in the spatial density of the critical zones (from 0.80 to 0.62 zones/m^2) is proposed as a possible explanation for the noted scale effects.

Due to the random nature of the critical zones, a design methodology which combines the statistical distributions for the zonal force, size, and number is proposed. Design pressures over small areas may be obtained from a preliminary design curve which is fitted to data from ice interactions with ships and stationary structures.

Acknowledgements

The author is greatly indebted to Dr. Ian Jordaan, NSERC/Mobil Industrial Research Professor in Ocean Engineering, Memorial University of Newfoundland, for his invaluable assistance in all aspects of research related to this project. His patience, especially in the latter stages of the analysis, is most appreciated.

Special thanks also to those people associated with Gulf Resources and Esso Resources who made access to the May 12, 1986 event of the Molikpaq possible. They include Mr. Ken Croasdale, Mr. Brian Wright, Mr. Ken Gaida, Mr. Michael Hardy, Mr. Brian Rogers and Mr. Paul Spencer. The many helpful discussions with them and their prompt provision of the requested materials is gratefully acknowledged.

The helpful comments and suggestions and the encouragement offered by Mr. Jing Xiao, Mr. Sanjay Singh, Mr. Bin Zou, Mr. Mark Fuglem, Mr. Peter Brown, and Mr. Bin Liu are also much appreciated. Thanks also to the members of the Center for Computer Aided Engineering; Mr. Lloyd Little, Mr. David Press, Mr. Tony Galway, Ms. Valerie Fortier, and Mr. Mervin Goodyear, who provided assistance on a daily basis. Numerous other special persons, including friends and family, offered inspiration and continual support for which I am truly grateful.

Financial support for this work was provided by the Natural Sciences and Engineering Research Council of Canada (NSERC) and Petro-Canada Resources Limited. The courtesy and generosity of these organizations is gratefully acknowledged.

Contents

List of Figures

List of Tables

Nomenclature

A_H	region denoting critical zone
A_L	region denoting background pressure
A_o	regions of spalled ice
γ	crushed ice layer profile parameter
r_s	circumferential radius of the critical zone
θ	angle (radians)
b	one-half ellipse minor axis length
e	elliptical eccentricity
h_s	layer thickness at the edges of an ellipse
h_o	layer thickness at the center of an ellipse
M	variable critical zone parameter which combines velocity, friction, viscosity, and crushed layer thickness (MPa/m^2)
K	friction factor
v_o	flow velocity of crushed ice (m/s)
μ	dynamic viscosity (MPa·s)
p_s	background pressure (MPa)
F_{cz}	force of a critical zone (MN)
$\bar{p}_{cz}$	average pressure of a critical zone (MPa)
p_o	peak pressure of a critical zone (MPa)
$A_{cz(T)}$	modified area of the critical zone (m^2)
F_{act}	Force of the actuator (MN)

$F_{cz(I)}$	Force of the critical zone in the instrumented region (MN)
$P_{cz(I)}$	Mean pressure of the critical zone in the instrumented region (MPa)
A_{cz}	Area of the critical zone (m^2)
K_n	Kelvin model parameter: stiffness
N_n	Kelvin model parameter: viscosity
p_e	probability of exceedance
x_1	constant for a specified area (MPa)
x_0	constant for a specified area (MPa)
α	inverse of the slope of $-ln(p_e)$ versus pressure (MPa)
m	number of impacts
i	rank of individual samples in a dataset
F_X	cumulative distribution function of X
X	random quantity denoting pressure
Z	maximum pressure per unit time
N	random number of events
n	fixed number of events
r	proportionality constant
a	area (m^2)
ε	severity (number of impacts per year)
X_k	time to the *kth* incident
Ω	scale parameter
κ	shape parameter
λ	rate of arrival of incidents (temporal and spatial)
m_s	mean of a sample
σ_s	standard deviation of a sample
$\Gamma(k)$	gamma distribution
P_y	initiation of plastic yield (MPa)
P_{eh}	initiation of plastic hinges (MPa)
P_{set}	initiation of permanent set (MPa)
P_{ult}	initiation of ultimate strength (MPa)

Chapter 1

Introduction and Scope

Two different pressure-area relationships exist during ice-structure interaction; global and local loads. Global loads refer to the total load sustained by the structure. These loads may be applied over an area which encompasses any number of smaller, local areas. Local ice pressures are required for the design of structural elements such as platings, stiffeners, and stringers. A unique association between the local and global forces generated during ice-structure interaction exists. The nonuniform distribution of pressure across the contact area strongly influences the magnitude of local pressures, and less directly the global pressures.

The nonuniform distribution of pressure in the contact area is caused by small zones of intense pressure which are dispersed throughout a larger matrix of background pressure. The zones of high pressure are termed **critical zones**. Critical zones are characterized by a parabolic distribution of pressure which is influenced by the degree of ice confinement, tributary contact area, strain rate and the ice strength.

Although representative of a small portion of the contact area, critical zones support most of the load within the interaction area. The region of background pressure accounts for a smaller percentage of the total load. The intense pressures of the critical zone are lower when the contact area is large , as evidenced by the pressure-area relationship.

Global loads are computed through a process of averaging. The pressures associated with global loads are substantially smaller than the locally experienced pressures. Design equations for the offshore environment should discriminate between local and global pressures. In view of the uncertainties associated with ice-structure interaction, design criteria have remained conservative. Knowledge of local pressures will lead to improved design equations which allow concentration of strengthening in those areas where it is most needed. A design methodology which incorporates the concept of critical zones is proposed. The model should account for the random nature of the high pressure zones and should also include a parameter which allows for the specific exposure of different structural components.

Several basic parameters of the critical zone must be defined before such a model may be established. Presently, little is known of the behavior of critical zones. An analysis which involved several sets of data, covering a wide range of contact areas, was conducted to determine the basic parameters of the critical zone. The analyzed data included medium scale indentation tests and full scale ice interactions involving ships and offshore structures.

Numerous differences between the selected data sets exist. The effects of instrumentation, ice strength, confinement, and the impact duration and velocity are expected to influence the results. Different methods of ice load monitoring were used for each test program, i.e. pressure transducers, strain gauges, and pressure panels. Figure 1.1 presents a comparison between the various areas of instrumentation. Spatial resolution of the instrumentation systems ranged from $0.045m^2$ for the Hobson's Choice Indentation Tests, to $3.08m^2$ for the Medof pressure panels installed on the Molikpaq.

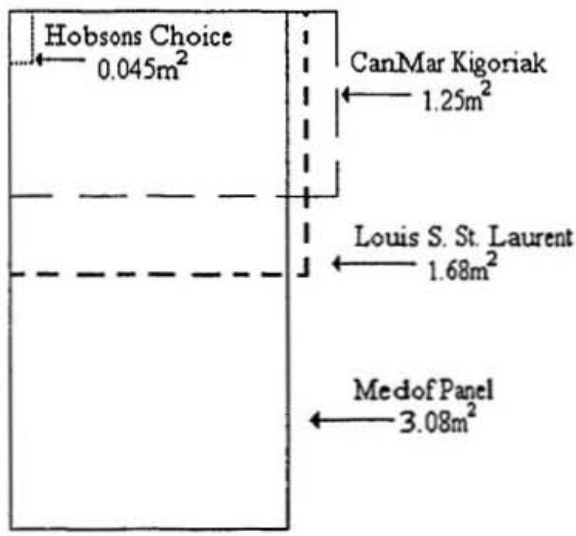

Figure 1.1 Spatial Comparison of the Various Instrumentation Systems

The concept of critical zones will be applied to each data set. The high pressure zones characteristic of the indentation tests will be compared with the pressures that are representative of ship ramming trials. The critical zone parameters obtained from the ship data will then be applied to the instrumented area of the Medof panels. Finally, the concept of critical zones will be extrapolated to an interaction which involved a 2.7m thick ice floe and the north face of the Molikpaq (see Figure 1.2).

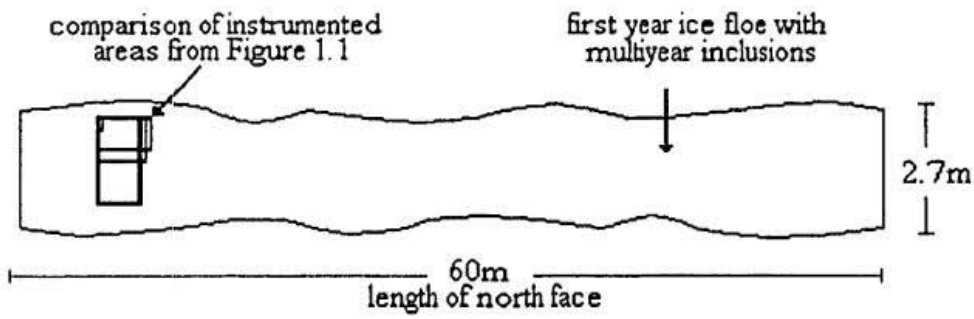

Figure 1.2 Ice Interaction Event Encompassing the North Face of the Molikpaq

Chapter 2

Critical Zones: Essential Elements in the Crushing Process

Crushing is a prevalent load limiting mode of ice failure during ice-structure interaction. Frequently occurring with vertical structures and with sloping structures at high rates of interaction, crushing is often accompanied by intense pressures and dynamic fluctuations in load. The cause of these load fluctuations has been the topic of much study (Xu 1981, Nadreau 1987, Timco and Jordaan 1987, Hallam and Kering 1988, for example). The following is a description of the interaction process when dominated by the failure mode of crushing. Critical zones are identified as important elements in the dynamics of crushing.

2.1 The Interaction Process

Investigation into the process of ice-structure interaction began in the 1960s, when the search for hydrocarbons and the need for navigational aids prompted the initial installation of offshore structures in the Baltic and at Cook Inlet, Alaska. At that time the mechanisms of ice-structure interaction were little understood. Design information regarding the magnitude and distribution of ice loads was virtually non-existent.

The integrity of bridge piers in Russia was adversely affected by ice as early as 1962 (Khorzavin, 1962). Määttänen (1977) describes the collapse of the Kemi I lighthouse in the Gulf of Bothnia as due to the dynamic effects of ice forces and greater than anticipated ice crushing strength or pressure ridge loading. More recently, the 'Molikpaq', a mobile arctic caisson located in the Canadian Beaufort, was subjected to intense dynamic vibrations which approximated design loads and compromised the integrity of the sand core, the primary mechanism of load resistance. Subsequently, attempts have been made towards further understanding the interaction process. Design criteria for the arctic environment continue to evolve as the process of ice-structure interaction becomes more clearly understood.

2.2 Interaction Zone Defined

Ice-structure interaction is characterized by varying intensities of pressure within the contact zone. Multiple failure mechanisms occurring in the contact zone affect three distinct regions of pressure. The first region, where intense local pressures are generated, is termed the critical zone. A second region exists in which lower pressures are present.

This region may be likened to an area of "background pressure". The third region is one in which pressures approximate zero. The cause of these distinct regions will be discussed in detail subsequently.

Critical zones, A_H, are subject to high local pressures and pressure gradients (see Figure 2.1). The presence of high stresses over local areas may be caused by spalls and may also be attributed to the forced extrusion of damaged ice in a very narrow layer between (nearly) solid ice and the structure (Jordaan et al., 1990). Critical zones may exist throughout the layer of ice immediately adjacent to the structure. They are more likely to occur towards the center of the ice sheet where confining pressures are greatest.

Background pressure, A_L, exists regardless of whether critical zones are present. The pressure is associated with the ejection of granular ice in wide spaces. Such pressures are not of sufficient magnitude to qualify as critical zones, but are nevertheless present, and do contribute to the overall pressure when considering the total interaction area.

Areas in which pressures are close to zero, A_0, are associated with spalls. Propagation of various fractures results in spall f rmation. In the process of ice-structure interaction, fracture usually results from the propagation of flaws in zones with low confining pressures (Jordaan et al., 1993). Medium scale indentor tests demonstrate that spalls occur near the free ice surface, where confining pressures are lowest (Frederking et al., 1990).

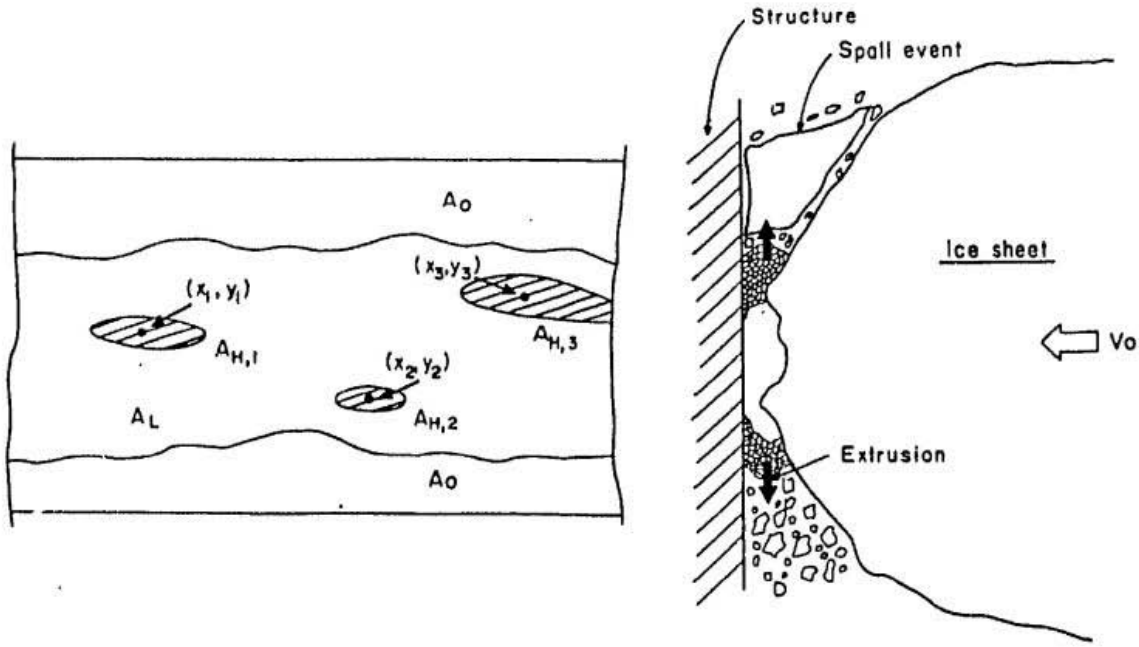

Figure 2.1 Three Regions of Pressure within an Interaction Zone
(Jordaan et al., 1990)

2.3 Damage Associated with the Crushed Layer

Dynamics associated with the crushing process have initiated much research in recent years. The idea of a crushed layer of ice was first introduced by Kheisin and Cherepanov (1970). A cast steel ball was dropped on natural freshwater ice. The impacted area comprised three distinct zones. The first zone (0-2cm) was one of total fracture and compression, exhibiting an upper layer of transparent ice as a result of partial melting. The second layer (2-8cm) exhibited considerable translocation of crystals. Ice in this zone contained numerous secondary inclusions in the form of air bubbles, which penetrated along cracks (Kheisin and Cherepanov, 1970). The third layer (8-68cm) consisted of radially distributed cracks transecting crystals irrespective of their size, shape, and crystallographic orientation.

Medium-scale indentation tests performed at Hobson's Choice Ice Island (Frederking et al., 1989) and laboratory experiments simulating the indentation process (Timco and Jordaan, 1987) also provide evidence of a distinct layer of crushed ice. As indentation proceeds, zones of damage, defined as the cracking of ice in essentially compressive states of stress (Jordaan and Timco, 1988), coalesce to form a well defined layer of crushed ice. Microcracking and the propagation of tensile cracks are two forms of fracture which occur in the interaction zone. Microcracking in the ice starts some distance ahead of the indentor in the zone of compressive stresses (Jordaan and Timco, 1988). Shear modulus reduction and the enhancement of creep are the most important aspects of ice degradation (Jordaan et al., 1988), and may be partly attributed to microcracking.

Spalling, defined as the movement of discrete ice pieces towards the free surface, is produced by the unstable propagation of cracks in tension. Recent work by Jordaan et al. (1993) used finite element analysis to simulate the occurrence of spalls. An immediate redistribution of stress occurs subsequent to spalling. In effect, this stress redistribution intensifies pressure in one or more regions within the interaction area, resulting in the formation of critical zones.

2.4 Dynamics of the Interaction Process

The dynamics of the interaction process may be attributed to the physical mechanisms active during the crushing and extrusion of ice in the contact zone. Repetitive crushing and cle- ing have been observed frequently in the field as well as in the laboratory (Timco and Jordaan, 1987). Indentation tests best illustrate the crushing process, simultaneously providing controlled conditions under which fracture processes may be observed. In

spherical indentation tests the fracture process is seldom continuous (Jordaan et al., 1988). Rather, periodic fracture events take place whereby pulverized material is extruded. Extrusion tests performed upon crushed ice by Singh et al. (1993) demonstrated that the extrusion of crushed ice was nearly continuous for slower tests (2.5mm/s), whereas dynamical processes became dominant with increasing test speed. Variation in force was reduced at the highest speeds (160mm/s).

Typical time series traces during indentation tests reveal sawtooth oscillations in load, generally increasing as the maximum penetration is attained (Gagnon and Sinha, 1991). As the indentor slowly proceeds forward, the state of stress in the contact zone rises and there is a corresponding increase in load. This causes a displacement in both the ice and structure which is proportionally dependent upon their relative stiffnesses (Timco and Jordaan, 1987). Microcracks start to form as the stress builds, relieving stress concentrations in the ice and, when sufficient in number, decreasing the stiffness of the ice sheet (Timco and Jordaan, 1987). As the contact area reaches its maximum sustainable load the ice immediately in front of the indentor fails. Ice failure initiates a sudden load drop and the indentor moves abruptly forward. Ice continues to be extruded, decreasing the crushed layer thickness. The lateral extent of the crushed layer was also seen to vary, fluctuating with the size of the fused zone (Singh et al., 1993). When the indentor encounters a zone of relatively undamaged ice, once again the stress states in both the ice sheet and indentor begin to increase.

This total process gives rise to an alternating series of ice pulverization events followed by crushing and clearing which is controlled by the interaction rate and the relative stiffness of the ice and the structure (Timco and Jordaan, 1987). Spalls and the pulverization of already crushed ice will produce characteristic imprints upon the load

trace. Typically, load fluctuations include several quite large decreases and many smaller decreases (Jordaan and Timco, 1988). The largest stress drops are a direct result of spalling, whereas the more numerous smaller drops are a consequence of pulverization of the existing crushed layer. The crushing process is dynamical in every aspect, from the instantaneous variation of the crushed layer to the temporal and spatial variability of the critical zones.

2.5 Pressure Melting

Pressure melting occurs as a consequence of intense pressures generated during the crushing process. Load and pressure oscillations characteristic of the crushed layer were examined by means of numerical analysis using finite element models (Jordaan et al., 1993). This analysis demonstrated that load fluctuations may be directly related to the process of pressure melting. It was proposed that variations in the viscosity and friction, induced by the presence of a liquid layer, were important parameters in the crushing process.

Dropped ball tests conducted by Kheisin and Cherepanov (1970) demonstrated the existence of a liquid within the crushed ice layer. A liquid layer was produced during the impact process by the transformation of work done by frictional forces into heat (Kheisin and Cherepanov, 1970). Under pressure, the crushed material was suspected to contain a certain amount of the liquid phase. It was suggested that the crushed layer behaves as a viscous liquid on impact.

Medium scale ice indentation tests conducted at Hobson's Choice Ice Isiand also indicated a liquid phase. Rounded particles in the crushed layer and a temperature of 0°C at the ice-indentor interface suggest the presence of a liquid. Further evidence of pressure melting was provided by the incorporation of rust particles from the face of the flexible indentor into grain boundary interstices (Gagnon and Sinha, 1991). A layer of ice with rust particle inclusions several millimeters thick existed in the outer regions of the indented face, indicating that substantial quantities of liquid water and rust accumulated in the low pressure regions during the indentation process (Gagnon and Sinha, 1991). The authors postulated that pressure melting, occurred at the ice-indentor interface and at interparticle contacts. The lubricant produced then percolated throughout the crushed layer.

Temperature measurements of the ice-indentor interface during indentation were obtained by a thermocouple mounted near the center of the indentor. Temperature trends from the ice indentation tests are in accordance with the dynamics of the crushing process. The thermocouple indicated regular decreases in temperature during increases in load. This may be explained by intense local pressures, particularly near the center of the indentor where critical zones are most likely to occur. Intense local pressures induce a reduction in the melting point of ice. The depression in melting point with increasing pressure arises from the fact that there is a reduction in volume when ice melts. If the melting temperature is less than the local temperature, the ice will start to melt, removing heat from the surroundings. Consequently, as the load increases, a drop in temperature will occur in the high pressure zones (Jordaan et al., 1993). Refreezing occurs as a result of reduced lateral confinement in the crushed layer. The pressure drops rapidly and the melting temperature increases.

Gagnon and Sinha (1991) postulated that after each abrupt movement of the indentor, the liquid, in direct contact with the cold indentor on one side and the cold intact ice on the other, begins to cool and refreeze. In general, the net rises in temperature were greater than the net falls since the time between events was insufficient for the heat produced to be conducted away from the interface (Gagnon and Sinha, 1991).

It has been stated previously that the extrusion of the crushed ice is the primary mechanism responsible for the dissipation of energy provided by the indentor. The energy required to form new surfaces, and that required to pulverize already crushed ice, is small in comparison to the energy required to extrude the ice, a process which is highly frictional. In order for pressure melting to proceed during the upswings in load, heat must be absorbed from the surrounding ice. As a consequence, the temperature decreases with increasing load. Pressure melting is not an energy dissipative process. It is a conservative process, whereby energy, in the form of heat, is cyclically transferred between adjacent regions of ice.

2.6 Sintered Ice: A Constituent of the Critical Zone

Relatively little work has been performed on the load bearing capacity of sintered ice. Sintering may be defined as the process of neck formation between powder particles that occurs when a powder compact is kept at temperatures below, but not far from, its melting point (Maeno and Ebinuma, 1983). Sintering is driven by a combination of excess free surface energy and externally applied pressures. Tests recently conducted on the extrusion of crushed ice indicate that under large confinement and intense pressures, the particulate ice loses its discrete, granular nature and becomes sintered, exhibiting behavior

similar to finegrained polycrystalline ice (Singh et al., 1993). Jordaan and Timco (1988) also noted that pulverized ice was capable of resisting volumetric shear stress in a manner similar to virgin ice. It is postulated that sintered ice, capable of sustaining intense pressures, is a viable constituent of the critical zone.

It has been noted that the pattern of temperature fluctuations in opposition to load oscillations is a direct consequence of pressure melting. It is possible to envision a scenario in which critical zones, coincident with the initiation of pressure melting, are present only during upswings in load for brief, random intervals. Given that the local melting at grain boundaries occurs at high pressure points, the melting could be short-lived, since the action of melting and subsequent viscous flow would relieve the high stress (Jordaan, personal communication). The transient nature of local melting is in accordance with characteristic behavior of critical zones.

2.7 Extrusion Tests: Evidence for Critical Zones

The flow properties of crushed ice under plane-strain conditions were examined by Singh et al. (1993). The following discussion is a synopsis of the tests resuits. A crushed layer of 100mm thickness and density of 0.55g/cm^3 was squeezed between rigid parallel plates at various speeds ranging from 2.5mm/s to 160mm/s at -10^{o}C. A solid mass of fused ice was observed in the central zone at the conclusion of the test (Singh et al., 1993; Sayed and Frederking, 1992). A distinct boundary existed between the granular and fused zones. This boundary, visible to the naked eye, was also supported by density measurements. The density of the solid mass was nearly equal to that of polycrystalline ice, while outside the fused zone, the density remained unchanged from the initial value of the crushed ice.

Sintering increased with the amount of applied pressure and the duration of loading. The largest pressures recorded by the transducers during the plane-strain extrusion tests were recorded near the center of the platen. In this region of high pressure, groups of particles stick together, forming a fused mass of solid ice. At the edges of the high pressure zone the presence of high shearing stresses enhances the damage process, resulting in the breakdown of the crystal structure.

High pressures and the fused, solidified material suggest the presence of critical zones. By definition, critical zones are small regions of ice experiencing intense local pressures and pressure gradients. It has been proposed that critical zones, sometimes referred to as "hard spots", are comprised of relatively undamaged ice (Gagnon and Sinha, 1991). As demonstrated by the crushed ice extrusion tests, sintered or highly compacted material is capable of resisting stresses in a manner similar to polycrystalline ice. Critical zones may actually be regions of highly damaged material which has fused to form a substance with properties similar to, but unique from, polycrystalline ice.

2.8 Pressure Variation within the Crushed Layer during Extrusion Tests

During crushed ice tests, pressures experienced by different transducers greatly varied, depending upon their location in the extrusion channel. Pressures along the extrusion axis ranged from maximum at the platen center to minimum near the channel exit. During initial stages of extrusion the load was carried by a narrow central zone. Pressure varied exponentially with a centralized peak. Increases in pressure effected a widening in the load carrying zone, accompanied by a more rounded, parabolic distribution of pressure.

Spalling alone does not account for the regular oscillation in load experienced during the extrusion of crushed ice. Failure was not simultaneous throughout the channel, but started just outside the critical zone, proceeding inwards towards the centralized zone. Figure 2.2 presents the cyclic variation of pressure during the dynamic process of extrusion. Initially the pressure distribution in the critical zone, extending 150mm radially from the platen center, is convex and increases both in magnitude and area when the mean pressure increases. A drop in pressure registers at point 2, indicating initiation of failure which then moves towards the center. At point 3 the pressure within the critical zone, currently reduced to 75mm radially from the center, drops as failure progresses. Reduction in the contact area of the critical zone effects a sudden increase in pressure at the center, whereby the pressure distribution momentarily becomes concave. The high pressure gradient near the center forces the ice in this area outwards towards low pressure zones and, at point 4, the pressure distribution again becomes convex in the critical zone. The process subsequently repeats itself.

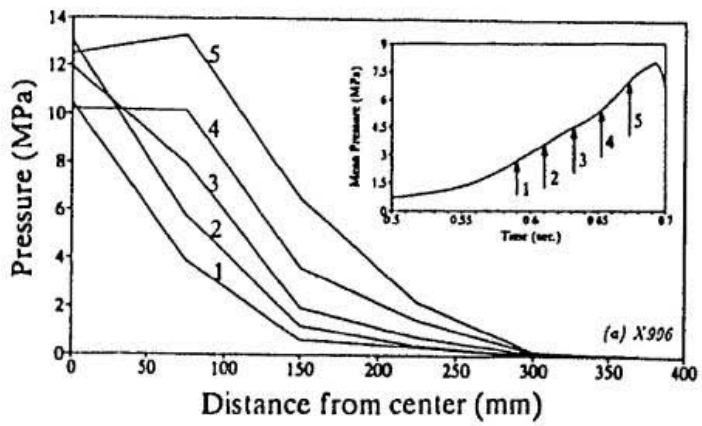

Figure 2 2 Cyclic Variation of Pressure
(Singh et al., 1993)

The lateral extent of compacted material is indicative of the approximate size of the fused zone. As previously discussed, regions of fused material are associated with critical zones. Extrusion tests demonstrated that critical zones formed at an early stage in the slower tests. Conversely, since rapid extrusion is characteristic of faster tests, less compaction occurs during the initial test stages.

2.9 Crushed Ice: Mohr-Coulomb versus Viscous Flow Theory

At low pressures, crushed ice behaves in a manner similar to snow and can be modelled as a frictional material following Mohr-Coulomb type behavior (Hallam and Pickering, 1988; Duthinh, 1991; Savage et al., 1992). In a series of tests executed by Singh et al. (1993) it was shown that Mohr-Coulomb theory accurately predicted the pressure near the exit for all cases examined. In comparison to centralized regions, ice towards the exit is under reduced confinement. As such, grain boundaries exhibit large degrees of freedom, enabling particles to act independently of one another. Additionally, laboratory experiments on the flow of crushed ice (Sayed and Frederking, 1992) demonstrated slip lines characteristic of Mohr-Coulomb behavior.

Mechanisms of compaction, pressure melting, and sintering transform areas of the crushed layer into a fused material. Mohr-Coulomb theory is limited to cases where the ice particles are distinct (Jordaan et al., 1990). It is not applicable to solidified material exhibiting viscoelastic behavior, nor does it apply to areas in which a liquid exists. As such, it does not pertain to central regions of the critical zone. Viscous flow theory is a more acceptable model for the pressure distribution in these regions. In most cases the distributions predicted by Mohr-Coulomb theory and viscous flow theory overlap, defining a transition zone.

2.10 Modelliag of the Critical Zone

In order to develop a model for ice-structure interaction which may be successfully applied to general engineering applications it is necessary to simplify the complex, heterogeneous process of ice crushing. Simplification of the interaction process involves consideration of the most influential parameters of ice mechanics and the failure process. The following sections (2.10-2.12) are based upon an ice load model developed by Jordaan et al. (1990) with significant contributions from M. Maes. This model approximates critical zones as elliptical in shape and models the extrusion of crushed ice using the Navier-Stokes equations. Equations for the pressure generated by the flow of a highly viscous, non-Newtonian, and possibly compressible material were also developed.

In developing a model to approximate the behavior of critical zones, an elliptical shape was assumed. Variation of the eccentricity, e, of the ellipse yields diverse shapes ranging from a perfectly circular critical zone (e=0) to a flat strip (e=1). It is assumed that the elliptical zones are random in position, magnitude, and shape. The eccentricity, e, is the only shape measure (see Figure 2.3).

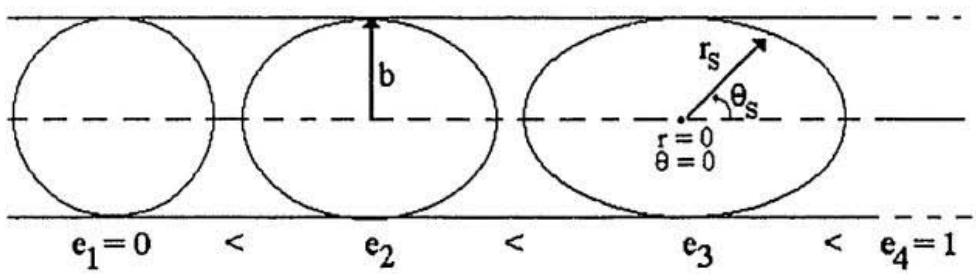

Figure 2.3 Variation of Elliptical Eccentricities

The thin space between ice and structure is modelled as an elliptic paraboloid with variable curvature factor, γ. Assuming the pole is in the center of the ellipse (r=0, θ=0 in polar coordinates) the polar equation of the ellipse at any point on its circumference (r_S, θ_S) may be described by Equation 2.1, i.e.

$$r_S = \frac{b}{(1 - e^2 \cos\theta_S)^{1/2}} \qquad 2.1$$

Consequently, the thickness of the intermediate layer of crushed ice, h, can be made to vary as a quadratic in such a way that, at any circumferential point on the edge of the critical zone, it has a thickness, h_S, which may be given by Equation 2.2, i.e.

$$h_S = h_0 (1 + \gamma) \qquad 2.2$$

Where h_O is the thickness at the center of the critical zone, its narrowest point (see Figure 2.4). The variable curvature factor, γ , is the relative increase in crushed ice layer thickness from its narrowest point (h_O) to its widest point (h_S) at the edge of the critical zone. As illustrated in Figure 2.4, the widening of the three dimensional zone can be adjusted with the variable curvature factor. A value of γ=0 indicates a zone of constant thickness, whereas larger values indicate a wider zone. The parabolic variation of the crushed layer thickness between h_O and h_S can be written as a function of r and θ :

$$h(r, \theta) = h_0 \left[\frac{1 + \gamma r^2 (1 - e^2 \cos^2\theta)}{b^2}\right] \qquad 2.3$$

Substitution of (r_S, θ_S) into Equation 2.3 yields the crushed ice layer thickness at the edge of the critical zone (h_S) in accordance with Equation 2.2.

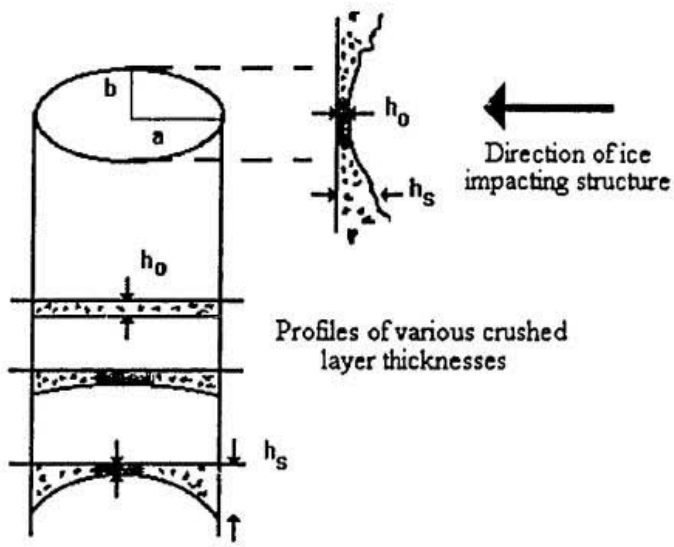

Figure 2.4 Various Crushed Layer Thicknesses

2.10.1 Pressure in the Extrusion Zone

A single partial differential equation for pressure in an extrusion zone with variable thickness was generated by Jordaan et al. (1990) based upon the case of incompressibility and Newtonian behavior.

$$\frac{1}{r}\frac{\partial}{\partial r}\left(r\left(\frac{h}{h_o}\right)^3\frac{\partial p}{\partial r}\right)+\frac{1}{r^2}\frac{\partial}{\partial \theta}\left(\left(\frac{h}{h_o}\right)^3\frac{\partial p}{\partial \theta}\right)=-M \qquad 2.4$$

where the constant M is equal to:

$$M = \frac{v_0 \; K \; \mu}{h_0{}^3} \qquad 2.5$$

K is the frictional boundary condition for the ice-structure interaction, v_o is the extrusion velocity of the crushed ice, μ is the viscosity of the ice, and p is the pressure.

Equation 2.4 was then applied to a single critical zone of elliptical shape with a short axis length of b, and an eccentricity, e. The assumed boundary conditions are, first, pressure at the edge of the critical zone is designated as p_s and second, for reasons of symmetry, the flow velocity at the center of the elliptical zone is equal to zero.

A general solution to the partial differential equation may be found after lengthy calculations involving the limiting cases of a circle (e=0) and a flat strip (e=1). The following solution to Equation 2.4 was presented in Jordaan et al. (1990).

$$p_{cz}(r,\theta) = p_s + \frac{M\,b^2}{4\gamma(2 - e^2)} \left\{ \frac{1}{[1+\gamma\,(r^2/b^2)\,(1 - e^2\cos^2\theta)]^2} - \frac{1}{(1+\gamma)^2} \right\} \qquad 2.6$$

Three profiles of the crushed layer were evaluated to determine the effect of layer thickness on the distribution of pressure in the critical zone. First was the limiting case of an extrusion zone with constant layer thickness (γ=0). Appropriate substitution yields the following pressure distribution equation:

$$p_{cz} = p_s + \frac{Mb^2}{2\,(2 - e^2)} \left[1 - \frac{r^2}{b^2\,(1 - e^2\cos^2\theta)} \right] \qquad 2.7$$

5.6.2 Average Pressures: Medof versus Strain Gauge Data

An analysis of the average pressure associated with two burst files (3:20 and 3:21) for each instrumentation system was conducted. Since the original data files were not available pressures were averaged using a graphical method. For instance, the high frequency loads recorded by the strain gauges were averaged by taking the mean of individual peaks and troughs throughout the 60 second file duration (see Appendix A). Similarly, the Medof panel pressures, obtained from the detailed panel plots, were also averaged during the interval 3:20-3:22, corresponding to the first and second burst files. Figures 5.18-5.20 demonstrate the comparison between the two instrumentation systems.

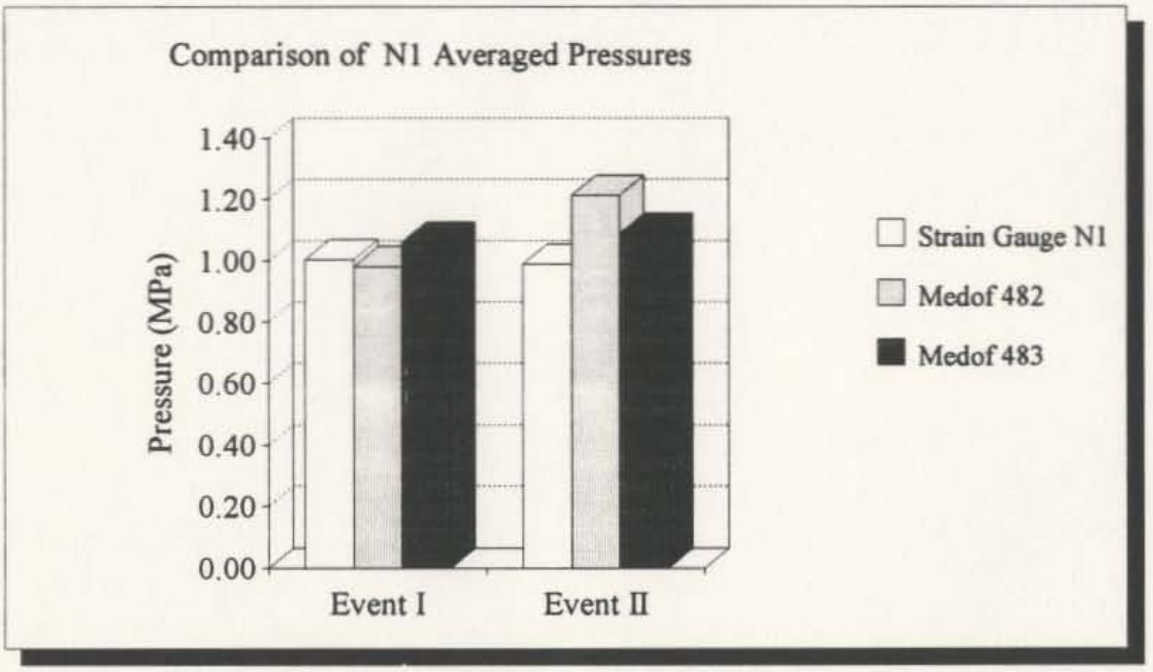

Figure 5.18 Comparison of N1 Instrumentation Average Pressures for Events I and II

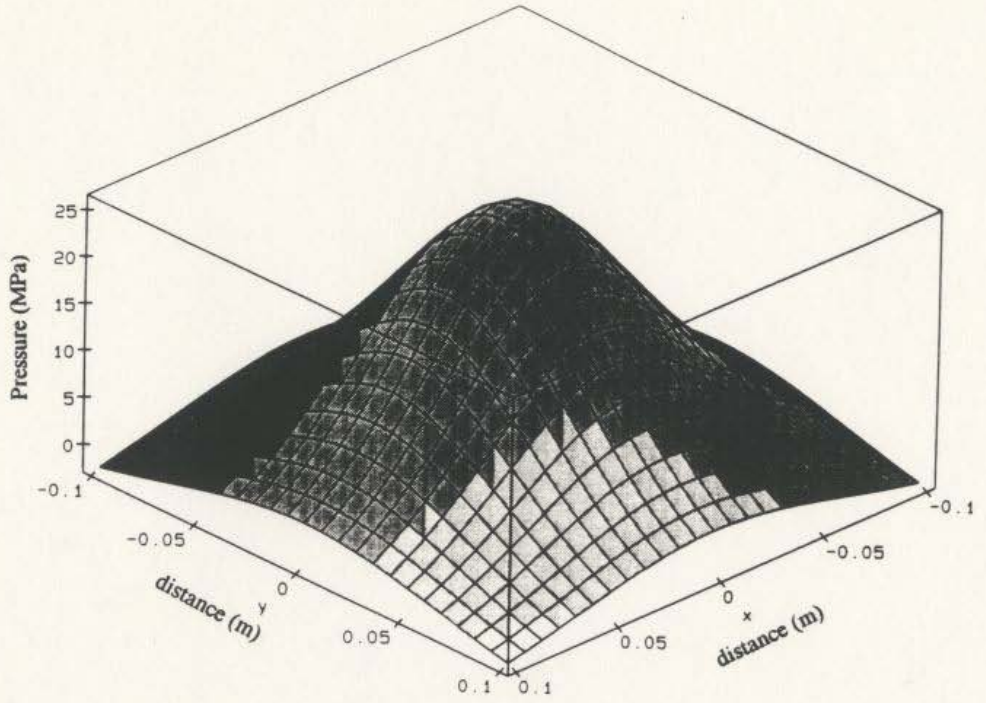

Figure 2.5 (b) Parabolic Distribution of Pressure within a Circular Critical Zone with a 0.10m Radius ($\gamma = 1$)

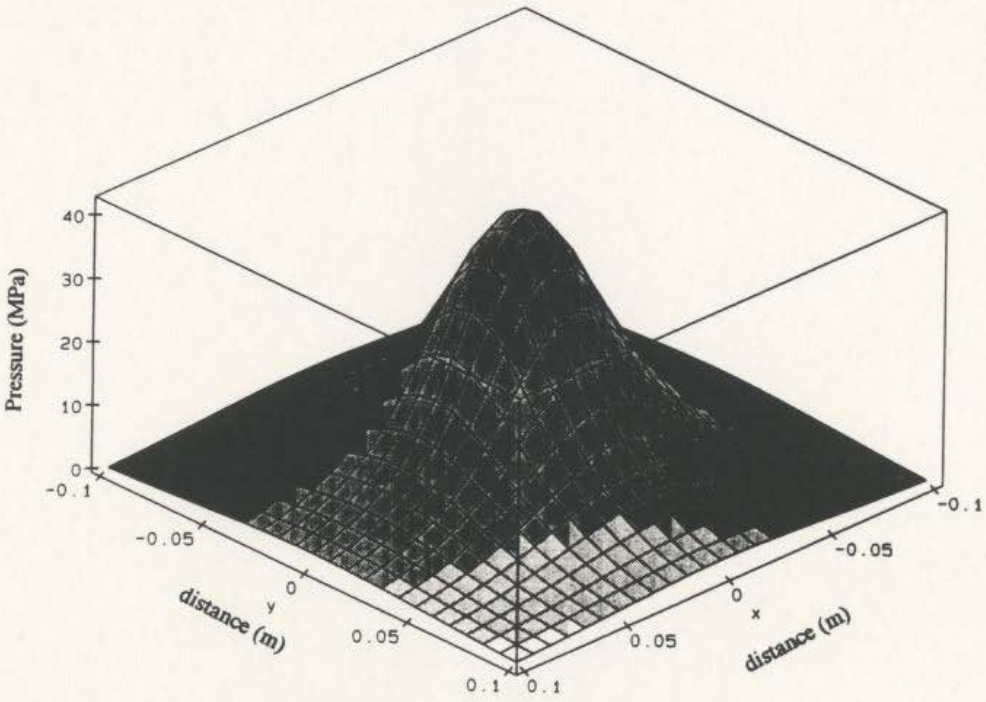

Figure 2.5 (c) Parabolic Distribution of Pressure within a Circular Critical Zone with a 0.10m Radius ($\gamma = 3$)

2.11 Application to Field Data

Jordaan et al. (1990) presented simplified equations governing the force and pressure within a critical zone. The total force associated with a critical zone of given dimension b, shape e, and curvature of the extrusion zone γ , can be calculated by integrating Equation 2.7 over the total area:

$$F_{cz} = \int p_{cz}(r,\theta)\, r\, dr\, d\theta \qquad 2.8$$

$$r^2 \leq b^2 (1-e^2\cos^2\theta)$$

$$0 \leq \theta \leq 2\pi$$

This integral can be solved in a closed form using the mapping $r->r^*=r(1+e^2cos^2\theta^*)^{1/2}$, $\theta->\theta^*=\theta$, which has a Jacobian equal to $r^*/(1-e^2cos^2\theta^*)$. This finally results in:

$$F_{cz} = \frac{\pi M b^4}{4(2-e^2)(1+\gamma)^2(1-e^2)^{1/2}} + p_s \frac{\pi b^2}{(1-e^2)^{1/2}} \qquad 2.9$$

Alternately, since the area of an ellipse is equal to πab, which is the same as $\pi b^2(1-e^2)^{-1/2}$, the above expression may be written as:

$$\bar{p}_{cz} = \frac{F_{cz}}{A_{cz}} = \frac{F_{cz}(1-e^2)^{1/2}}{\pi b^2} = p_s + \frac{Mb^2}{4(1+\gamma)^2(2-e^2)} \qquad 2.10$$

where $\bar{p}_{cz}$ is the average pressure of the entire critical zone.

Referring to Equation 2.6, a general expression for the peak pressure p_o, occurring at the center of the zone ($r = 0$, $\theta = 0$) may be stated as follows:

$$p_o = p_s + \frac{Mb^2 (2+\gamma)}{4(1+\gamma)^2(2 - e^2)} \qquad 2.11$$

Equations 2.9-2.11 are instrumental in the application to field scale data. Using the knowledge of the peak instantaneous pressure in an individual critical zone and the approximate size of the critical zone (both parameters readily available in field data) the force associated with that particular critical zone may be determined. Average pressure over one critical zone may then be calculated from the corresponding total force and area of the zone.

2.12 Critical Zones: Setting a Stress Threshold

In order to determine the size of a typical critical zone a decision must be made about which pressures are considered "critical" on a localized scale. Definition of a "threshold stress" enables the construction of spatial boundaries for the critical zone. The threshold stress is a set pressure above which, areas are deemed "active", and below which, areas are considered "inactive". In this manner the size of a critical zone may be determined.

The threshold stress was determined from two theories that are jointly used to describe the pressure distribution within a critical zone. A clearer picture of the high pressure-area is obtained by assuming the transition from Mohr-Coulomb behavior to viscous flow theory defines the threshold stress for a particular critical zone. Using density and compaction measurements, a distinct boundary may be drawn between the highly centralized fused zone and the granular zone.

Ice in the outer extremities of the critical zone has a density not much different from the initial crushed, granular layer ($0.5g/cm^3$), hence it is suitable for Mohr-Coulomb analysis. Mohr-Coulomb theory has been proven to accurately predict pressure near the edges of the critical zones for all cases, as well as the overall pressure distribution during initial stages of extrusion. The edges of the critical zone are areas of intense activity producing radical variations in the size and shape of critical zones. Spalls and various other forms of damage, ranging from the decomposition of crystal structure to cracking, may occur at the perimeter of the critical zone. Intergranular cohesion and friction significantly influence the distribution of pressure in these regions.

The innermost region, modelled using viscous flow theory, is considered to be incompressible due to significant amounts of compaction which occurred during the initial stages of extrusion. Experiments conducted by Singh et al. (1993) have shown that ice in these highly confined regions has a density close to that of polycrystalline ice ($0.8g/cm^3$). The boundary between the two radically different regions of ice may be used to determine the approximate distance from the center and pressures at which the transition between Mohr-Coulomb and viscous flow theories occurs.

Previous work by Jordaan et al. (1990) demonstrated that the transition may occur between 35-50 percent of the radial dimension of the critical zone (see Figure 2.6). Experiments conducted on crushed ice show that the fused zone approximates 150cm radially from the center of the critical zone. This value is a very rough estimate considering that zonal dimensions vary in time with pressure, the failure mechanism, and the crushed layer thickness. Crushed ice extrusion tests (Singh et al., 1993) indicate that the transition from Mohr-Coulomb to viscous flow occurs roughly at 40 percent of the short axis dimension of the critical zone. Stresses corresponding to this transition point may be approximately 20-40 percent of the peak pressure at the center of the critical zone. Using this criterion the transition from Mohr-Coulomb to viscous flow theory occurs at a pressure of 2MPa, a reasonable value according to the crushed ice tests.

Definition of a threshold stress enables a distinction to be made between regions of high pressure and regions of background pressure. The approximate size, force, and pressure of the critical zones may be determined from field scale data, based upon the previously discussed ideas. The concept of critical zones may be directly applied to the medium scale indentation tests, discussed subsequently.

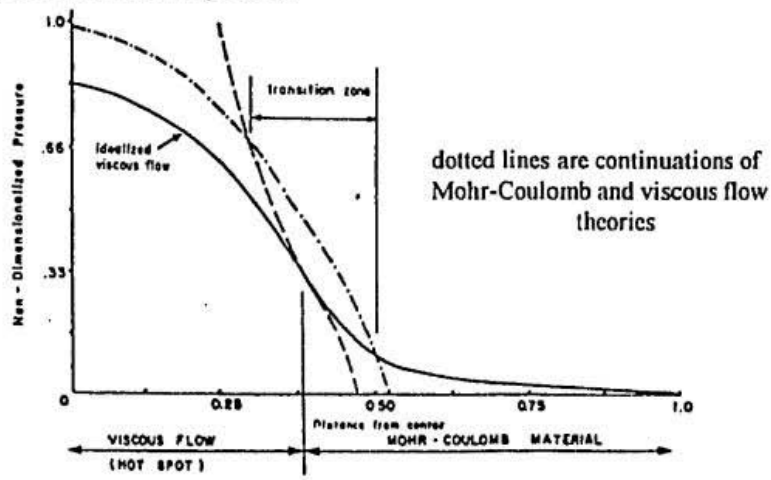

Figure 2.6 Transition from Mohr-Coulomb to Viscous Flow Behavior (Jordaan et al., 1990)

Chapter 3

Medium Scale Ice Indentation Tests

3.1 Introduction

Ice indentation tests provide a controlled environment in which to observe ice failure. An investigation into the contact pressures generated by various interaction geometries and indentor stiffnesses was conducted at Hobson's Choice Ice Island in 1989 and 1990. Data from the 1989 and 1990 Ice Island Program provide a basis for the practical application of the critical zone concept. Numerous pressure cells installed on the face of the indentor documented the rapidly fluctuating pressures across the contact area as penetration proceeded. The actuator force was also recorded, enabling a comparison to be drawn between the applied load and the predicted force of the critical zone.

The Ice Island was a 20km^2 ice floe that calved from the Ward Hunt Ice Shelf in 1982. Located northwest of Ellef Ringnes Island, the 45m thick shelf ice was bounded on either side by multiyear landfast sea ice and multiyear pack ice (see Figure 3.1). The indentation experiments were conducted in consolidated pack ice, 10-11m in thickness. Crystallographic analysis of cores taken at the test site revealed layers of snow ice, frazil ice, and columnar ice, with salinities ranging from 0‰ to 4‰ (Gagnon and Sinha, 1991).

MLSI:	multiyear landfast sea ice previously attached to the front of Ward Hunt Ice Shelf and still attached to the ice island
MYPI:	multiyear pack ice that has become attached and consolidated since the ice island calving

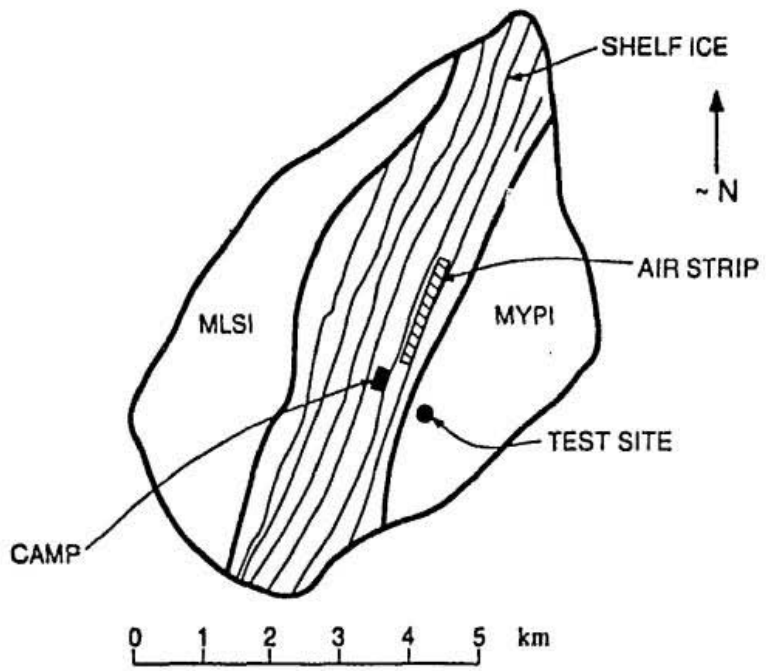

Figure 3.1 Location of Test Site on Hobson's Choice Ice Island
(Frederking et al., 1989)

A description of the ice indentation system was provided by Frederking et al. (1990). In contrast to the three actuator configuration for the 1990 test program, the 1989 test series used a single hydraulic actuator, mounted upon a large skid for facilitation of positioning. The single actuator had a force capacity of 4.5MN, a stroke of 300mm, and a maximum velocity of 100mm/s. The actuator motion was controlled by a servovalve which operated under closed loop control. Energy to operate the actuator was supplied from a bank of hydraulic accumulators (oil over air pressurized to 35MPa). A high speed data acquisition system was used to record local ice pressures, the actuator force, and the displacement with respect to the ice face. Scan rates as high as 1000 readings per second for each channel were used.

The tests were performed in an excavated trench, 3m deep and 65m long. The indentor was lowered into the trench and towed the three meter distance between successive test faces. The indentation surface was molded into a truncated vertical wedge, with shallow sloping sides at 1:3 and a flat face. The wedge shape was selected to ensure an initial contact area sufficiently small to initiate crushing failure at a load less than the capacity of the actuator (Frederking et al., 1989). The vertical wedge also allowed for the rapid increase of contact area with penetration of the indentor into the ice.

Two tests from the 1989 test program have been selected for analysis, NRC06 and NRC07 (see Table 3.1). Both tests used an $0.8m^2$ compliant indentor, designed to simulate the hull section of a ship. Loads and pressures measured with the flat flexible and flat rigid indentors are similar in value, indicating that the indentor stiffness does not significantly affect ice pressures and loads (Masterson et al., 1993). Additionally, velocity was not found to have a substantial effect upon nominal ice pressures. The data recorded during tests NRC06 and NRC07 may be applied to a wide range of loading conditions.

Table 3.1 Test Results of 1989 Ice Indentation Program

(Frederking et al., 1989)

Test Number	Ice Face Shape	Rate (mm/s)	Max Load (MN)	Loading Period (s)	Initial Area (m^2)	Final Area (m^2)	Ice Pressure (MPa)*
NRC06	120mm 1:3 slope	19	1.8	1.9	0.12	0.24	6.7
NRC07	240mm 1:3 slope	68	4.5	0.4	0.24	0.37	12.2

* maximum average ice pressure

The flexible indentor was constructed from 17mm thick plate, welded to stiffeners at a 300mm spacing. It conformed to the current proposals for revision to the Canadian Arctic Shipping Pollution Prevention Regulations (CASPPR). These revisions predict ice pressures ranging from 7.7MPa to 15.4MPa, depending upon the class of ship, for a 300mm frame spacing. Based upon a plate thickness requirement of 20-28mm for 310MPa steel, plastic deformation could be expected in the 17mm thick plate selected for the indentor. No permanent deformation was observed after NRC06 (maximum average pressure 6.7MPa). Permanent deformations of 17, 4, and 13mm were observed in the center of each of the three indentor panels after NRC07 (maximum average ice pressure 12.2MPa).

Extreme pressure gradients existed across adjacent pressure cells on the indentor face. Total load versus penetration and nominal pressure versus penetration typically exhibited high frequency sawtooth behavior, particularly at high rates of indentation, accompanied by vibrations of the order of 20-40Hz (Masterson et al., 1993). The dynamics of the indentation process indicate load buildup followed by pulverization and an enhanced rate of ice extrusion.

3.2 Characterization of the Failure Zone

The following discussion of the failure zone is based upon an analysis of the 1990 Hobson's Choice test series by Meaney et al. (1991). The analysis is taken as representative of both the 1989 and 1990 field tests.

Crushing was observed during indentation for all tests. Characteristically, a fine matrix of ice particles was ejected from the perimeter of the interaction zone. Three regions were identified in the impacted area. First, spalled areas were present at the periphery of the contact surface. There was also evidence of zones of crushed or pulverized ice, generally associated with lower pressures and of a white or lighter hue. The whitish hue may be caused by pockets of air which became entrained in the ice during the crushing process. Third, regions of blue or darkly shaded areas existed where the crushed layer was absent. The dark blue regions appeared undamaged when viewed on a macroscopic scale. However, thin section analysis of the darkened regions revealed significant damage to the crystal structure. Typically, these regions occurred at the ice-indentor interface and immediately behind the crushed layer.

Transition from the crushed ice to the parent ice was generally quite distinct (Frederking et al., 1990). The crushed layer was designated as pulverized or sintered material, white in color, and usually isolated from the less granular material behind it by an individual macrocrack or a network of cracks. This layer typically contained large, 25mm diameter or greater, relatively undamaged particles surrounded by finely pulverized ice. It was noted during the test program that the crushed material at the periphery of the contact face appeared to be less consolidated than the material at the center. Ice near the edge of the contact area was soft and could be easily broken off by hand (Frederking et al., 1990). Ice was quite solid near the center of the contact area. The ability to extract an ice sample from the crushed layer and prepare thin sections suggests that the material may have undergone pressure melting and sintering during the interaction.

Crushed layer profiles were obtained by measuring the layer thickness on an incremental grid imposed on the impacted face. The surface in Figure 3.2 represents the test face with the crushed layer removed. Peaks correspond to a crushed layer thickness of zero. A mean crushed layer thickness of 41mm, with the maximum thickness reaching 173mm, was obtained for the first test of the 1990 program. The crushed layer is thinnest in the stiffened regions. Contrary to what one might have expected, zones of intense pressure did not coincide with areas in which no distinct crushed layer existed. This was shown by an analysis that superimposed the final recorded pressures on the interaction area (Meaney et al., 1991). A comparison of damaged ice at equal distances from the ice-indentor interface revealed that ice situated behind the crushed layer sustained less damage than ice behind regions without a crushed layer. It was postulated that the pulverized material acted as a buffer for the mechanical energy input by the indentor (Meaney et al., 1991).

Thin section analysis revealed significant damage in regions where the crushed layer was absent. The term "intact" ice is a misnomer. The darkened regions of ice should not be considered characteristic of the virgin material. In contrast to the parent crystal structure of 5-10mm, regions with no distinguishable crushed layer are characterized by a finegrained matrix with grain sizes of the order of one millimeter. In all zones, the severity of damage decreased with increasing distance from the ice-structure interface.

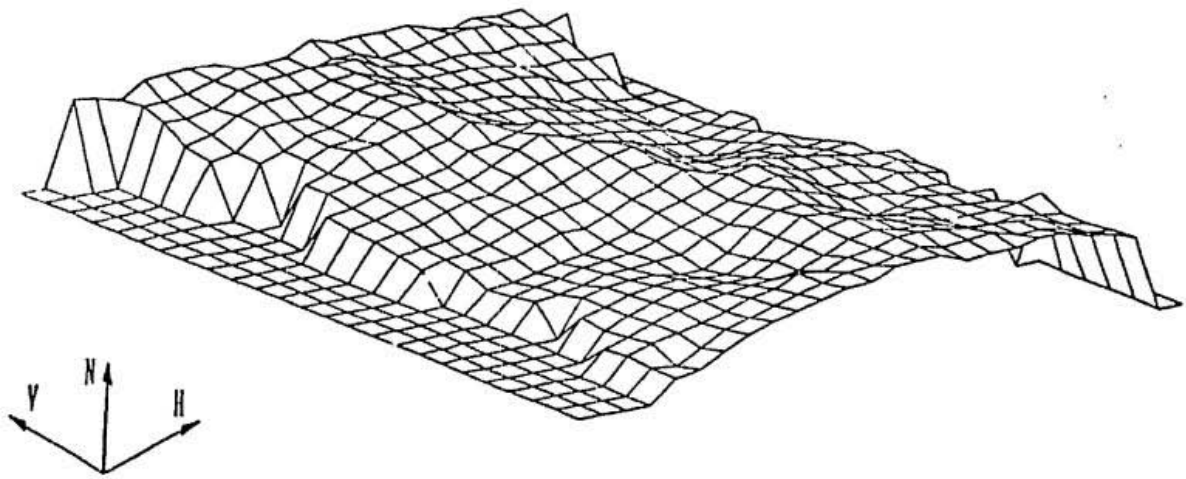

Figure 3.2 Surface Profile of Impacted Face with Crushed Layer Removed
(Meaney et al., 1991)

3.3 Distribution of Pressure within the Contact Zone

As previously discussed, critical zones are regions of ice that are subject to extreme pressures. These zones, highly variable in space and time, sustain extensive damage. Healing of the ice through the combined processes of pressure melting and sintering forms a matrix similar to the parent material, which is capable of supporting pressures of the order of 70MPa. Unlike the parent ice, the fused matrix has a higher compliance and is more prone to viscous flow.

The indentor plating was instrumented with eight 12.7mm diameter pressure sensors (Figure 3.3). The sensors provide valuable information about the fluctuating pressures within the contact area. Typically, a sawtooth pattern was characteristic of all pressure transducers (see Figure 3.4). Intense pressures across the contact area indicate the presence of critical zones. An investigation into the spatial and temporal variations of pressure across the contact area was conducted by analyzing individual cycles of sawtooth dynamics. Figure 3.5 presents three cases chosen for NRC06, where the mean pressure was obtained by averaging data from the activated transducers. The cyclical rise and abrupt decline of loading were examined in detail at numerous points for the three cases (see Figure 3.6 for cases I, II and III).

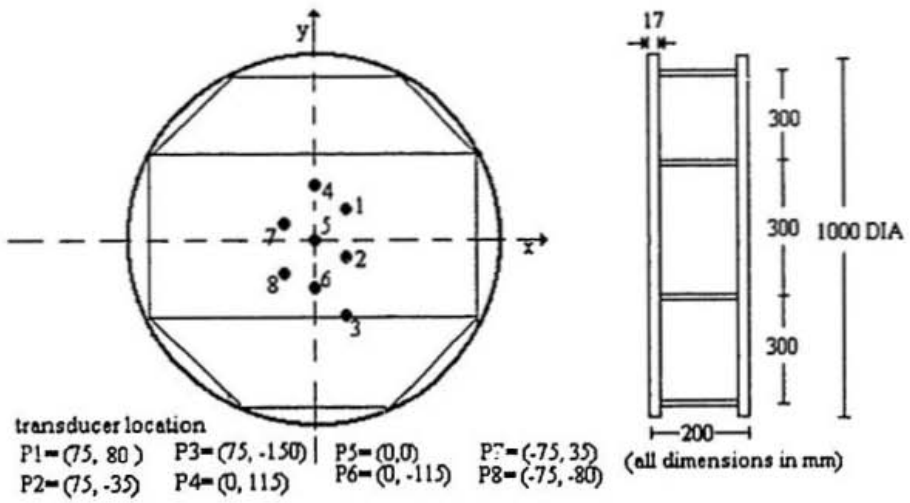

Figure 3.3 Location of Pressure Sensors on the Flexible Indentor

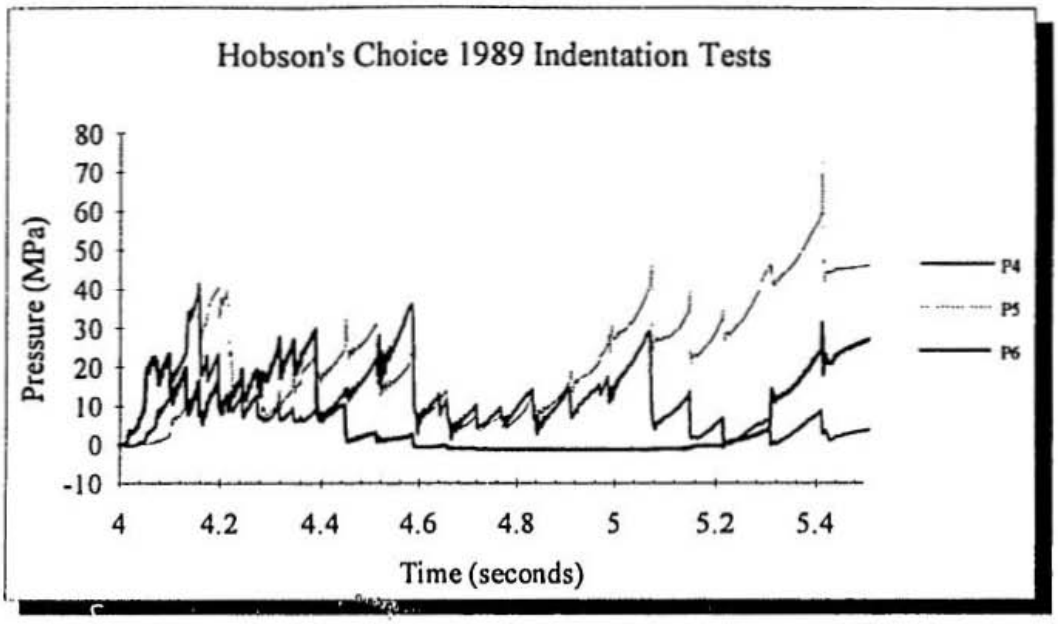

Figure 3.4 Characteristic Sawtooth Pressure Pattern for NRC06 (sensors P4-P6)

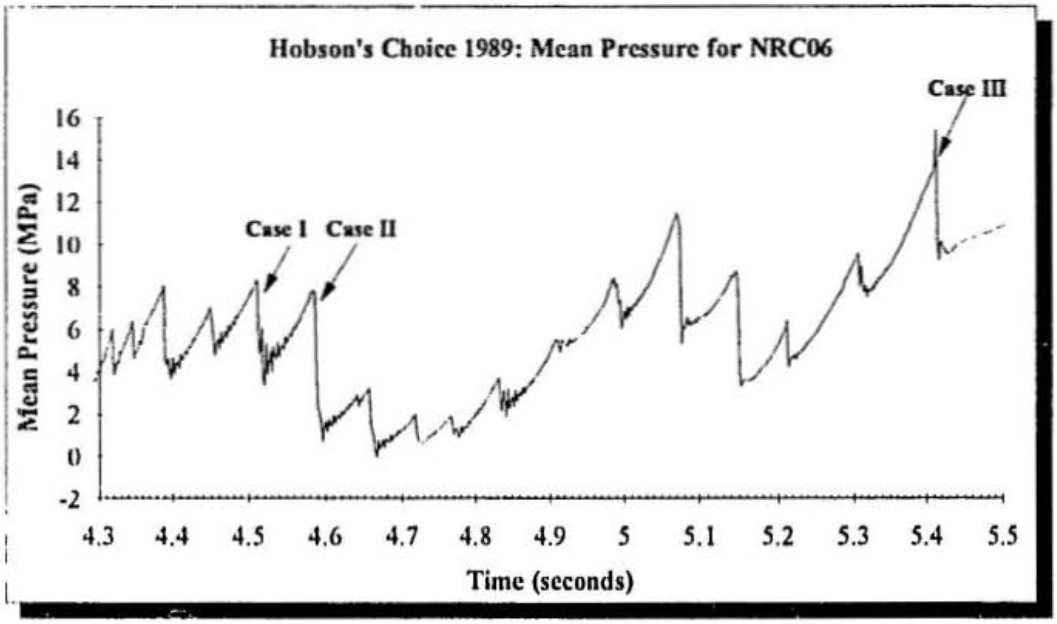

Figure 3.5 Cases Chosen for a Detailed Analysis of NRC06

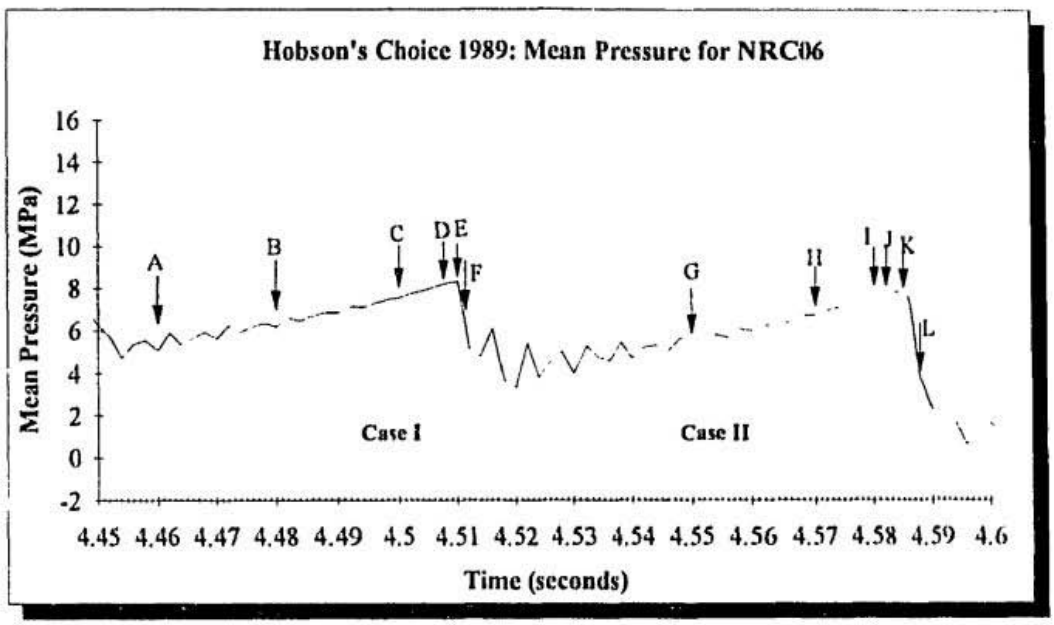

Figure 3.6 Cases I and II: Selected Points for the Examination of Critical Zones

A visual presentation of the active transducers for selected points in time is presented in Figure 3.7. All transducers above a 2MPa threshold stress are considered active, hence they are shaded. Regions of intense pressures are limited to very small areas, usually encompassing only 3-4 transducers. A comparison of the actuator force to the force of the critical zone reveals that the critical zone accounts for as much as 98 percent of the total load exerted on the contact zone. The force of a critical zone (directly proportional to its radial extent and to its average pressure) is underestimated when the high pressure zone extends beyond the instrumented area.

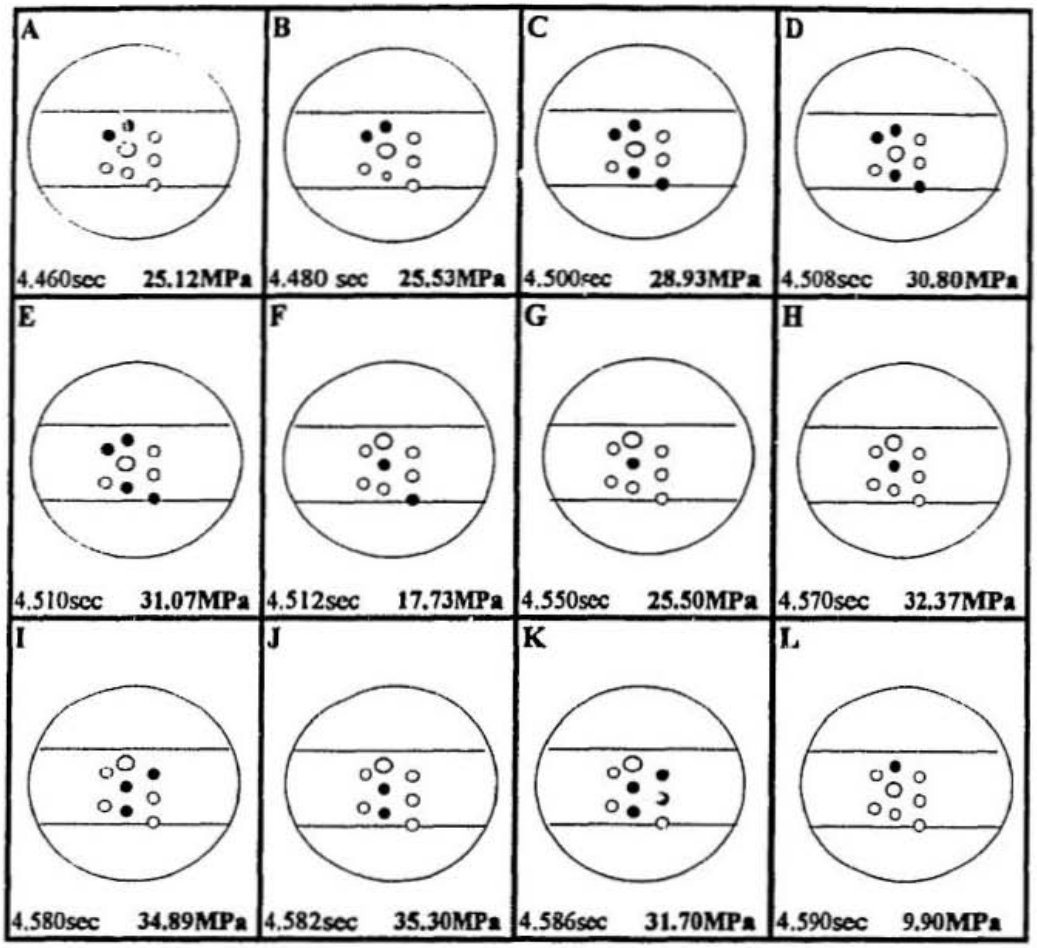

○ Indicates transducer of maximum pressure
Instantaneous peak pressure noted in lower right corner

Figure 3.7 Critical Zone Activity for Cases I and II, NRC06

Tests conducted on the extrusion of crushed ice (Singh et al., 1993) indicate that in areas of high pressure, ice failure occurs at the perimeter of the critical zone, where the ice is less dense and more prone to viscous flow. Failure then proceeds inwards towards the center of the critical zone. The sequence of events that occurs during the failure process has a pronounced effect upon the pressure distribution in the critical zone. Once failure is initiated, the pressure in the center of the critical zone suddenly increases and the pressure distribution momentarily becomes concave. The higher pressure near the center of the critical zone forces ice in this area out towards zones of lower pressure, creating a convex pressure distribution.

Indentation tests also provide evidence of the above mentioned failure process. Case I shows the gradual inclusion of an increasing number of transducers as the load rises from point A to point E (Figure 3.7, previous page). Immediately after point E, the ice fails and there is a substantial decrease in pressure. The region of background pressure increases while the radial extent of the critical zone decreases. Within 0.002 seconds a 58 percent reduction in the area of the critical zone occurs. The critical zone shrinks from 0.044m^2 to 0.026m^2, with the largest drops in pressure occurring on transducers P5, P6, and P7 (see Table 3.2). As the size of the critical zone decreases so does its corresponding force. Similarly the greatest decrease in pressure for Cases II and III occurs in the central region of the critical zone (see Figures 3.8-3.11).

Table 3.2 Pressure Decreases for Individual Transducers

	Pressure Decrease (MPa)			
	NRC06			NRC07
Pressure Cell	Case I (E-F)	Case II (K-L)	Case III (Q-R)	Case I (D-E)
1	-1.2MPa	+0.8MPa	-2.2MPa	-4.5MPa
2	+1.1	+0.7	+2.0	-1.8
3	-0.9	-0.1	+0.1	-0.1
4	-5.0	-23.2	+0.5	-2.4
5	-14.7	-14.7	-25.7	0.0
6	-2.4	-2.8	-13.0	-13.3
7	-5.2	-0.2	0.0	-4.8
8	-0.1	+0.50	+0.6	-13.62

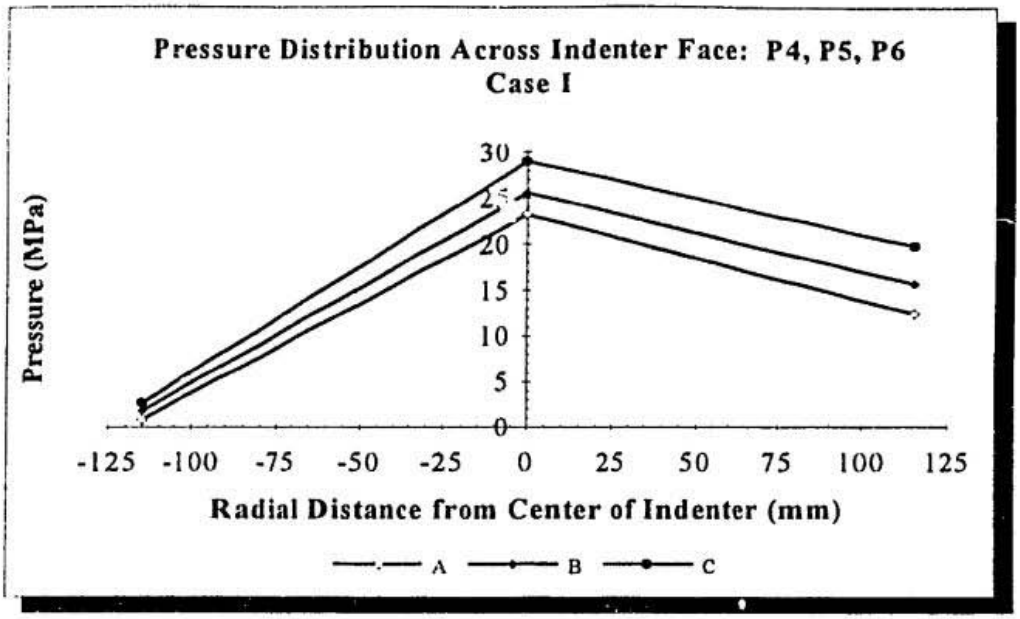

Figure 3.8 (a) Case I: Pressure Fluctuation Across Central Cells (Points A-C)

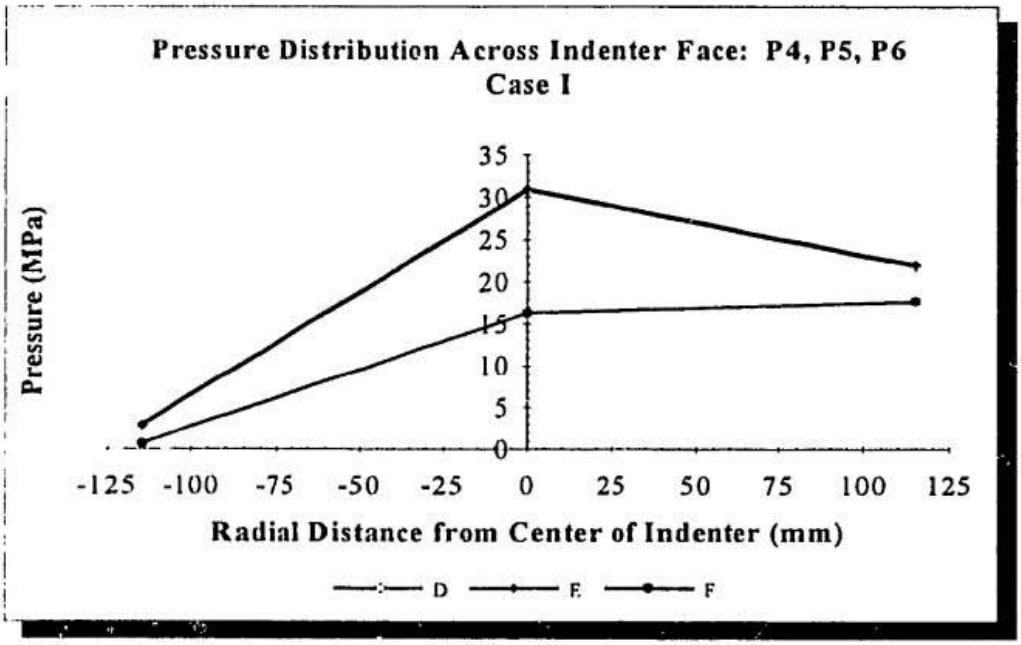

Figure 3.8 (b) Case I: Pressure Fluctuation Across Central Cells (Points D-F)

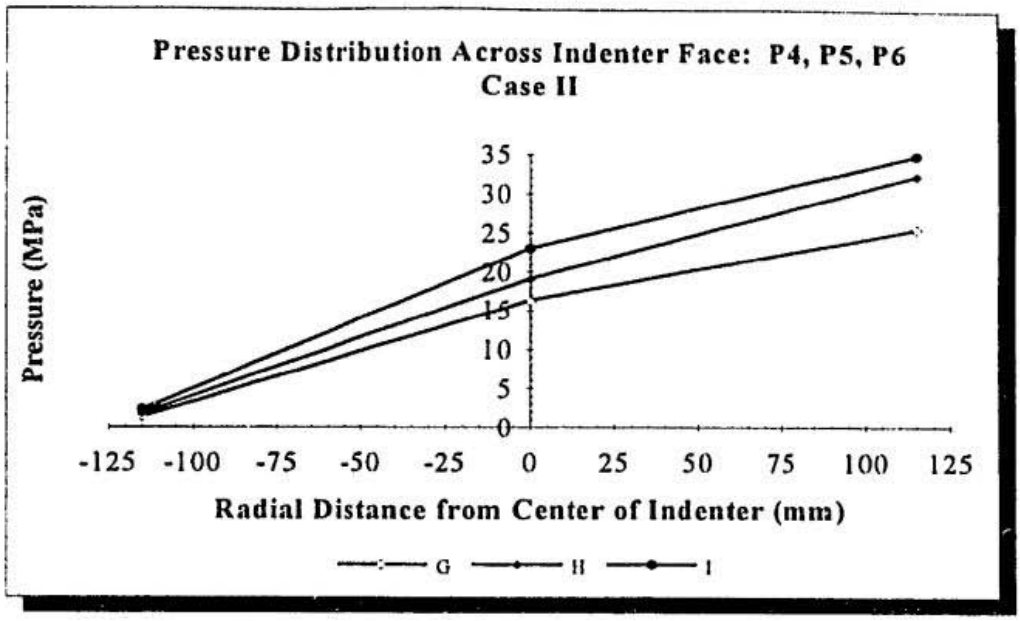

Figure 3.9 (a) Case II: Pressure Fluctuation Across Central Cells (Points G-I)

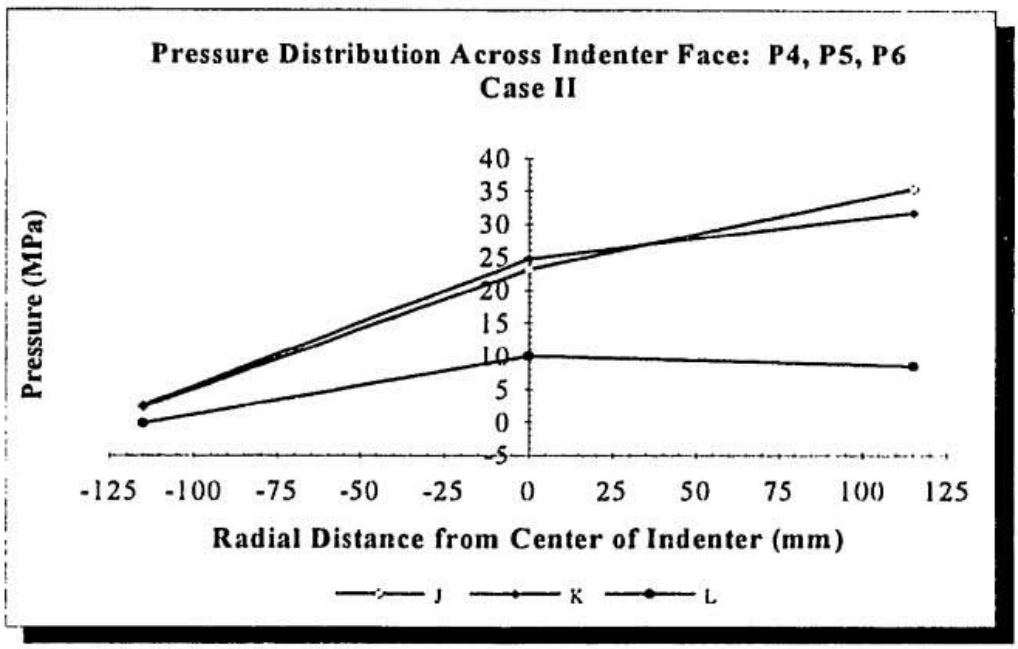

Figure 3.9 (b) Case II: Pressure Fluctuation Across Central Cells (Points J-L)

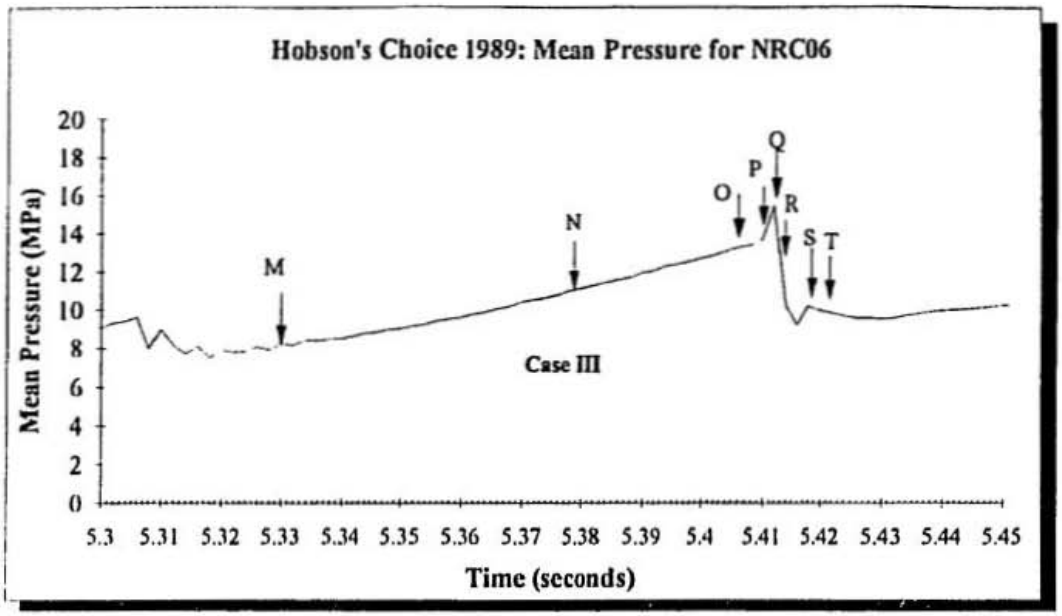

Figure 3.10 Case III: Selected Points for the Examination of Critical Zones

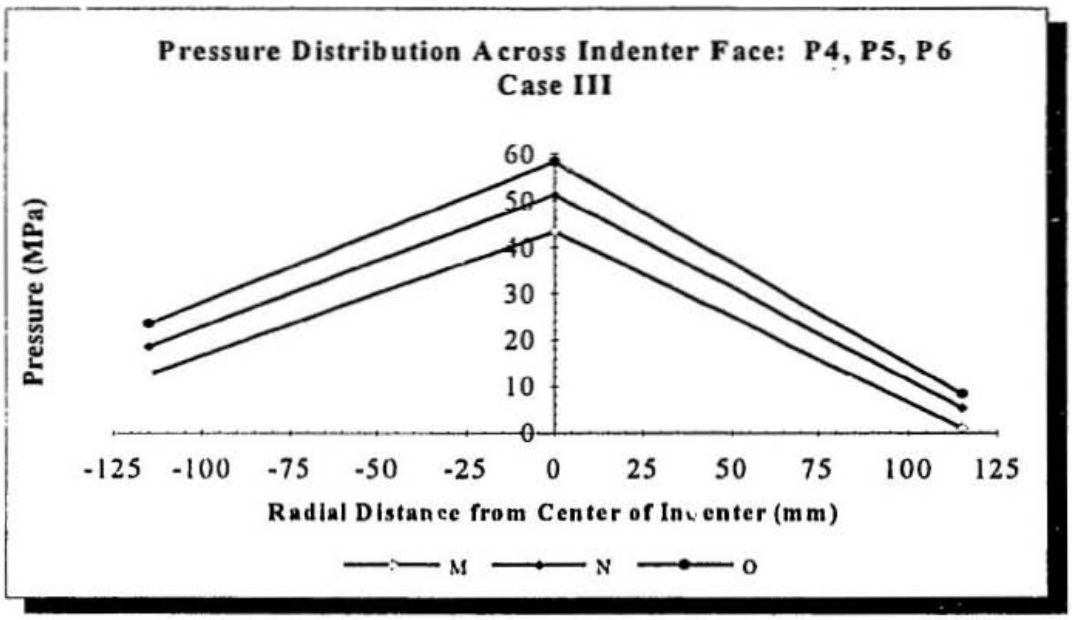

Figure 3.11(a) Case III: Pressure Distribution Across Central Transducers (Points M-O)

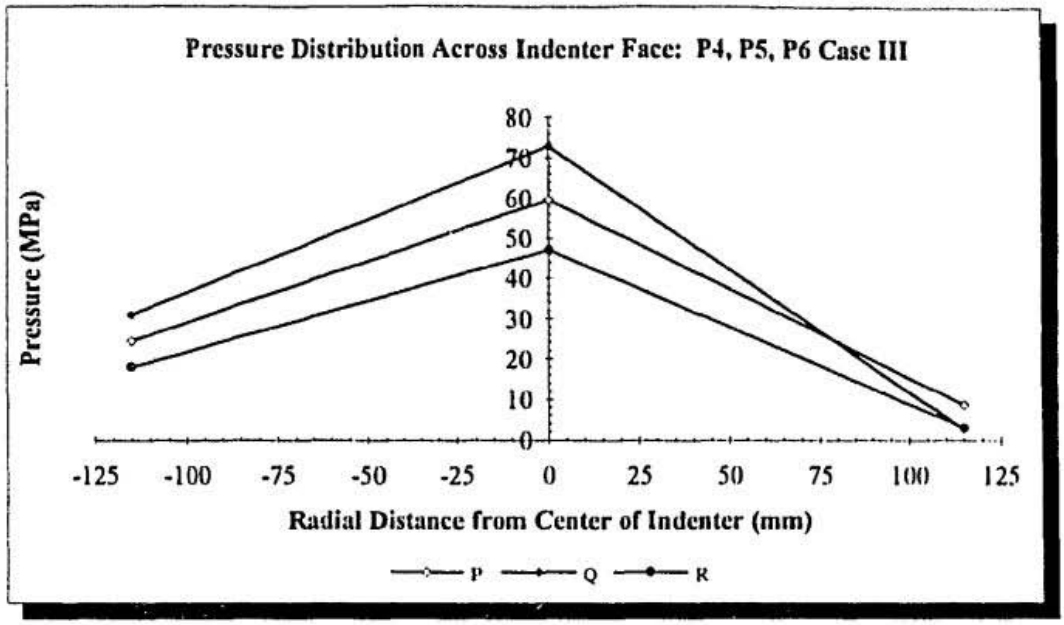

Figure 3.11 (b) Case III: Pressure Distribution Across Central Transducers (Points P-R)

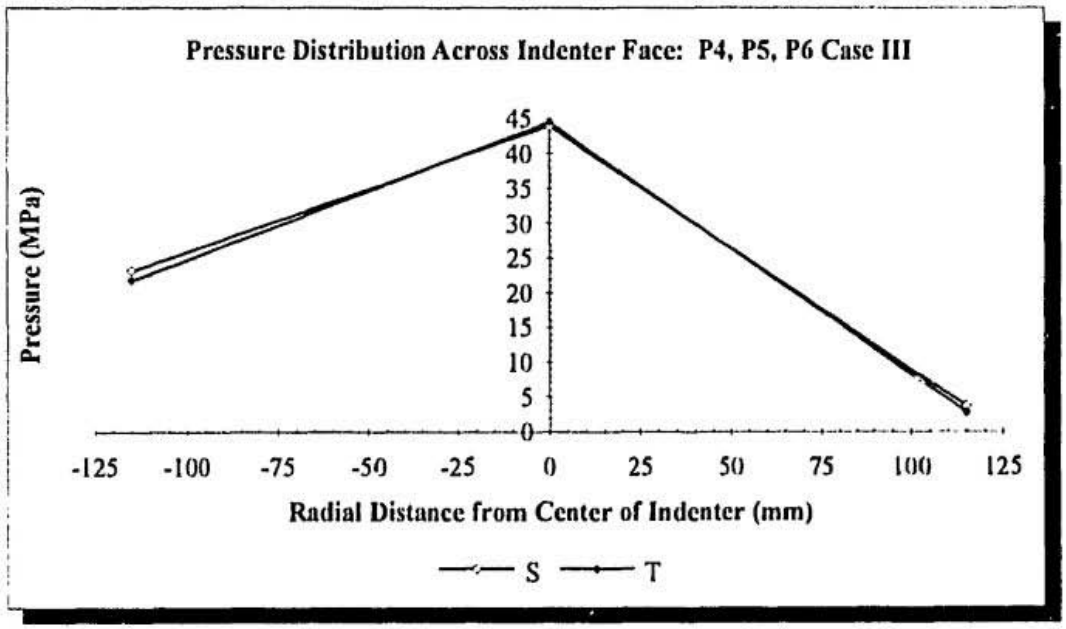

Figure 3.11 (c) Case III: Pressure Distribution Across Central Transducers (Points S-T)

Case III documents the greatest single difference in pressure on one transducer at consecutive instants in time. During the 0.002second interval between Q and R, pressure decreases of 25MPa and 13MPa were registered on P5 and P6, respectively. Less radical drops in pressure occurred towards the periphery of the zone. A decrease in the critical zone area was expected to occur as a result of the drop in central pressure. A reduction in the radial extent of the critical zone after ice failure was evident from Cases I and II. Similarly, the size of the critical zone should decrease during Case III. However, since the full extent of the critical zone was not detected by the relatively small region of instrumentation, the high pressure zone appears to remain constant (point Q to point S in Figure 3.12). Fluctuations in area occur at the perimeter of the zone, in a region which extends beyond the instrumentation.

The abrupt failure after load buildup for Case III was further investigated by constructing three dimensional pressure distributions for several instants in time (see Figures 3.13-3.15). The time intervals 5.411sec, 5.413sec and 5.417sec correspond to points Q, R, and S in Figure 3.10. In addition to demonstrating the spatial and temporal variability of the critical zones, the three dimensional plots confirm that the zonal distribution of pressure may be accurately modelled as a paraboloid (see Chapter 2). Contour plots of the pressure distribution over the instrumented area accompany the three dimensional graphs. The two dimensional representation of the pressure distribution illustrates the steep gradient between the critical zone and the surrounding regions of background pressure.

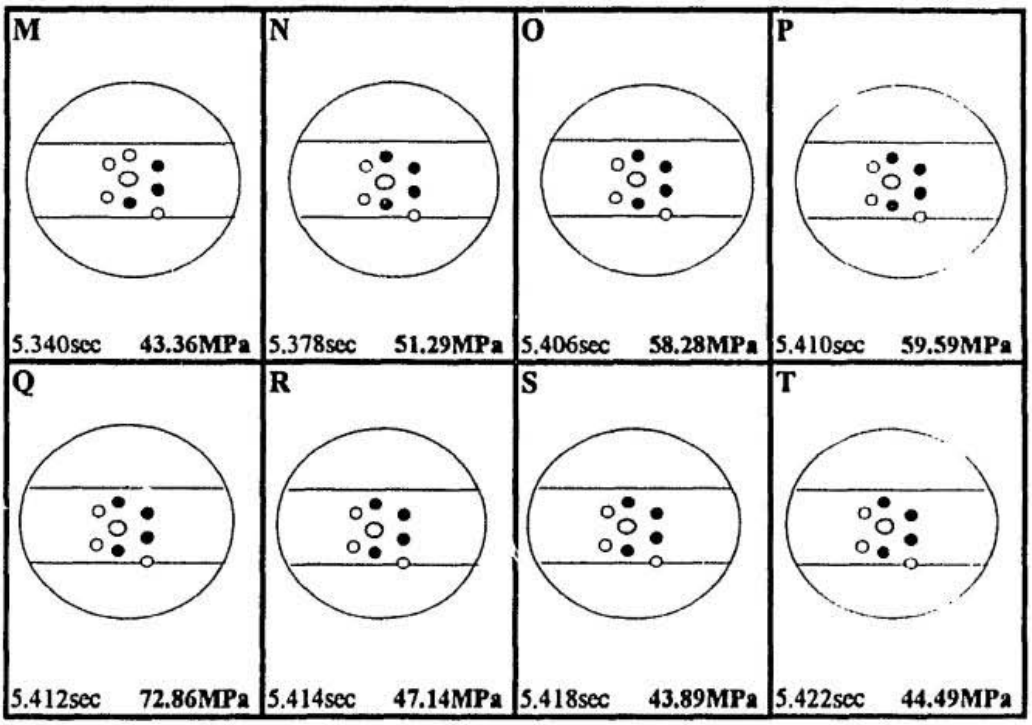

○ Indicates transducer of maximum pressure
Instantaneous peak pressure noted in lower right corner

Figure 3.12 Critical Zone Activity for Case III

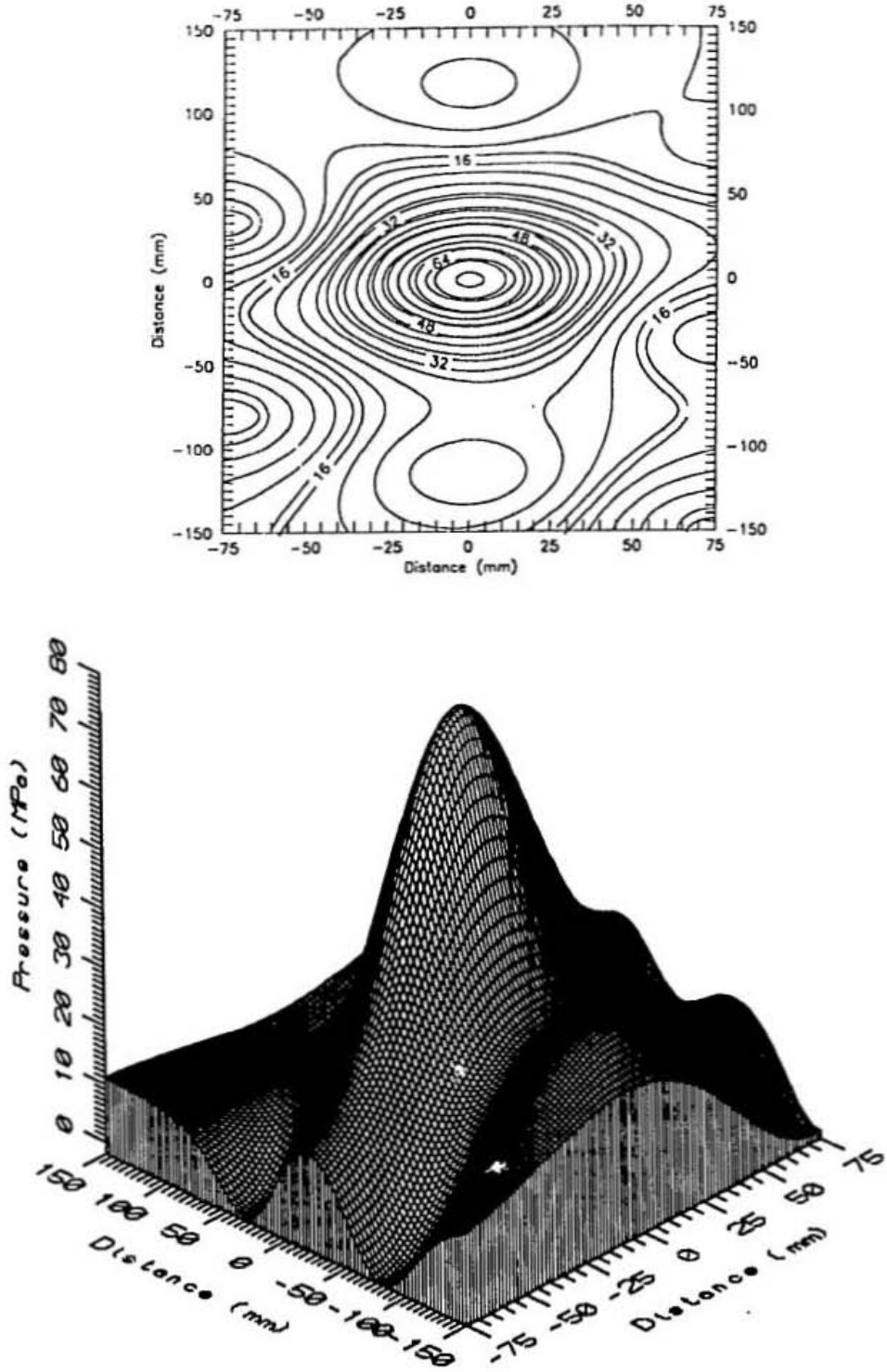

Figure 3.13 Three Dimensional Pressure Plot Accompanying Contour Plot of NRC06 Case III (Point Q)

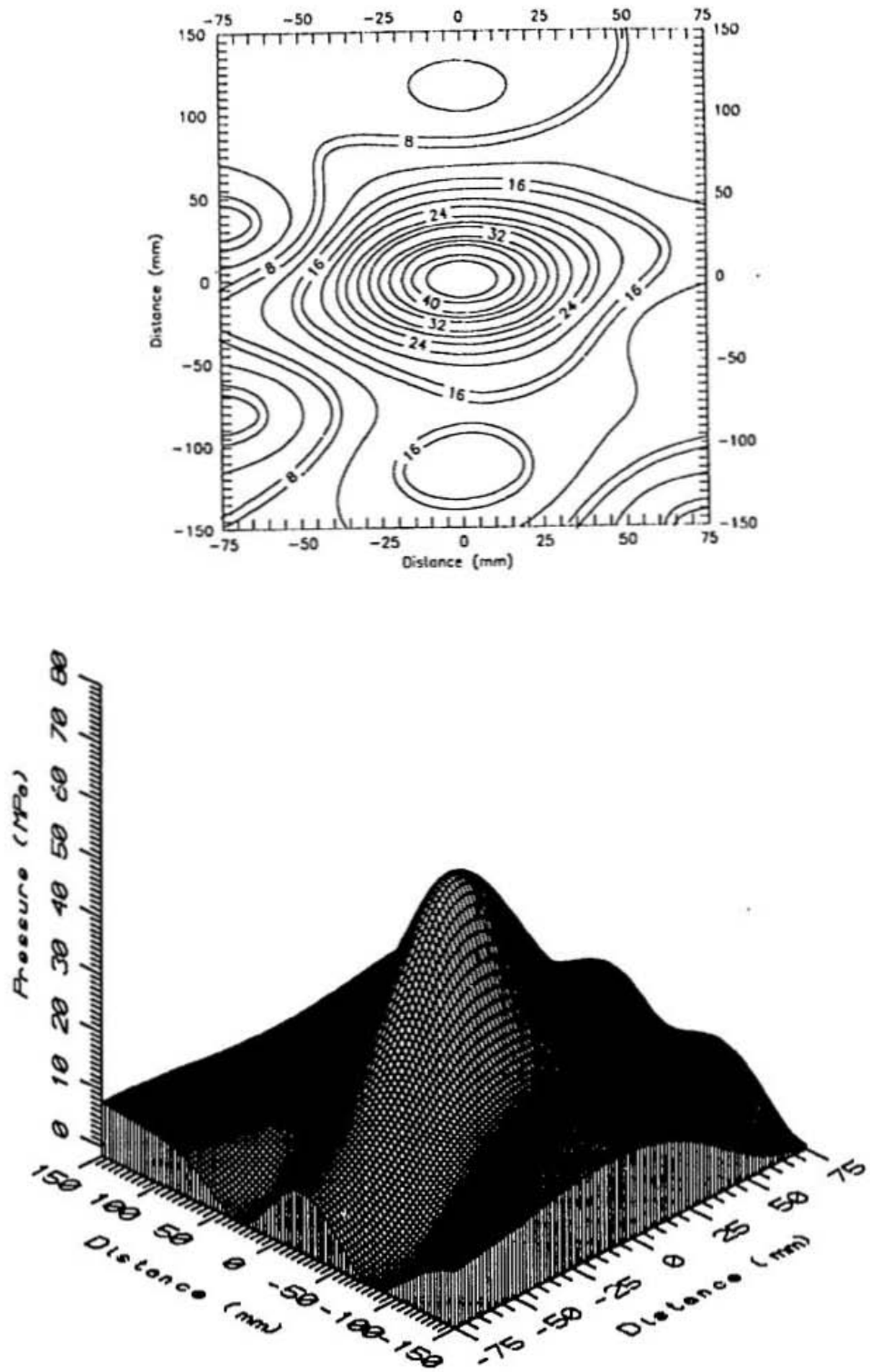

Figure 3.14 Three Dimensional Pressure Plot and Accompanying Contour Plot of NRC06 Case III (Point R)

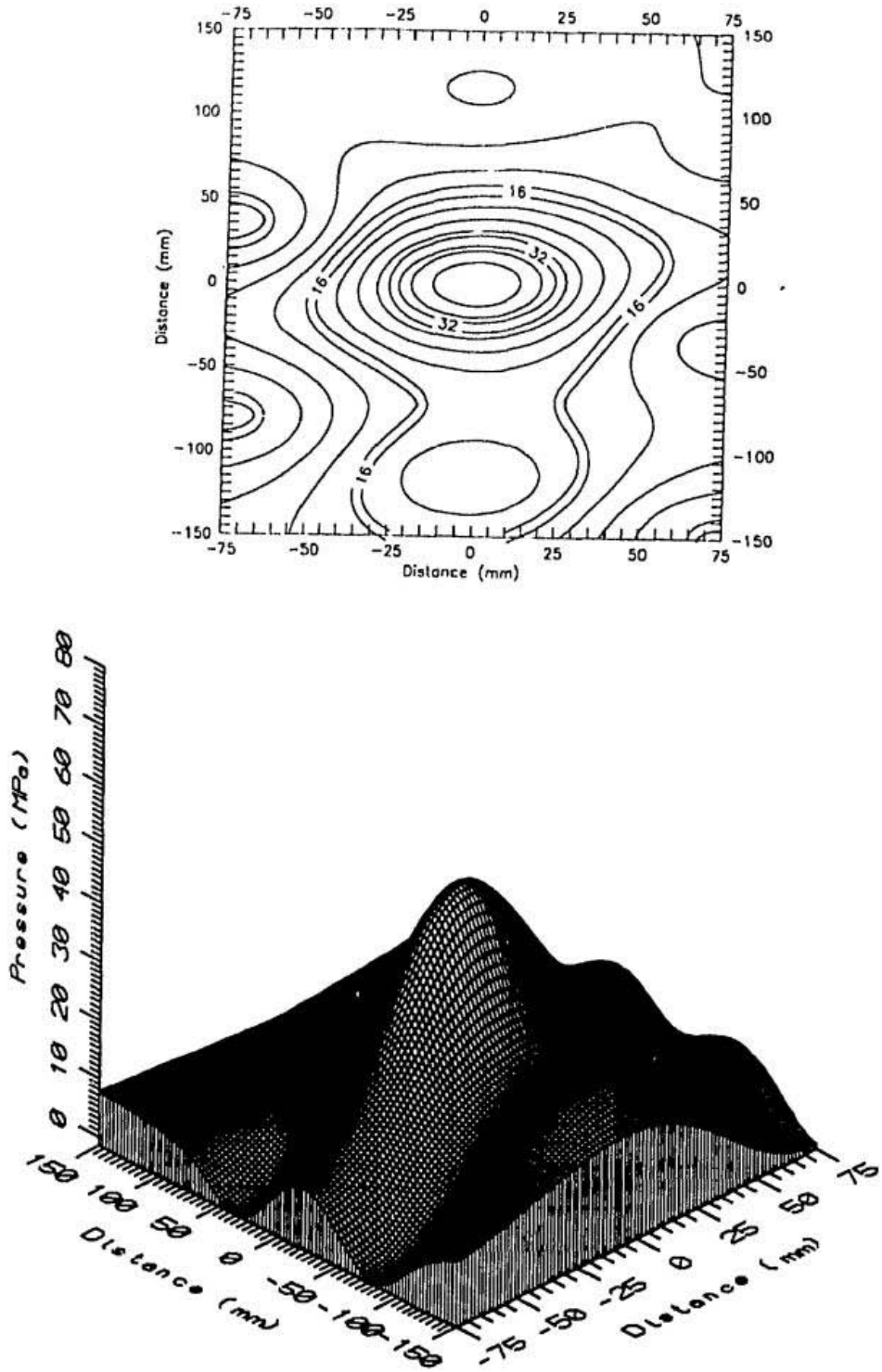

Figure 3.15 Three Dimensional Pressure Plot and Accompanying Contour Plot of NRC06 Case III (Point S)

3.4 Extrapolation of the Critical Zone Area Beyond the Instrumented Region

During ice-structure interaction, the contact area is comprised of three distinct regions of pressure, i.e. critical zones, background regions, and spalled areas. The high pressure zone supports a major portion of the applied load. Regions of background pressure account for the remainder of the applied load, which is expected to be minimal. Spalled areas have no load bearing capacity. The 4.15-4.20 second interval of NRC06 demonstrates that the force of the critical zone, as estimated from the pressure sensor data, represents 98 percent of the actuator force (see point A, Figure 3.16). Subsequent to this interval, the comparison between the critical zone and actuator force reveals a consistent underprediction of the critical zone force (over the instrumented area). The average force of the critical zone for combined tests NRC06 and NRC07 is 0.82MN, only 43 percent of the mean actuator force.

The underprediction of the critical zone force (see Figures 3.16, 3.17) may be attributed to the small region of the indentor that was instrumented. While the pressure cells are an excellent indication of what is happening at the center of the indentor, they do not provide information about other regions of the interaction zone. The difference between the actuator and critical zone force increases as the interaction proceeds, i.e. as the contact area broadens. During the initial stages of loading, the critical zone approximates a shape previously identified as a "contact line" (Riska, 1987). As the indentor advances, the critical zone widens, occupying a circular area which, typically, extends beyond the instrumented region (Figure 3.18). At best, the pressure sensors account for only 23 percent and 13 percent of the contact areas for NRC06 and NRC07, respectively. Consequently, there is an improved correlation between the compared forces for NRC06.

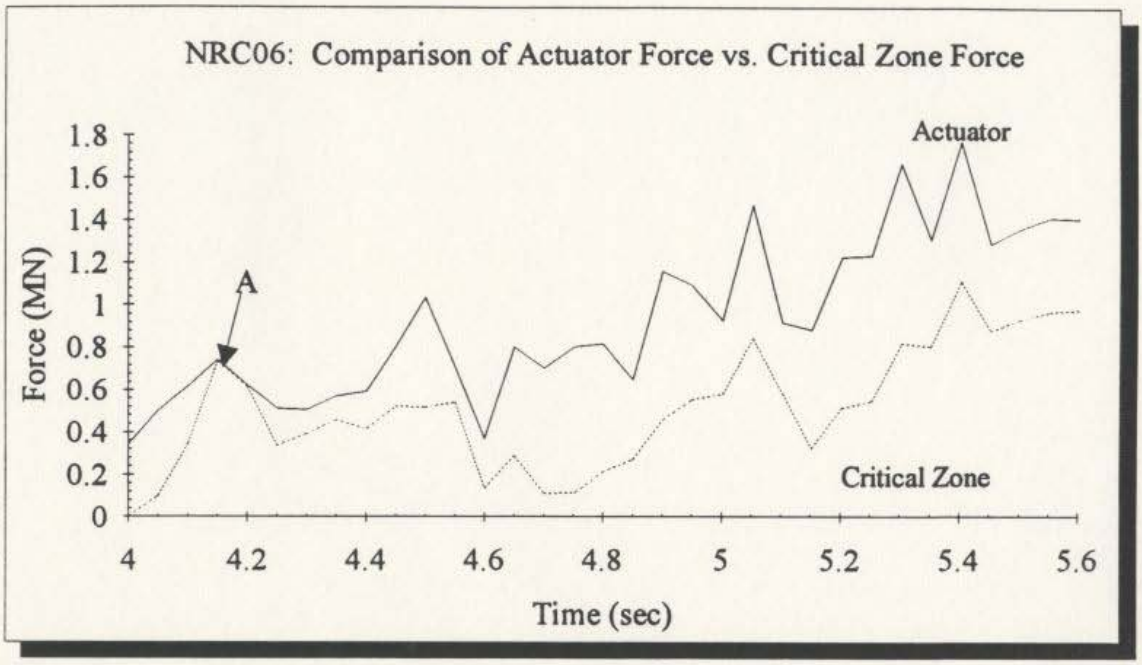

Figure 3.16 Actuator Force in Comparison to the Force of the Critical Zone over the Instrumented Area for NRC06

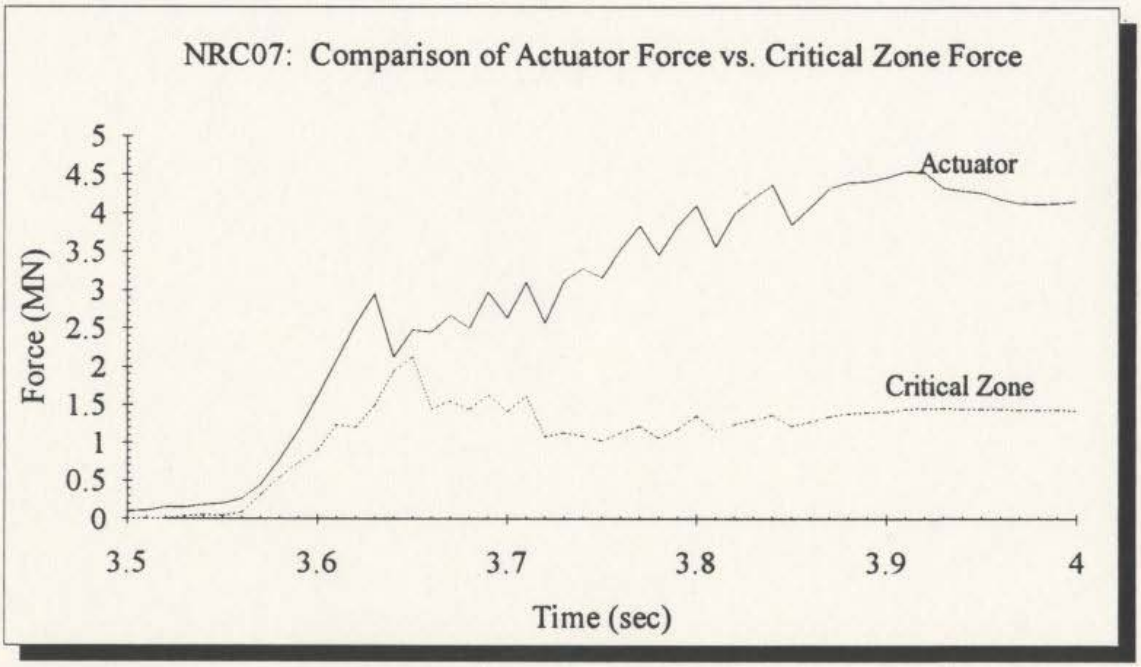

Figure 3.17 Actuator Force in Comparison to the Force of the Critical Zone over the Instrumented Area for NRC07

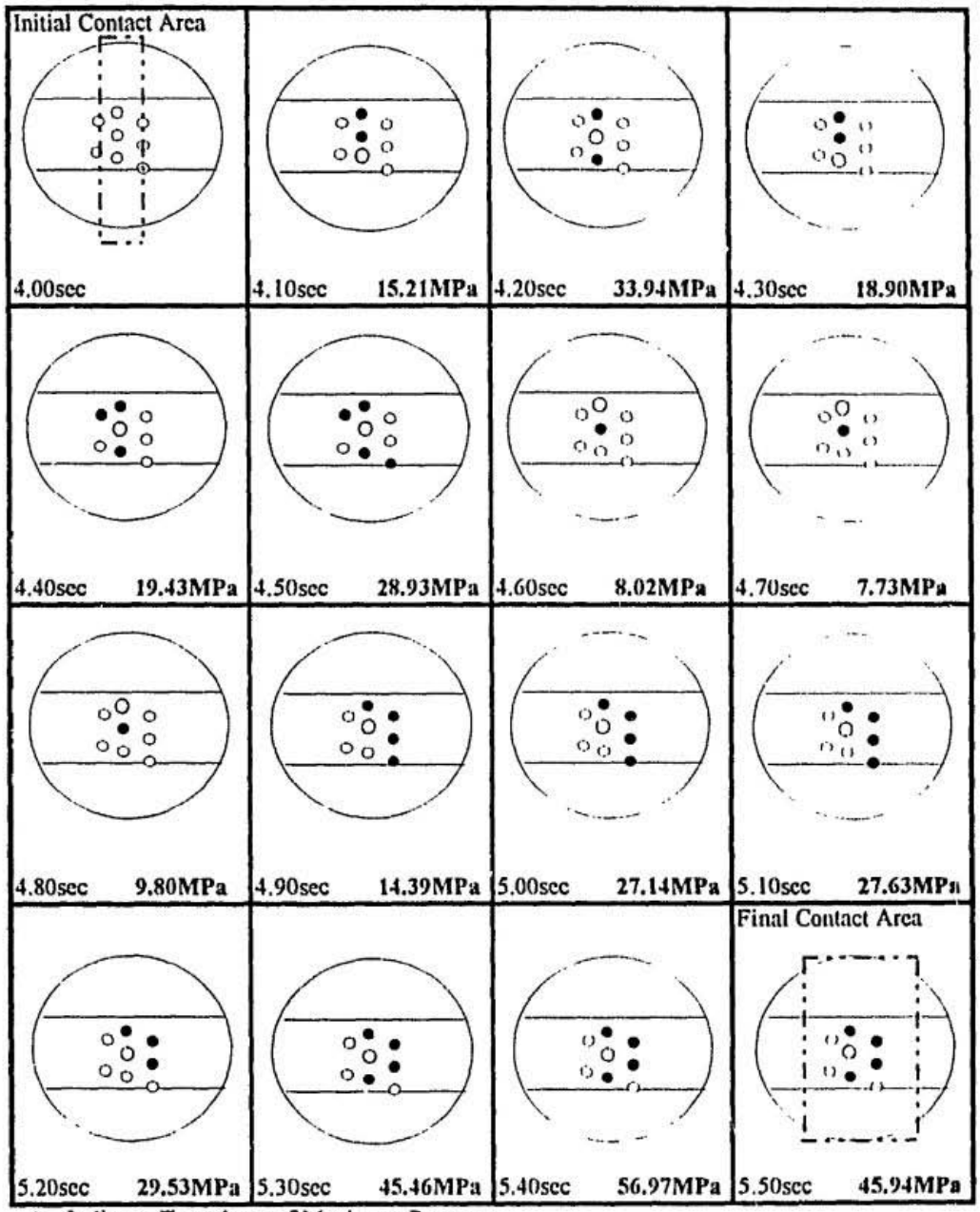

○ Indicates Transducer of Maximum Pressure
Instantaneous peak pressure noted in lower right corner
Dashed region outlines contact area

Figure 3.18 Radial Expansion of the Critical Zone with Increasing Contact Width

3.4.1 Quantifying the Extended Area of the Critical Zone

If the critical zone is to be accurately depicted, its extent beyond the instrumented region should be assessed. The maximum area of the critical zone is obtained by assuming that the critical zone supports the total load applied by the indentor. Equation 3.1 was formulated to account for the maximum extent of the critical zone.

$$A_{cz(max)} = \frac{F_{act}}{P_{cz(I)}} \qquad 3.1$$

where $A_{cz(max)}$ = Maximized area of critical zone

F_{act} = Force of the actuator

$P_{cz\,(I)}$ = Mean pressure of the critical zone in the instrumented region

In Equation 3.1 it is assumed that the maximum area of the critical zone supports the total force of the indentor. In actuality, regions of background pressure would support a certain portion of the applied load and spalled regions would not carry any load. The bearing capacity of the background region is not able to be assessed from the available data. As a result, the actual area of the critical zone is indicated by a range of estimates. The lower bound for the area of the critical zone is provided by the instrumented area and an upper bound (the modified area of the critical zone) is provided by Equation 3.1. Equation 3.1 assumes that the average pressures in the instrumented and extrapolated areas of the critical zone are equal.

Figures 3.19 and 3.20 present a comparison of the maximum critical zone area (calculated from Equation 3.1) to the instrumented area of the critical zone (indicated from the pressure cell data) for tests NRC06 and NRC07. The compared areas are substantially different during the 4.85-5.10 second interval of NRC06. During this period, the maximum area of the critical zone ranges from 0.08-0.13m^2, 38-66 percent of the contact area, respectively. The pressure sensors indicate an unchanging area of 0.052m^2 for the critical zone during the interval noted.

The overall shape of the critical zone and the direction in which it extends may be inferred from information about the contact width and the location of the active sensors (with respect to the inactive sensors). During the 4.85-5.10 second interval the contact width, 194mm, does not greatly exceed the instrumented width, 150mm. Additionally, the critical zone is bounded on the left side by a row of inactive transducers (see Figure 3.21). Since the lateral expansion of the critical zone is limited by the relatively narrow contact width, it is presumed that the high pressure zone extends along the longitudinal axis of the indentor. The maximum area of the critical zone, as extrapolated beyond the instrumented region, is sketched in Figure 3.21. The most extensive critical zone occurred at 4.90 seconds during the NRC06 testing period (see Figure 3.19). An upper bound for the area of the critical zone at this point is 0.13m^2, 66 percent of the contact area.

Upon concluding test NRC07 photographs were taken of contact zone (Frederking et al., 1989). These photographs reveal a long, slender region with a dark, blue hue, extending along the imprint left by the indentor. No distinct layer of crushed ice exists in this region. It is inferred that recent pressures were of sufficient magnitude to extrude the layer of crushed ice. As mentioned in Chapter 2, superimposing the final pressures on the

contact face did not reveal a correlation between the highest pressures and the dark blue region. The critical zone is believed to correspond to those areas of the contact area where a distinct layer of crushed ice is present. As pressure in the critical zone peaks, the layer of crushed ice is extruded, and the zone alters its shape and position. It is possible that regions previously occupied by critical zones correspond to the darkened zones (at times, incorrectly termed "intact" ice) which have little or no layer of crushed ice.

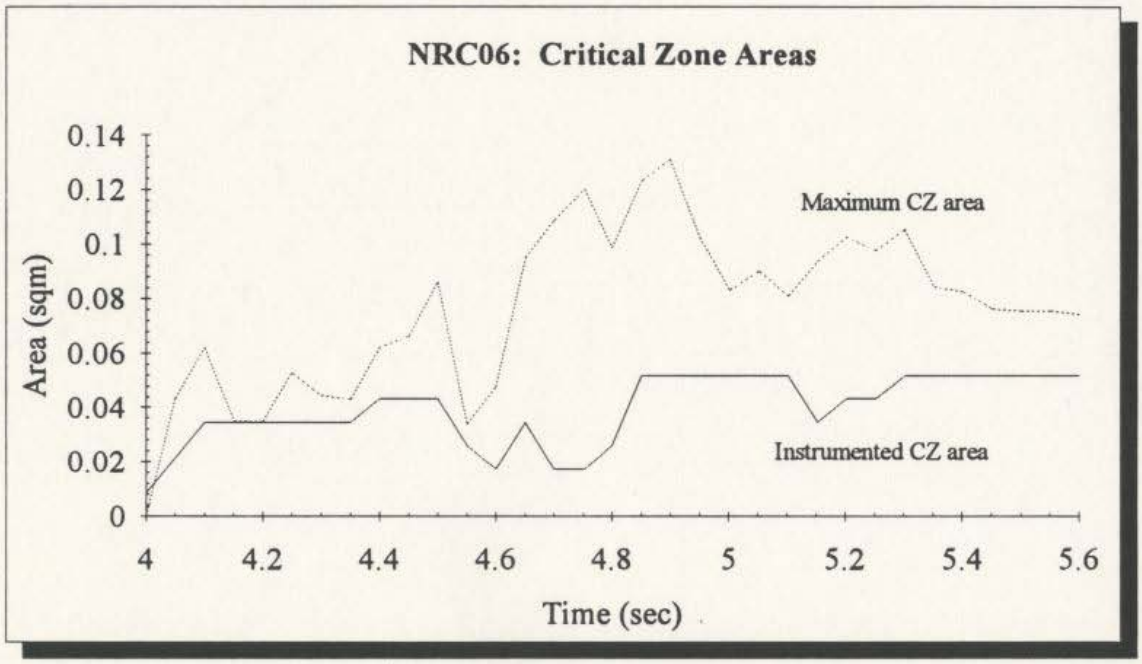

Figure 3.19 Comparison of Maximum and Instrumented Critical Zone Areas for NRC06

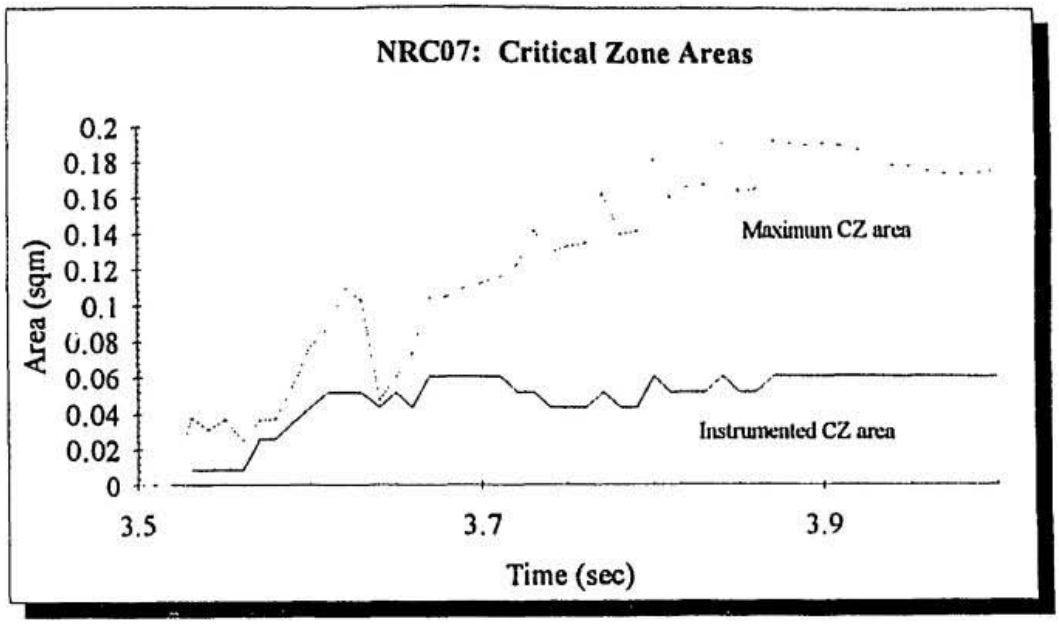

Figure 3.20 Comparison of Maximum and Instrumented Critical Zone Areas for NRC07

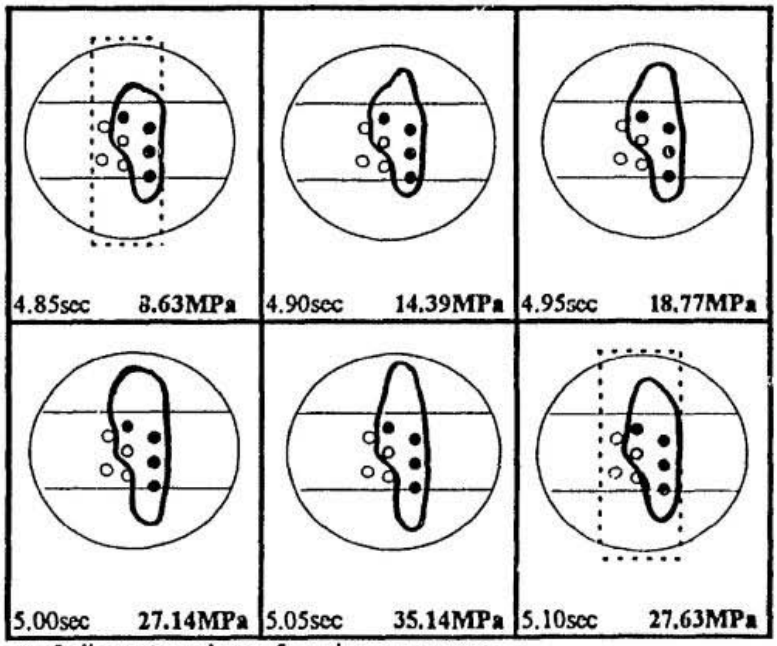

o Indicates transducer of maximum pressure
Instantaneous peak pressure noted in lower right corner
Dashed lines indicate contact area

Figure 3.21 Extrapolation of the Critical Zone beyond the Instrumented Region (NRC06)

3.5 Establishing Representative Values for the Basic Critical Zone Properties

To incorporate critical zones into a statistical or deterministic model for ice load prediction, several properties of these high pressure zones must be defined. Fundamental properties such as the zonal size, force, mean pressure, and the frequency with which critical zones occur over a given area should be established. As previously noted, critical zones are highly variable in space and time. Statistical methods were used to reduce the inherent variability of the critical zones to a distribution which is representative of the entire data set. From these distributions, mean values of the required parameters may be obtained.

A substantial amount of data from the indentation tests exist. Analysis of the entire Hobson's Choice test program is beyond the scope of the present study. In keeping with the previous analysis, data from the two flexible indentor tests were examined. The loading period for NRC06 and NRC07 was divided into intervals of 0.05 seconds. The following tasks were completed for each interval:

1. The maximum pressure registered on any single transducer was recorded.
2. The number of active transducers was recorded and was used to compute the area of the critical zone.
3. The pressures recorded on all active transducers were averaged to obtain a mean pressure for the critical zone.
4. The force of the critical zone was computed based upon the average pressure (task 3) and active area (task 4).
5. The computed force of the critical zone was compared to the actual force exerted by the actuator during indentation.

Distributions for the critical zone size, force, and mean pressure are presented in Figures 3.22-3.25. Examination of the histogram of the maximum area for the critical zone (Figure 3.22) reveals a relatively even distribution of area over the range of 0.04-0.20m^2. Conversely, the histogram which takes into account only the instrumented region of the critical zone reveals a peak in the range 0.04-0.06m^2.

Similarly, Figure 3.23 demonstrates that the force over the modified critical zone is considerably larger than that of the instrumented region. The extreme value of force occurring over the maximized critical zone area is 4.55MN. The force may be distributed between several zones, coincidentally active in the contact region. The maximum area of the critical zone may be the summed areas of several critical zones, each located in close proximity to one another. As mentioned previously, the mean pressure in the instrumented and extrapolated regions of the critical zone were assumed to be equal. The average pressure that occurs most frequently is between 20-25MPa. The most extreme value of average pressure was in the range 40-45MPa, occurring approximately 4 percent of the time.

A mean value comparison of the critical zone parameters is presented in Tables 3.3 and 3.4. The instrumented region is compared to the maximum critical zone area. The mean area of the maximum critical zone was 0.104m^2 for tests NRC06 and NRC07 combined. The mean force of the maximized zone for the two tests was 1.93MN. Additionally, the mean pressure of the critical zone was 17.2MPa. The instrumented area accounts for approximately half of the mean load and area of the maximum critical zone.

Table 3.3 Statistical Parameters of the Critical Zone for the Modified and Instrumented Areas

	NRC06		NRC07	
Critical Zone Parameter	**Instrumented Region**	**Modified Critical Zone**	**Instrumented Region**	**Modified Critical Zone**
Mean Area	$0.039m^2$	$0.079m^2$	$0.046m^2$	$0.129m^2$
Mean Force	0.52MN	0.93MN	1.13MN	2.92MN
Mean Pressure	12.4MPa	12.4MPa	21.9MPa	21.9MPa
Mean Peak Pressure	25.5MPa	--	29.7MPa	--

Table 3.4 Statistical Parameters for the Critical Zone (tests NRC06 and NRC07 combined)

	Average of NRC06 and NRC07	
Critical Zone Parameter	**Instrumented region only**	**Instrumented and extrapolated regions combined**
Mean Area	$0.042m^2$	$0.104m^2$
Mean Force	0.82MN	1.93MN
Mean Pressure	17.2MPa	17.2MPa

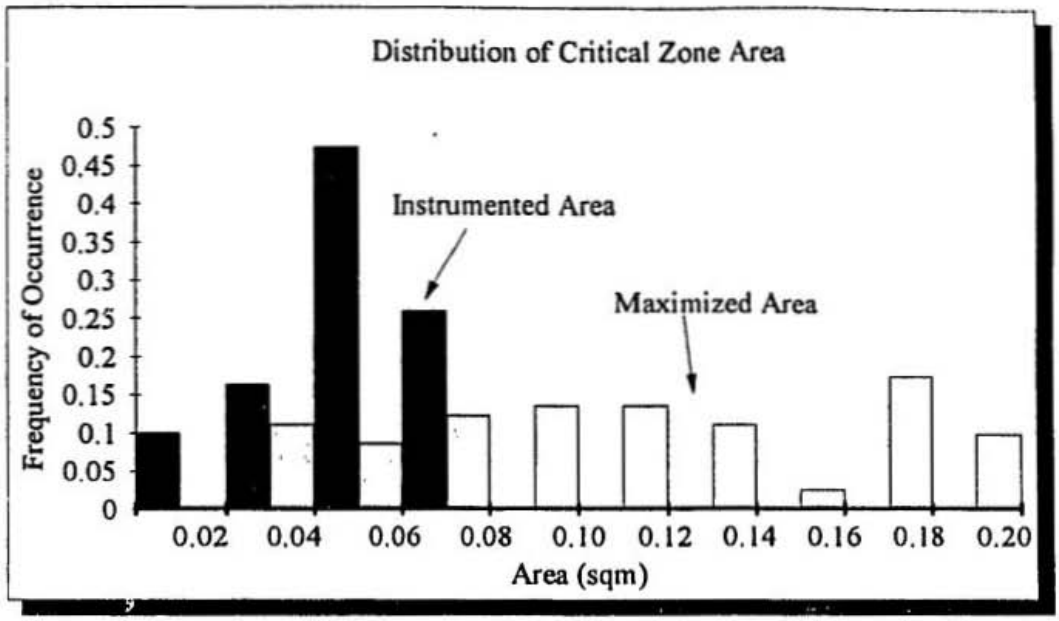

Figure 3.22 Distribution of Critical Zone Area for Instrumented and Modified Regions

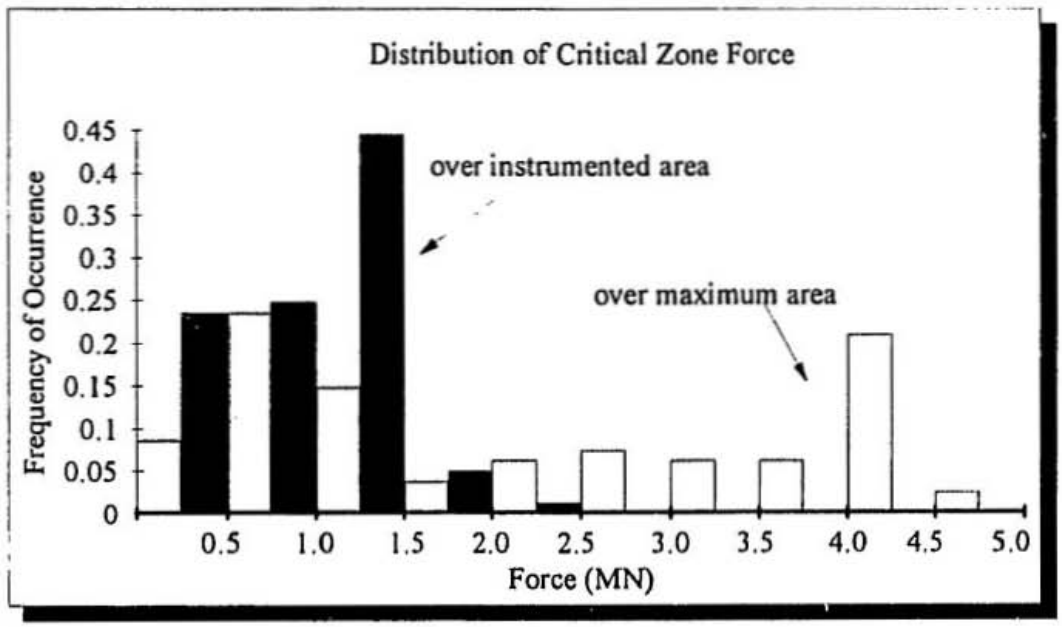

Figure 3.23 Distribution of Critical Zone Force for Instrumented and Extrapolated Regions

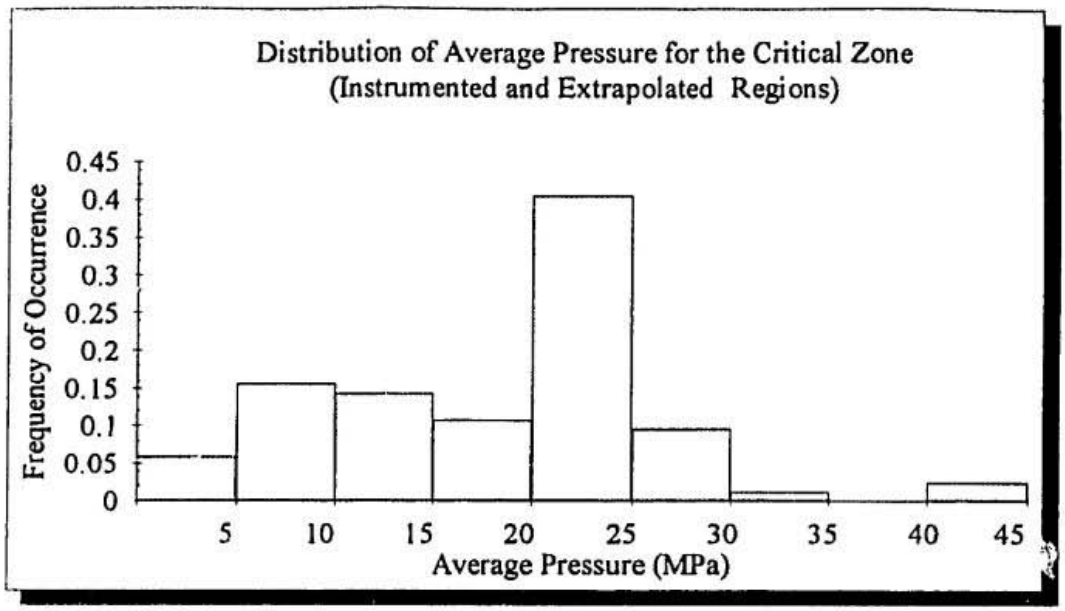

Figure 3.24 Distribution of Average Pressure for the Critical Zone (Instrumented and Maximized Regions Alike)

3.6 Conclusions

Fundamental critical zone parameters have been established for two of the indentation tests, NRC06 and NRC07. Mean values of the area, force, and pressure of the critical zones have been defined. Maximum and minimum estimates for the area of the critical zones were provided by calculations based upon the activated pressure cells and the total force of the indentor, respectively. A comparison between the instrumented area and the maximum area of the critical zone (as extrapolated beyond the instrumentation) revealed that the pressure sensors account for approximately half of the mean area and mean force of the high pressure zone. The mean pressure within the maximized area of the critical zone was assumed to be equal to the mean pressure in the instrumented area.

The Hobson's Choice Indentation tests are unique in that they provide well documented information of the forces exerted by the indentor. Determination of the driving force in the cases of ship ramming and ice interaction with offshore structures is complicated by the effects of numerous environmental factors. Comparison of the calculated force of the critical zone and the theoretical driving force for the interaction becomes much more difficult. Data from the indentation tests has enabled an assessment of the basic properties of the critical zone. The concept of critical zones may now be applied to more complex loading conditions, i.e. ship ramming trials.

Chapter 4

Full Scale Trials of the Louis S. St. Laurent and the CanMar Kigoriak

4.1 Introduction

Ships of the order of the offshore drilling platform 'Molikpaq' (200,000 tonnes) are contemplated for ice-covered water navigation (Masterson and Frederking, 1993). During ice-structure interaction these massive vessels generate forces which are many times larger than smaller vessels are capable of producing. The strength requirement of icebreakers is strongly influenced by ship geometry and size. Table 4.1 presents a comparison of the contact area and maximum force for the Louis S. St. Laurent, CanMar Kigoriak, and two vessels typical of those proposed for the future. A thorough understanding of local loads is needed to improve existing design criteria. A model which incorporates small high pressure zones into the design equations for local and, ultimately, global elements should be developed.

Information about the relationship between local pressures and global loads may be obtained from measurements collected during full scale interactions. Numerous test programs have investigated the local variation of pressure within an impact zone. The results of two arctic programs, the CCGS Louis S. St. Laurent and CanMar Kigoriak, were examined to assess the behavior and magnitude of localized pressures during ship-ice interaction.

Table 4.1 Various Contact Areas for Ships

(Masterson and Frederking, 1993)

	Kigoriak	Louis S. St. Laurent	Future I	Future II
Displacement	7 KT	14.28 KT	80 KT	200 KT
Power	13MW	20MW	36MW	48MW
Maximum Force	37.8MN	71.2MN	301.5MN	648.9MN
Contact Area	25.2m^2	47.5m^2	201.0m^2	432.6m^2
Contact Depth *	1.8m	2.4m	5.0m	7.4m
Contact Width *	14.2m	19.5m	40.1m	58.8m

*Dimensions of contact area, based on an aspect ratio of 8:1 (depth, width)

4.2 Ice-Ship Interaction

The force generated during ice-ship interaction is a direct result of the bow of the ship penetrating and sliding onto the ice (Riska, 1987). Frequently the actual contact area is substantially smaller than the bow print area, i.e., typical contact areas were 1/3 of the bow print area for the Kigoriak trials. The bow imprint illustrated in Figure 4.1 reveals regions of crushed ice (A) and regions where vertical cracks produced distinct pieces of ice (B). Characteristically, the pressure distribution within the interaction zone is highly variable in space and time (see Figure 4.2). Several critical zones may be present simultaneously in the contact area.

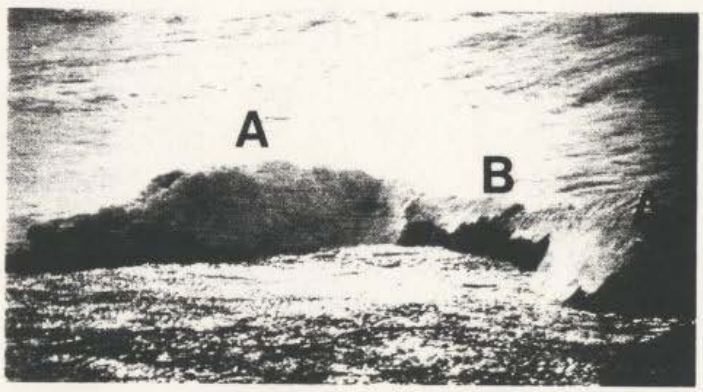

Figure 4.1 Bowprint on a 3m Thick Ice Floe
(Riska, 1987)

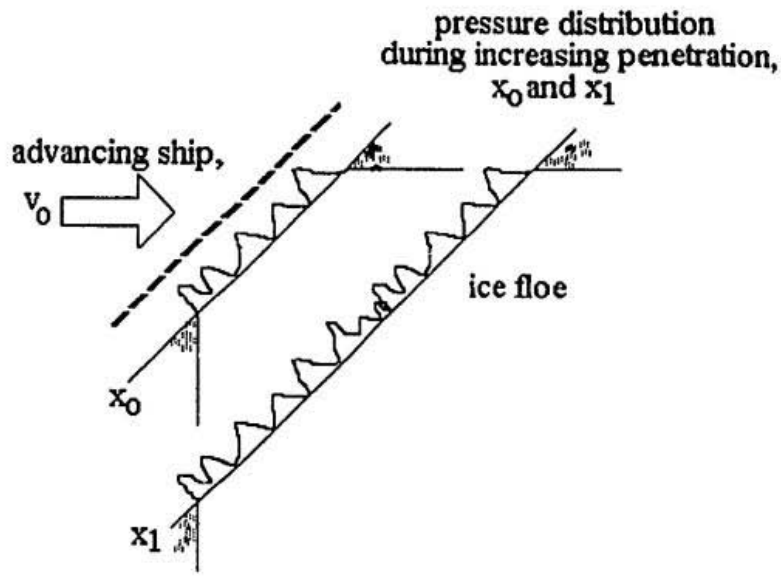

Figure 4.2 Typical Pressure Distribution During Ship-Ice Interaction
(Riska, 1987)

Three phases are associated with ship ramming, i.e. impact, slideup, and forefoot. Figure 4.3 illustrates the variation of force with the sequence of events that occurs during ship-ice interaction. The following is a brief description of each stage, based upon a report by CanMar (1985).

The impact phase begins with first contact between the ship and ice and ends when the horizontal velocity of the ship is significantly reduced. Impact typically lasts less than one second and is assumed to be symmetrical about the centreline of the ship. A large amount of ice deformation occurs through the mechanisms of ice crushing, shearing, and flaking, in addition to the radial and circumferential propagation of cracks. Figure 4.4 identifies the failure processes dominating various regions of the interaction zone during impact.

Subsequent to impact, the ship slides up the ice face. There is a gradual transfer of kinetic energy to potential energy which shows as a decrease in the contact force and in all velocity components. Local and global deformation of the structural components may occur with the increase in trim and rising vertical position of the ship. Minor amounts of ice are destroyed in the interface during this process. This phase ends when all of the kinetic energy is expended or when there is a second impact between the vertical forefoot and the ice. If sufficient kinetic energy exists, the forefoot will hit the ice. The ice forefoot stops the ship by expending the remaining kinetic energy through the additional crushing of the ice.

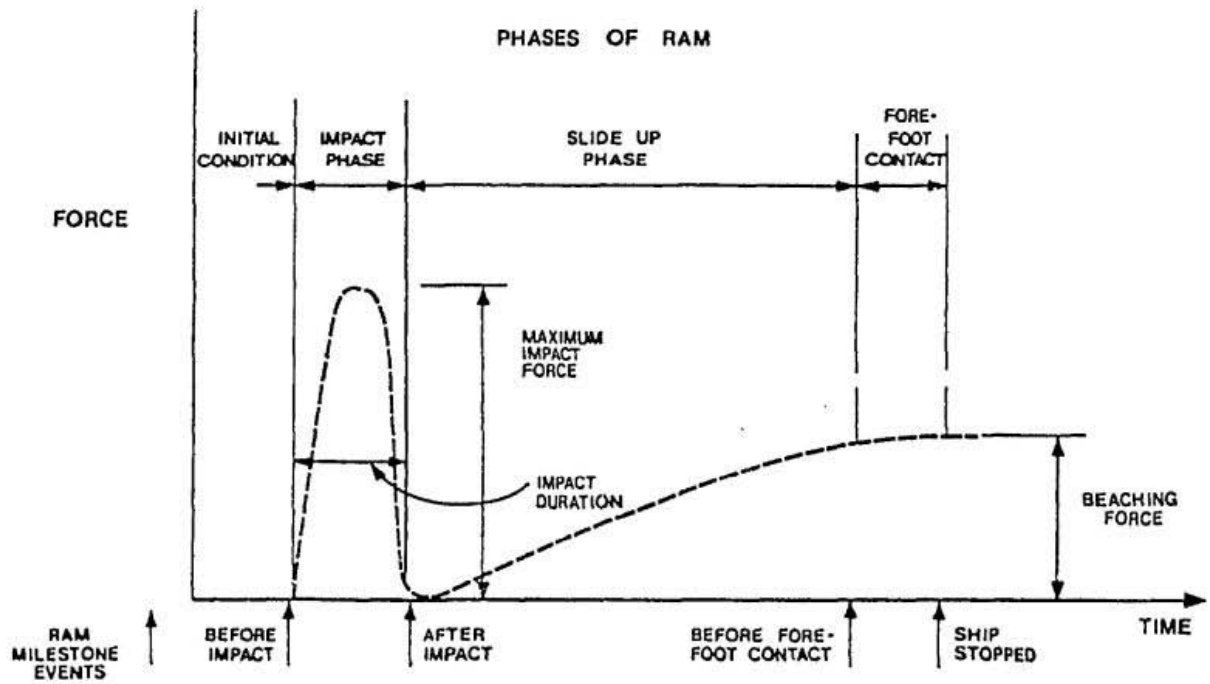

Figure 4.3 Variation of the Contact Force during Ice-Ship Interaction
(CanMar, 1985)

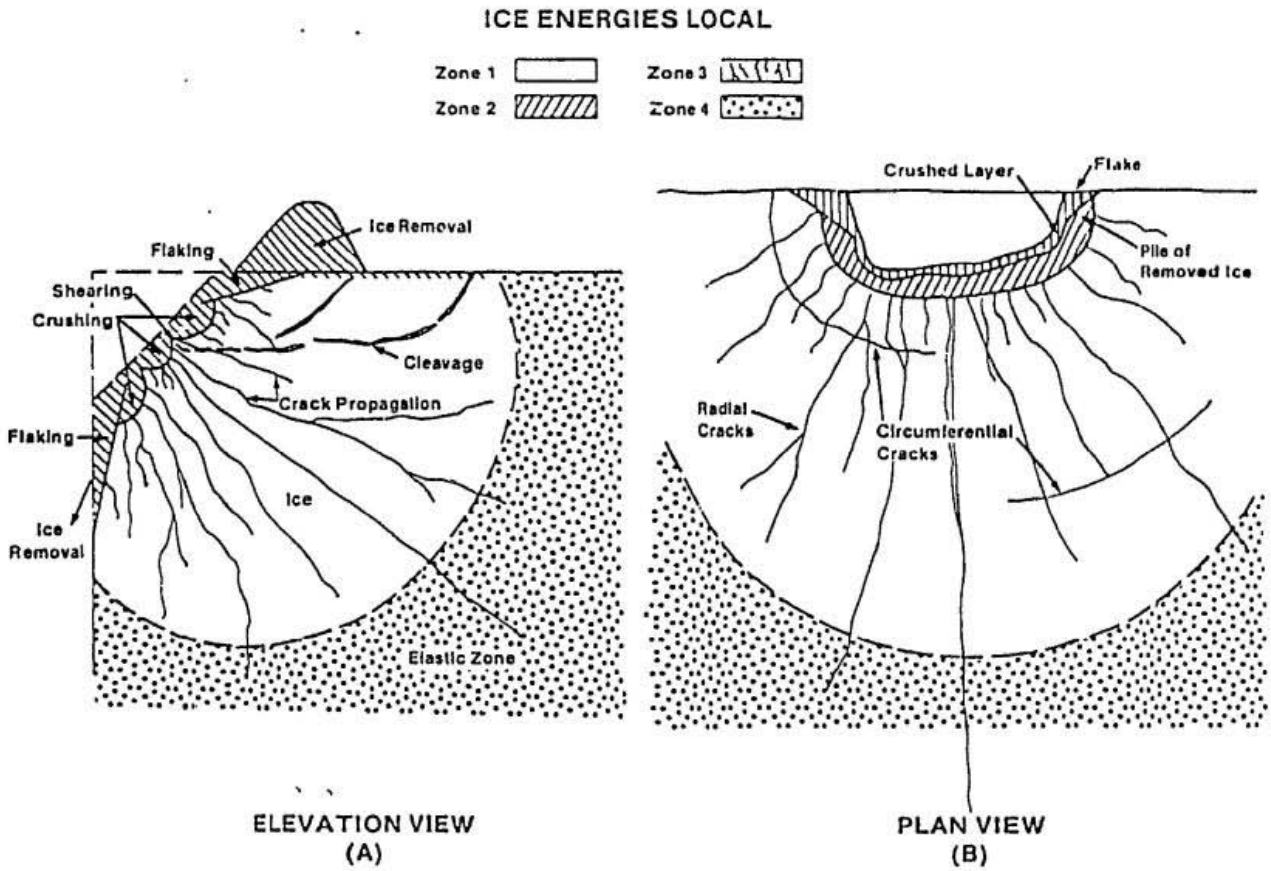

Figure 4.4 Failure Mechanisms Active in the Contact Zone

(CanMar, 1985)

4.3 Louis S. St. Laurent Ship Trials

In November 1980 the Canadian Coast Guard conducted impact tests on multiyear ice with the CCGS Louis S. St. Laurent. These tests were the first direct measurements of ice pressure in the high arctic (Daley and Riska, 1990). With a displacement of 14.28 kilotonnes, and a length of 101m, the Louis S. St. Laurent was the largest and most powerful unit of the Canadian Coast Guard fleet. However, her effectiveness was limited by an inefficient icebreaking form and inadequate structural strength for heavy icebreaking (Kendrick and Carter, 1987). Since the conception of the Louis S. St. Laurent, advances in both knowledge and technology have improved icebreaking designs. Figure 4.5 presents a comparison of bow shapes for various icebreaking vessels.

The 1980 Louis S. St. Laurent ship trials provide valuable information on the pressures experienced during ice-ship interaction. The principle objective of the fall 1980 trials was to measure the pressure generated in the impact zone between the ship and ice. Controlled impacts against selected multiyear floes up to 4m in thickness were executed. On November 12 and 13 backing and ramming was conducted on large multiyear floes off the coast of Bylot Island. Direct impact to the instrumented area of the hull was difficult due to high winds and the complications associated with avoiding propeller damage while backing up in multiyear pieces (Glen and Blount, 1984). Of the twenty trials thought to exhibit direct impact to the hull, only nine demonstrated well defined impacts to the panel of pressure transducers. Characteristically, crushing accompanied the ice-ship interaction.

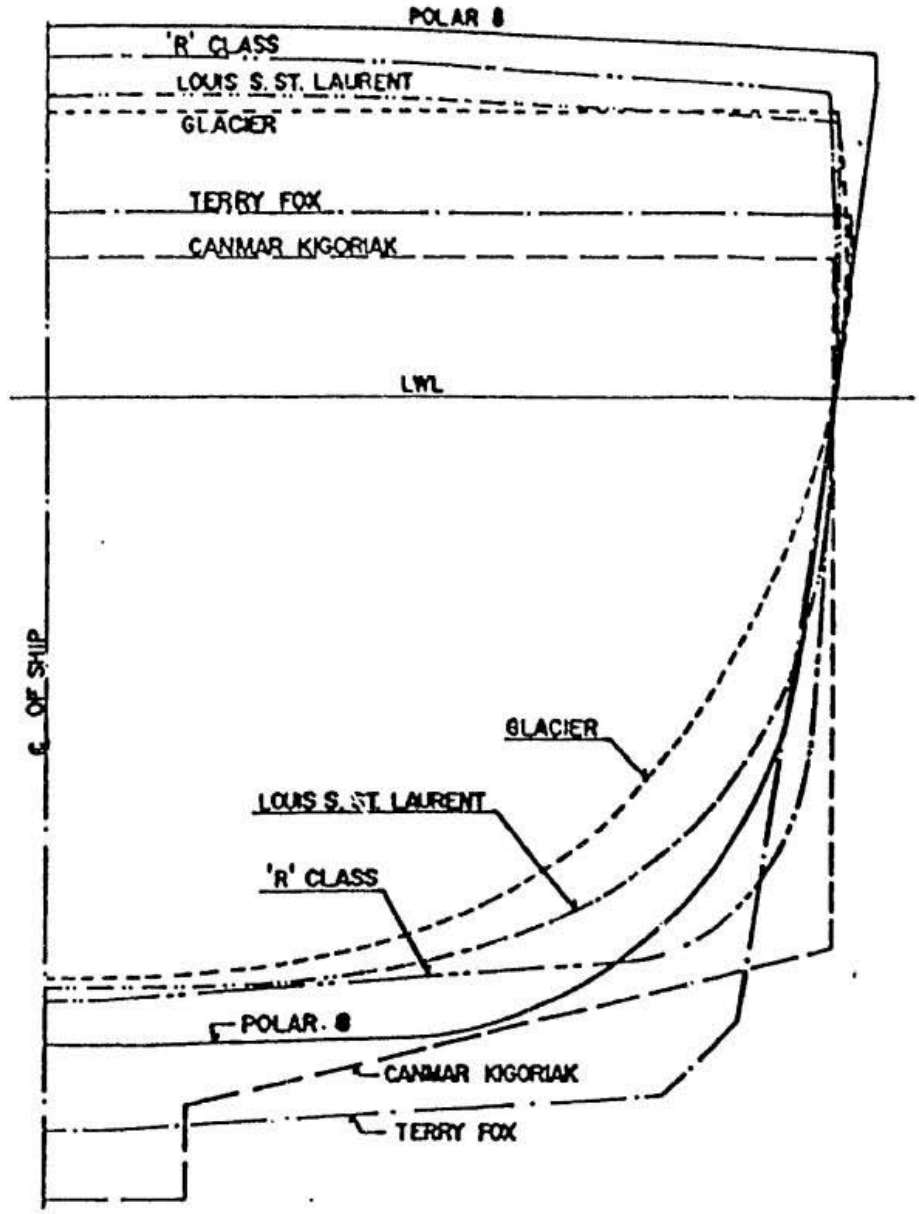

Figure 4.5 Comparison of Bow Shapes for Several Icebreaking Vessels
(Kendrick and Carter, 1987)

4.3.1 Pressure Distribution of the Louis S. St. Laurent Critical Zones

An array of 25 pressure sensors and 12 strain gauges were installed in the bow thruster compartment. The pressure transducers, distributed over an area of 1.67m^2, were of the strain gauge diaphragm type. The sensors, 7.94mm in diameter and 94mm long, were designed and manufactured in 316 stainless steel and threaded through the hull of the vessel (Glen and Blount, 1984). Additional stiffening compensated for structural alterations caused by installation of the pressure sensors. Horizontal stringers, spaced at approximately 200mm, were fitted between the 406mm frames.

The transducers recorded numerous peaks during a pressure pulse, typically 10-100ms (Glen and Blount, 1984). Six of the twenty-five pressure transducers were considered to be in regions of inactivity, i.e. at no point did they experience loads (see Figure 4.6). A computer program searched and identified the time of maximum pressure response for each gauge and simultaneously scanned the values registered on all gauges (Blount et al., 1981). In the present context, transducers are considered active when they exceed a threshold stress of 2MPa.

A graphical representation of the spatial and temporal variation of critical zones may be obtained from the number and location of active transducers. The activity sequence for a case of direct impact to the pressure panel is presented in Figure 4.7. Initially one transducer was active over the entire panel. The highest pressure during the interaction occurred at 7.605seconds, when a peak instantaneous pressure of 51.5MPa was registered.

As the interaction progressed, the critical zone changed size and position. Glen and Blount (1984) noted that no recognizable pattern in critical zone activity was evident. The apparently random fluctuation of the critical zones is caused, in part, by failure processes occurring within the interaction zone. The formation of spalls near the free surface dramatically alters the contact area, in turn affecting the pressure distribution and location of the critical zones. Additionally, the extrusion of crushed ice influences pressures within the critical zone.

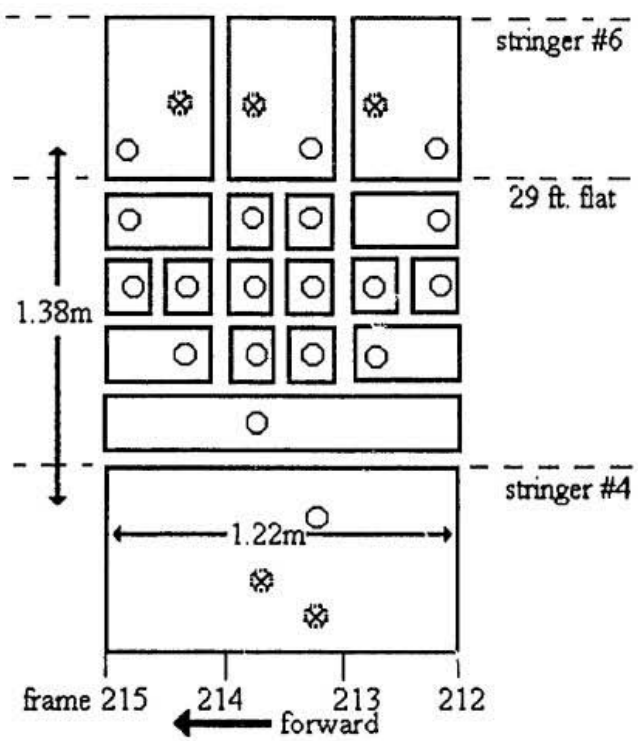

Figure 4.6 Location of Various Pressure Sensors
(dashed circles indicate sensors in inactive regions)

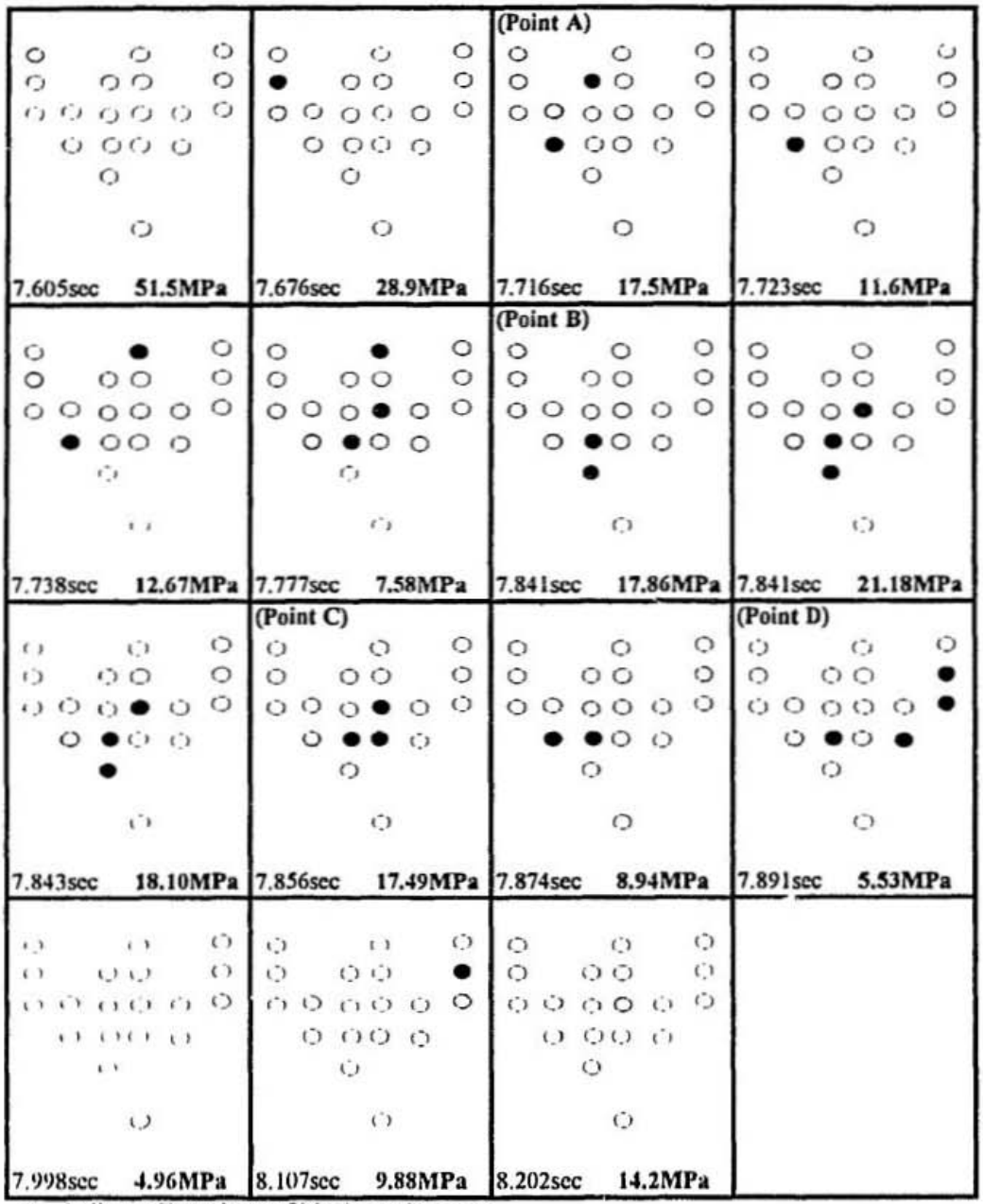

○ Indicates Transducer of Maximum Pressure
Instantaneous peak pressure noted in lower right corner

Figure 4.7 Critical Zone Activity within the Contact Area, Case I

Three dimensional pressure distributions for selected intervals of Case I (points A-D in Figure 4.7) are presented in Figure 4.8(a)-(d). The first three plots indicate the presence of two critical zones over the instrumented panel. As the interaction proceeds, the magnitude of the peak pressure changes, as does its location. Figure 4.8(d), representative of the latter stages of interaction, demonstrates considerably decreased pressures over the two existing critical zones.

Two or three critical zones may exist simultaneously on the instrumented panel. For instance, in the transducer activity series for Case I, six of the 15 time intervals indicate the presence of two critical zones. High pressure zones are not always separate and distinct from one another. Failure processes occurring within the interaction zone cause the critical zones to merge and divide. At any given instant the area of individual critical zones is small, i.e. 0.047-0.189m^2 for Case I. Frequently, a solitary transducer on the periphery of the transducer panel will register a very high pressure (see Figure 4.7, 7.605seconds). Similarly, Figures 4.8(b) and (c) indicate that pressures at the perimeter of the transducer panel approximate 5MPa. Under these circumstances the critical zone may extend beyond the instrumented region. Therefore, areas of the critical zone may be underestimated.

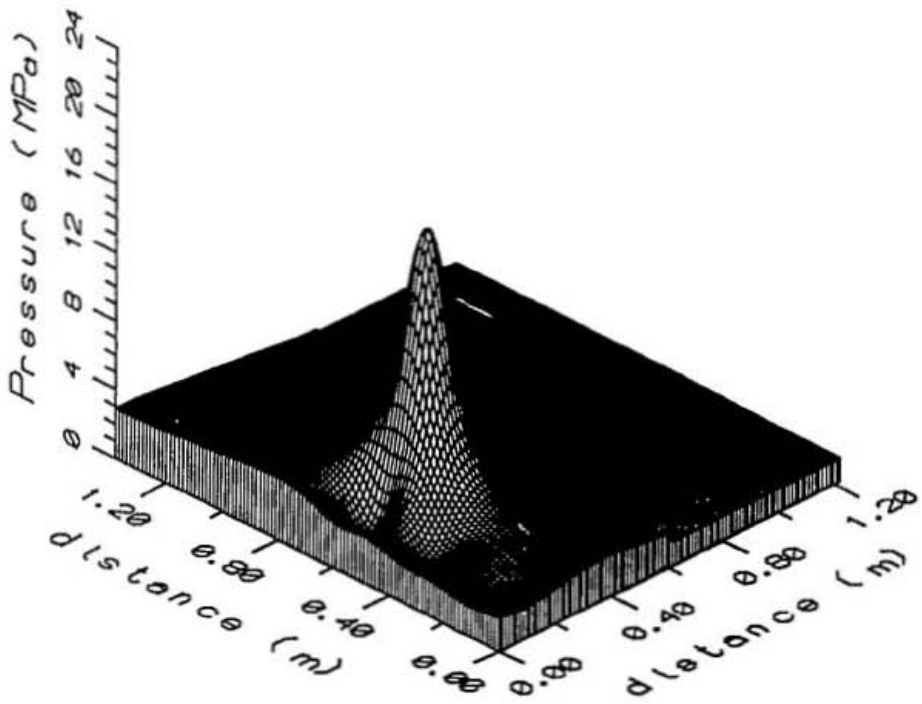

Figure 4.8 (a) Pressure Distribution of Case I (point A, 7.716sec.)

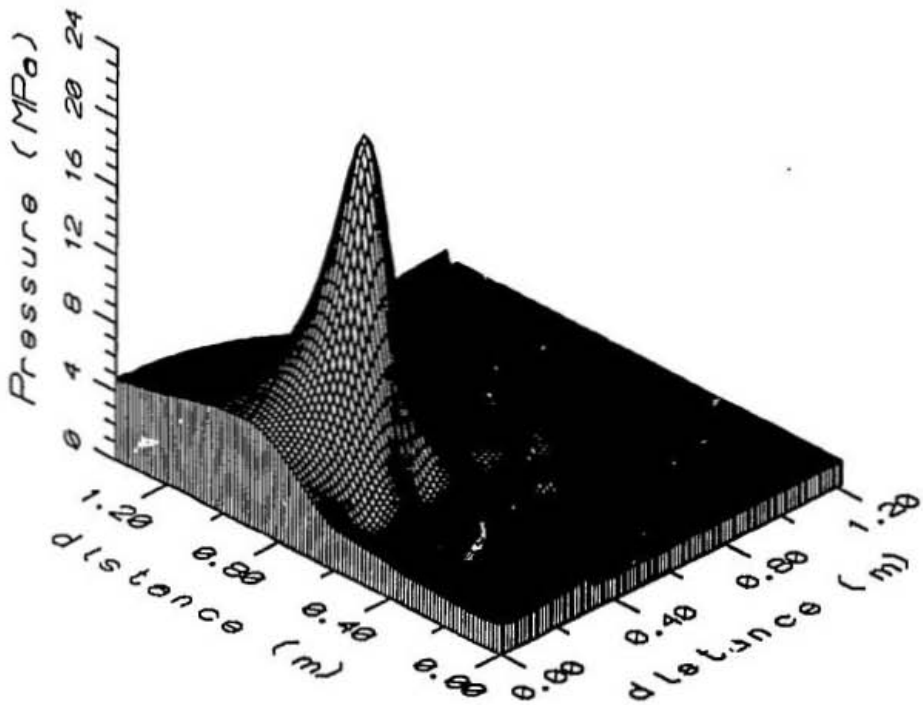

Figure 4.8 (b) Pressure Distribution of Case I (point B, 7.841sec.)

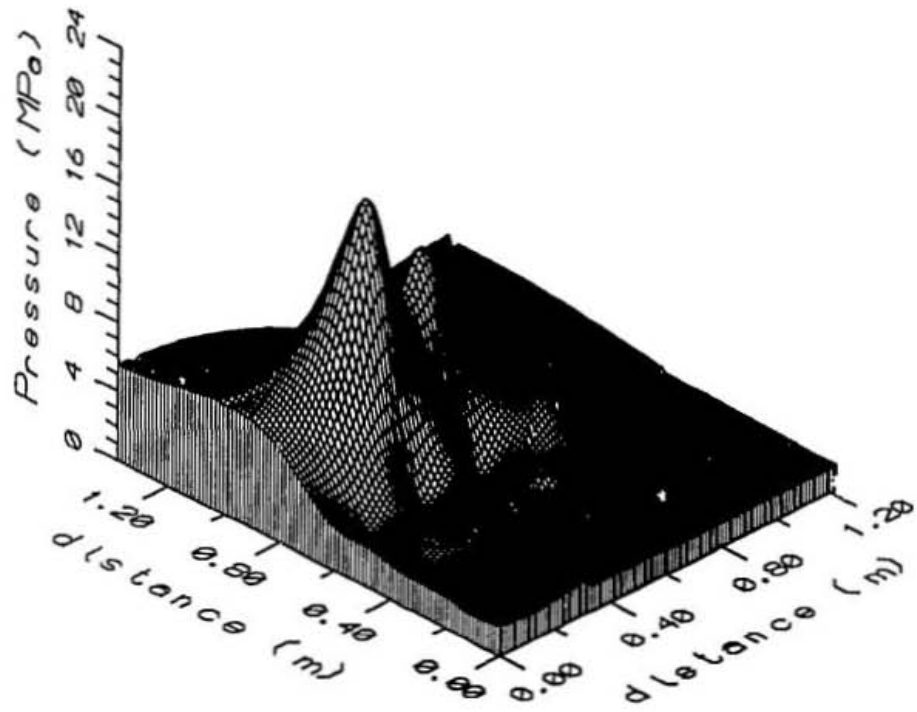

Figure 4.8 (c) Pressure Distribution of Case I (point C, 7.856sec.)

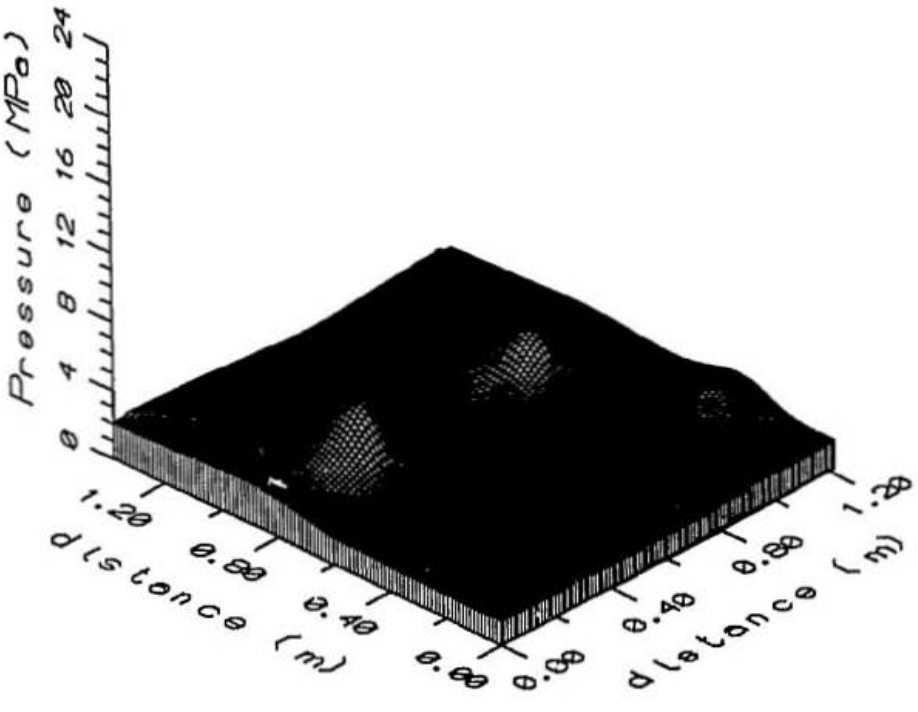

Figure 4.8 (d) Pressure Distribution of Case I (point D, 7.891sec.)

4.3.2 Determining the Force of the Critical Zone from Pressure Cell Data

The force of a critical zone may be determined from the area and mean pressure of the high pressure region. These two parameters are readily available from pressure cell data. Mean pressure was computed by averaging the pressures registered on the active transducers included within the individual critical zone. The size of the critical zone is obtained by multiplying the number of active transducers by their representative area, $0.05m^2$, allowing for the regions not instrumented with pressure cells.

Alternately, the force of a critical zone may be computed from Equation 4.1 (previously derived in Chapter 2).

$$F_{cz} = \frac{\pi M b^4}{4(2 - e^2)(1 + \gamma)^2(1 - e^2)^{1/2}} + p_s \frac{\pi b^2}{(1 - e^2)^{1/2}} \qquad (4.1)$$

Assuming the crushed layer thickness is constant (γ=0), and denoting the elliptical area of the critical zone as A_{cz}, Equation 4.1 simplifies to:

$$F_{cz} = \frac{A_{cz}\, M\, b^2}{4(2-e^2)} + p_s\, A_{cz} \qquad (4.2)$$

Several parameters in the above equation may be estimated from the sequential plots of transducer activity. For instance, the parameter M, which takes into account the crushed layer thickness, the ice viscosity, and the curvature of the crushed layer, may be computed from the peak pressure of the critical zone by Equation 4.3.

$$p_0 = p_s + \frac{M\, b^2}{2\,(2-e^2)} \qquad (4.3)$$

Where p_S is a background pressure of 2MPa (see Chapter 2). The eccentricity of the ellipse may be calculated from the horizontal and vertical dimensions of the critical zone. Substituting the equation for peak pressure (Equation 4.3) into Equation 4.2 results in a simplified formula for calculating the critical zone force.

$$F_{cz} = A_{cz} \frac{1}{2} (p_o + p_s) \qquad (4.4)$$

Equation 4.4 demonstrates that computation of the force of a critical zone reduces to the basic formula of mean pressure multiplied by the area of the critical zone. The area of the critical zone may be approximated by means of an ellipse or by summing the representative areas of the individual pressure sensors, with little difference resulting.

4.3.3 Representative Values for the Louis S. St. Laurent Critical Zones

Twenty trials were conducted on November 12 and 13. Blount et al. (1981) classified many of these trials as "poor impacts", i.e. the impacted area was unable to be determined, or, when it was determined, was off the instrumented panel. Most transducer plots for cases of poorly defined impacts demonstrate a single critical zone which includes one transducer only. However, several of the eccentric impacts produced significant pressures on the t ..sducer panel.

In particular, Case 11 classified as a poor impact yet the impact produced a relatively large critical zone ($0.118m^2$), in which pressures of 20-25MPa were registered on three adjacent transducers. These pressures may have been generated by a broken piece of ice abutting the panel. The impact description from the video records states that ice fragments were crushed during Case 11 (Blount et al., 1981).

No distinction was made between direct and eccentric panel loads for the initial evaluation of the critical zone parameters. Twenty trials were included in the original analysis. The force, area, mean pressure, and peak pressure of various critical zones were computed for numerous impacts. Limiting the case histories to those in which direct panel impact was attained (Table 4.2) significantly influenced the results. Elimination of cases in which impact was fore or aft of the panel effected an increase in the mean values of the critical zone force, area, peak pressure, and average pressure. The increases in the mean values of the peak pressure and average pressure of the critical zone were not substantial, 1.9MPa and 3.7MPa, respectively. However, exclusion of the poorly defined impacts from the analysis revealed a 58 percent increase in the area of the critical zone and a 46 percent increase in the zonal force (Table 4.3).

Distributions of the critical zone properties for the nine cases of direct impact are presented in Figures 4.9-4.13. The mean critical zone area was $0.112m^2$. The area of the critical zone most often experienced was $0.05m^2$ (42 percent frequency of occurrence). The frequency of occurrence of critical zones less than $0.05m^2$ (or absent altogether) was not able to be determined for two reasons. First, the spatial resolution of the pressure cells was $0.05m^2$. Second, the nature of the previously described computer program was to search for incidents of peak pressure.

The critical zone force most often experienced was between 0.50-1.0MN, with a frequency of occurrence of 31 percent. Extreme critical zone forces in the range 3.0-3.5MN occurred only 2 percent of the time. Similarly, the peak and mean pressures of the critical zone most frequently experienced were in the 5-10MPa range. Extreme pressures of 50-55MPa occurred with a 1 percent frequency for the cases analyzed. Further examination of the transducer activity for the cases of direct impact revealed that, characteristically, the instrumented area contained one critical zone. Two critical zones occurred over the $1.67m^2$ instrumented area 24 percent of time. Three critical zones were present in the instrumented area only 2 percent of the time (Figure 4.13).

It is useful to look at the mean number of zones per square meter to provide an indication of how many zones might occur within the area outside the instrumented region. The mean number of zones per square meter is 0.76, as obtained from the average of 1.28 zones per instrumented panel ($1.69m^2$).

The fundamental parameters of the critical zone have been defined by methods similar to those employed in the Hobson's Choice Indentation analysis. We now examine the ship ramming trials of the Kigoriak, to which the concept of critical zones may be applied on a slightly larger scale.

Table 4.2 Impact Description of Selected Ramming Trials

(Blount et al., 1981)

Case	Hull Normal Velocity (m/s)	Impact Description (from Video Records)
1	0.986	Good impact-hits all transducers from front to rear in sequence. Ice crushing.
2	1.180	Good impact-hits all transducers simultaneously. Local crushing.
3	0.429	Clear impact-hits all transducers simultaneously. Local crushing. Cracked ice field breaks up during impact.
4	0.327	Good impact in front of panel, then sliding along panel. Local crushing .
5	0.443	Very clear impact-hits all transducers simultaneously. Local crushing. Impacts fore and aft of panel.
6	1.420	Good impact. Initial impact fore of the panel. Ice sheet slides along panel. No visible crushing.
9	1.141	Good impact-simultaneous impact on entire transducer panel. Visible crushing. Impacts also fore and aft of panel.
19	0.955	Good impact. Initial impact fore of panel. Local crushing very prevalent. Ice piece slides aft.
20	0.517	Impact occurs at an indistinguishable point. Broken ice passes panel. Crushing occurs.

Table 4.3 Evaluation of the Critical Zone Properties

Critical Zone Parameters	20 Cases Examined (all cases)	9 Cases Examined (direct impact only)
Mean Area	0.065 m^2	0.112m^2
Mean Force	0.51MN	1.09MN
Mean Peak Pressure	13.8MPa	15.7MPa
Mean Pressure	7.8MPa	11.5MPa

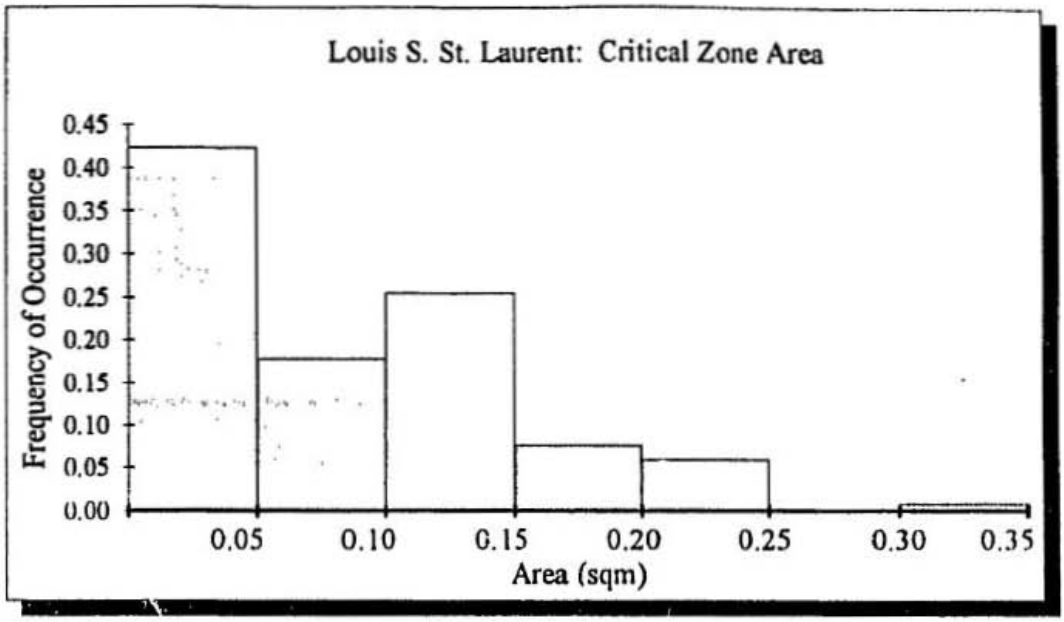

Figure 4.9 Distribution of Critical Zone Area for the Louis S. St. Laurent (nine cases)

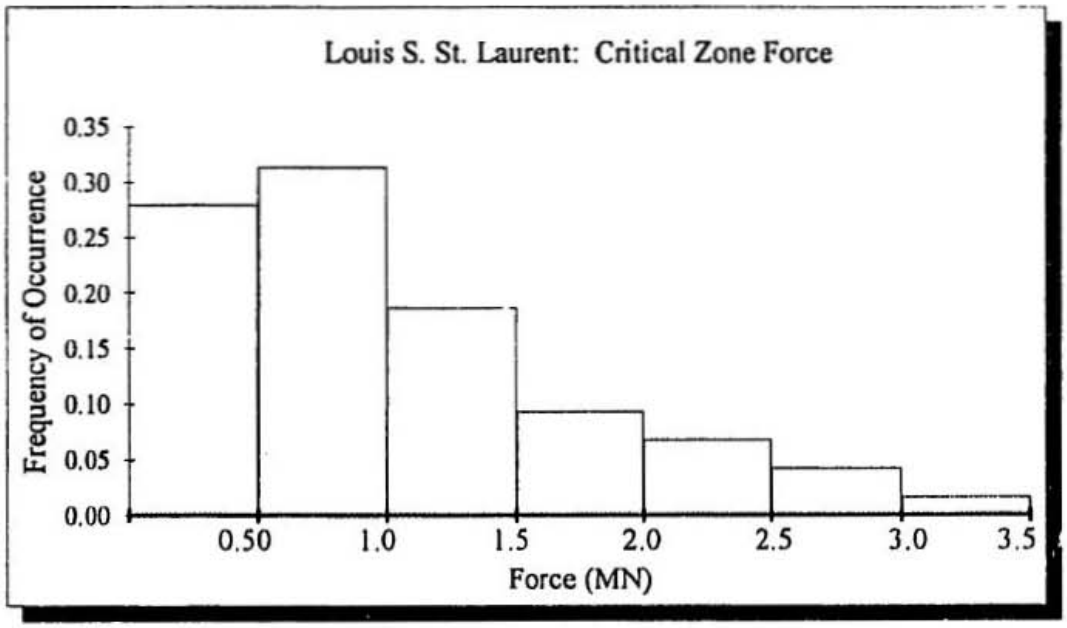

Figure 4.10 Distribution of Critical Zone Force for the Louis S. St. Laurent (nine cases)

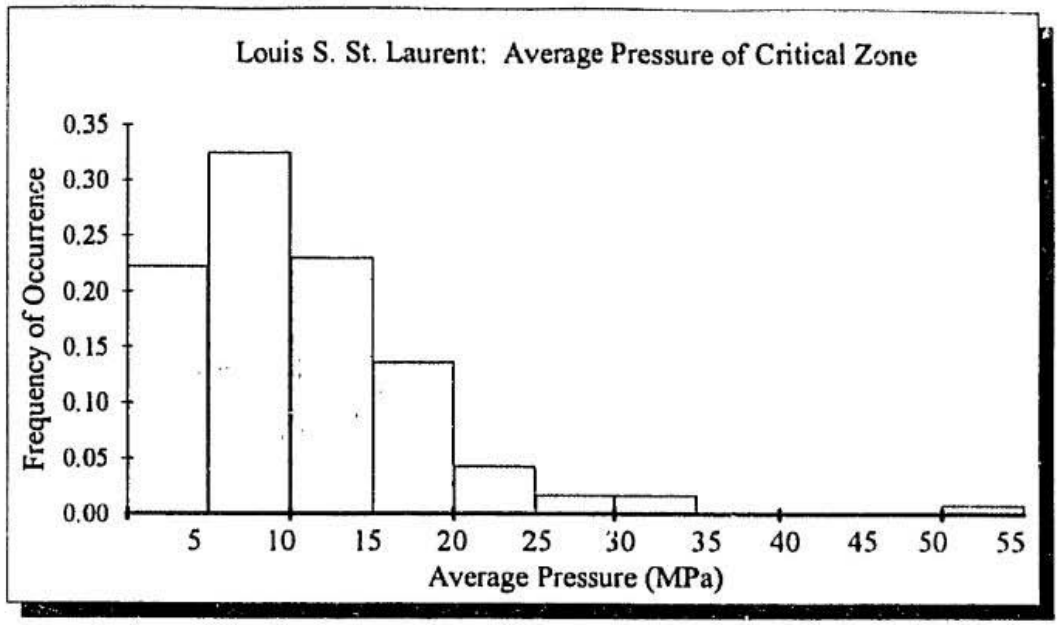

Figure 4.11 Distribution of the Average Pressure of the Critical Zone for the Louis S. St. Laurent (nine cases)

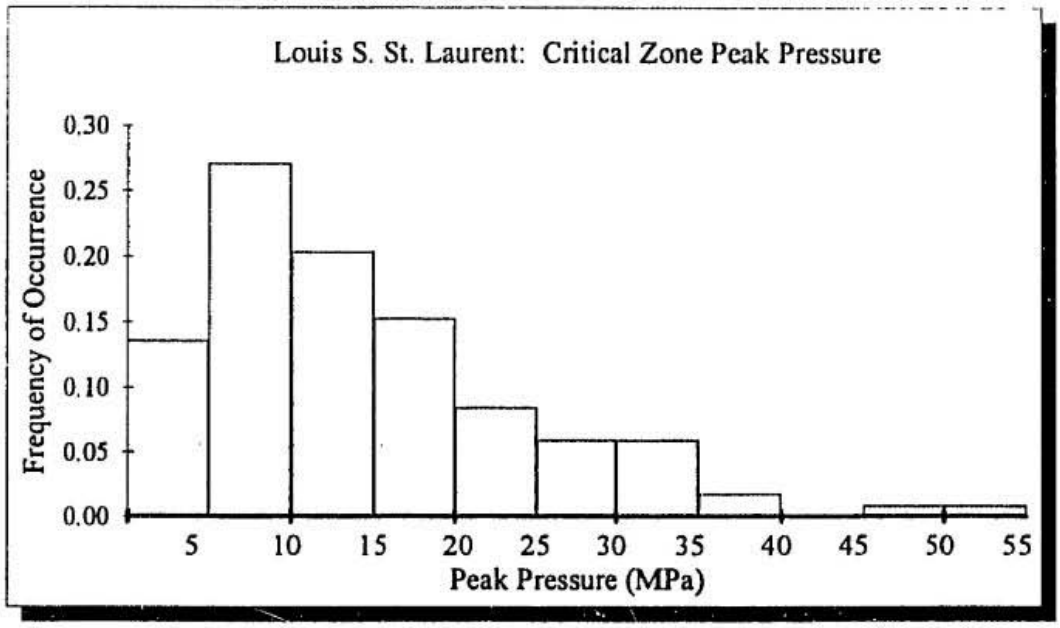

Figure 4.12 Distribution of Peak Pressure of the Critical Zone for the Louis S. St. Laurent (nine cases)

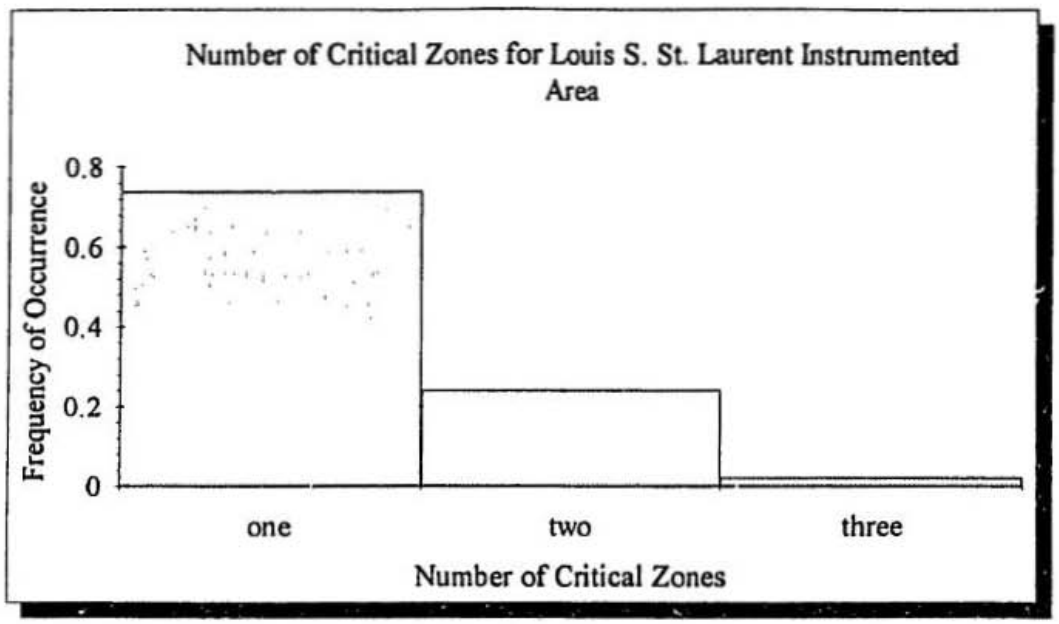

Figure 4.13 Number of Critical Zones Present within the Instrumented Area of the Louis S. St. Laurent (1.67m^2)

4.4 CanMar Kigoriak Ship Trials

The Kigoriak is a Canadian Arctic Class 3 icebreaker, designed and owned by Canadian Marine Drilling, Ltd. With a displacement of 7kilotonnes and a length of 90 meters, the Kigoriak is not considered to be a large or powerful icebreaker on a world scale (Figure 4.14). However, since 1979 the Kigoriak has successfully operated under conditions in the Beaufort Sea which exceed class 3 requirements (Keinonen and Duff, 1983).

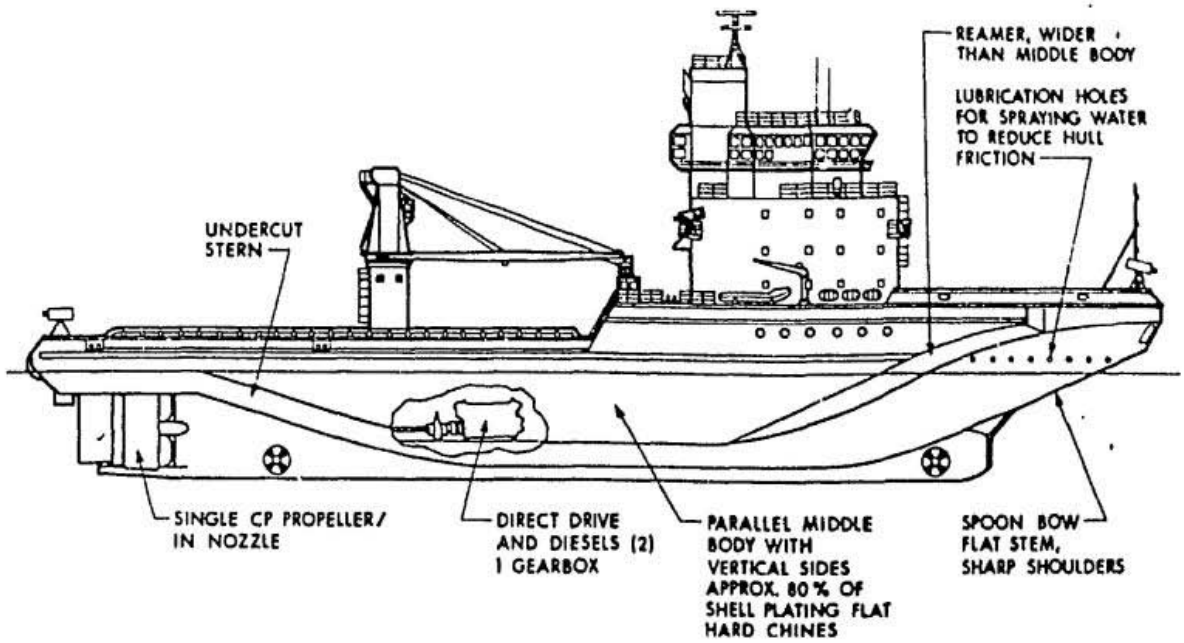

Figure 4.14 The CanMar Kigoriak

Canadian Marine Drilling, Ltd. conducted ramming trials with the Kigoriak during two periods in 1981. The first test period, conducted in August, took place in relatively weak, but thick, first and second year ice (denoted as A rams). In October, a second program was executed in generally strong multiyear ice, denoted as B rams. Average impact velocities for the August tests ranged from 2.36-6.31m/s and, for the October tests, ranged from 1.54-2.10m/s. Ice loads were measured on two areas of the port side of the Kigoriak (area A1, 1.25m^2 and area A2, 6.0m^2). Loads were calculated by measuring and summing the shear differences in the intermediate and web frames. This enabled the ice load over an area of several square meters to be determined.

4.4.1 Representative Values for the Kigoriak Critical Zones

The impact pressures on area A1 were examined from seventeen backing and ramming events during the August and October trials. Area A1 was subdivided into 6 panels, each with an area of 0.208m^2 (see Figure 4.15). Impact durations for the 17 cases ranged from 0.35-0.85seconds (CanMar, 1985). The average duration of impact was 0.52seconds. Figure 4.16 presents the frequency with which the impact durations were experienced. Fifty-two percent of the impacts were in the 0.40-0.60second range.

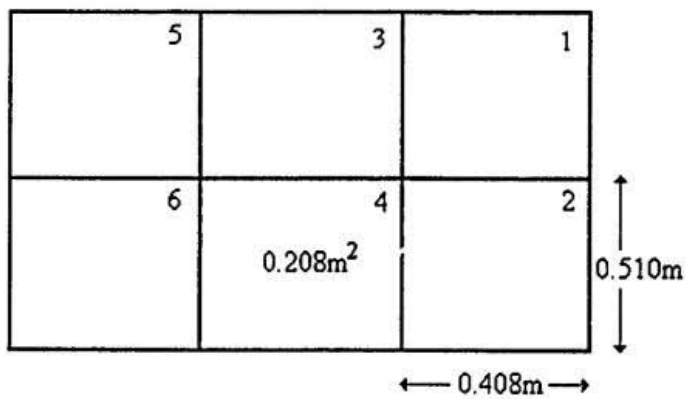

Figure 4.15 Instrumented Area A1 of Kigoriak (1.25m^2)

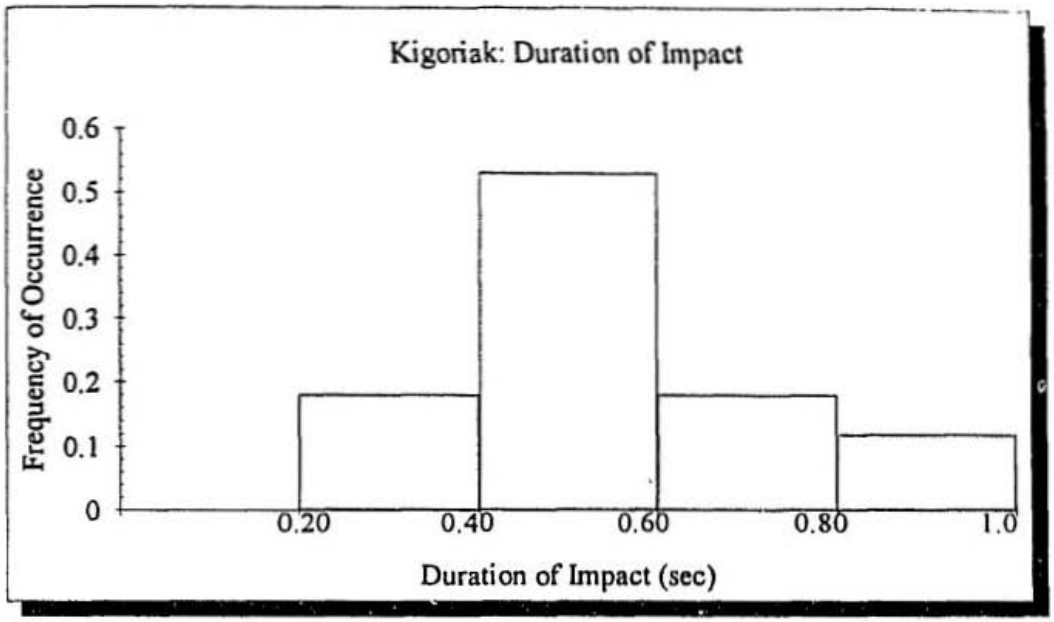

Figure 4.16 Distribution of Impact Duration for Seventeen Selected Trials

Examination of the pressure versus time plots for these cases revealed zones of spatially and temporally varying pressures (CanMar, 1985). Several of the impacts involved one or two panels only. Typically, pressures on the activated panels did not change considerably for the cases involving one or two subpanels. In contrast, numerous rams involved larger contact areas, simultaneously encompassing three or four panels, with rapidly fluctuating pressures. Figure 4.17 illustrates an impact during which six panels were loaded simultaneously. The configuration of the activated panels indicates the shape of the loaded area. Maes and Hermans (1991) conducted an extensive study of the possible loading patterns for the instrumented areas A1 and A2, taking into consideration partial loading of the panel and load sharing between adjacent panels.

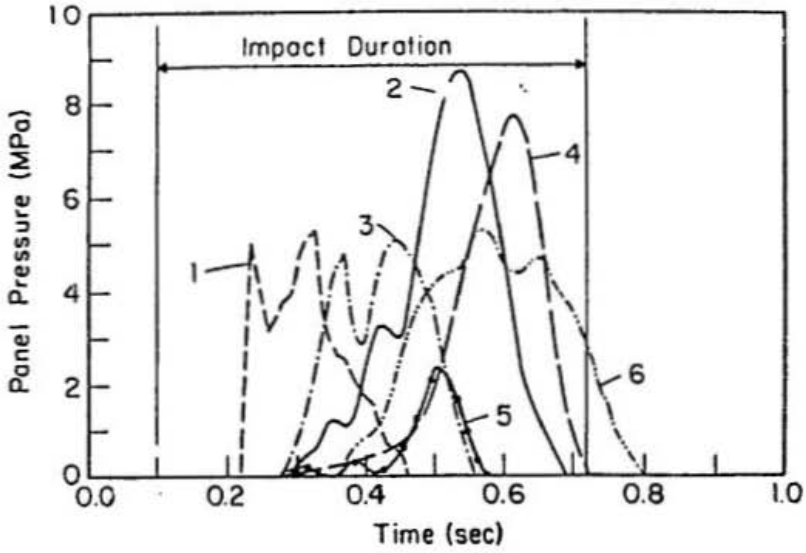

Figure 4.17 Six Loaded Subpanels during a Kigoriak Ramming Event

Figure 4.18 presents the frequency distribution for the number of panels coincidentally loaded during impact. During the initial and final stages of impact the panels may experience pressures below the 2MPa threshold. Sixty percent of the impact phase is characterized by no critical zone activity on the instrumented panel. Alternately stated, pressures exceeded 2MPa during an interval which was equal to approximately 40 percent of the loading period. The critical zone moved off the instrumented panel during the period of inactivity.

The area of the critical zone was obtained form the number of panels activated at particular instants in time (intervals of 0.05seconds). Fifty-three percent of the critical zone areas were registered as $0.21m^2$ (see Figure 4.19). The mean area of a critical zone, as calculated form the number of active panels is $0.352m^2$. Smaller critical zones may exist within the subpanel area. However, the spatial resolution of the instrumentation system does not allow areas smaller than an individual subpanel to be distinguished.

Subpanel pressures were recorded throughout the impact phase of each event at intervals of 0.05seconds. These values were then averaged, yielding a mean instantaneous pressure of 3.91MPa for an individual subpanel. A distribution of the instantaneous panel pressures is presented in Figure 4.20. Fifty-five percent of the panel pressures are within the 2-4MPa range. Extreme panel pressures, between 14-18MPa, occur only 0.7 percent of the time.

The highest instantaneous pressure recorded on a subpanel during the seventeen ramming events was 18MPa. The peak instantaneous pressures for individual subpanels were substantially lower than the peak pressures registered on the Louis S. St. Laurent pressure sensors (at times, the latter exceeded 50MPa). The large discrepancy between the peak pressures of the two data sets is primarily due to the differing spatial resolutions of the instrumentation systems. Additionally, the pressure sensors have an increased stiffness over the surrounding structure. Consequently, the pressure gauges may measure the limits of ice strength, rather than the actual ice pressure experienced by the hull.

Figure 4.21 presents a distribution of the forces that were registered on individual subpanels during impact. Forces between 0-2.0MN account for 74 percent of the distributed values. Extreme forces exceeding 4MN have a 6 percent frequency of occurrence. The mean of the forces recorded by individual subpanels is 1.31MN.

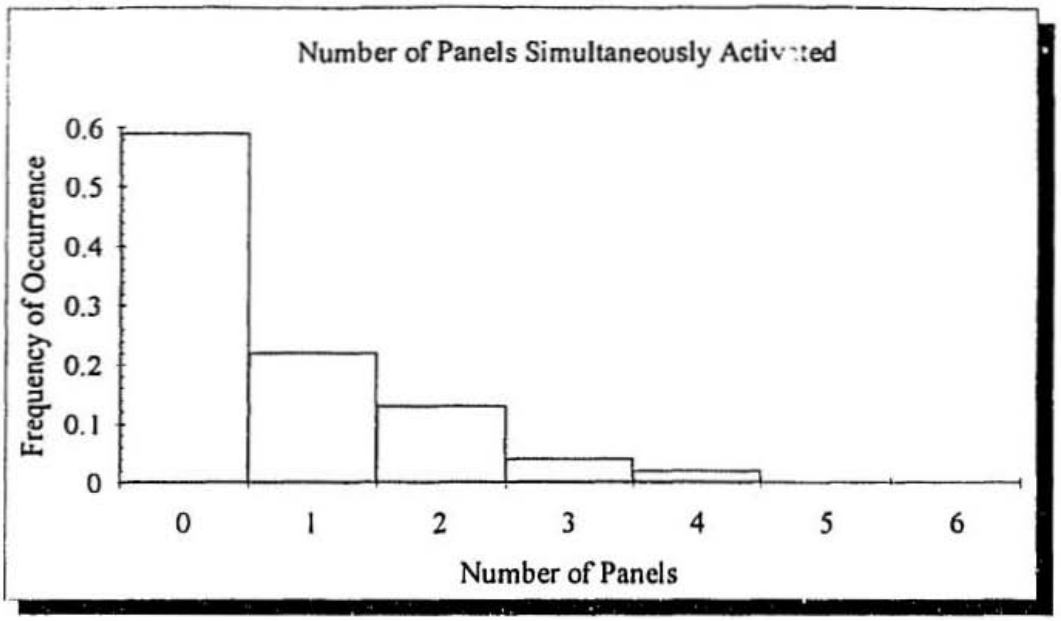

Figure 4.18 Number of Panels Simultaneously Activated

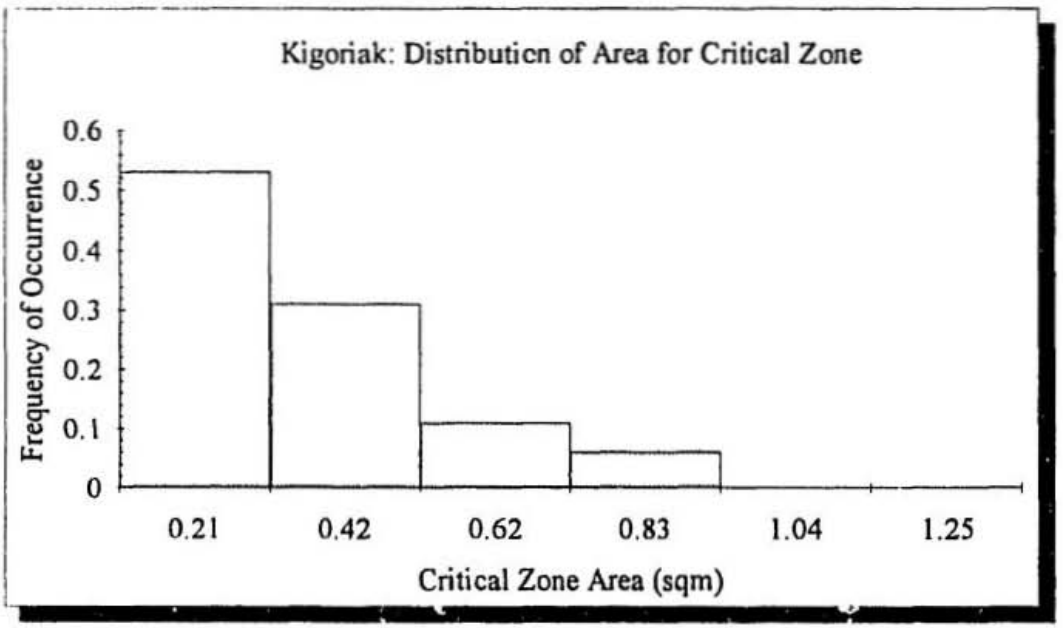

Figure 4.19 Distribution of Critical Zone Area for Kigoriak

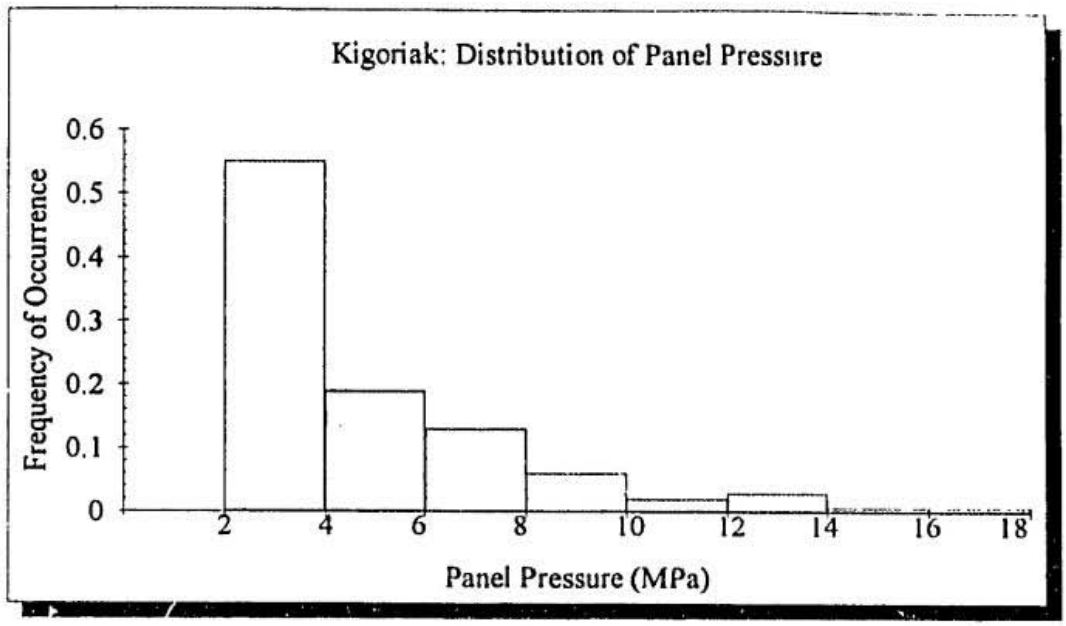

Figure 4.20 Distribution of Pressure Recorded by Individual Panels

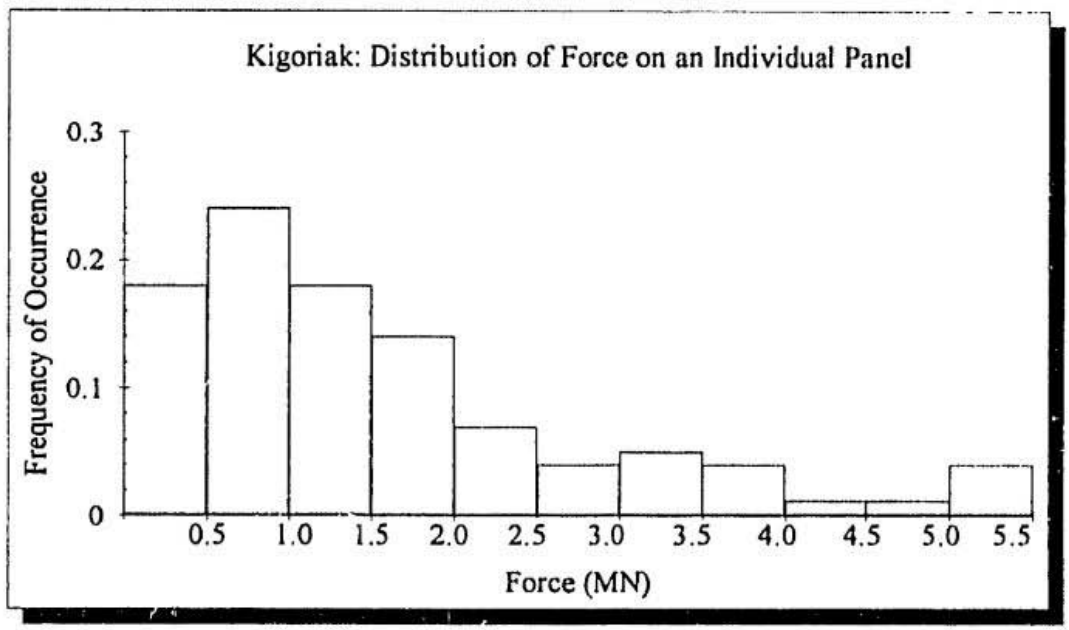

Figure 4.21 Distribution of the Applied Force to an Individual Panel

4.5 Comparison of Critical Zones for Louis S. St. Laurent and Kigoriak

Table 4.4 presents a comparison of the critical zone parameters for the Louis S. St. Laurent and the Kigoriak data sets. Substantial differences in the mean values of area and pressure of the critical zone exist. The size of the Louis critical zones is 1/3 of the area of the Kigoriak zones. Additionally, the mean pressure of the critical zones for the Louis is approximately 3 times the mean zonal pressure for the Kigoriak. Little difference between the compared forces exists.

Table 4.4 Comparison of Critical Zones for the Louis S. St. Laurent and Kigoriak Data Sets

Critical Zone Parameter	Louis S. St. Laurent Trials	Kigoriak Trials
Area	$0.112m^2$	$0.352m^2$
Average pressure	11.5MPa	3.91MPa
Force	1.09MN	1.31MN

The significant differences in zonal area and average pressure may be attributed to the spatial resolution of each instrumentation system. As previously noted, the pressure transducers represent an area of $0.05m^2$, approximately 1/5 of the area of a subpanel on the Kigoriak. As a result, loads applied over areas smaller than $0.208m^2$ were not recognized by the Kigoriak strain gauges. Similarly, the effects of intense pressures acting individually over (perhaps multiple) areas within one subpanel are "smeared out" through the process of averaging.

Suppose that the active area of the Kigoriak encompasses numerous critical zones, similar in size and force to those zones characteristic of the Louis S. St. Laurent. Under these circumstances the pressure registered on the active area is, in effect, an average pressure of 3.91MPa. The corresponding force over the active area of $0.352m^2$ is 1.31MN. If zonal properties are similar for the Louis S. St. Laurent and the Kigoriak, it is possible that one critical zone with a force of 1.09MN and an area of $0.112m^2$ exists within the activated area ($0.352m^2$) of Kigoriak. Consequently, 32 percent of the active area is occupied by the critical zone. The remaining 68 percent of the area consists of a region of background pressure (see Figure 4.22). The modified critical zone for the Kigoriak has an area of $0.112m^2$, a force of 1.09MN, and an average pressure of 9.73MPa. The region of background pressure occupies $0.24m^2$, has a force of 0.22MN, and an average pressure of 0.92MPa.

The average pressure of an active area which has one critical zone with a force of 1.09MN and an area of $0.112m^2$ is 5.3MPa (see Figure 4.22). Conversely, the mean pressure of the activated area, as obtained from seventeen cases of impact is 3.91MPa. Discrepancies between the hypothetical and actual average pressures of the activated region may be a result of the chosen critical zone parameters. Perhaps the critical zones of the Kigoriak are smaller, have a reduced force, or are less frequent in number, than those zones of the Louis S. St. Laurent. As discussed previously, it is expected that differences in the data sets were largely caused by the effects of instrumentation.

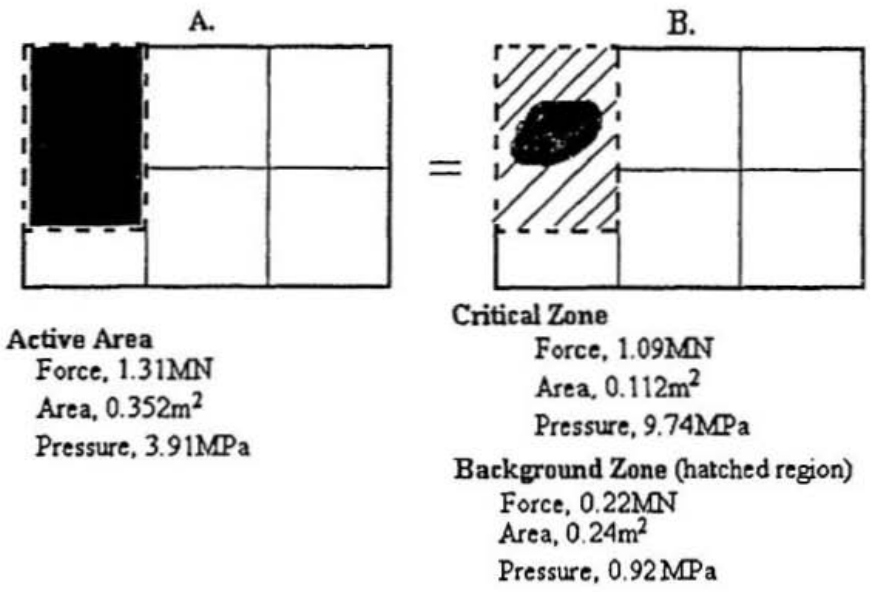

Figure 4.22 Conceptual Presentation of the Active Area of the Kigoriak (based upon critical zone data from the Louis S. St. Laurent)

The above analysis is an initial approach which attempts to relate the fundamental properties of critical zones from two different data sets. The analysis shows that it is possible that critical zones of equivalent size and force occur in both data sets. Table 4.5 presents a comparison of the critical zone and background region based upon the assumption that the high pressure zones are similar for the Louis S. St. Laurent and the Kigoriak.

An estimate for the number of critical zones per square meter was calculated for the Kigoriak based upon critical zone data from the Louis S. St Laurent. In the highly exposed bow section of the Kigoriak, the mean number of critical zones per square meter is 0.80. The modified critical zone represents 9 percent of the 1.25m^2 instrumented area (which translates to 0.80 zones/m^2).

Table 4.5 Modified Critical Zone of the Kigoriak based upon the Louis S. St. Laurent Critical Zones

Critical Zone Parameter	Active Area*	Critical Zone	
Area	0.352	Critical zone area	0.112m^2
		Background region	0.24m^2
Force	1.31MN	Critical zone force	1.09MN
		Background region	0.22MN
Pressure	3.91MPa	Critical zone pressure	9.74MPa
		Background pressure	3.91MPa

* obtained from subpanel activity

4.6 Conclusions

Pressure cell data from the Louis S. St. Laurent ramming trials provide important information about the behavior of critical zones in space and in time. This information was used to interpret strain gauge data from the Kigoriak trials in terms of zones of high pressure. In an initial attempt to relate the two data sets and to demonstrate the practical application of the concept of critical zones to field data, critical zones were assumed to be equivalent in size and force. It was shown that in the case of the Kigoriak, critical zones may be smaller and may have a higher average pressure than is apparent from the data recorded by individual subpanels.

Uncertainty associated with the assumption of critical zones of equivalent size and force may be attributed to several factors. Differences in the spatial resolution of the instrumentation systems had notable effects upon the recorded data. Additionally, differences in the bow shape of the Louis S. St. Laurent and the Kigoriak may be expected

to influence the critical zone parameters. Specifically, the location of the instrumented panels on the bow, the ice failure mode initiated by the bow shape, and the duration of the interaction (as related to the effective penetration of the ice) each play a role in characterizing the failure process. Finally, variable ice properties may be expected to influence the results of the analysis. Despite the effects each of these factors had on the data examined, the importance critical zones have in the failure process was consistently demonstrated. Further research is needed in this area to more firmly establish the parameters associated with high pressure zones.

Analysis of the ship ramming trials has provided important information about the critical zones and their frequency of occurrence. This information will aid in understanding the interaction process between an offshore structure and an ice sheet, to be discussed subsequently.

Chapter 5

Offshore Structures: Case Study of the Molikpaq

5.1 Introduction

Currently Arctic platforms are designed to resist horizontal forces of the order of 30 percent of their weight (Jefferies and Wright, 1988). Mechanisms such as local crushing may generate intense pressures over very small areas. These intense local pressures may not be directly representative of the global loads. Due to their random nature in space and time, intense local pressures should be averaged over the global area. As a result, the structure will experience reduced global loads in comparison to those experienced locally. For instance, the Molikpaq experienced global pressures of the order of 1-2MPa, while local pressures may have approximated 20MPa. A thorough understanding of ice-structure interaction is necessary to provide design criteria which are accurate and also economical.

5.2 History of the Molikpaq

During the winter 1985-86 season the Gulf Molikpaq was deployed at Amauligak I-65 in the Canadian Beaufort Sea. The site was approximately 75km offshore at a water depth of 32m. The Molikpaq was located within the transition zone, where it typically experienced mobile ice conditions (Figure 5.1).

The winter of 1985-86 proved to be more severe than the previous few years. Numerous interactions involving firstyear and multiyear floes produced significant structural loading. An event occurring on April 12, 1986, involving a multiyear floe, is believed to have caused intense dynamic vibration in the platform. Vibrations were of sufficient severity to induce fatigue of the sand core, the principal element by which the Molikpaq resists ice loads, threatening the global stability of the platform. This event is said to have been less severe than the design '25-year' case (Jefferies and Wright, 1988). The April 12 event is testimony to the fact that an understanding of ice-structure interaction is needed for the establishment of adequate design criteria.

The May 12, 1986 event is the most important of the entire 1985-86 data set. It provides well-conditioned information on the simultaneity of crushing and pressure-area effects (Jefferies, 1988). The event of May 12 occurred when a 110km^2 free floating floe, comprised of a matrix of thick firstyear ice with several multiyear inclusions, impacted the Molikpaq at 0.18m/s. The event, approximately 30 minutes in duration, involved the north and north-east faces.

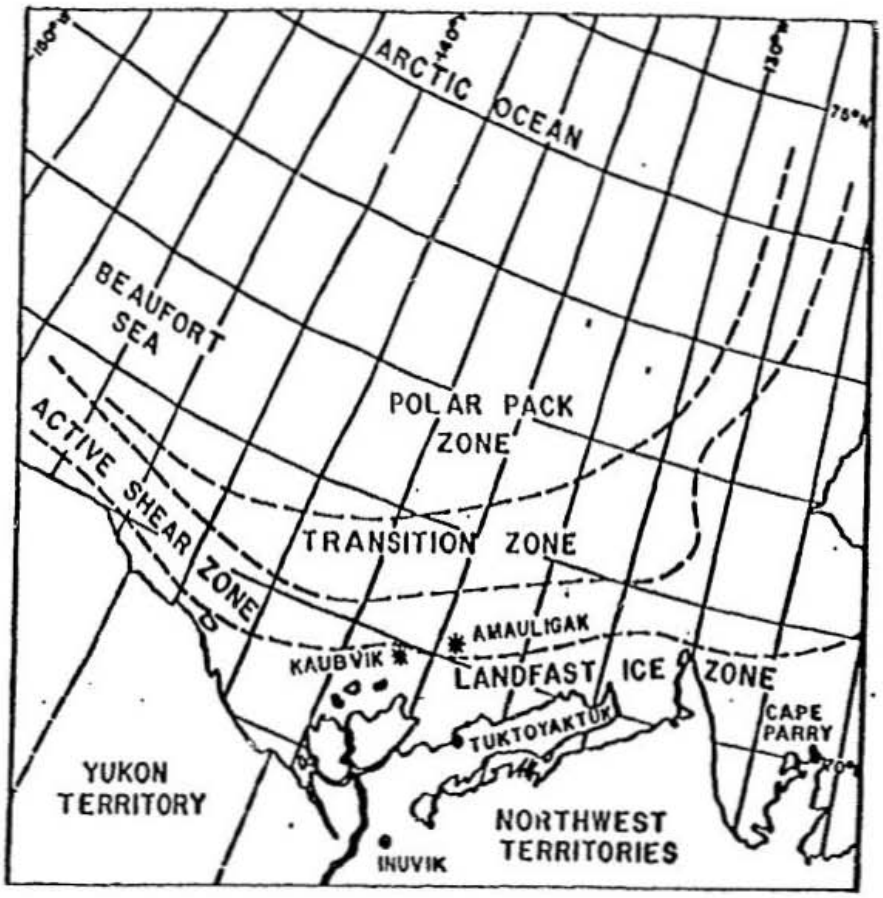

Figure 5.1 Molikpaq Location in the Canadian Beaufort Sea

5.3 Dynamics of the Interaction Process

Ice-structure interaction is a complex process involving cyclic oscillations in load which arise from the ice mechanics of the process and its associated structural response. Typically, numerous peaks and troughs constitute an ice-structure interaction load trace. Most significant ice loading (>100MN globally) of the Molikpaq was accompanied by a

cyclic response. This was due, in part, to the inherent flexibility of the Molikpaq which accentuated the forced vibration process (Rogers et al., 1986). Cyclic loads, commonly of the order of 0.5-3Hz, induced vibration of the structure often producing event durations as long as 30 minutes (Jefferies and Wright, 1988).

Pilkington et al. (1983(b)) state that vibrations may be divided into mainly two groups. The first group is the random type which exhibits essentially high frequencies, with no definite pattern, for limited amounts of time. Fourier analysis reveals no constant frequency during the whole interval. The second division of vibrations is the periodic type. Periodic vibrations, usually ranging from 0.3-3Hz, exhibit a clear build up of force followed by a sudden collapse of the ice. This induces elastic motion of the structure.

Dynamic response may be induced by both nonsimultaneous and simultaneous crushing, although other failure modes may be present. Nonsimultaneous failure implies that at any one point in time, different local areas of the failure regions are in different stages of failure (Kry, 1978). In contrast to load traces representative of simultaneous failure across the structural face, regions of nonsimultaneous failure characteristically do not exhibit patterns of synchronized stress drops (see Figure 5.2). In addition, corresponding loads may be five times less than those experienced during simultaneous crushing.

As with the May 12 event, transition from nonsimultaneous to simultaneous crushing occurs quickly, of the order of one loading period. Examination of a particular series of strain gauges reveals identical phases of loading across the face, indicative of simultaneous crushing. Phaselocked behavior does not preclude the existence of pressure variations across the structural face.

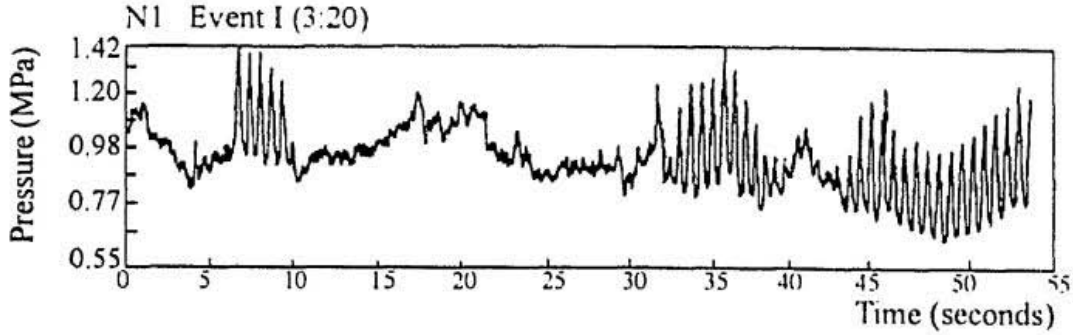

Figure 5.2 Strain Gauge Load Trace Illustrating Phaselocked Transition Zone

From observations of lighthouses in the Gulf of Bothnia (Engelbrektson, 1989) certain trends were found to be characteristic of cyclic load traces. Following is a descriptive commentary of the load trace presented in Figure 5.3. Coordinated ice failure is followed by structural rebound (A-B). The structure reaches the limit of rebound, slows down, and turns, at which point the strain-rate decreases and the contact pressure increases to a peak before the forward velocity increases. The structure tends to move ahead from the ice (B-D). As the structure decelerates, the contact pressure increases once more in a ductile manner until the ice strength is exceeded and a sudden coordinated failure occurs (D-E).

The sudden stress drop following the peak pressure is the most important feature regarding ice-structure interaction. Stress drops, typically of the order of 50 percent of the peak load in cases of strong resonant vibrations, occur almost simultaneously at various contact zones. Brittleness of the ice after fracture nucleation leads to progressive cracking within the individual fractured zones, which triggers progressive collapses when the load at one collapsed zone is overtaken by adjacent zones (Engelbrektson, 1989).

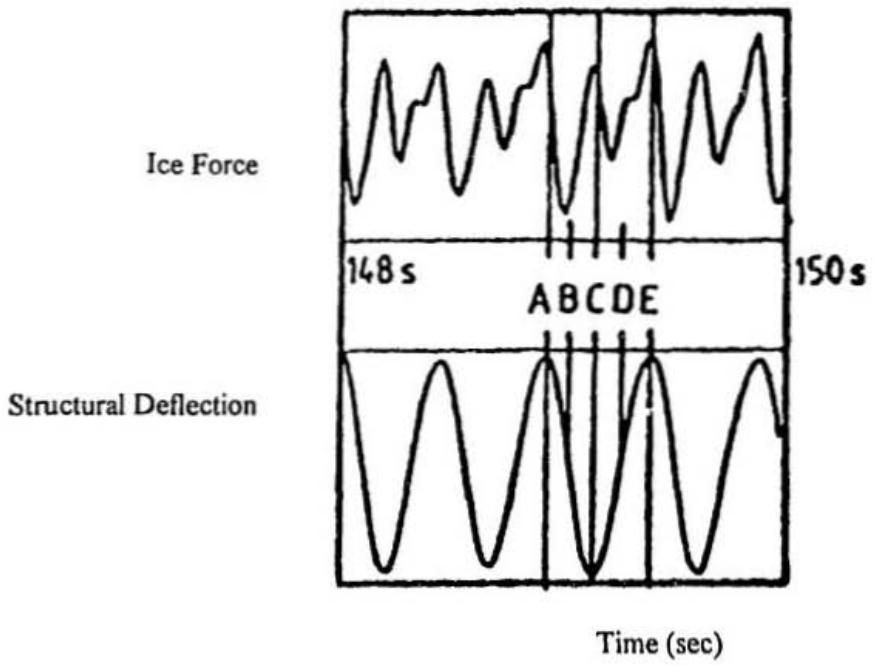

Figure 5.3 Various Phases of Ice-Structure Interaction during a Cycle of Oscillation (Engelbrektson, 1989)

5.4 Molikpaq Specifications

The Molikpaq is a hybrid platform consisting of a steel annulus infilled with dredged sand (Jefferies and Wright, 1988). Maximum ice strengthening of the caisson hull occurs from 12m-24m elevation. This portion is also protected by a Zebron coating to reduce friction and adfreeze of ice (Rogers et al., 1986). All steel in bulkheads above the 19.8m waterline is grade EH36-060. Steel in bulkheads below elevation 19.8m is grade DH36. Outer shell plating thickness is 32mm. The distance between consecutive main bulkheads is 2.44m. For detailed spacing and location of bulkheads and ribs see Figure 5.4.

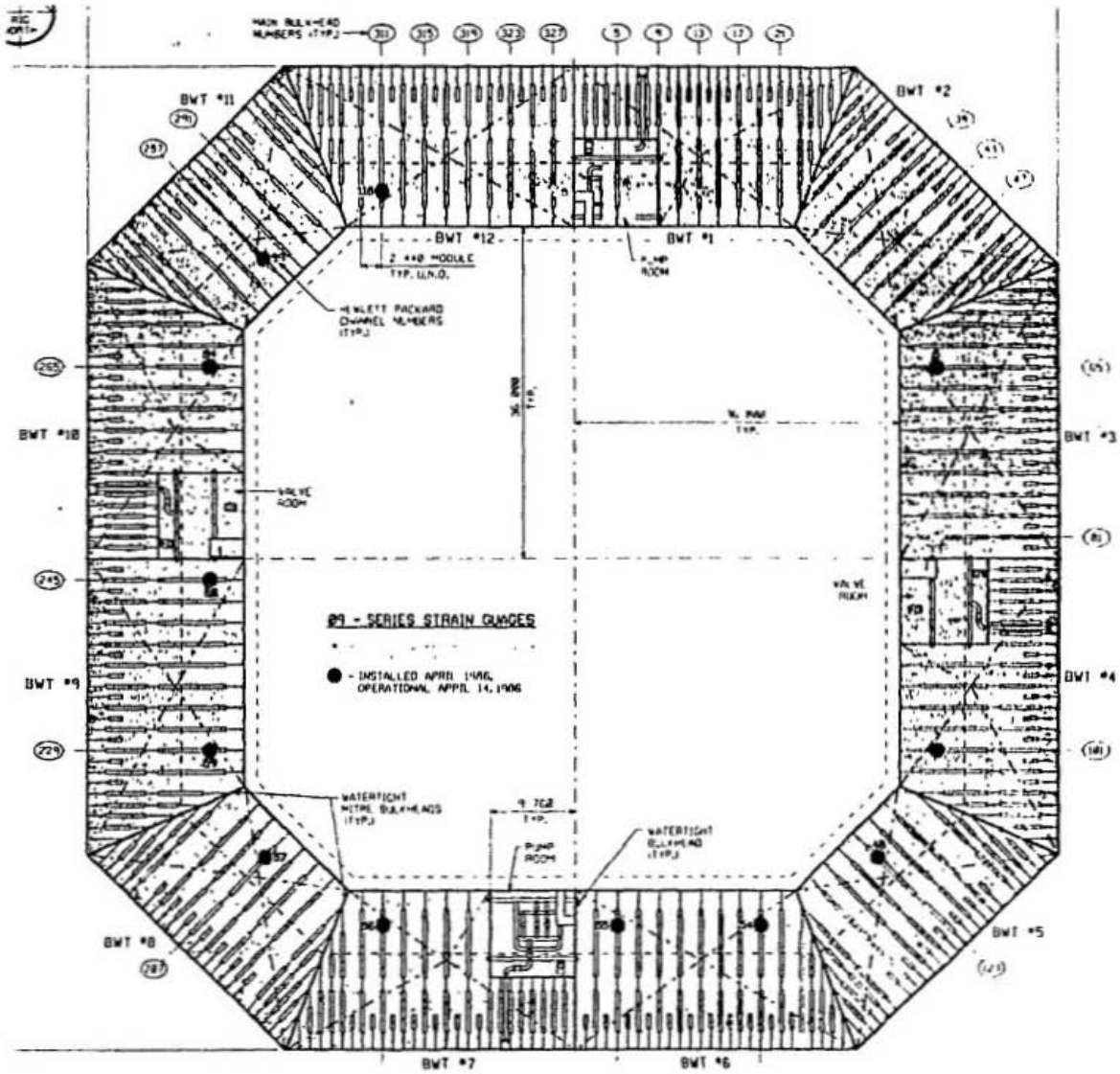

Figure 5.4 Detail of Molikpaq Rib and Bulkhead Spacing
(Gulf Resources, 1988)

5.5 Instrumentation

Ice load measurement on the Molikpaq was carried out using two instrumentation systems, i.e. strain gauges and Medof panels. Discrepancies in the load data from each instrumentation system exist. The Medof panels exhibited a limited capacity when registering high frequency loads. Although the strain gauges were calibrated based upon Medof panel data (Gulf Resources, 1988) they are believed to be a more accurate representation of the loads experienced by the Molikpaq.

5.5.1 Strain Gauges

A total of 316 strain gauges, mounted at several locations on the main bulkheads of the caisson, were installed on the Molikpaq steelwork. Experience with the response of these gauges showed that those referred to as the '09' series had the best sensitivity and linearity for load measurement (Jefferies and Wright, 1988). Positioned in zones of relatively uniform stress, they were less subject to influences from exact gauge location and large stress gradients than would be gauges at other locations (i.e. mounted on the flange). Finite element studies indicated that the '09' strain gauges had a tributary area 5m wide. The strain gauges were capable of registering cyclic ice forces of the order of 50Hz (Jefferies, 1988).

Strain gauge factors for converting measured steel strains to ice loads were calculated. Determination of the strain gauge factors relied heavily upon the ice creep event of March 25, 1986. This event was chosen since the ice loads were relatively uniform across the face (the Medof panels corresponded well), the ice thickness was well quantified, and the

event was slow enough so that the limited high frequency response of the panels did not cause a significant error (Jefferies and Wright, 1988). Calculation of a strain gauge factor involved a cross plot of the Medof panel data and strain gauge data, taking into account the effects of panel creep. The slope of the cross plot yielded the strain gauge factor in tonnes/m/microstrain. Using three '09' series strain gauges north face loads were calculated for the two cases of mulityear and first year interactions. The error associated with the gauges was estimated as 17.9 percent for the multiyear event and 21.5 percent for the firstyear event (Rogers et al., 1991).

5.5.2 Medof Panels

The Medof panel, designed in a joint effort between Dome Petroleum, M. Metge, and FENCO Consultants, consisted of two large steel plates (1.135m x 2.715m) separated by 2.54mm (see Figure 5.5). Steel thicknesses, 12.7mm and 3.175mm for the front and back plates, respectively, were designed to prevent denting from local ice stresses as intense as 20MPa on 0.05m^2 (Pilkington et al., 1983(a)). The edges of the front and back plates were welded to form a large contained structure which encased regularly interspersed urethane buttons, each of 9.525mm diameter at a 12.7mm spacing (Hamza and Blanchet, 1984). The interstices were filled with aqueous calcium chloride, a nonfreezing fluid (Spencer, 1991).

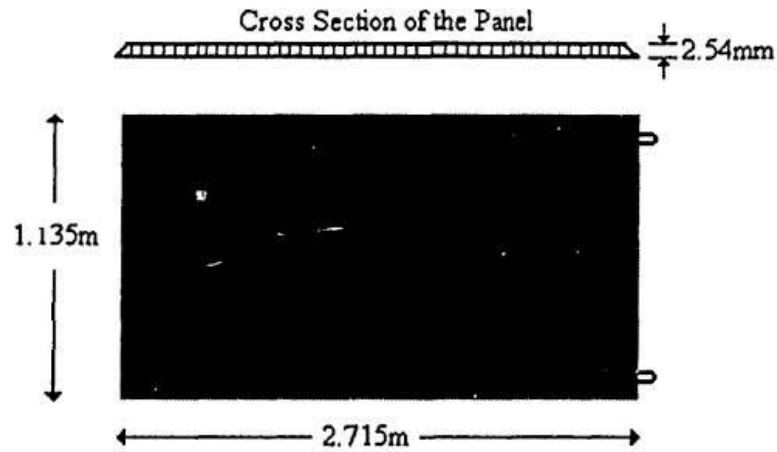

Figure 5.5 Plan View of Section Through Standard Medof Panel

During periods of high frequency loading, consecutive load spikes register as multiple instantaneous loads upon the panel. Initially the fluid offers immediate resistance to loading, becoming the primary load bearing mechanism. The fluid responds to applied stress by exiting the panel into the sight tube (Figure 5.6). The change in hydrostatic head is registered and recorded by a sensitive electronic pressure transducer (Spencer, 1991). As stress upon the fluid is relieved by fluid displacement, the load is transferred to the urethane buttons. The buttons compress, displacing larger quantities of fluid into the exit tube. The panel load continues to increase until ice failure ensues, resulting in an immediate stress drop whereby pressure upon the fluid and buttons is relieved. The buttons recover their original shape, allowing fluid to enter previously compacted areas.

As previously mentioned, several processes are occurring simultaneously within the Medof panel. The variability of these components makes it very difficult to interpret panel behavior at any particular time. The load could be carried by the fluid alone, as in the initial stages of panel compression, by a combination of fluid/button response, or solely by

the urethane buttons, depending upon the particular instant of loading. Although the exact mechanics of panel response are not clear, the contributing components have been identified. Inaccuracies associated with the various panel components are addressed in the following sections.

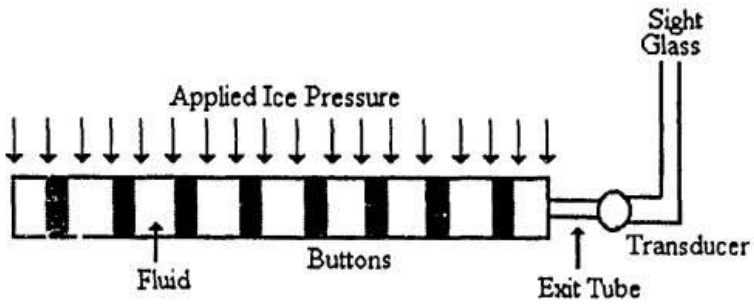

Figure 5.6 Detailed Drawing of Medof Urethane Buttons
(Spencer, 1991)

5.5.2.1 Factors Influencing Medof Panel Accuracy

Numerous factors influence the accuracy of the Medof panel response, in turn affecting the interpretation of results. Comparison between load traces from the strain gauges and Medof panels demonstrates that the latter suffers from a sluggish response to high frequency loads. Parameters which influence Medof output include the inherent creep of the urethane buttons, the finite fluid viscosity of the aqueous calcium chloride, the non-uniform distribution of load over the panel area, and the spatial and temporal variations of ice temperature over the panel area, each to be discussed subsequently.

Medof Panel Frequency Response

Although the ice load panels provide a direct measure of the ice load, they are limited since their response time to a step change in load is of the order of 5 to 10 seconds. They do not provide an accurate account of cyclic ice forces with fundamental frequencies in the range of 0.5-3.0 Hz (Jefferies and Wright, 1987). Examination of the May 12, 1986 event indicates that loading frequencies were commonly of the order of 0.18-1.4Hz, for this particular event (see Appendix A).

Two major physical causes for the time dependent response of the panel exist. The first is the finite fluid viscosity of the panel fluid. Several seconds are required to completely expel the fluid through the orifice and the length of tubing connecting the panel to the sight glass. Due to the viscosity factor, loads fluctuating at high frequencies will only be partially registered. Second, the polyurethane buttons were found to creep. Panel compression, hence the displaced fluid, will increase with time even under a constant load (Jefferies, 1988).

Nonuniform Distribution of Panel Load

Calibration work performed upon the Medof panels (Geotechnical Resources, Inc., 1988) indicated a non-linear response to applied load. This non-linearity results in a panel output which is dependent upon the applied load as well as the load distribution. Application of a point load poses an interesting problem for the panel response. Suppose the load is applied over a very small area. Elastomer buttons in the area immediately surrounding the load would be fully compressed. Those located more remotely would remain virtually unaffected. The response of an individual panel area is governed by an

operating curve which is representative of its stress state. That particular operating curve does not apply to the panel as a whole. An "average pressure", obtained by integrating the force over the entire loaded area, is not representative of intense zones of localized pressure.

Gulf Resources has undertaken studies to determine the effects of nonuniform loading on panel response. In a case where half of the panel is loaded at 1MPa compared with all of the panel at 0.5MPa, the predicted elastic load would be 6 percent low (Gulf Resources, 1988). Conversely, Pilkington et al. (1983) addressed partial panel loading and concluded that the Medof panel measures total load independently of the area of application. In view of the above discussion, the study conducted by Gulf Resources is believed to be a more accurate assessment of the Medof panels.

Temperature Dependence

The elastic response of the Medof panel is temperature dependent. Despite a 15 percent increase in panel stiffness from 0°C to -20°C substantial agreement was found between load data collected at -5°C and -10°C (Gulf Resources, 1988). Thermal stress gradients within the ice sheet also had an effect upon the panel response. Ice near the water/ice interface may have been of very low elastic modulus and as a result may not have transferred stress into the panel very well (Strandberg, 1986). In addition, the fluid response may have been increasingly sluggish with decreasing temperatures. Theoretically the calcium chloride was to remain in a liquid state. It is possible that the physical state of the hydraulic fluid may have been altered due to low temperatures. The possibility of emulsification of the aqueous calcium chloride at low temperatures was raised by Blanchet et al. (1992).

5.5.2.2 Kelvin Model Representation of Revised Medof Panel Loads

Creep and the elastic response of the Medof panels were evaluated by Gulf Resources (1988). The aim of that analysis was to produce a mathematical description to be used in the correction for panel creep. A revised representation of the Medof panel load response was produced using four Kelvin elements and an elastic element (see Figure 5.7). Springs and dashpots were used to account for the time and creep constants of individual Medof panels. No particular significance was attached to the individual parameters in the Kelvin model (Gulf Resources, 1988). Equivalent Medof panel output was calculated as the total compression of all elements. Since the panels have a limited high frequency response, the elastic element was converted into a Kelvin element by the addition of a parallel dashpot (Gulf Resources, 1988).

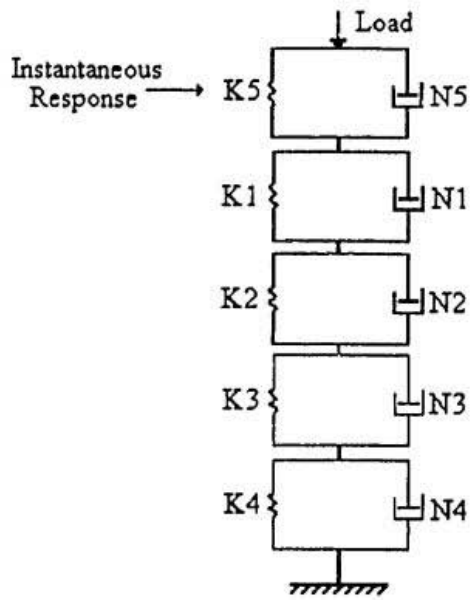

Figure 5.7 Kelvin Model Representation of Medof Panel Response

Amplitude and time delay plots were derived using the Kelvin model parameters (Gulf Resources, 1988). Figures 5.8 and 5.9 demonstrate that panel creep causes an overprediction in load at frequencies less than 0.01Hz. Conversely, the limited response of the Medof panels at higher frequencies leads to underprediction of the applied load. The maximum contribution to the output by panel creep, seen to occur at input frequencies of the order of 10^{-3}Hz, is 20 percent greater than a perfect panel without creep (Gulf Resources, 1988). Panel output is expected to be very close to the elastic case for frequencies of 10^{-2}Hz (Gulf Resources, 1988). At these frequencies, load overprediction and underprediction act in opposition, thereby cancelling out one another.

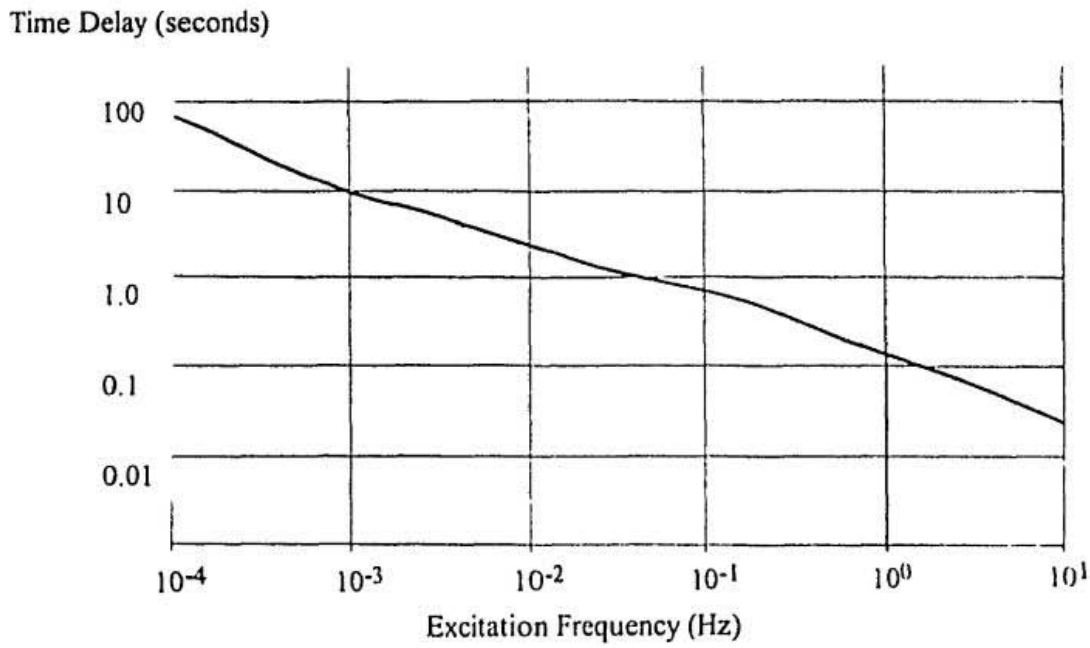

Figure 5.8 Time Delay Response of Medof Panel Model
(Gulf Resources, 1988)

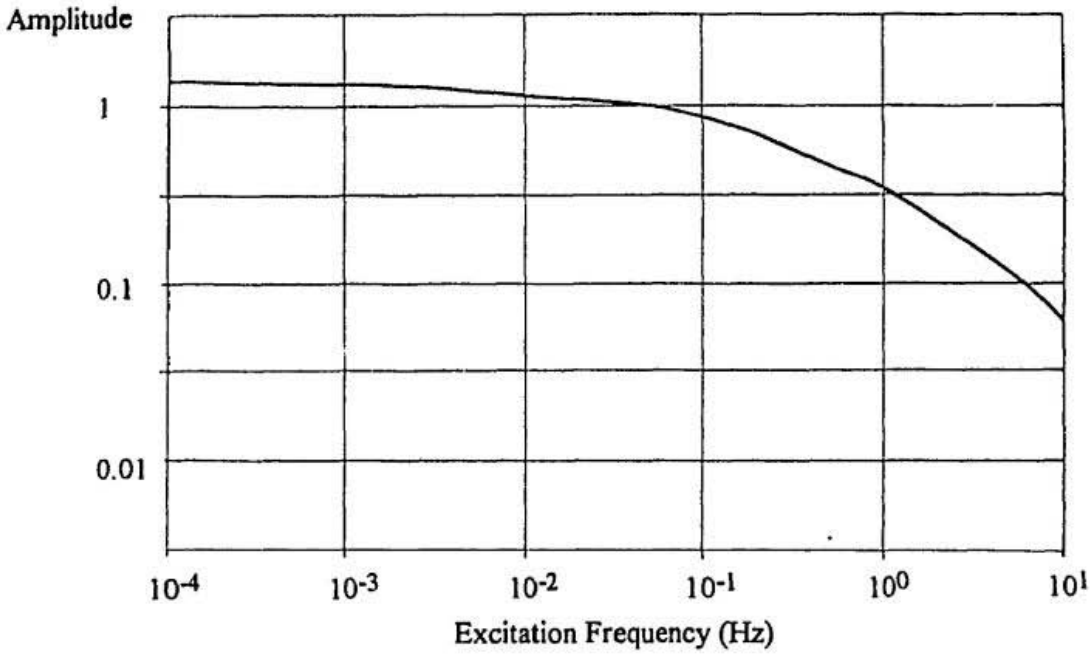

Figure 5.9 Amplitude Response of Medof Panel Model
(Gulf Resources, 1988)

5.5.2.3 Estimation of Medof Panel Accuracy using Kelvin Model Representation

Frequencies typical of the May 12, 1986 event were obtained by examining the corresponding strain gauge plots for the burst files. Burst files are defined as files sampled by the '09' series strain gauges at 50Hz for a 60 second duration. Three such files exist for the May 12 event (3:20, 3:21, 3:25). The first and second files were sampled approximately 10-11 minutes after the ice floe impacted the Molikpaq. The third burst file was sampled 15 minutes into the event. Typical loading frequencies for the first two files were 1.4-1.5Hz. The third file, sampled as the event closed, exhibited significantly lower frequencies (0.24-0.40Hz).

These frequencies may be used in conjunction with the Figures 5.8 and 5.9 to ascertain time delay constants characteristic of the May 12 event. The Medof panels experienced a time delay of 0.1 seconds and 0.75 seconds during the intermediate and final stages of event loading, respectively. Similarly, amplitude response of the Medof panel taken into consideration was underpredicted by 25 percent and 50 percent during the intermediate and final stages of loading, respectively. These data are indicative of the Medof panel inaccuracy when sampling high frequency loads. At worst, the input frequency was reduced by 50 percent (reduction in amplitude from 1 to 0.5). Conversely, Gulf estimated the accuracy of a typical Medof panel as 13 percent, based upon a characteristic event frequency of 10^{-2}Hz (Gulf Resources, 1988).

5.5.2.4 Creep Evaluation of the Medof Panels

The applicability of the Kelvin model to the May 12 event was tested by substituting loading rates typical of the second and third burst files. Loading rates, calculated first, from the Medof panels and second, from the strain gauges, were used to determine the effect of creep on panel response (see Appendix A). Representative stress rates were obtained from the high frequency response strain gauges. Burst files demonstrate the brief temporal nature of the load, comparable to impulse loading. Stress rates of 32MPa/min and 13MPa/min, (see Appendix A) representative of the intermediate and latter stages of loading, yield 0.5mm and 0.2mm of creep within one second, respectively (see Figure 5.10). It is expected that insufficient time had elapsed for significant creep to occur during the May 12 event. Therefore, data from this particular event were not contaminated by panel creep.

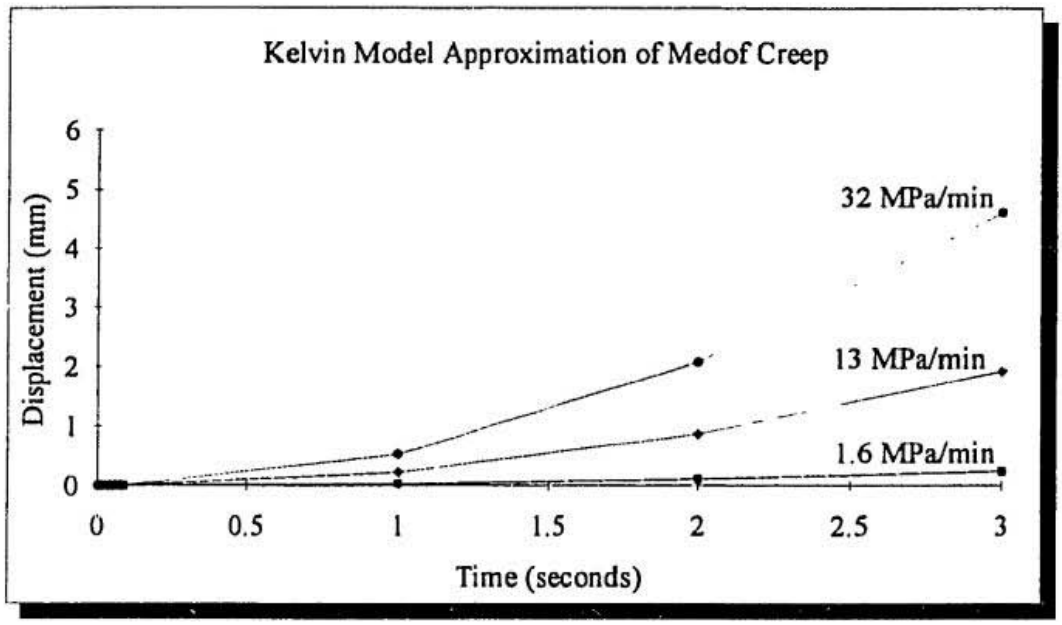

Figure 5.10 Medof Creep Corresponding to Various Loading Rates

5.5.2.5 Medof Panels Activated during the May 12 Event

The May 12 ice-structure interaction involved predominantly the north and northeast faces. Figure 5.11 identifies the loaded area of the activated Medof panels. Ice thicknesses were determined from visual observations recorded during the event and from Medof panel activity (see Appendix A). The lower Medof panels on the northeast face and in the center of the north face were partially loaded. This implies that ice thicknesses were 2.8m and 3.3m at the east and center of the north face, respectively. Panels above the waterline are not considered active since they registered no load activity.

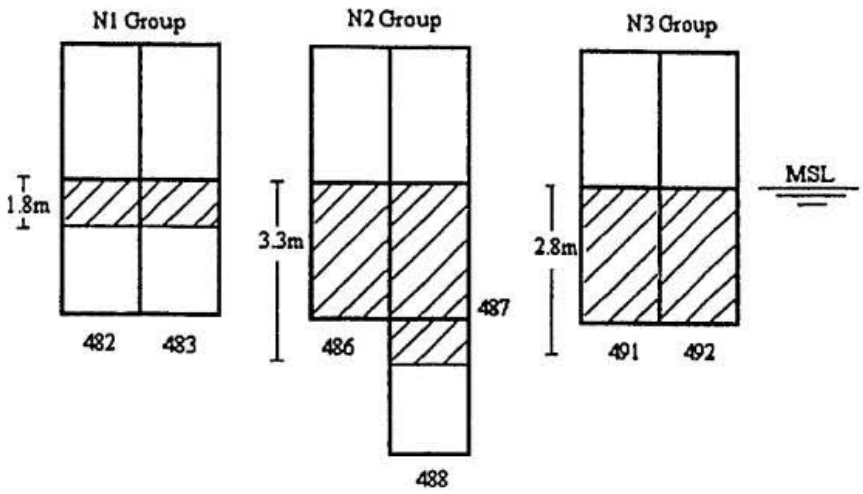

Figure 5.11 Medof Panel Loaded Area during the May 12 Event

5.6 Comparison of Medof Panel Data to Strain Gauge Data

The following discussion is based upon graphs provided by Gulf Resources. The actual data files for the May 12, 1986 event were not available. Consequently, Medof panel data and strain gauge data may not always be presented in the clearest fashion, i.e. dissimilar scales.

5.6.1 Peak Pressures: Medof versus Strain Gauge Data

Comparison of a typical burst file to a detailed Medof plot (see Figures 5.12, 5.13) demonstrates the incompatibility between the two instrumentation systems. As previously discussed, the Medof panels do not exhibit the high frequency dynamics typical of the strain gauge traces. The load spikes registered by the Medof panels do not correspond very well with the dynamics recorded by the strain gauges. Nevertheless, similarities exist between the data sets.

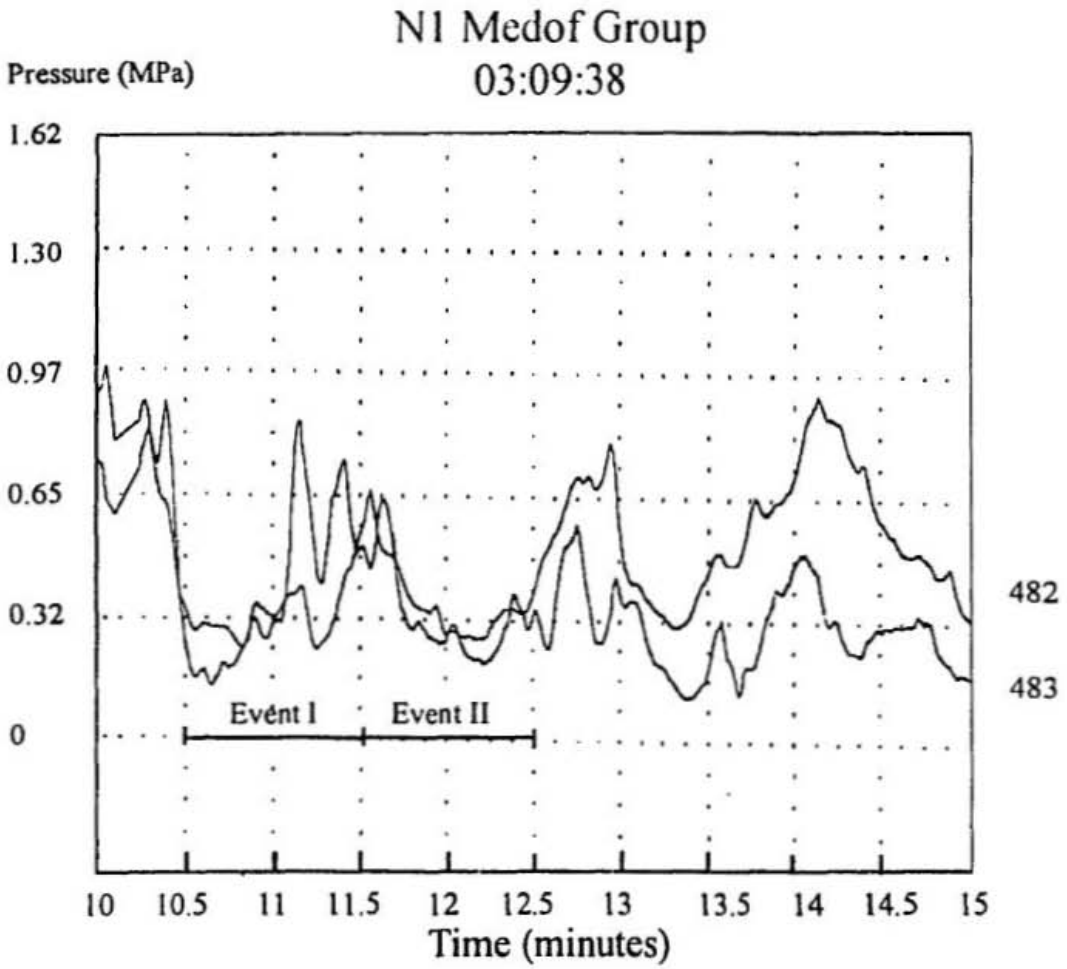

Figure 5.12 Detail of Medof Group N1 Load Trace

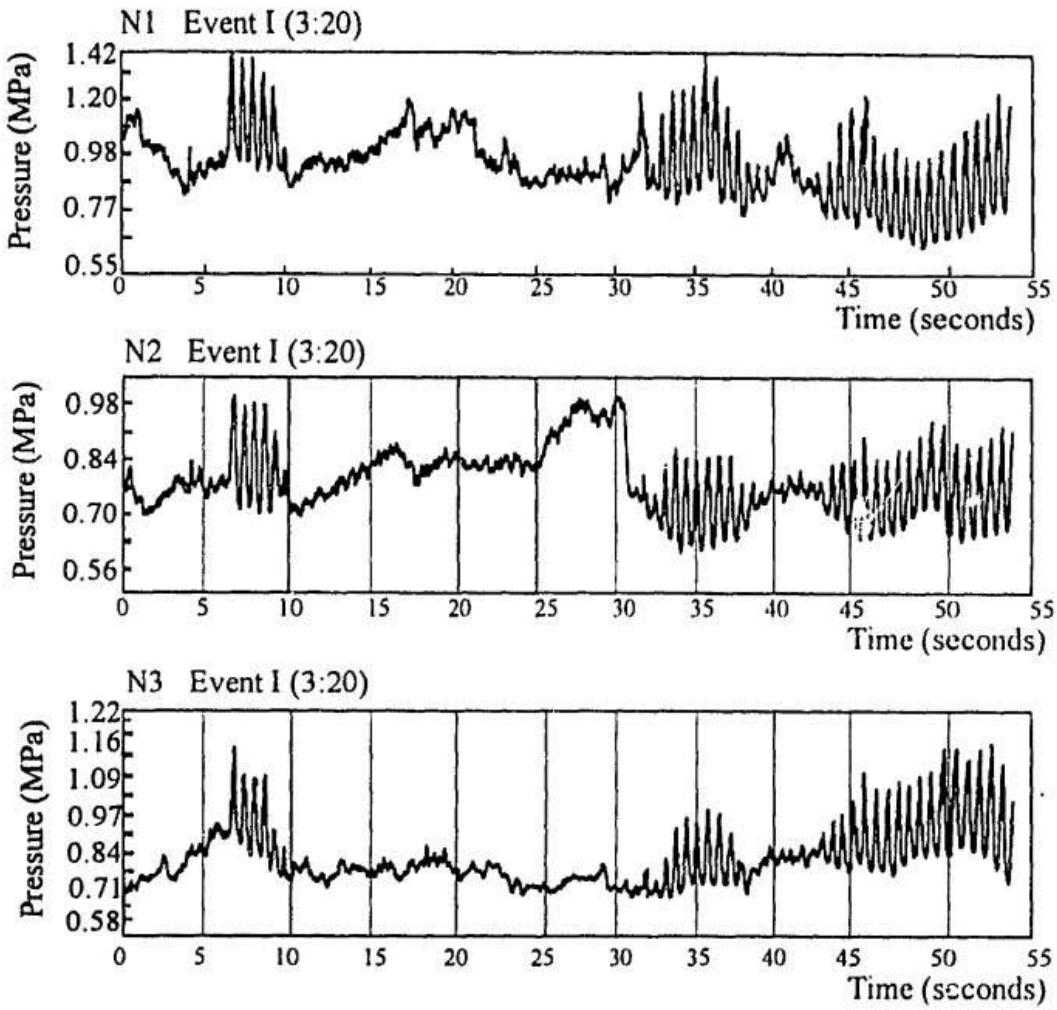

Figure 5.13 Strain Gauge Profiles N1, N2 and N3 for Burst File 1

The first burst file is unique in that it provides a good description of the transition from nonsimultaneous to simultaneous behavior (see Figure 5.13). Three zones of simultaneity occur within the sixty second period. The Medof panels, due to their limited time response, were unable to register each individual peak, occurring at a frequency of 1.4Hz, within the three zones of simultaneity. However, it is possible that discrete load spikes registered by Medof panels correspond to the individual zones of phaselock as recorded by the strain gauges (see Figure 5.14). Agreement between the two data sets is especially favorable during the first burst file where zones of simultaneity may be averaged and taken as individual load spikes. Figures 5.15-5.17 illustrate the compatibility between the peak pressures for the two instrumentation systems when compared in this manner.

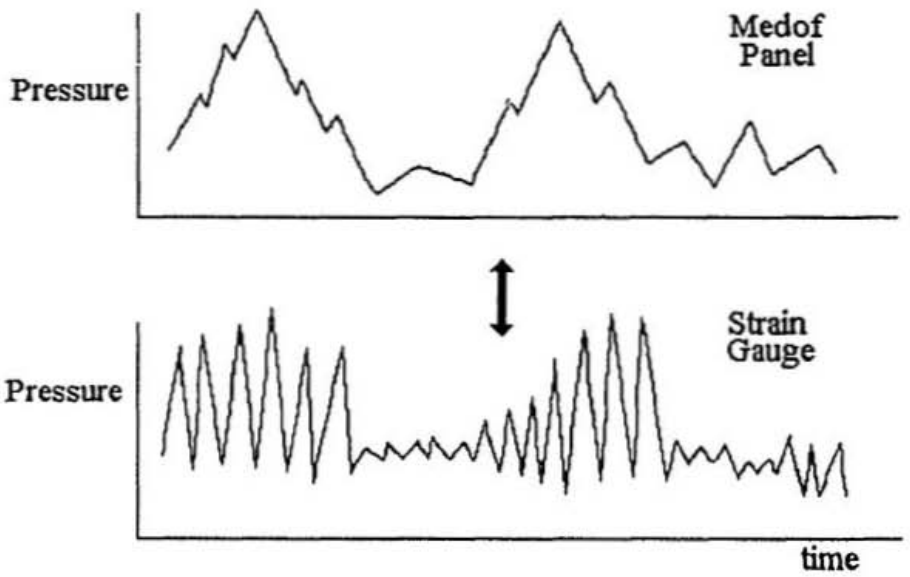

Figure 5.14 Dynamic Response of the Medof Panels versus the Strain Gauges

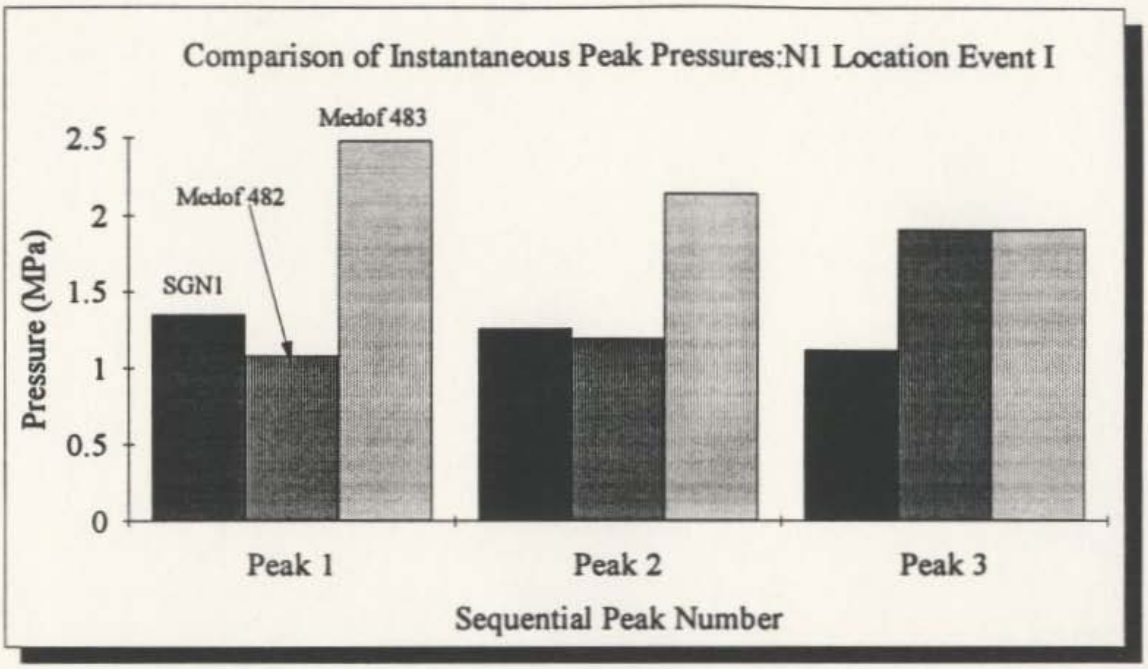

Figure 5.15 Comparison of N1 Medof Panel and Strain Gauge Peak Pressures

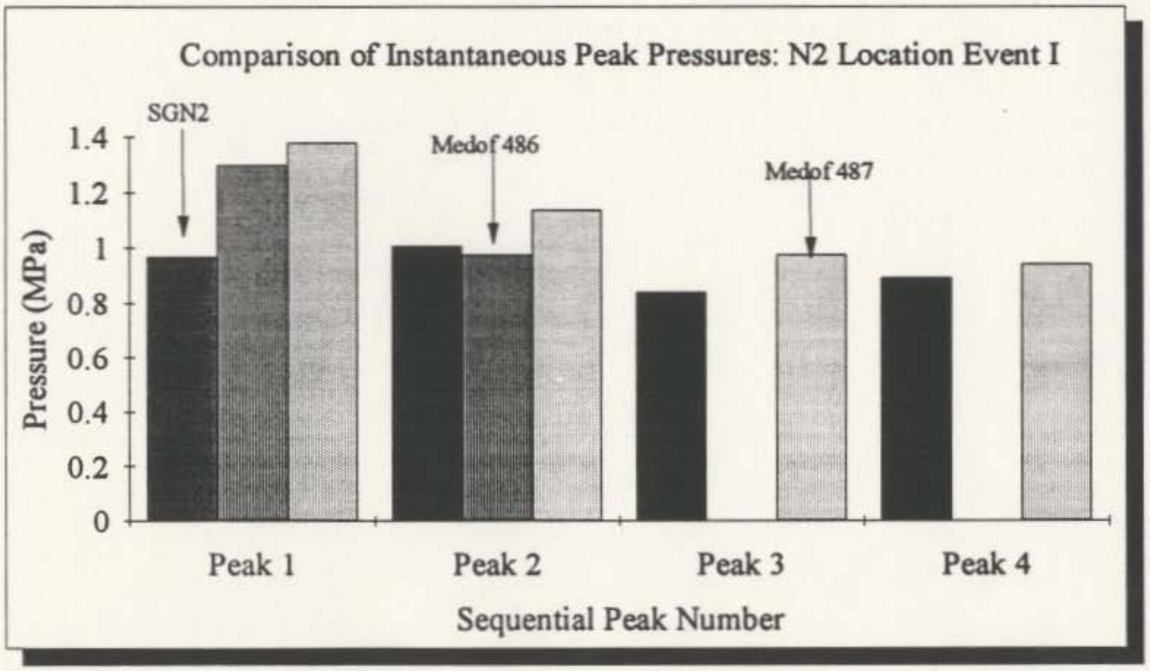

Figure 5.16 Comparison of N2 Medof Panel and Strain Gauge Peak Pressures

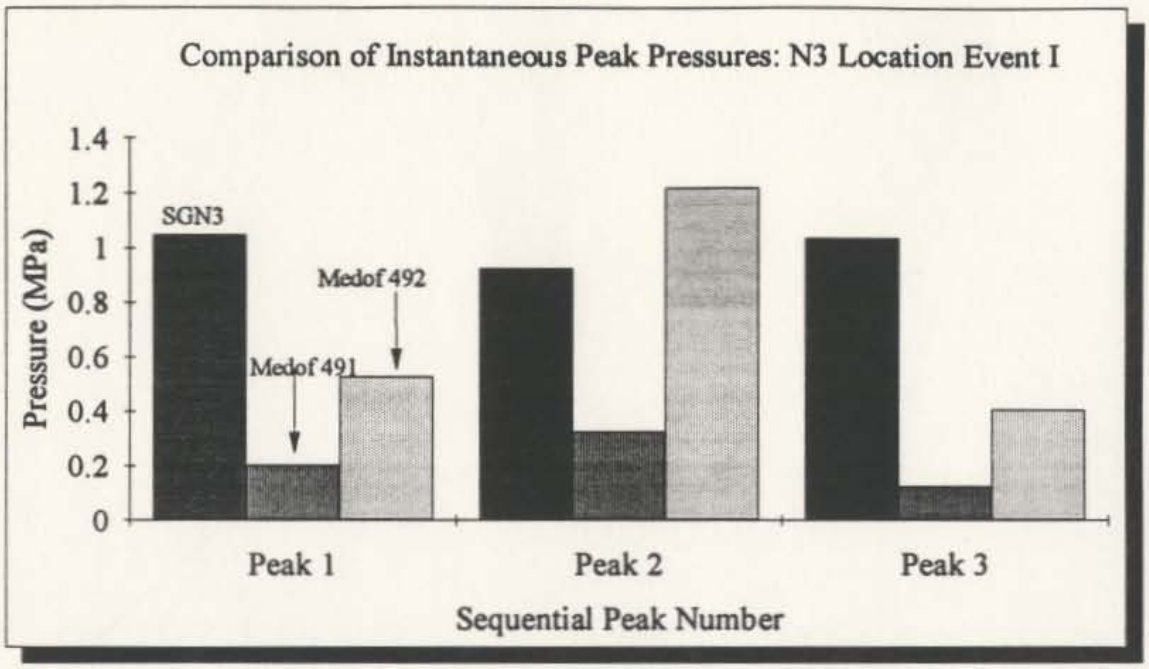

Figure 5.17 Comparison of N3 Medof Panel and Strain Gauge Peak Pressures

The second and third burst files consistently demonstrate phaselocked loading (see Appendix A). Inadequate panel response during continual phaselock makes it difficult to associate peak forces between the two instrumentation systems. Zones of simultaneity in the burst files (3:21 and 3:25) do not correspond to discrete load spikes. During the latter two burst files the Medof panels consistently underpredict the ice loads, frequently by as much as 1-2MN.

5.6.2 Average Pressures: Medof versus Strain Gauge Data

An analysis of the average pressure associated with two burst files (3:20 and 3:21) for each instrumentation system was conducted. Since the original data files were not available pressures were averaged using a graphical method. For instance, the high frequency loads recorded by the strain gauges were averaged by taking the mean of individual peaks and troughs throughout the 60 second file duration (see Appendix A). Similarly, the Medof panel pressures, obtained from the detailed panel plots, were also averaged during the interval 3:20-3:22, corresponding to the first and second burst files. Figures 5.18-5.20 demonstrate the comparison between the two instrumentation systems.

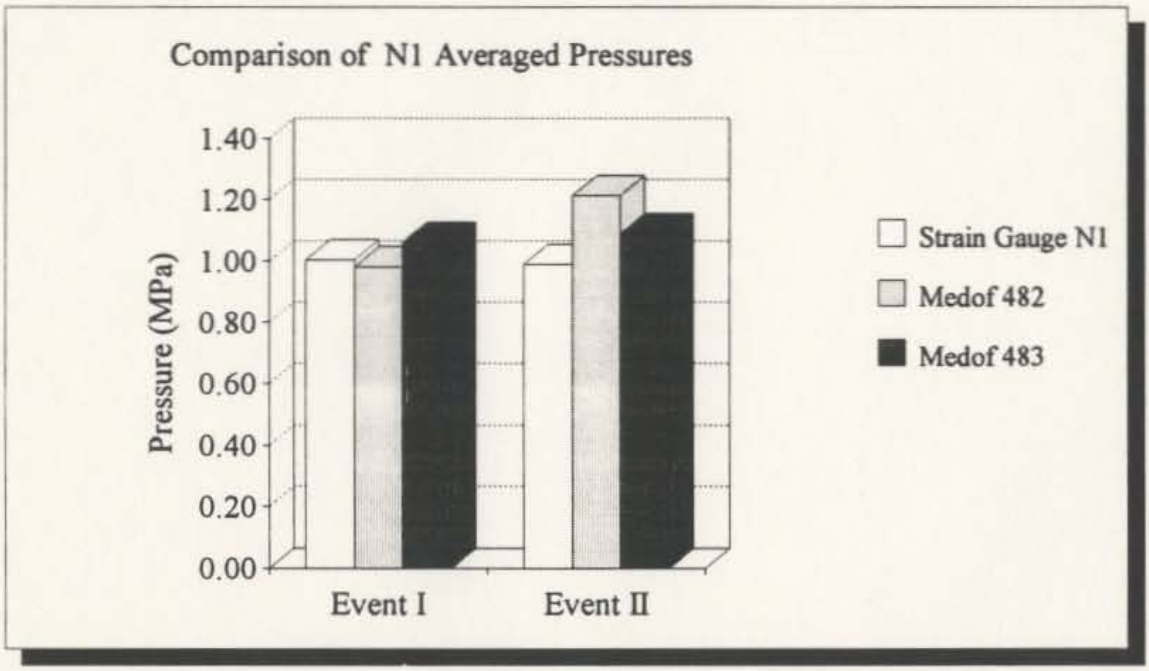

Figure 5.18 Comparison of N1 Instrumentation Average Pressures for Events I and II

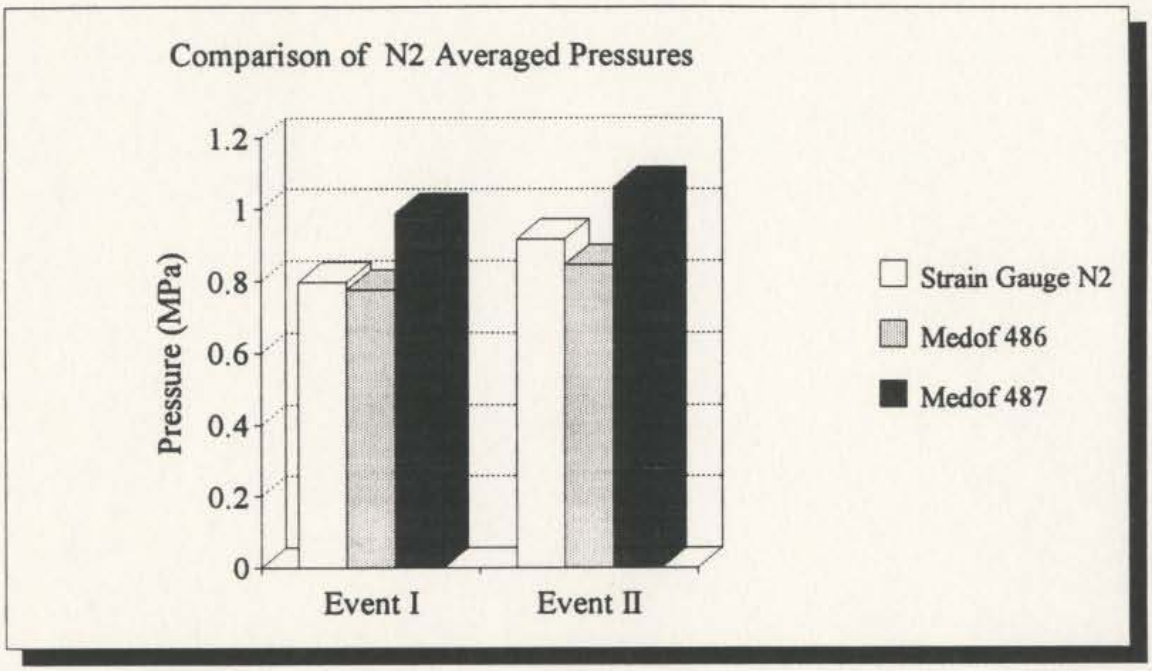

Figure 5.19 Comparison of N2 Instrumentation Average Pressures for Events I and II

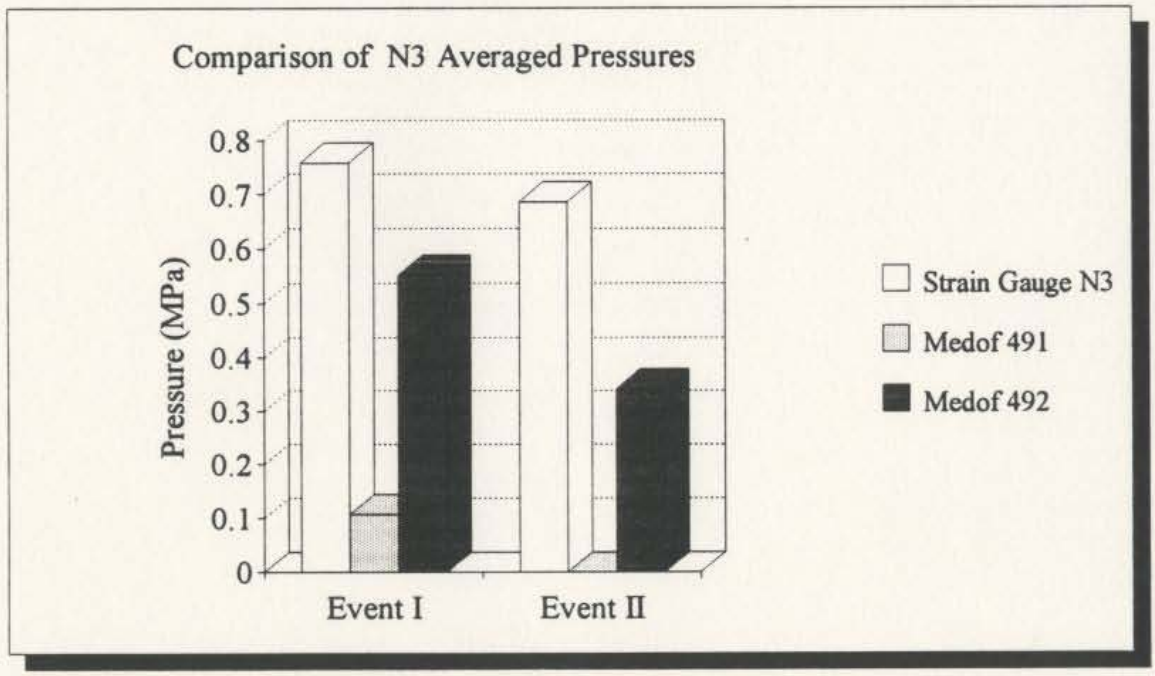

Figure 5.20 Comparison of N3 Instrumentation Average Pressures for Events I and II

Taking an average of the pressure exerted on adjacent Medof panels in each of the three groups along the north face, it is possible to obtain the mean group pressure. This pressure may be compared to the load registered by the corresponding strain gauges on an equivalent area. Correlation was greatest between the second Medof group (panels 486, 487) and the N2 strain gauge for the first and second events. In these two cases, the error associated with the Medof panel was minimized, 9 percent and 16 percent, respectively. Errors associated with panels at other locations ranged from 40-76 percent. Figures 5.21-5.23 demonstrate the comparison between the two instrumentation systems for group pressures.

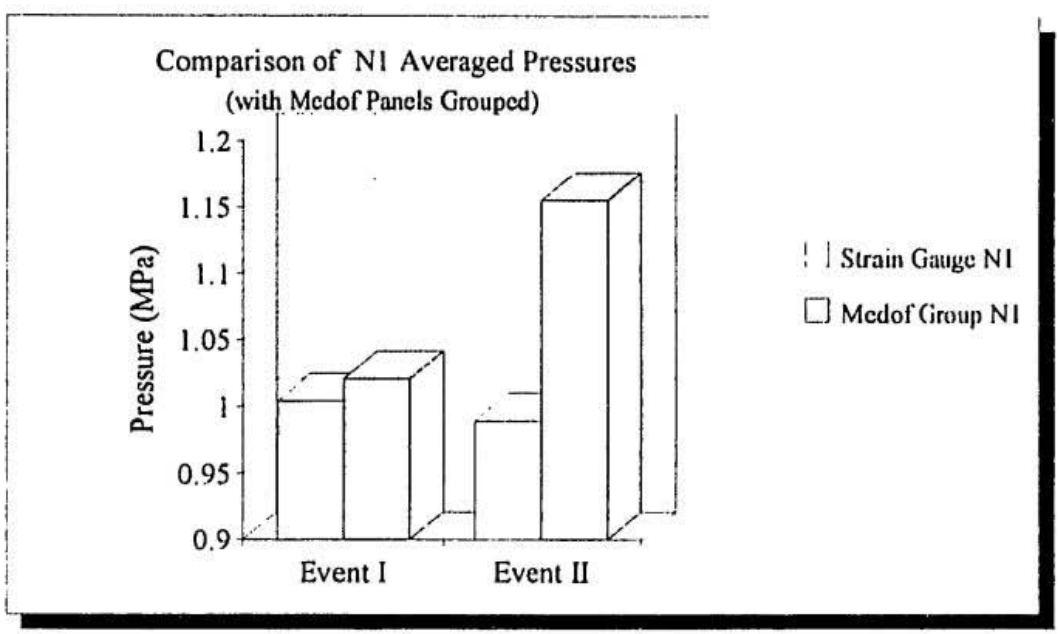

Figure 5.21 Comparison of N1 Average Group Pressure

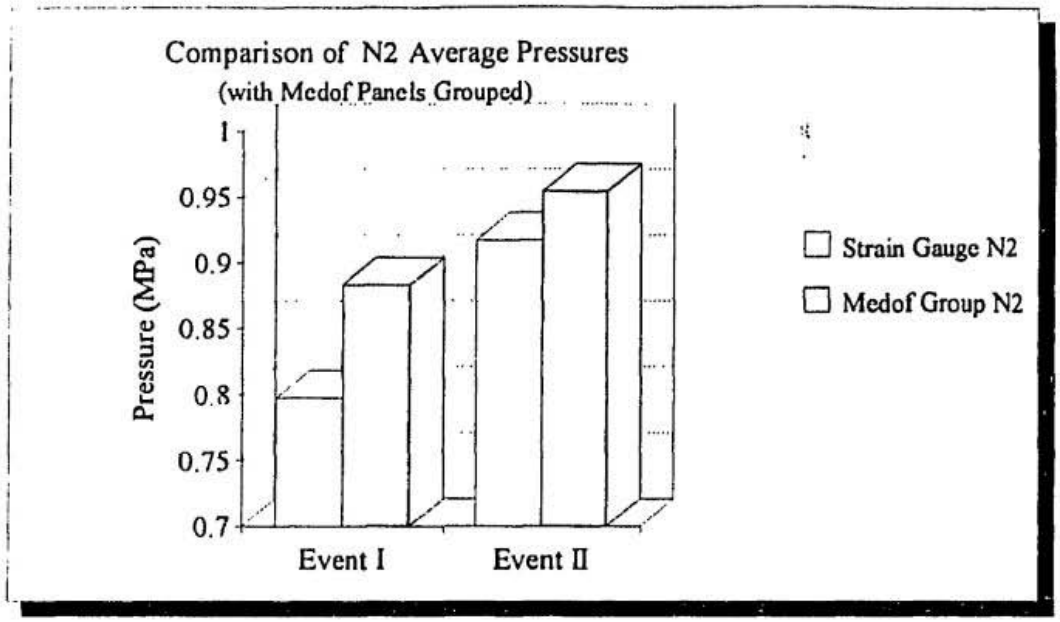

Figure 5.22 Comparison of N2 Average Group Pressure

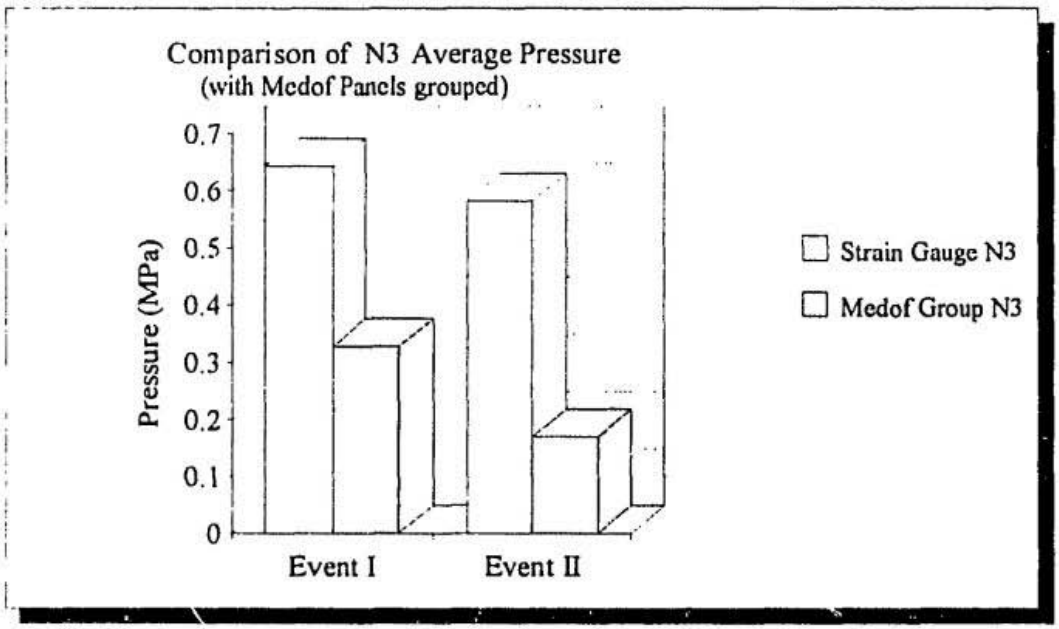

Figure 5.23 Comparison of N3 Average Group Pressure

5.7 An Overview of the Medof Panel Performance

The previous analysis compared the Medof panels with the strain gauges in three areas:

1. Instantaneous pressures
2. Average panel pressures during individual burst files (over 60 seconds)
3. Average group panel pressures during individual burst files (over 60 seconds)

Examination of the instantaneous peak pressures demonstrated the sluggish response of the pressure panels when compared with the strain gauges. It was difficult to determine a correspondence between the load spikes registered on the Medof panels and the sawtooth loads registered on the strain gauges. A notable exception is during the initial stages of dynamics, when it is possible that the intermittent intervals of simultaneous loading were recorded as unique load spikes on the Medof panels.

Comparison of the average panel pressure (for both group and individual panels) to the strain gauge data for the burst files demonstrated reasonably close correlation between the two instrumentation systems. Although disparities in the instantaneous loads for each of the two systems is substantial, loads averaged over one minute intervals are not significantly different. Correspondence between the pressure panels and the strain gauges is closest when the panels are fully loaded.

Differences in the instantaneous loads for the two systems may be attributed to the finite viscosity of the fluid and to the effects of nonuniform loading of the panel. The two factors would sufficiently inhibit the response of the panel to high frequency loading. It is expected that the effect creep on the panels during the May 12 event was negligible. Insufficient time had elapsed for creep of the urethane buttons to significantly alter the results.

The error analysis revealed that inaccuracies associated with the Medof panels ranged from 9 percent to 76 percent, depending upon the panel considered. Fully loaded panels more accurately depicted the loads than did partially loaded panels. This analysis was based upon the assumption that the strain gauge data is reliable and truly depicts the actual forces exerted on the Molikpaq, an assumption that is supported by certain authors, i.e. Jefferies (1988); Jefferies and Wright (1988). Other members of the engineering community consider the strain gauge approximation of loads to be an overestimation of the forces actually experienced (Blanchet, 1990; Blanchet et al., 1992). Strain gauge accuracy aside, the ice loads predicted by the Medof panels are believed to have an accuracy of 30 percent for most loading cases (Croasdale et al., 1986).

The large contact area which characteristically occurs during ice interaction with offshore structures renders many systems of ice load monitoring economically unfeasible. Consequently, strain gauges were installed on numerous bulkheads of the Molikpaq, thus providing information on global and semi-local loads. Resolution of the strain gauges over areas with a tributary width less than approximately 2.44m becomes questionable. Medof pressure panels were designed to indicate the loads on areas as small as $3.08m^2$. Despite the recognizable limitations of the Medof panel, it is regarded as an effective means of monitoring ice loads (Croasdale et al., 1986; Croasdale and Frederking, 1986; Metge et al., 1975; Croasdale, 1984). The information that they provide may be used to further understand the dynamics associated with the ice failure process. Critical zones are expected to be of the order of $0.10m^2$. They require an instrumentation system which provides data on a localized scale. It is for this reason that further analysis is based upon Medof panel data.

5.8 Applying the Concept of Critical Zones to the Medof Panel Data

Based upon the Medof panel plots it was found that the most active period of structural loading was experienced between the 10 and 15 minute interval of the May 12, 1986 event. Elimination of the rise and decline periods of loading was expected to provide a more accurate account of the actual forces, considering only the period during which the panels were solidly loaded. Each Medof plot of force versus time was subjected to an analysis which determined the percent of time that a panel exceeded a certain load threshold (see Appendix A).

Frequency distributions of the total load applied to individual Medof panels during the 10-15 minute interval are presented in Figure 5.24(a)-(g). At no time during the 30 minute event of May 12 did any Medof panel experience a total load in excess of 5MN. As previously noted, the loaded area for each Medof panel was dependent upon the ice thickness at that location. Consequently, panels which experienced higher loads may have been loaded over their total area. The average pressure of individual panels reflects the area over which the load was applied (see Table 5.2).

The loaded area of various panels was affected by undulations in the upper and lower surfaces of the ice sheet. Spalled pieces of ice were most likely generated near the free surfaces of the ice sheet, reducing the actual contact area in that region. Accumulated piles of rubble on the upper surface of the ice sheet would also have influenced the loaded panel area. These factors were not accounted for in the calculation of the mean ice thickness.

Table 5.2 Mean Values of the Medof Panel Force and Average Pressure (averaged over the 10-15 minute interval)

Panel	Percent Loaded Area*	Total Panel Force (MN)	Average Panel Pressure (MPa)
482	66%	1.59	0.78
483	66%	1.13	0.56
486	100%	2.39	0.78
487	100%	2.57	0.83
488	30%	0.89	0.96
491	100%	0.74	0.24
492	100%	1.60	0.52

*obtained from measurements of ice thickness (see Appendix A)

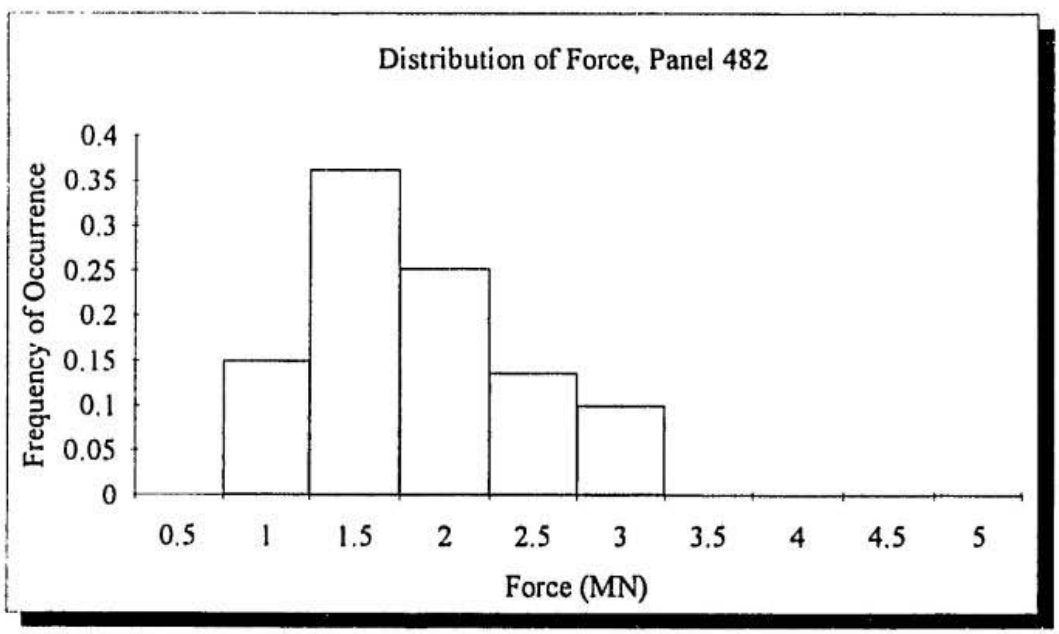

Figure 5.24(a) Distribution of Force for Medof Panel 482 (10-15 minute interval)

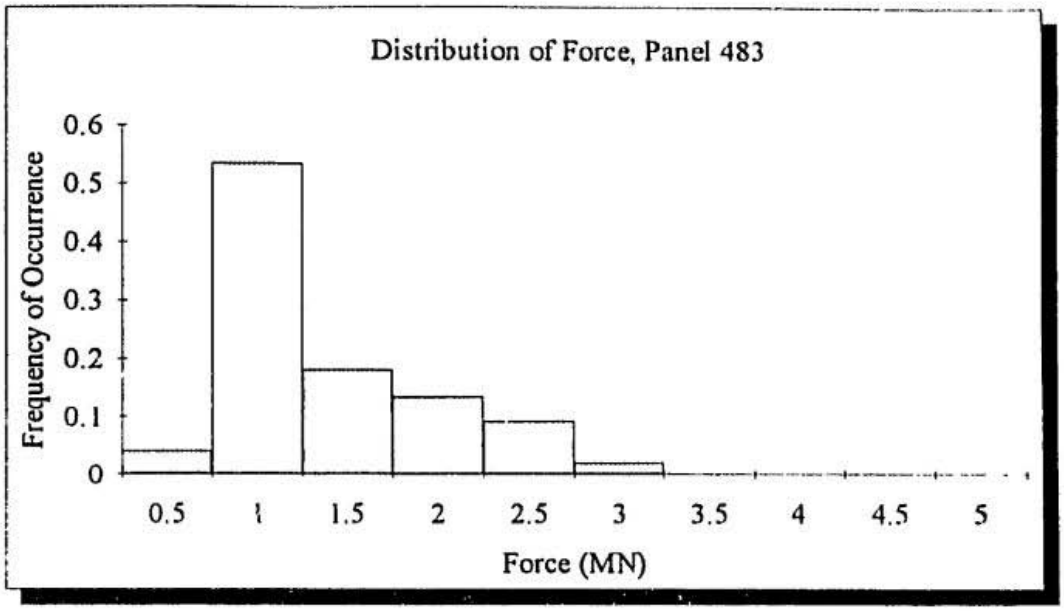

Figure 5.24(b) Distribution of Force for Medof Panel 483 (10-15 minute interval)

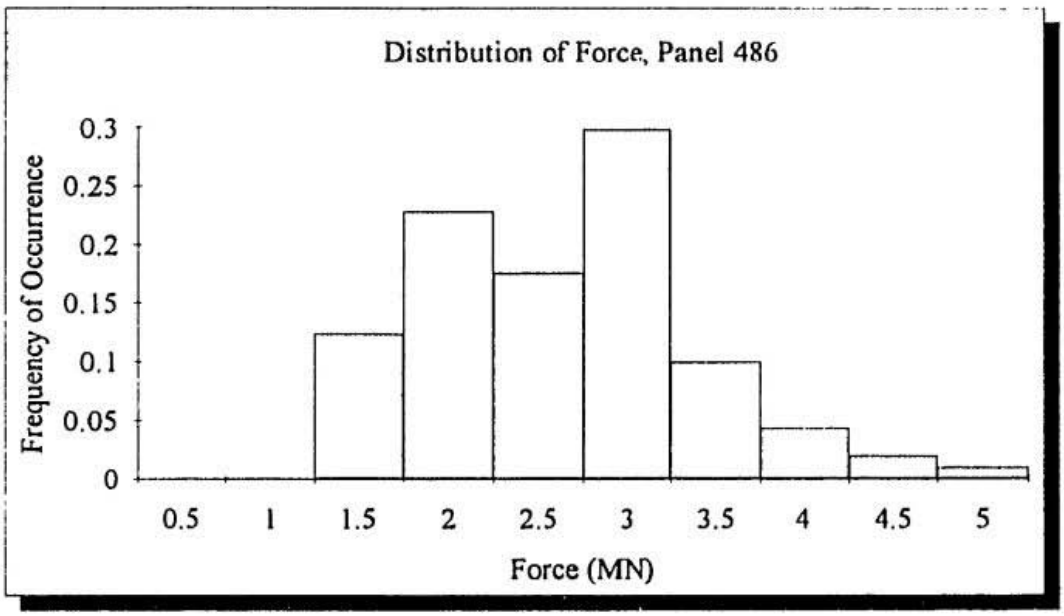

Figure 5.24(c) Distribution of Force for Medof Panel 486 (10-15 minute interval)

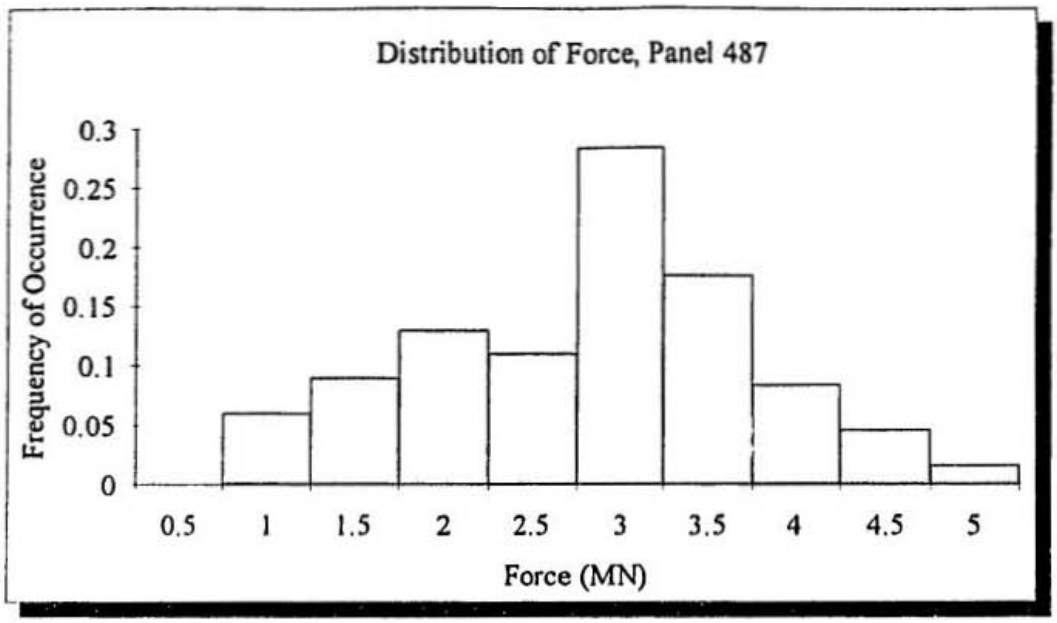

Figure 5.24(d) Distribution of Force for Medof Panel 487 (10-15 minute interval)

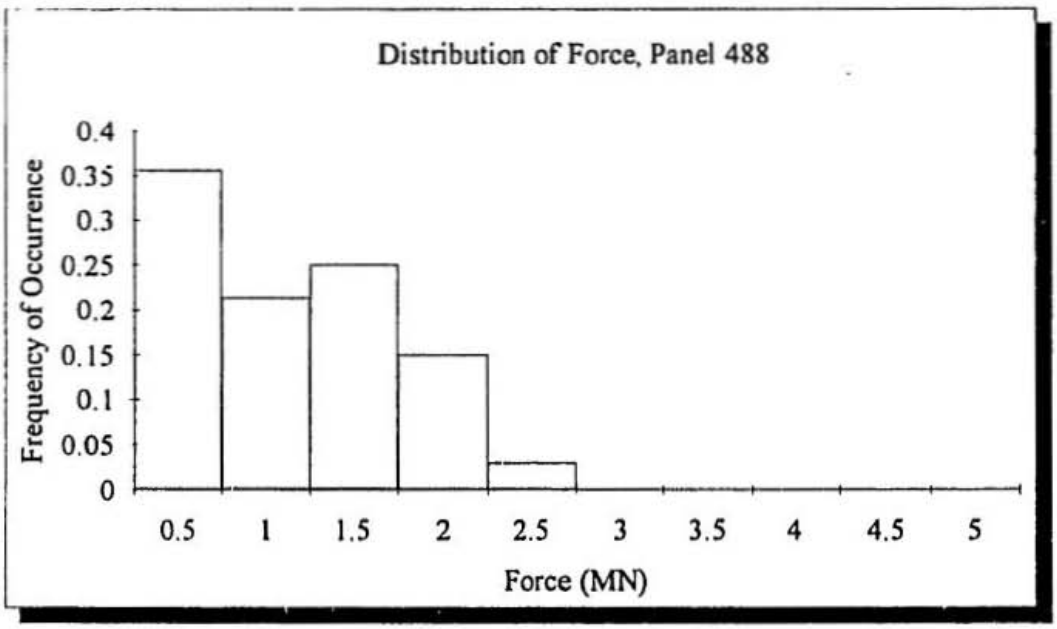

Figure 5.24(e) Distribution of Force for Medof Panel 488 (10-15 minute interval)

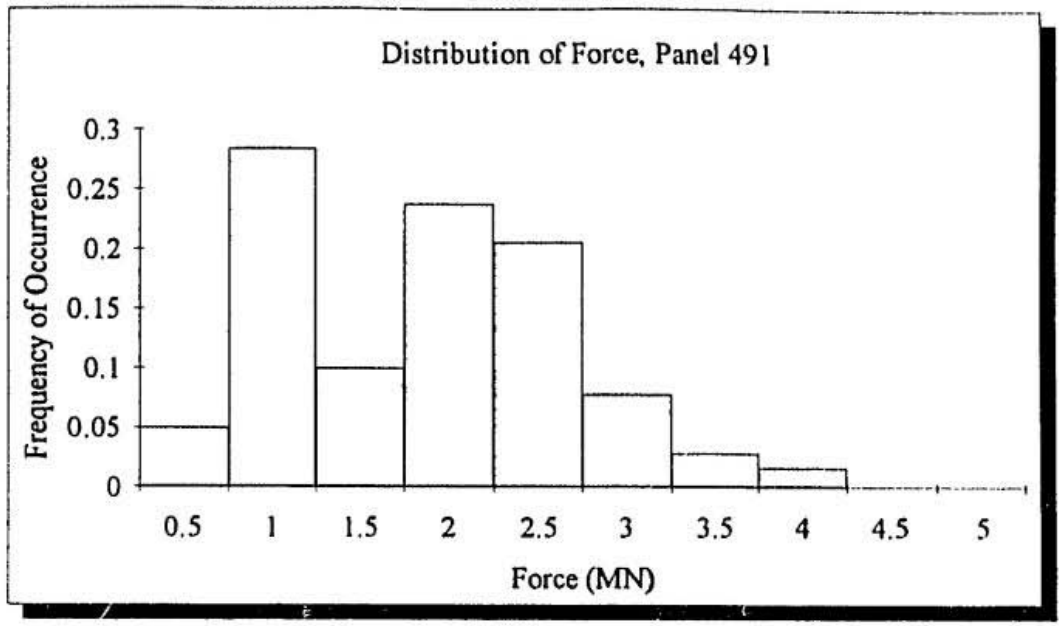

Figure 5.24(f) Distribution of Force for Medof Panel 491 (10-15 minute interval)

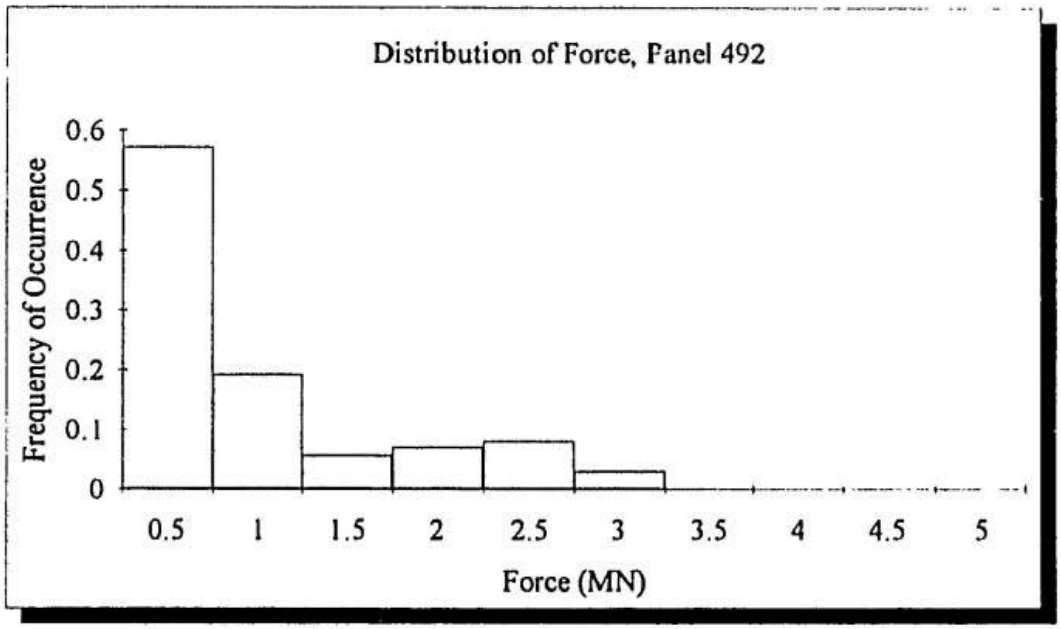

Figure 5.24(g) Distribution of Force for Medof Panel 492 (10-15 minute interval)

Typical values of the critical zone size, force, and spatial density were previously derived from the instrumented areas of the Louis S. St. Laurent ($1.69m^2$) and the Kigoriak ($1.25m^2$) ship ramming trials. The defined parameters of the critical zone may be extrapolated to the slightly larger area of the Medof panel ($3.08m^2$).

Dividing the mean forces of the Medof panels by the 1.09MN force of the critical zone (as obtained from the ship data) results in a range of estimates for the number of critical zones over the area of the instrumented pressure panel (see Table 5.3). An average number of critical zones per square meter may be obtained from the individual estimates of the zones present over the panel area of $3.08m^2$. The mean number of critical zones per square meter is 0.62 (see Table 5.3). This estimate assumes that each critical zone carries a force of 1.09MN (as derived from the Louis S. St. Laurent data).

Table 5.3 Approximate Number of Critical Zones per Panel Area

Panel	Total Panel Force (MN)	Number of Critical Zones (per loaded panel area)*	Number of Critical Zones (per square meter)**
482	1.59	1.5	0.74
483	1.13	1.0	0.49
486	2.39	2.2	0.71
487	2.57	2.4	0.78
488	0.89	0.8	0.87
491	0.74	0.7	0.23
492	1.60	1.5	0.49

*obtained by dividing the mean panel force by 1.09MN

**obtained by dividing the number of critical zones by the loaded area of the panel

A comparison of the analyzed data sets reveals a decrease in pressure with increasing area (see Table 5.4). Average pressures of the order of 7MPa occurred over areas of 0.12-0.32m^2 during the Hobson's Choice Indentation Tests (1989). The average pressures on the instrumented areas of the Louis S. St. Laurent and the Kigoriak were 2.78MPa and 3.91MPa, respectively. Finally, the average pressure exerted on an individual Medof panel was 0.67MPa. A very high estimate for the number of zones per square meter (8.3 zones/m^2) was obtained from the indentation test data. This is a direct result of the intense confining pressures applied over the small contact area. The mean number of critical zones per unit area for full scale interactions ranges from 0.62-0.80 zones per square meter (see Table 5.4). These estimates are based upon an assumption that the force of an individual critical zone is 1.09MN (as obtained from the Louis S. St. Laurent data).

Table 5.4 Spatial Densities of Critical Zones for Various Data Sets

Data Set	Instrumented Area (m^2)	Average Pressure over the Instrumented Area (MPa)	Mean Number of Critical Zones (per square meter)
Indentation Tests	0.12-0.32	7.0	8.3
Louis S. St. Laurent	1.69	2.78	0.76
CanMar Kigoriak	1.25	3.91	0.80
Medof Panel	3.08	0.67	0.62

The estimated number of critical zones per square meter enables the concept of high pressure zones to be applied to much larger contact areas. The interaction zone encompasses the entire length of the north face for the May 12 event. The north face load during the event is given by the strain gauge data. It would be useful to determine the approximate number of critical zones instantaneously active in the interaction area, particularly when the applied load was at a maximum value.

The highest face load applied during the May 12 event was 200MN (Gulf Resources, 1988). The contact area was roughly 2.7m deep and 60m long, yielding an overall contact area of $162m^2$. Using an estimate of 0.62 critical zones per square meter (as derived from the Medof panel data) yields approximately 100.4 active zones in the contact region at the instant of peak loading. This is expected to be an upper bound, as discussed subsequently.

Figure 5.25 conceptually presents the interaction zone at the instant of maximum loading. The contact area consists of 100.4 zones of high pressure, with a cumulative area of $11.2m^2$ and a cumulative force of 109.4MN. Typically these zones are concentrated near the center of the ice sheet where confining pressures are greatest. The interaction zone is also comprised of regions of recently spalled ice, which cause a reduction in the contact area. Spatially, the largest component of the interaction zone is the region of background pressure, covering $150.8m^2$. The pressure within the background region is relatively uniform with a magnitude of roughly 0.60MPa, thereby contributing 90.6MN to the total face load. Average pressure for the overall contact zone is 1.23MPa.

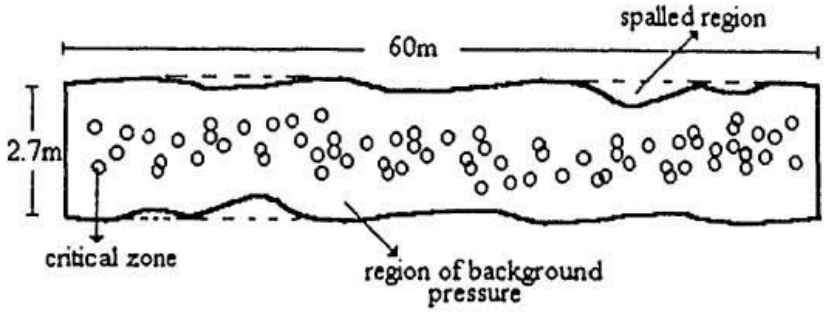

Contribution to Interaction Zone	Critical Zone (A)	Background Region (B)*	Total at Peak Load (C)
Contributing Area	11.2m^2	150.8m^2	162m^2
Contributing Force	109.4MN	90.6MN	200MN
Contributing Pressure	9.73MPa	0.60MPa	1.23MPa

*Background force = total peak load-critical zone force (B=C-A)

Figure 5.25 The Interaction Zone during Ice Interaction with the Molikpaq

The interaction zone as depicted above is based upon numerous assumptions. Critical zones distributed over the contact area were assumed to have a constant size, force and spatial density. The size and force of the critical zones, estimated from ship ramming trials, were used to quantify the contribution of numerous critical zones in the contact area to the total applied load. The results, previously presented in Figure 5.25, were reasonable. Multiple high pressure zones, with average pressures of 9.7MPa, populate the interaction zone. Regions of background pressure (0.60MPa) and spalled areas (which have no load bearing capacity) also occupied the contact area.

Several different combinations of the critical zone parameters may satisfy the conditions at any given instant of loading. Considering the case in Figure 5.25, increasing the area of the critical zones, in conjunction with reducing the number of zones per square meter, is one alternative to the load scenario. Similarly, perhaps the background regions should be characterized by a pressure closer to 2MPa, a threshold stress which previously qualified an area as "active". This would effect an increase in the total applied load which could be compensated by reducing the number of zones per square meter.

5.9 Plasticity Methods: An Upper Bound for the Loads Applied to the Medof Panels

In order to determine an upper bound for the local and global pressures experienced on the Molikpaq, it is useful to consider the loads at which plastic hinges form. Initially, plastic hinges will be formed at the edges of the clamped plate, and finally, in the center of the plate. A rectangular plate, clamped on all edges and subjected to a uniform distributed load, undergoes cylindrical bending. A typical transverse width may be treated as a beam of unit width. The pressure to cause initial yielding P_y, edge hinges P_{eh}, permanent set P_s, and ultimate strength P_{ult}, may be determined using these assumptions (see Appendix B).

No denting of the Medof panels occurred as a result of the 1985-1986 loading season (B. Wright, personal communication). This information may be used to quantify the peak pressures experienced during the May 12, 1986 event. A plasticity analysis of the Molikpaq plating was performed. The frame spacing for the Molikpaq was 1.22m, and the

rib spacing was 0.4m. The corresponding pressures and forces for an area of $0.488m^2$, i.e. corresponding to 0.4m by 1.22m, are presented in Table 6.3. These values were then used to determine the ultimate strength for an area equivalent to the Medof panel area of $3.08m^2$.

The actual force applied to the Medof panel area was substantially lower than the load required to cause yielding of the plate (15.4MN). At no time did the Medof panels register a force in excess of 5MN during the May 12, 1986 event. Depending upon the force of the individual critical zones (demonstrated to range from 0.5-4.0MN) as few as four or as many as 30 critical zones could exist on the Medof panel before yielding would be initiated.

Table 5.5 Results of the Plasticity Analysis of the Medof Panel Area

Pressure Limit	Pressures (MPa)	Force Limits	Force on $0.488m^2$ (MN)	Force on $3.08m^2$ (MN)
P_y(1)	5.0	F_y	2.4	15.4
P_{eh}(2)	7.5	F_{eh}	3.7	23.1
Peh_3(3)	12.1	Feh_3	5.9	37.3
P_{se}(4)	28.0	F_{set}	13.7	86.2
P_{ult}(5)	34.6	F_{ult}	16.9	106.6

1. onset of plate yielding
2. formation of edge hinges
3. formation of center hinge (3 hinge mechanism)
4. initiation of permanent set
5. upper bound (ν_p=0.5)

5.10 Conclusions

Pressure cell data from the Louis S. St. Laurent demonstrated the spatial and temporal variability of the high pressure zones. This information was used to demonstrate that the concept of critical zones may be applied to the quasi-static loads characteristic of ice-offshore structure interactions. Numerous factors influence the compatibility of the two data sets. First, the dynamics associated with the two loading scenarios, although different, are similar in that crushing is the predominant mode of failure. Critical zones are an important element in this process.

An initial attempt to relate multiple data sets requires certain assumptions regarding the properties of the critical zone, i.e. regardless of the loading scenario, critical zones support a load of 1.09MN. Further research in this area is required to justify such an assumption or, alternately, to present a more accurate value for the force of the high pressure zone. The type of interaction and the area of the interaction zone should be taken into account. In addition, the duration of loading was not accounted for when combining the various data sets. For instance, ship ramming trials characteristically have loading durations less than one second. The more static case of an ice interaction with the Molikpaq had a loading duration of approximately 30 minutes. The effect of loading duration on the behavior of critical zones and their associated pressures will be addressed in Chapter 6.

The Medof panels were used to quantify the critical zone parameters in the case of the Molikpaq. These pressure panels were chosen over the strain gauges since the former provide data on a smaller scale than do the strain gauges. It was also shown that the error associated with the fully loaded pressure panels did not preclude their use in this analysis. An estimate of 0.62 zones per square meter was obtained based upon a critical zone force of 1.09MN.

The assumption of a critical zone of constant size and force (as derived from the Louis S. St. Laurent data) was used to estimate the spatial density of high pressure zones during the ship ramming trials of the Kigoriak and the ice-structure interaction involving the Molikpaq. Ultimately, researchers and engineers hope to formulate a model for the ice failure process which addresses the particular loading conditions and may be universally applied. Such a model would yield the expected loads during ice-structure interaction. In view of the inherent variability of the critical zones, a stochastic model which accounts for the random nature of the high pressure zones is appropriate. An initial formulation for a statistical model which incorporates the concept of critical zones into the design criteria is presented in the following chapter.

Chapter 6

Statistical Analysis of Local Ice Pressures

6.1 Introduction

The problem of determining local pressures is a longstanding one which has faced the designers of ships and offshore structures throughout the history of operations in ice covered waters (Masterson and Frederking, 1993). One of the objectives of this research project was to further the understanding of localized pressures. Evidence of a scale effect, in which local effective ice pressures decrease with increasing loaded area, has been widely discussed in the literature. Size effects are influenced by the confinement of the ice, the distribution of natural flaws in the ice structure, and whether the interaction zone may be characterized by simultaneous or nonsimultaneous failure.

Figure 6.1 illustrates the pressure versus area effects as demonstrated by the medium scale indentation tests, ship ramming trials, and offshore structure-ice interaction. The average pressure decreases with increasing area. Several points should be noted regarding the pressure versus area curve. First, the duration of loading is not accounted for when combining various data sets into a generalized plot. Statistically, the probability of experiencing extreme pressures increases with increasing loading periods. Second, confinement significantly influences the magnitude of the average pressure, which is not intuitively obvious from the pressure versus area plot.

Table 6.1 illustrates the effects of confining stress on the spatial density of the critical zone and, indirectly, on the average pressure of the instrumented area. The mean number of critical zones remains relatively constant for the ship-ice and offshore structure-ice interactions. Conversely, the spatial density of the critical zones for the indentation tests is substantially higher (3.1-8.3 zones/m^2). The intense confining pressures which developed during the indentation tests resulted in a larger estimate for the number of critical zones per unit area. The spatial density for the critical zones as obtained from the instrumented area of the indentation tests is not representative of larger areas. The indentation tests may be taken as representative of the highly confined conditions which characterize the central region of an ice sheet during ice-structure interaction. During an interaction, the spatial density of the critical zones is not constant for the entire interaction area. The number of critical zones increases as the central regions of the ice sheet are approached (see Figure 6.2).

The instrumented regions of the Louis S. St. Laurent, Kigoriak, and the Molikpaq represent larger areas and less confined conditions. Whereas a smaller area might yield a large estimate for the number of critical zones per unit area (the critical zone potentially represents a large portion of the area), a larger area may include several zones, which represent only a small percentage of the overall area. (see Figure 6.3).

Table 6.1 Comparison of the Spatial Density of Critical Zones for Various Data Sets

Data Set	Instrumented Area (m^2)	Average Pressure over the Instrumented Area (MPa)	Mean Number of Critical Zones (per square meter)
Indentation Tests	0.045	7.0	3.1-8.3
Louis S. St. Laurent	1.69	2.78	0.76
CanMar Kigoriak	1.25	3.91	0.80*
Medof Panel	3.08	0.67	0.67*

*assuming a critical zone force of 1.09MN

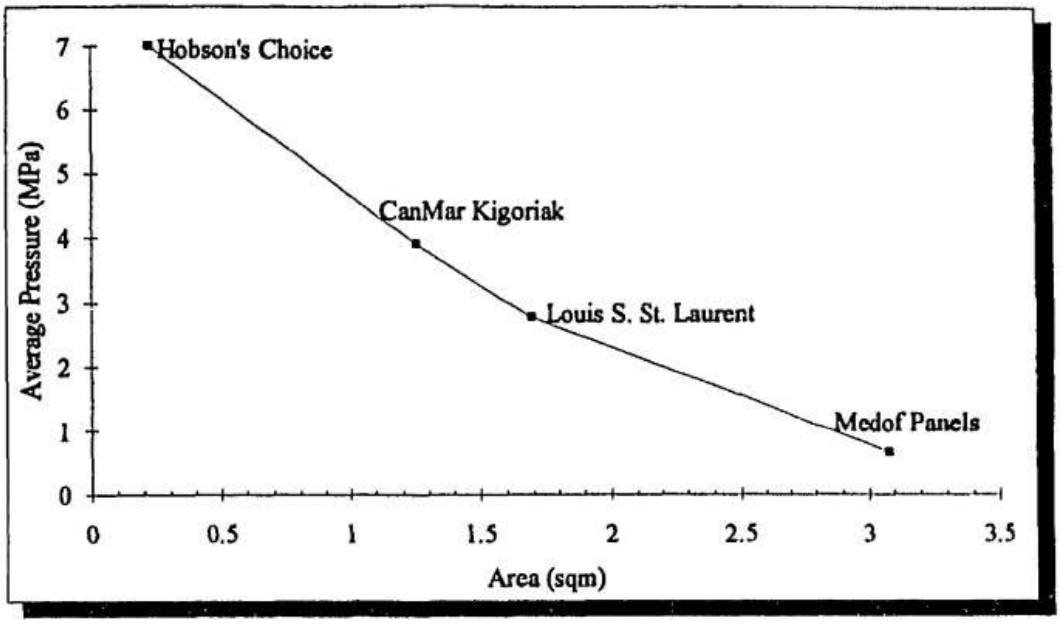

Figure 6.1 Average Pressure over the Instrumented Areas of Various Data Sets

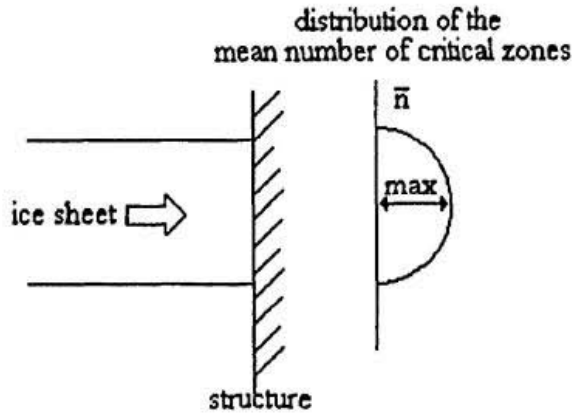

Figure 6.2 Variation of the Number of Critical Zones with Ice Depth

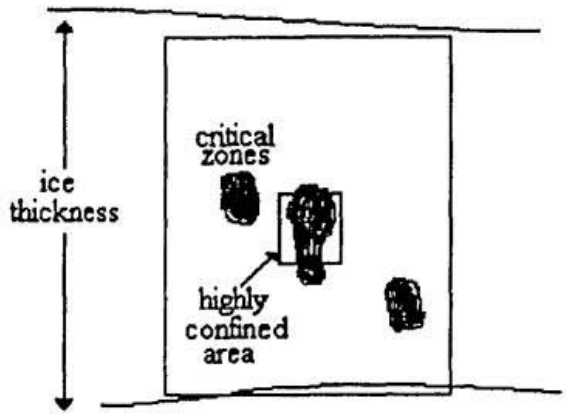

Figure 6.3 Effects of Confinement on the Number of Critical Zones

It is proposed that the concept of critical zones be incorporated into design criteria. This would enable local areas, which need to withstand higher pressures, to be distinguished from larger areas, which are exposed to substantially lower pressures. Due to the random nature of the critical zones, design criteria should be based upon statistical methods.

A possible approach to the formulation of a critical zone model would be to determine the statistical distributions for the critical zone size, area, and spatial density. The area of the critical zone is of the order of $0.10m^2$. If the zones of high pressure-area taken as point loads, the distribution of area may be eliminated from the model; reducing the input parameters to the distributions for the spatial density and the force of the critical zone. A computer model could be developed which iterates combinations of these critical zone parameters according to the specified design pressure. Local pressures could be calculated from their corresponding exceedence probabilities, as discussed subsequently. Figure 6.4 identifies the statistical distributions required for this type of approach to a critical zone model.

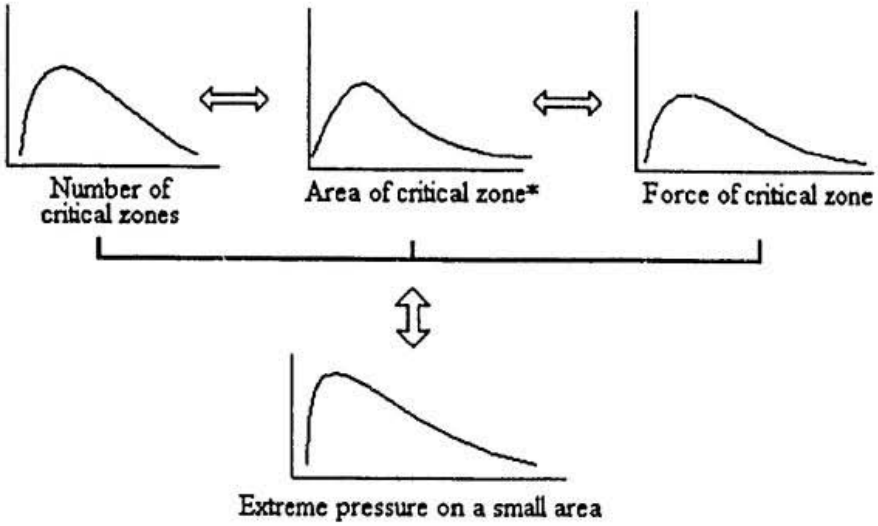

Figure 6.4 Schematic of the Proposed Design Methodology

6.2 Localized Pressure as Obtained from Exceedence Probabilities

An analysis method for local pressures was presented in Jordaan et al. (1993). Pressures were determined for specific values of exceedence probabilities whereby problems of exposure (length, position, and number of impacts) as well as the area of exposure were taken into account. The analysis involved two data sets from ship-ice interactions, the USCGC Polar Sea (Daley et al., 1986) and the MV CanMar Kigoriak (Dome Petroleum Ltd., 1982). These data sets were combined and the peak panel pressures for individual subpanels were plotted against the natural logarithm of $[i/(m+1)]$, where i is the rank and m is the number of rams producing pressures greater than zero on the instrumented panels.

The authors note that little evidence of a limiting value for peak pressures exists; portions of the critical zone may experience pressures upwards of 70MPa. The failure process is likely to cause a physical cutoff for pressures near the center of the critical zone. For practical purposes, no limiting value was used for the panel sizes of interest.

Jordaan et al. (1993) state that for most practical cases, the tail of the pressure distribution can be represented by an exponential distribution of the form

$$p_e = \exp\left[\frac{-(x - x_0)}{\alpha}\right] \qquad 6.1$$

where p_e is the probability of exceedence of $[1\text{-}F_X]$, F_X is the cumulative distribution function of X, a random quantity denoting pressure, and α and x_o are constants for a given area (see Figure 6.5).

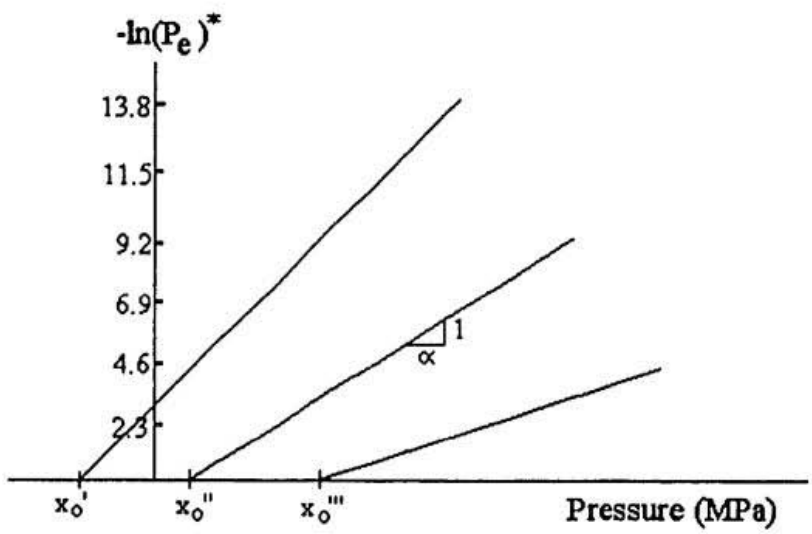

[* $P_e=10^{-1}$ corresponds to $-\ln(P_e)=2.3$]

Figure 6.5 Schematic Diagram Showing Notation for Exceedence Probability

For most loading cases the maximum pressure Z per unit time is sought, i.e.

$$Z = \max (X_1, X_2, X_3 .... X_N) \qquad 6.2$$

where there are N events in the given time interval, a year being a convenient reference measure. Only those events which produce impacts are of interest. Therefore a proportionality constant, r, is introduced whereby

$$m = r\,n \qquad 6.3$$

where m = number of "hits" and n is the total number of events.

If equation 6.1 applies, and the number n of events is fixed and large, then the distribution of the maximum Z is given by the close approximation (which follows from the distribution of the extreme value based upon the cumulative distribution corresponding to Equation 6.1 with n events)

$$F_Z(z) = \exp \{-\exp[\frac{-(z - x_0 - x_1)}{\alpha}]\} \qquad 6.4$$

where $x_1 = \alpha (\ln n + \ln r)$.

6.3 Application to the Ice-Structure Interaction

Figure 6.6 is a graphical representation of the parameter α as obtained from the detailed analysis of the CanMar Kigoriak and USCGC Polar Sea data (Jordaan et al., 1993). The authors present a tentative curve for use in design. This curve, shown in Figure 6.6, corresponds to the equation

$$\alpha = 1.25\, a^{-0.70} \qquad 6.5$$

where a is the area in m^2.

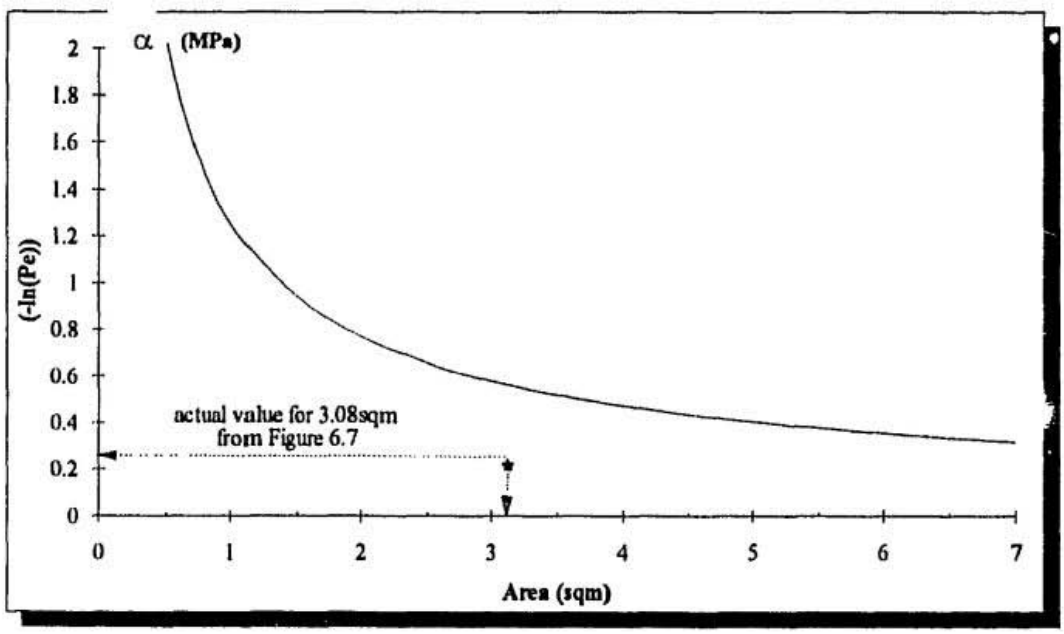

Figure 6.6 Results of Analysis of α for $-\ln(p_e)$ versus Pressure

Equation 6.5 was noted to apply to the range of areas 0.6-6.0m^2. As previously mentioned, the above analysis was derived from a database of ship-ice interactions. In order to determine the applicability of Equation 6.5 to an ice interaction with a stationary structure, the Molikpaq in particular, a similar analysis was conducted of the Medof panel data.

Two Medof pressure panels, believed to be totally encompassed by ice during the interaction, were investigated. The 10-15 minute interval of the selected event of May 12, 1986 proved to be the most active period of loading (see Chapter 5). Figure 6.7 presents the parent distribution of the individual peak pressures registered on panels 486 and 487 during the five minute interval. The tail of the pressure distribution can be represented by an exponential form, as predicted by Equation 6.1. Each pressure peak for these two panels was ranked in descending order and plotted against the natural logarithm of $[i/(m+1)]$ as demonstrated in Figure 6.8. A linear regression of the data in Figure 6.8 reveals an α value (the inverse of the slope of the regressed line) of 0.25MPa for panels 486 and 487, combined.

Although an α value of 0.25MPa is lower than the value of 0.57MPa as predicted by Equation 6.5 for an area of 3.08m^2, it is surprisingly close considering the questionable response of the Medof panels. As previously mentioned, the error associated with the pressure panels is roughly 30 percent. Consequently, the peak loads registered by the Medof panels may be 30 percent higher than indicated in Figure 6.8. The slope of the regressed line would decrease producing an α value which more closely corresponds to the design equation (see Figure 6.6, previous page).

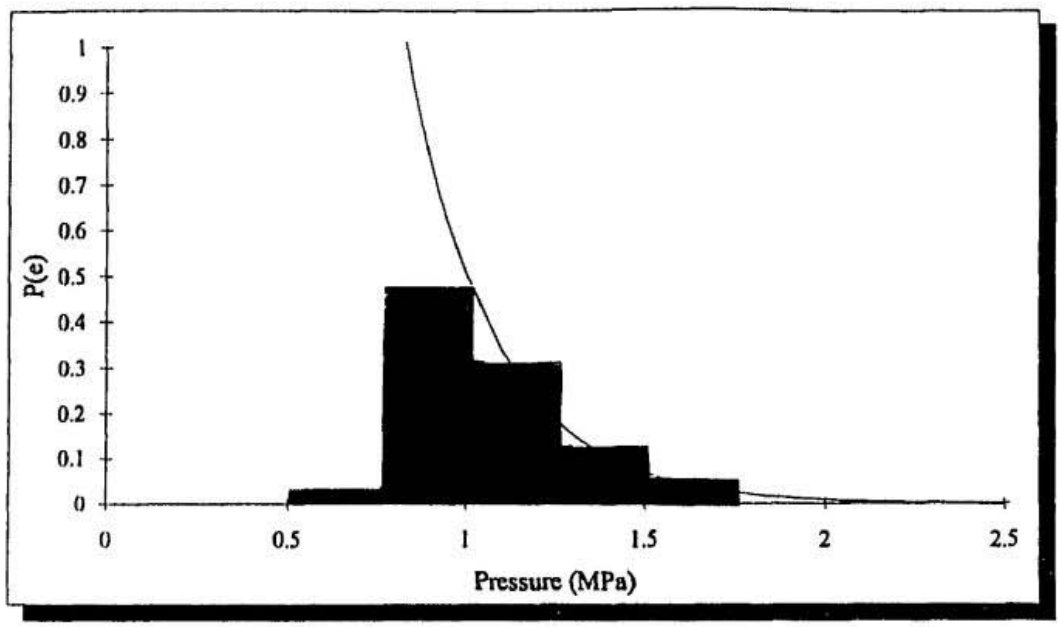

Figure 6.7 Exponential Fit to the Tail of the Parent Distribution of Peak Pressures on Panels 486,487

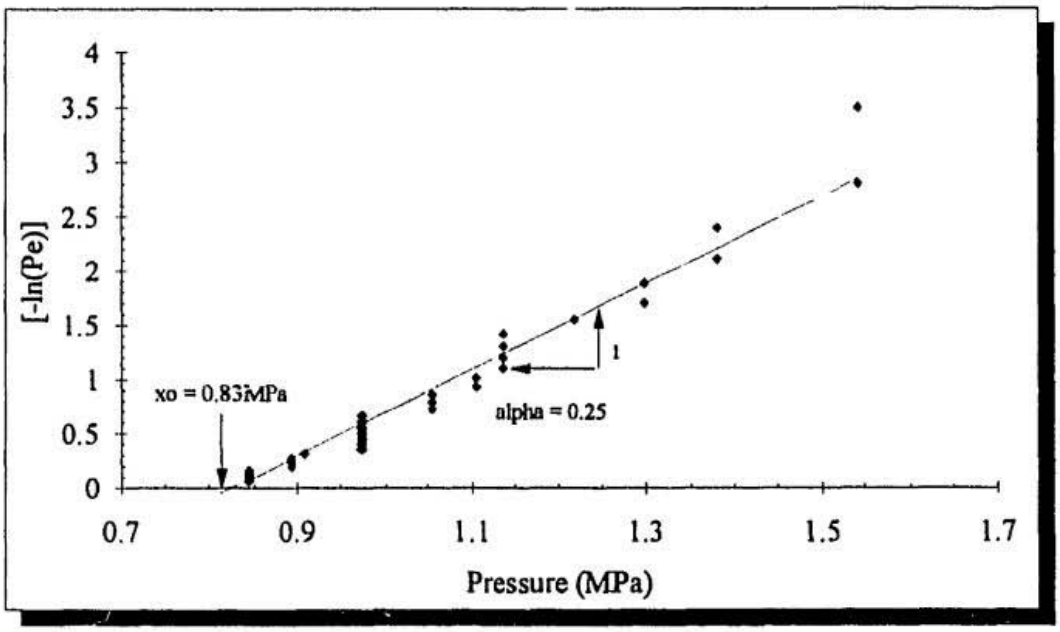

Figure 6.8 -ln (p_e) versus Pressure for Medof Panels 486, 487 combined

The correlation between the α parameters of the Medof panel data and Equation 6.5 suggests that an extremal analysis of ice pressures is applicable to the local pressures generated during ice interaction with offshore structures. In order to apply the methods outlined in section 6.2 to the pressures on the Medof panel, slight modifications should be made with regard to the exposure of the structure, as discussed below.

Jordaan et al. (1993) noted that the exposure of the structure is important. The authors present four aspects of exposure which should be considered when formulating a model for the prediction of ice pressures. First, the number of panels or the areas in the measurement program must be considered when analyzing data. The second aspect that must be considered is the length of interaction for an individual event. Two extremes which illustrate the duration of loading are ship ramming interactions, typically lasting of the order of seconds, and ice interaction with offshore structures, potentially lasting several weeks.

The third aspect of exposure is related to position on the ship or structure. The bow of a vessel is more susceptible to impact than may be a stationary panel on the face of an offshore structure. The fourth and final aspect of exposure is the number of events during a given time period. In general this number will be random and various distributions can be considered, i.e. the number of events may be fixed, or may be distributed according to a binomial or Poisson process.

Determining a correlation between the different exposures of ice-structure interactions is complex. An ice-ship interaction lasts several seconds and may have, by nature of the interaction, higher peak pressures than the continuous interaction between ice and an offshore structure. The duration of the event also affects the magnitude of pressures. There is an increased probability of experiencing higher pressures with longer events.

An initial approach to determining a correlation between the loads generated during ice-ship and ice-structure interactions consists of examining the probability densities of extreme pressure for both loading scenarios. Figure 6.9 represents graphically the transformation from pressures in the tail of the parent distribution to a probability density function of extreme pressures. Specifically, the severity corresponding to the maximum pressure experienced during the May 12 event (1.54MPa) is sought. Figure 6.8 indicates an exceedence probability of 0.061 for a pressure of 1.54MPa. The severity, expressed in terms of the number of peaks per event, may be determined by taking the inverse of the exceedence probability, i.e. $1/P_e$ yields a severity of 16.4 peaks (see Figure 6.9).

Probability densities of extreme pressure may be calculated by substituting the known parameters of x_o, α, r, and n (alternately stated as ε in the case where n is random) into the derivative of Equation 6.4, i.e.

$$f_Z(z) = \frac{1}{\alpha} \exp\{-[\frac{(z - x_0 - x_1)}{\alpha}]\} \exp\{-\exp[\frac{-(z - x_0 - x_1)}{\alpha}]\} \qquad 6.6$$

where $x_1 = \alpha(\ln(\varepsilon) + \ln(r))$.

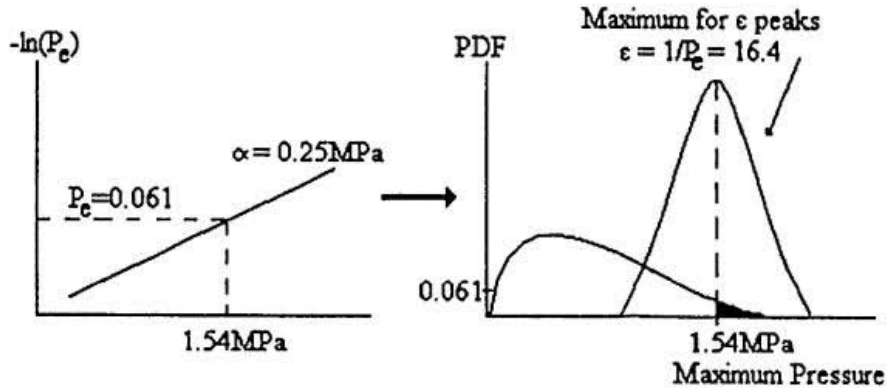

Figure 6.9 Calculation of Severity based upon Figure 6.8

Figure 6.10 presents the probability densities of extreme pressure for two severities corresponding to the May 12 event. A severity of 16.4 was calculated from the maximum pressure experienced during the May 12 event and its corresponding exceedence probability. Alternately, the severity may be calculated from the product of the estimated number of peaks occurring per minute and the event duration, i.e.

$$\varepsilon = \lambda t \qquad 6.7$$

where ε = severity

λ = average rate of arrival of peaks

t = duration of the event

An estimate for the rate of arrival of peaks was determined from the number of peaks registered on two individual pressure panels during a five minute interval (see Appendix C). Statistically, pressures obtained from two panels for five minutes each are equivalent to the pressures on a single panel for ten minutes. The estimated rate of arrival for panels 486 and 487 combined is 3.2 peaks per minute, for a ten minute duration, yielding a severity of 32 peaks (see Figure 6.10). Figure 6.10 illustrates that during the ice-structure interaction of May 12, a pressure of 2.68MPa corresponds to the "100 year load" and a severity of 16.4 peaks. Similarly the "100 year load" produces a pressure of 2.85MPa for a severity of 32 peaks.

Jordaan et al. (1993) presented the probability densities of extreme pressure for a 1.25m^2 panel area for several severities of ice-ship interactions (see Figure 6.11). In the case of ship ramming, the severity is expressed in terms of the number of impacts per year (versus peaks/event for interaction with stationary structures). The proportion of "hits" to "misses" is taken as 0.5. This is a lower value in comparison to a 100 percent success rate for ice-structure interaction (r =1.0). Based upon the input parameters of x_o, α, r, area and a severity (ε) of 16.4 impacts, the pressure corresponding to the "100 year load" is 7.17MPa. The pressures associated with the "100 year load" are roughly 2.5 times higher for ship rams than for the ice interaction with the Molikpaq.

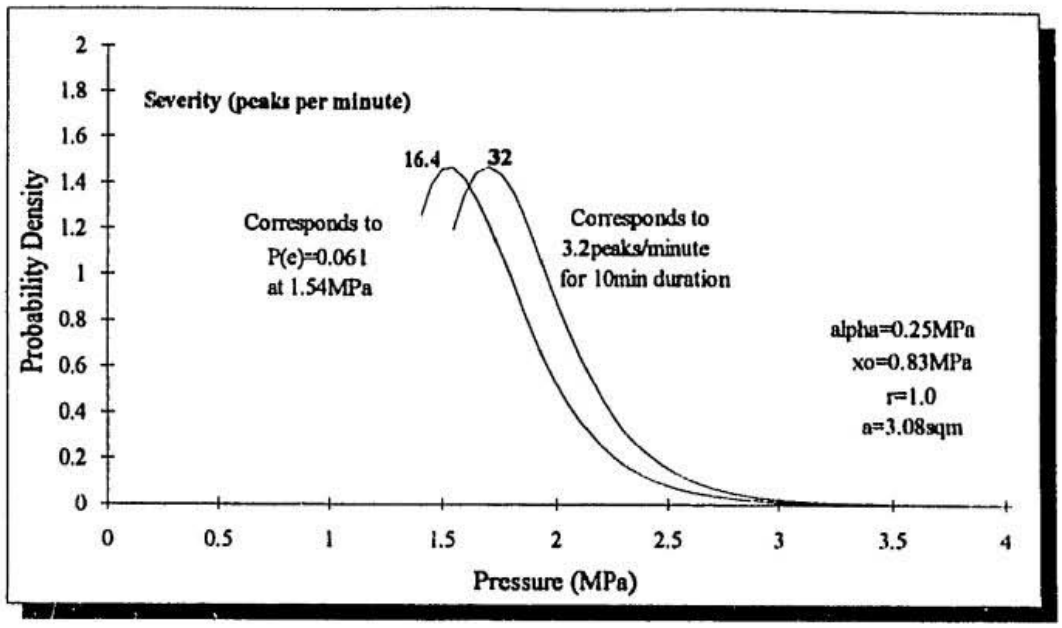

Figure 6.10 Probability Density of Extreme Pressure for the May 12 Event (based upon estimated severities of 16.4 peaks and 32 peaks)

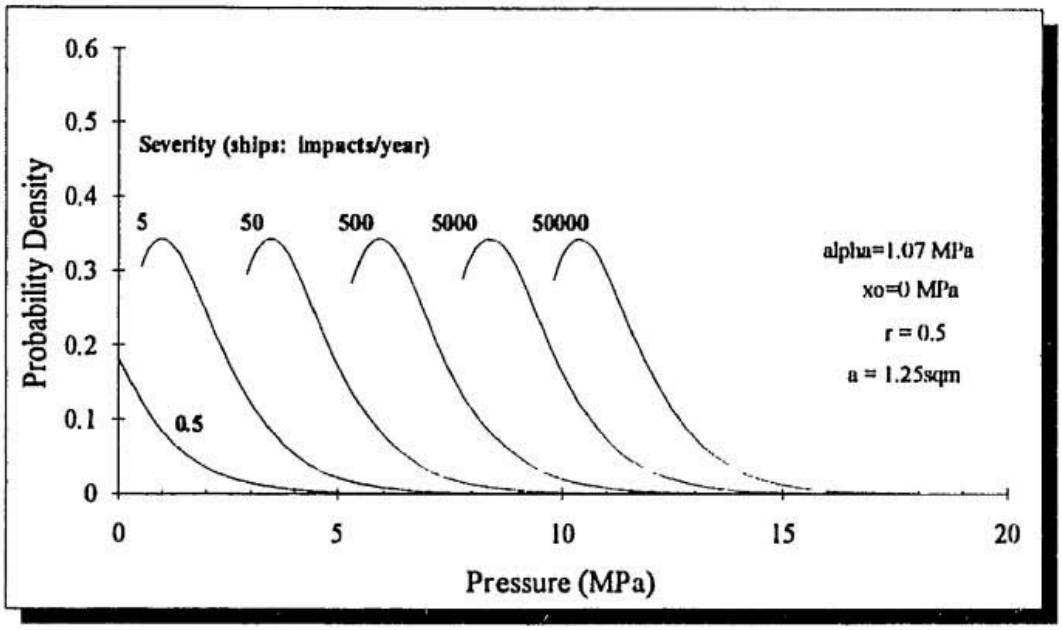

Figure 6.11 Probability Density of Extreme Pressure for Ice-Ship Interactions

A measure of the relative intensities of pressures for the two loading scenarios may be established by determining the severities corresponding to a given pressure. For instance, a pressure of 2.68MPa (ε=16.4 for ice-structure interaction) for the "100 year load" correlates to a severity of 0.24 impacts/year for ice-ship interactions. Typically, ship rams last approximately 0.05 seconds during which time they exhibit a single load spike (CanMar, 1982). Based upon this information, a severity of 0.24 impacts/year is equivalent to 0.24 peaks, a value which corresponds to a severity of 16.4-32 peaks for ice-structure interactions. Consequently, one peak generated during a ship ram is equivalent to 68.3-133.3 peaks during the more continuous interaction between ice and an offshore structure.

Two other areas should be addressed when comparing ice-ship and ice-structure interactions. First, what is the rate of arrival of peaks as estimated from strain gauge data? Second, what are the extreme pressures corresponding to an α value of 0.57MPa, as predicted by equation 6.5? An estimate for the rate of arrival of peaks as obtained from the strain gauges during the same five minute interval, reveals an occurrence of 74 peaks per minute. The severity of 740 peaks corresponds to an arrival rate of 74 peaks/minute and an event duration of 10 minutes.

The pressures associated with a severity of 740 peaks are substantially higher than the actual pressures experienced during the May 12 event. The strain gauge traces indicated high frequency, phaselocked behavior during the five minute interval under consideration (see Appendix C). Consequently, the strain gauges may have been strongly influenced by structural vibrations, causing the number of peaks per unit time to be overestimated. The limited frequency response of the Medof panels resulted in fewer peaks being registered

(see Chapter 5). The peaks recorded by the Medof panels during the 10-15 minute loading interval are expected to correspond to a series of high frequency peaks registered on the strain gauges during periods of phaselock. It is believed that the Medof panels provide a more accurate assessment of the severity for the May 12 event.

As previously stated, the Medof panels suffer from a sluggish response to high frequency loads. The pressure panels may only partially register the applied loads. Underestimated loads would result in an a value which falls below the design curve in Figure 6.6 (α = 0.25MPa versus α=0.57MPa). The probability densities of extreme pressure were calculated based upon a revised estimate of a (0.57MPa), and an x_O, r, and area consistent with the previous analysis (see Figure 6.10). The modified probability densities are presented in Figure 6.12.

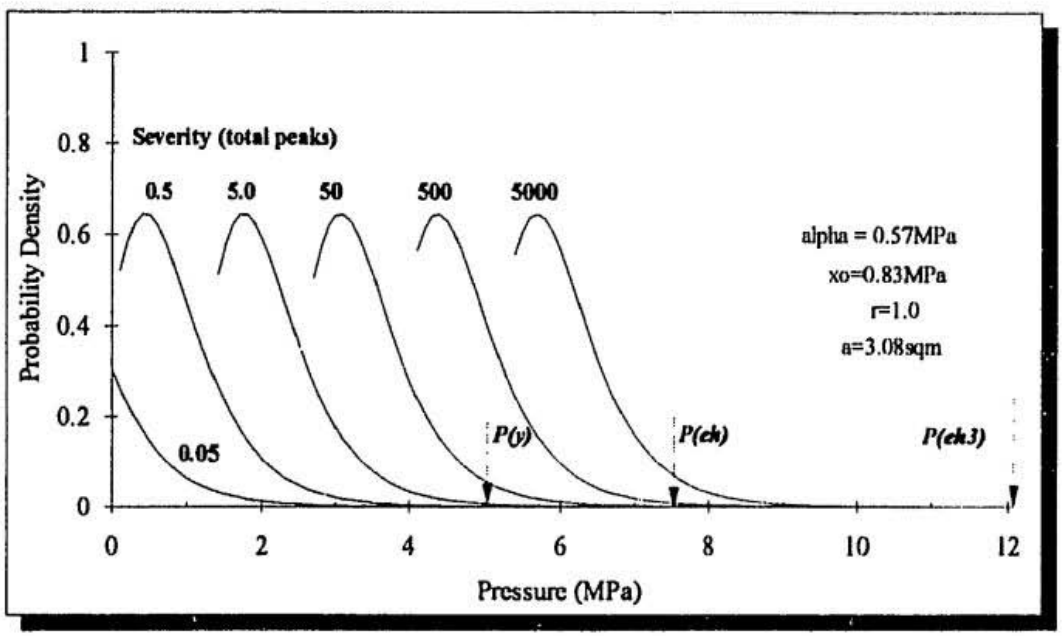

Figure 6.12 Probability Density of Extreme Pressure for Ice-Structure Interactions (α of 0.57MPa)

It is of interest to relate the expected number of peaks per event to the plastic limits for a specified design area. The plasticity analysis discussed in Section 5.9 corresponds to an area of the Molikpaq for which the frame spacing was 0.4m by 1.22m. Figure 6.12 indicates the various stress levels at which plastic mechanisms form for the area considered, i.e. P_y yield, P_{eh} two hinge mechanism, and P_{eh3} three hinge mechanism. Plate yielding (5.0MPa) is first seen to occur in the tail of the distribution of a 50 peak severity. Plate yielding occurs more frequently at severities greater than 500 peaks. Similarly, the two hinge mechanism is initiated at 7.5MPa. At this pressure, a severity of 500 peaks is remotely affected (in the extreme tail) by the formation of edge hinges. The formation of edge hinges is much more likely to occur for severities in excess of 5000 peaks. Plastic hinge formation at the center of the plate occurs at 12.1MPa, a pressure not likely to affect severities within the range of 0.5-5000 peaks. From the probability densities of extreme pressure for the May 12 event (Figure 6.10) it may be concluded that plate yield did not occur. A maximum recorded pressure of 1.54MPa supports this conclusion.

A comparison of the plastic limits and the probability densities of extreme pressure has important consequences for future design criteria. Establishing a relationship between the expected severity of an interaction and the limits of plasticity enables structures to be designed more efficiently. The large reserve of strength in the plating may be utilized by determining acceptable limits of plate deformation.

Table 6.2 lists the extreme pressures of various severities of ice ship and ice-structure interaction. Two trends are evident from Table 6.2. First, differences in pressure for the same severities for the two interactions increases with increasing severity, i.e. a severity of 0.05 indicates a difference in pressure of 0.77MPa for the two interactions, whereas the

difference in pressure between ice-ship and ice-structure interaction is 4.98MPa for a severity of 5000. The second trend which should be noted is that for very large severities, i.e. greater than 500 peaks, the extreme pressures are not significantly altered in comparison to the quantum leap in the number of peaks for a given exceedence probability. For instance, a severity of 500 peaks produces a pressure only slightly less than a severity of 5000 peaks (change in pressure is 1.32MPa versus a difference of 4500 peaks for the two severities). Consequently, the estimated rate of arrival of peaks becomes less important with increasing severity. One would expect the extreme pressures predicted by the strain gauges and the Medof panels to be very similar at severities upwards of 5000 despite conflicting estimates for the rates arrival (80-90 peaks/min. versus 3.2 peaks/min., respectively).

Table 6.2 Pressures Corresponding to the"100 year load" for Ice-Ship and Ice-Structure Interactions

Severity (impacts/year, peaks/event)	Pressures corresponding to "100 year load"	
	Ice-Ship Interaction ($1.25m^2$)	Ice-Structure Interaction ($3.08m^2$)
0.05	0.97MPa	1.74MPa
0.5	3.43MPa	3.06MPa
5	5.90MPa	4.37MPa
50	8.37MPa	5.68MPa
500	10.83MPa	6.99MPa
5000	13.29MPa	8.31MPa

In summary, an initial attempt to correlate the pressures generated during ice-ship and ice-structure interaction has been presented. The comparison was based upon two icebreakers, the Kigoriak and the Polar Sea (Jordaan et al., 1993) and the offshore structure, Molikpaq. Comparison of the distributions of extreme pressures for the May 12 event and a typical ice-ship interaction indicate that the pressure associated with one peak during a ship ram is roughly equivalent to the maximum pressure experienced for 68.3-133.3 peaks during the continuous interaction between ice and an offshore structure. Probability densities of extreme pressure for ice-ship and ice-structure interactions more closely correspond when a values are taken directly from the design curve in Figure 6.6. It was demonstrated that discrepancies in the rate of arrival of peaks per event are less significant for the larger severities. For severities greater than 500 peaks, pressures are similar, regardless of whether strain gauges or pressure panels are used to determine the number of peaks per minute.

6.4 Statistical Distributions of the Critical Zone Parameters

Once the design pressure of a specified area has been established, it is necessary to determine which combinations of the critical zone size, force, and spatial density satisfy the given pressure. The spatial and temporal fluctuations of pressure associated with that area should also be determined. Critical zone properties such as size, force, and the number of zones per unit area may be modelled using various statistical distributions. A birth and death process has been suggested for determining the temporal variability of the critical zones (Jordaan et al., 1990).

6.4.1 Representation of the Pressure and Force of a Critical Zone by the Gamma Distribution

As demonstrated previously, the pressures on the Medof panels ($3.08m^2$) approximated an exponential form in the tail of the parent distribution. Jordaan et al. (1993) state that the pressure on a small area may be represented by the gamma distribution. The gamma distribution is a generalized form of the exponential distribution as given by the following expression

$$f_X(x) = \frac{1}{\Gamma(\kappa)} \left| \Omega^{-\kappa} x^{\kappa-1} e^{-x/\Omega} \right| \qquad 6.6$$

where Ω is the scale parameter and κ governs the shape of the distribution. The mean and standard deviation of a sample may be used to determine the scale parameter Ω, and the shape parameter κ of the gamma distribution from the following equations.

$$m_S = \kappa\Omega \qquad 6.7$$

$$\sigma_S = \kappa\Omega^2 \qquad 6.8$$

where m_S and σ_S are the mean and standard deviation of the sample, respectively.

One advantage of using the gamma distribution to represent the pressures on a small area is the ease with which those pressures may be converted into a distribution of force for the same small area. A change of the scale parameter (in this case from pressure to force) enables the transformation from one distribution to another. Using this property of the gamma distribution, the pressure on a small area may be transformed into the force on the small area. This distribution of force may be compared to a force distribution which is representative of the cumulative effects of numerous critical zones acting over the given area (see Figure 6.13). In this manner, the concept of critical zones may be used to quantify the expected pressures on a given design area.

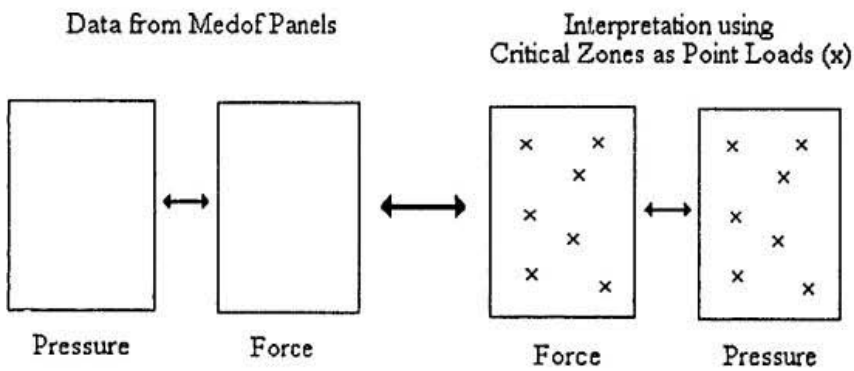

Figure 6.13 Statistical Transformation Relating the Medof Panel Pressure to Critical Zones

The mean and standard deviation of the Louis S. St. Laurent data were used to obtain the scale and shape parameters for a gamma distribution of the force of an individual critical zone (see Figure 6.14). Similar curves could be generated for the force associated with multiple zones on a common area. As the number of critical zones increases, the distribution of the property being evaluated tends to a normal form, i.e., all curves have the same mean, but the standard deviation is reduced by $1/n^{0.5}$.

The force distribution in Figure 6.14 may be combined with the distribution of spatial densities of critical zones over a specified area to determine the total applied load. In view of the design areas of interest (compared to the areas of individual critical zones) the zones of high pressure are taken as point loads. Consequently, the distribution of critical zone area may be eliminated when deriving the gamma distribution for the pressure on a given area. The next section addresses the means by which the spatial densities of the critical zones may be estimated.

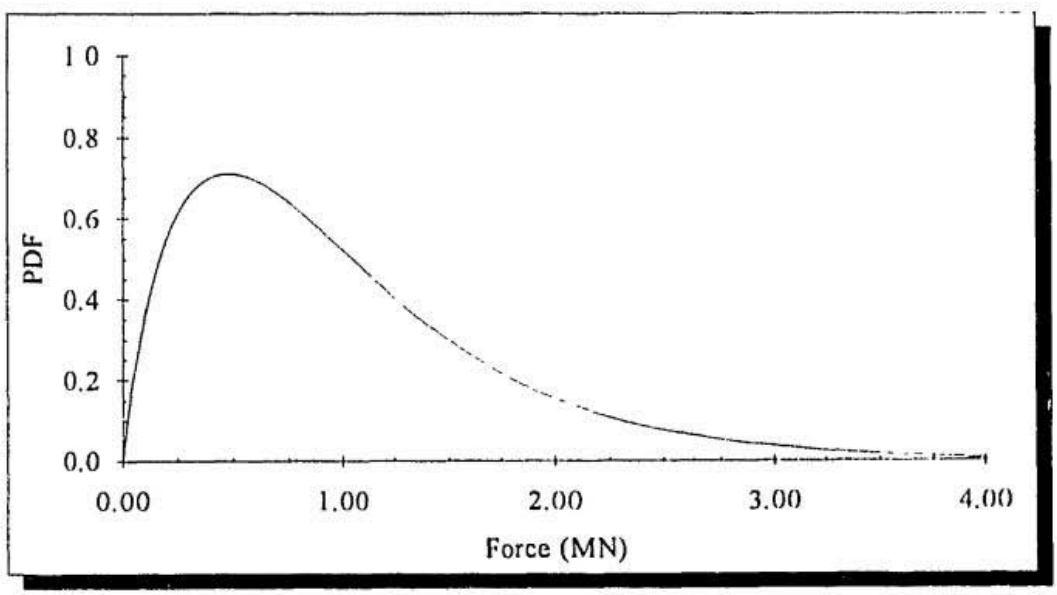

Figure 6.14 Gamma Distribution for the Force of One Critical Zone

6.4.2 Distribution for the Number of Critical Zones per Unit Area

The spatial density of the critical zones for a given area may be modelled using a Poisson process. The Poisson process arises from the basic mechanism of independent incidents occurring along a continuous axis (temporal or spatial) with a constant rate of occurrence. Benjamin and Cornell (1970) state that the Poisson process is governed by the following assumptions:

1. Stationarity. The probability of an incident in a short interval of time $t = t+h$ is approximately $\lambda(h)$, for any t.
2. Nonmultiplicity. The probability of two or more events in a short interval of time is negligible compared to $\lambda(h)$ (i e. it is of smaller order than $\lambda(h)$).
3. Independence. The number of incidents in any interval of time is independent of the number in any other (nonoverlapping) interval of time.

When considering the number of critical zones per unit area, the spatial reference frame should be substituted for the temporal reference frame mentioned above. The rate of arrival of incidents may be designated as λ and the instrumented area t. The resulting distribution for the number of critical zones over a specified area is given by

$$p_N(n) = \frac{(\lambda t)^n \exp -\lambda t}{n!} \qquad 6.9$$

A Poisson distribution was used to generate the number of critical zones present on the instrumented areas of the Louis S. St. Laurent, the CanMar Kigoriak, and the Medof panels (see Figures 6.15-6.17). Spatial densities ranged from 0.62 to 0.80 zones/m^2, decreasing with increasing area. The number of critical zones per unit area as represented by a Poisson process may be used in conjunction with the gamma distributions for the force of a critical zone to determine a design pressure which is suitable for the given loading conditions.

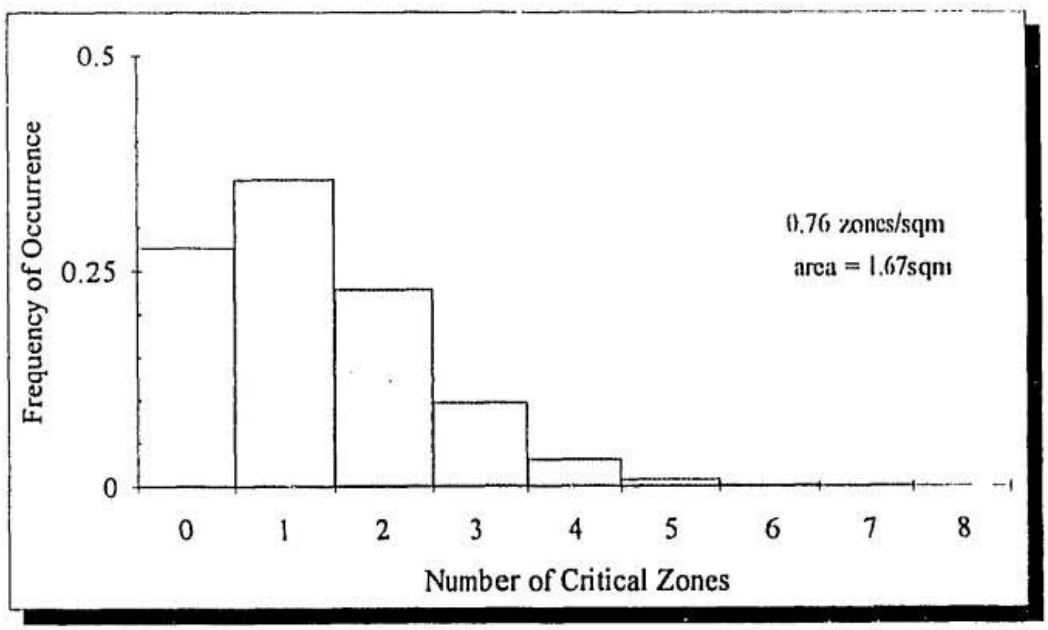

Figure 6.15 Distribution of the Number of Critical Zones for the Instrumented Area of the Louis S. St. Laurent

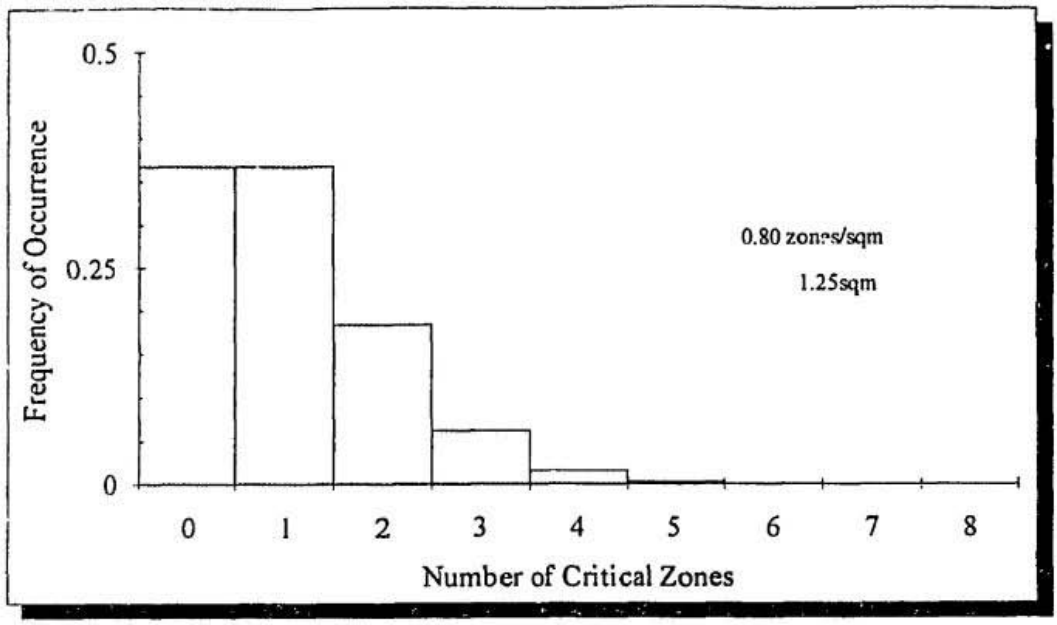

Figure 6.16 Distribution of the Number of Critical Zones for the Instrumented Area of the Kigoriak

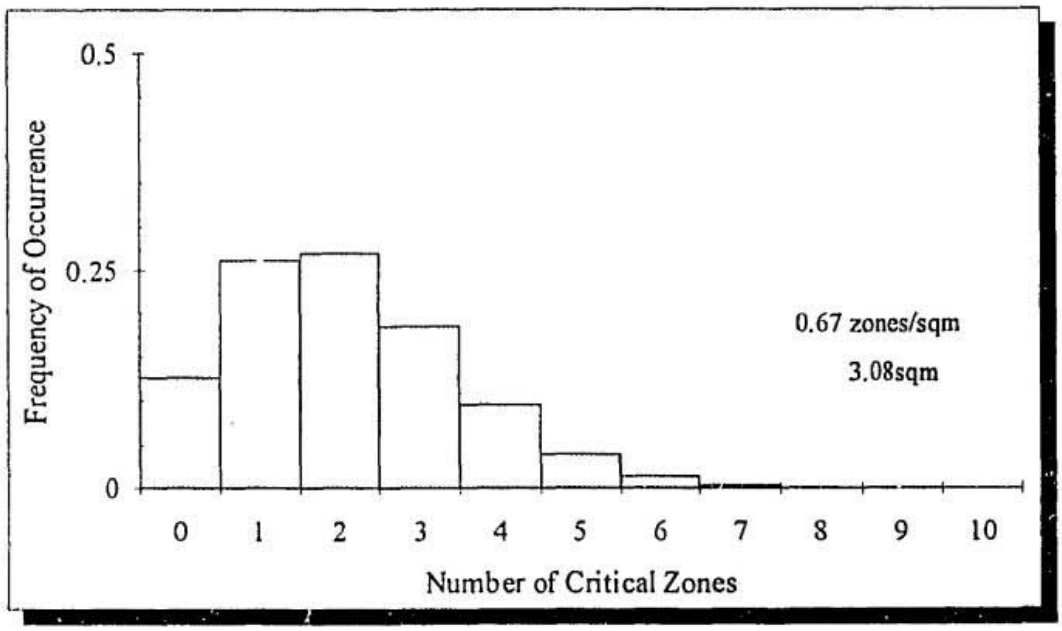

Figure 6.17 Distribution of the Number of Critical Zones for the Medof Panel

6.5 Simulation of the Critical Zone Parameters using the Monte Carlo Method

Statistical distributions have been established for the force of a critical zone (represented by the gamma distribution) and the spatial density of the critical zones (represented by the Poisson distribution). These two distributions were combined using Monte Carlo methods. Random numbers were generated for the zonal force and the spatial density over a specified area of $3.08m^2$ (equivalent to the Medof panel area). An upper limit of ten zones was used for the possible number of critical zones over the panel area. The Louis S. St. Laurent data provide the only means of directly estimating the forces associated with individual critical zones. Based upon this information, 4MN was taken as an upper bound for the force of a single critical zone present on the panels at any instant in time.

The tail of the pressure distribution resulting from the Monte Carlo simulation was then examined. The natural logarithm of the exceedence probability was plotted against pressure to determine α, the inverse of the slope of the regressed line. The simulation yielded an α value of 0.50MPa. This value of α falls within the range of estimates provided by the actual Medof panel data (0.25MPa) and a value of 0.57MPa as predicted by Equation 6.5 (see Figure 6.6). The results from the Monte Carlo analysis are surprisingly close to the actual May 12 data, especially considering the numerous approximations made in the analysis, i.e. spatial density of the critical zones and the force of individual high pressure zones as estimated from ship data, and the size of the pressure zones.

The above results are encouraging. Statistical methods are a viable means of quantifying the pressures exerted on small areas. The present analysis used the force of a critical zone and the spatial density of the zones as input parameters. Future analyses should be conducted in this area to elaborate upon the model and to further investigate the contribution of critical zones to pressures on various design area.

6.6 Conclusions

An extremal analysis was conducted on the pressures recorded by the Medof panels during the May 12 event. Probability density functions of the extreme pressures were determined based upon the severity of loading, the specified area of loading, the proportion of impacts to non-impacts, and the inverse of the slope of the regressed line for $-\ln(P_e)$ versus pressure. The extremal pressures for an ice-ship and an ice-structure interaction were compared in terms of equivalent severities. The pressures corresponding to the "100 year load" were approximately 2.5 times higher for ship rams than for the case of an ice interaction with an offshore structure. It was also noted that for severities in excess of 500 peaks the differences in pressure associated with dissimilar rates of arrival of incidents (3.2 peaks/minute versus 80 peaks/minute) were lessened.

The concept of critical zones was used to quantify the pressures experienced by the Medof panels during the May 12 event. A Monte Carlo simulation was used to generate a matrix of pressures and their corresponding probabilities of exceedence. The inverse slope of the regressed line was calculated from a plot of $-\ln(P_e)$ versus pressure, resulting in an

α value of 0.50MPa. The results of the simulation were in accordance with the range of α values as indicated by the actual May 12 data (0.25MPa) and as predicted from the proposed design equation (0.57MPa). The results of the Monte Carlo simulation are encouraging. The model should be further developed so that critical zones may be directly incorporated into design criteria for ships and structures in the arctic environment.

Chapter 7

Conclusions and Recommendations

This research project was undertaken to further the understanding of ice mechanics by investigating the local pressures generated during ice-structure interaction. The interaction zone consists of three distinct regions of pressure, i.e. critical zones, background regions and spalled areas. Critical zones were demonstrated to be important elements in the crushing process. These zones of intense pressure rapidly fluctuate in time and in space. Three sets of data were analyzed in order to gain a more complete understanding of the role of critical zones in the crushing process. These data included Hobson's Choice indentation tests, ship ramming trials of the Louis S. St. Laurent and the CanMar Kigoriak, and an ice-structure interaction involving the offshore structure Molikpaq.

Pressure versus time traces for the indentation tests exhibited a typical sawtooth pattern. From the data recorded by specific pressure sensors, an activity series of the critical zones present on the face of the indentor was able to be constructed. This series of graphics indicated that small zones of rapidly fluctuating pressures (up to 70MPa or more) were present on the face of the indentor during the tests. Data from the indentation tests enabled the effects of confinement, spalling, and extrusion on the behavior of the critical zones to be evaluated. Intense confining pressures are believed to cause an increase in the number of critical zones per unit area. Spalling and extrusion were shown to be related to the variation in the size of the critical zone at any particular instant. Significant decreases in the size of the critical zone may occur as a result spalling, caused by the propagation of fractures towards the free surface.

A substantial portion of this research was based upon data from the Louis S. St. Laurent. The pressure sensors on the Louis S. St. Laurent comprised the only instrumentation system by which to evaluate the fundamental properties of the critical zones. Small zones of rapidly fluctuating pressures were found to be characteristic of ice-ship interactions. Mean values for the force and area of the Louis S. St. Laurent critical zones were 1.09MN and 0.112m^2, respectively.

The information provided by the strain gauged subpanels on the Kigoriak was shown to represent an average pressure, which indicated only the cumulative effects of the critical zones. The contribution of individual zones of high pressure was unable to be ascertained. Consequently, the force and area of the high pressure zones as derived from the Louis S. St. Laurent were used to interpret data from the Kigoriak ramming trials. It was proposed that in the case of the Kigoriak, critical zones were smaller and had a higher average pressure than was apparent from the subpanel data.

An ice-structure interaction involving the offshore structure Molikpaq was investigated. Much of the analysis for this particular interaction consisted of evaluating the accuracy of the Medof pressure panels in comparison to the strain gauges. The error associated with the Medof panels was found to be roughly 30 percent. Medof panel inaccuracies may be attributed primarily to their sluggish response to high frequency loading. The duration of the May 12 event was 30 minutes, during which time creep of the urethane buttons was not expected to contaminate the data. Despite the uncertainty surrounding the Medof panel, it is an effective means of monitoring loads on local areas ($3.08m^2$).

Data from the pressure panels was used to establish a model for the probability densities of extreme pressure characteristic of ice-structure interaction. Input parameters for the model were the design area of interest, the proportion of impacts to non-impacts, the inverse of the slope of the regressed line $-\ln(P_e)$ versus pressure, and the severity of the interaction (defined as the number of peaks/event). A comparison of the pressures associated with the "100 year load" for ice-ship and ice-structure interactions demonstrated that the peak pressures associated with the former are 2.5 times larger than the latter. It was also noted that for severities greater than 500 peaks, the difference in pressure between successive levels of severity decreases. As a result, the estimated number of peaks per minute becomes less important for larger severities (an estimate of 3.2 peaks/minute yields a pressure on par with that estimated from 74 peaks/min).

The basic parameters of the critical zone, as derived from the Louis S. St. Laurent were used to interpret data from two fully loaded pressure panels. Statistical distributions of the force and spatial density of the critical zones characteristic of the Medof panel were combined to yield the pressure over $3.08m^2$. Monte Carlo methods were used to combine the distributions, thereby generating a matrix of random numbers representing the pressure on a specified small area. The inverse of the slope of the regression of $-\ln(P_e)$

versus pressure was used to compare the simulated results to the actual data from the May 12 event. It was shown that the inverse slope (α) agreed with the range of estimates provided by the actual data and by the proposed design equation (formerly used in the extremal analysis of pressures). The results were encouraging and served to establish the role of critical zones in the failure process and also to relate critical zones to the pressures exerted on specified design areas.

A significant portion of this research was based upon the premises that critical zones are equivalent in size and force for different loading conditions. Other sets of data should be examined to determine if this is a valid assumption. Further analysis should not rely solely upon the results from the Louis S. St. Laurent to estimate the fundamental parameters of the high pressure zones. The force and size of the critical zone should be evaluated from several sets of data.

Comparison of dynamic ice-ship interaction, to the more continuous and quasi-static interaction between ice and an offshore structure should be further investigated. Although both interactions involve the crushing mode of failure they may not exhibit critical zones which are equivalent in size, force, and pressure. The effect of different aspect ratios on the behavior of critical zones should also be examined for various loading scenarios. For instance, the bow geometry of the Louis S. St. Laurent and the Kigoriak should be compared to one another and also to the sloped face of the Molikpaq.

The effect of loading duration upon the probability densities of extreme pressure for various loading scenarios should be elaborated upon. Additionally, the scale effect phenomenon should be more closely investigated. Examining similar loaded areas for the two different data sets would help in this regard, i.e. the pressure on the 6.0m^2 panel of the Kigoriak could be compared with the pressures on two adjacent Medof panels

($6.16m^2$). Additionally, the pressures generated during continuous transit of ice covered waters, as opposed to the more specific case of ship ramming, could be compared to the interaction between an offshore structure and an ice floe. In this manner the load comparison could be based upon the equivalent number of ship rams to ice-structure events, versus a comparison which determines the number of peaks experienced during an event.

It is suggested that an iterative model be developed to determine which combinations of the statistical distributions of the critical zone satisfy a given design pressure. Statistical distributions for the critical zones should represent numerous data sets. These distributions should be refined by further investigating the effects of ice confinement, coverage of the instrumentation (partial panel loading), and exposure, on the fundamental properties of the critical zone.

The temporal nature of the critical zones should be clarified. It is recommended that a birth and death process be used to evaluate the variation of the critical zones in time. Critical zones should also be related to processes such as spalling and flaking. In this manner, the crushing process may be more fully understood.

References

Benjamin, J.R., and Cornell, C.A., 1970, **Probability, Statistics, and Decision for Civil Engineers**, McGraw Hill Book Company, New York, 684pp.

Blanchet, D., 1990, "Thirteenth Canadian Geotechnical Colloquium: Ice Design Criteria for Wide Arctic Structures", Canadian Geotechnical Journal, Vol. 67, pp. 701-725.

Blanchet, D., Hewitt, K.J., and Sladen, J.A., 1992, "Comparison between Measured Global Ice Loads and Geotechnical Response of Arctic Offshore Structures", Society of Petroleum Engineers, pp. 1-11, paper no. 22088.

Blount, H., Glen, I.F., Comfort, G. and Tam, G., 1981, **Results of Full Scale Measurements Aboard CCGS Louis S. St. Laurent During a 1980 Fall Arctic Probe**, Report for Canadian Coast Guard by Arctec Canada Ltd, Vol. I and II, 1981.

CanMar, 1982, **Final Report on Full Scale Measurements of Ice Impact Loads and Response of the Kigoriak**, A report by Canadian Marine Drilling, Ltd., to Coast Guard Northern, TP5871E.

CanMar, 1985, **Kigoriak and Robert Lemeur 1983 Ice Impact Tests, Refinement of Model Ship-Ice Interaction Energies**, A final report by Canadian Marine Drilling, Ltd., to Coast Guard Northern, TP6813E.

CanMar, 1985, **Kigoriak and Robert LeMeur 1983 Ice Impact Tests Refinement of Model Ship/Ice Interaction Energies (Final Report)**, Report for Coast Guard Northern by Canadian Marine Drilling Ltd, Appendices.

Croasdale, K.R. and Frederking, R.M.W., 1986, "Field Techniques for Ice Force Measurements", Proceedings, 8th International Symposium on Ice, **IAHR '86**, Vol. 2, pp. 443-482.

Croasdale, K.R., Graham, B.W., Comfort G., and Marcellus, R.W., 1986, "Evaluation of Ice Pressure and Strain Sensors in a Large Test Basin", Proceedings, 8th International Symposium on Ice, **IAHR '86**, Vol. 3, pp. 213-225.

Croasdale, K.R., 1984, **Evaluation of Ice Pressure Sensors and Strain Meters in a Large Ice Test Basin**, Report for Arco Oil and Gas Company, Department of Public Works, Esso Resources Canada, Ltd, Mobil Research and Development Company, and Sohio Petroleum Company by K.R. Croasdale and Associates, 139pp.

Daley, C. and Riska, K., 1990, **Review of Ship-Ice Interaction Mechanics**, Report from Finnish-Canadian Joint Research Project No. 5 "Ship Interaction with Actual Ice Conditions", Interim Report on Task 1A.

Daley, C.G., St. John, J.W., Brown, R., and Glen I., 1986, **Consolidation of Local Ice Impact Pressures Measured Aboard the USCGC Polar Sea (1982-1984)**, Report No. TP8533E, submitted to Transportation Development Center, Arctec Canada Limited, Kanata, Ontario, 214pp.

Dome Petroleum Ltd., 1982, **Report on Full Scale Measurements of Ice Impact Loads and Response of the 'CanMar Kigoriak' - August and October 1981**, Prepared by Dome Petroleum Ltd.

Duthinh, D., 1991, **Pressure of Crushed Ice as a Mohr-Coulomb Material Against a Flat Axisymmetric Indentor**, an internal report to Memorial University of Newfoundland, 1991.

Engelbrektson, A., 1983, "Observations of a Resonance Vibrating Lighthouse Structure in Moving Ice", Proceedings, 7th International Conference on Port and Ocean Engineering Under Arctic Conditions, **POAC '83**, Vol. II, pp. 855-864.

Engelbrektson, A. , 1989, "An Ice-Structure Interaction Model based on Observations in the Gulf of Bothnia", Proceedings, 10th International Conference on Port and Ocean Engineering Under Arctic Conditions, **POAC '89**, Vol. I, pp. 504-517.

Ferregut, C., and Daley, C., 1988, "ASPEN-Structural Modelling Using Limit States", Report for Transport Canada by Fleet Technology Ltd., TP9472.

Frederking, R., Blanchet, D., Jordaan, I.J., Kennedy, K., Sinha, N.K., and Stander, E., 1989, **Field Tests of Ice Indentation at Medium Scale Ice Island, April 1989**, Report submitted to Canadian Coast Guard and Transportation Development Center, Submitted by Institute for Research in Construction and National Research Council Canada.

Frederking, R.M.W., Jordaan, I.J., and McCallum, J.S., 1990, "Field Tests of Ice Indentation at Medium Scale: Hobson's Choice Ice Island 1989", Proceedings, 10th International Symposium on Ice, **IAHR '90**, Espoo, Finland, Vol. 2, pp. 931-944

Gagnon, R.E. and Sinha, N.K., 1991, "Energy Dissipation through Melting in large Scale Indentation Experiments on Multi-year Sea Ice", Proceedings, Proceedings, Offshore Mechanics Under Arctic Environments, **OMAE '91**, Vol. 4, pp. 157-161.

Geotechnical Resources, Ltd., 1988, **Laboratory Testing of the Medof Panel**, April, 1988, company report.

Glen, I.F. and Blount, H., 1984, "Measurements of Ice Impact Pressures and Loads Onboard CCGS Louis S. St. Laurent", **OMAE '84**, New Orleans, Vol. III, pp. 246-252.

Gulf Resources, 1988, **Dynamic Horizontal Ice Loading on an Offshore Structure Phase I-B, Ice-Structure Interaction and Response: Detailed Review of Medof/Strain Gauge Calibration, Appendix A**, Internal Report Gulf Canada Resources Ltd.

Hallam, S.D. and Pickering, J.G., 1988, "Modelling of Dynamic Ice Loading of Offshore Arctic Structures", **POLARTECH '88**, Vol. I, pp. 235-248.

Hamza, H., and Blanchet, D., 1984, "A Study of the Creep Effect upon the Response of a Pressure Sensor Embedded in an Ice Sheet", **Cold Regions Science and Technology**, Vol. 9, pp. 97-107.

Jefferies, M.G., 1988, **Draft Report on Dynamic Ice/Structure Interaction with the Molikpaq at Amauligak I-65, Main Report, Volume I of II**, Internal Report Gulf Canada Resources Ltd.

Jefferies, M.G., and Wright, W.H., 1988, "Dynamic Response of Molikpaq to Ice-Structure Interaction", **OMAE '88**, Vol. IV, pp. 790-799.

Jordaan, I.J., Maes, M.A., Brown, P.W. and Hermans, I.P., 1993, "Probabilistic Analysis of Local Ice Pressures", Proceedings, 11th International Conference on Offshore Mechanics and Arctic Engineering, **OMAE '93**, Vol. III, 1992, pp. 7-13.

Jordaan, I.J., Maes, M.A., and Nadreau, J.P., 1988, "The Crushing and Clearing of Ice in Fast Spherical Indentation Tests", report by the Ocean Engineering Center of Memorial University.

Jordaan, I.J., McKenna, R.F., Duthinh, D., Fuglem, M.K., Kennedy, K.P., Maes, M.A. and Marshall, A., 1990, **Development of New Ice Load Models**, Report for Canada Oil and Gas Lands Administration (COGLA) by C-CORE, Memorial University, St. John's, NF, 1990,167 pp.

Jordaan, I.J., and Timco, G.W., 1988, "Dynamics of the Ice-Crushing Process", **Journal of Glaciology**, Vol. 34, No. 118, pp. 318-326.

Jordaan, I.J., Xiao, J. and Zou, B., 1993, "Fracture and Damage of Ice: Towards Practical Implementation", 1993, **Ice Mechanics**, AMES, Vol. 163, pp. 251-259.

Keinonen, A.J., and Duff, J., 1983, "Canmar Kigoriak - Demonstration of Arctic Capability", Proceedings, 7th International Conference on Port and Ocean Engineering Under Arctic Conditions, **POAC '83**, Vol. II, pp. 620-633.

Kendrick, A., and Carter, J., 1987, **CCGS Louis S. St. Laurent Mid-Life Modernization Design Studies**, 20 pp.

Kheisin, D.E. and Cherepanov, N.V., 1970, "Change of Ice Structure in the Zone of Impact of a Solid Body Against the Ice Cover Surface", Proceedings, **Problemy Arktiki i Antarktiki**, Vol. 34, pp. 79-84.

Khorzavin, K.N., 1962, "Action of Ice on Engineering Structures", translated by U.S. Joint Publications Research Service for the U.S. Army Cold Regions Research Engineering Laboratory.

Kry, P.R., 1978, "A Statistical Prediction of Effective Ice Crushing Stresses on Wide Structures", **Proceedings, IAHR Symposium on Ice Problems**, Part I, pp. 33-47.

Kujala, P.J., 1991, "Safety of Ice-Strengthened Ship Hulls in the Baltic Sea", **Transactions of the Royal Institution of Naval Architects**, Part A, Vol. 133, pp. 83-93.

Maes, M.A. and Hermans, I.P., 1991, **Review of Methods of Analysis of Data and Extreme Value Techniques for Ice Loads**, Report to Memorial University, St. John's, NF, 1991, 51pp.

Määttänen, M.P. , 1977, "Ice Force Measurements at the Gulf of Bothnia by the Instrumented Kemi I Lighthouse", Proceedings, 4th International Conference on Port and Ocean Engineering Under Arctic Conditions, **POAC '77**, Vol. II, pp. 730-740.

Maeno, N. and Ebinuma, T., 1983, "Pressure Sintering of Ice and its Implication to the Densification of Snow at Polar Glaciers and Ice Sheets", **Journal of Physical Chemistry**, Vol. 87, pp. 4103-4110.

Masterson, D.M., Frederking, R.M.W., Jordaan, I.J., and Spencer, P.A., 1993, "Description of Multiyear Ice Indentation Tests at Hobson's Choice Ice Island-1990", Proceedings **OMAE '93**, Vol. 4, pp 145-149.

Masterson, D.M. and Frederking, R.M.W., 1993, "Local Contact Pressures in Ship-Ice and Structure-Ice Interactions", **Cold Regions Science and Technology**, Vol. 21, no. 2, pp 169-185.

Meaney, R., Kenny, S., and Sinha, N.K., 1991, "Medium-Scale Ice-Structure Interaction: Failure Zone Characterization", Proceedings, 11th International Conference on Port and Ocean Engineering Under Arctic Conditions, **POAC '91**, Vol. I., pp. 126-140.

Metge, M., Strilchuck, A., Trofimenkoff, P., 1975, "On Recording Stresses in Ice", **Third International Symposium on Ice Problems**, pp. 459-466.

Nadreau, J.P., 1987, "Ice Induced Dynamic Behavior of Structures", Proceedings, **OCEANS '87**, Vol. I, pp. 30-34.

Pilkington, G.R., Metge, M.I., and Strandberg, A.G., 1983, "A New Sensor for Measuring Ice Forces on Structures", Proceedings, 7th International Conference on Port and Ocean Engineering Under Arctic Conditions, **POAC '83**, Vol. 4, pp. 790-801.

Pilkington R., Blanchet, D., and Metge, M., 1983, "Fullscale Measurements of Ice Forces on an Artificial Island", Proceedings, 7th International Conference on Port and Ocean Engineering Under Arctic Conditions, **POAC '83**, Vol. IV, pp. 818-834.

Riska, K. 1989, "Theoretical Modelling of Ice-Structure Interaction", Proceedings, International Union of Theoretical and Applied Mechanics/International Association for Hydraulic Research Symposium on Ice-Structure Interaction, St. John's, 1989, pp. 595-618.

Riska, K., 1987, **On the Mechanics of the Ramming Interaction between a Ship and a Massive Ice Floe**, Technical Research Center of Finland, Publication 43, pp. 86.

Rogers, B.T., Hardy, M.D., Neth, V.W., and Metge, M., 1986 **Performance Monitoring of the Molikpaq while Deployed at Tarsiut P-45**, Internal Report Gulf Canada Resources Ltd.

Rogers, B.T., Spencer, P.A., and Hardy, M.D., 1991, **Load Measurement on the Molikpaq at Amauligak I-65**, Internal Report Gulf Canada Resources Ltd.

Savage, S.B., Sayed, M., and Frederking, R.M.W., 1992, "Two-Dimensional Extrusion of Crushed Ice, Part 2: Analysis", **Cold Regions Science and Technology**, Vol. 21, pp. 37-47.

Sayed, M. and Frederking, R.M.W., 1992, "Two-Dimensional Extrusion of Crushed Ice, Part 2: Experimental", **Cold Regions Science and Technology**, Vol. 21, pp. 25-36.

Singh, S.K., Jordaan, I.J., Xiao, J. and Spencer, P.A., 1993, "The Flow Properties of Crushed Ice", **OMAE '93**, Vol. 4, p. 11-19.

Spencer, P.A., 1991, "The Frequency Response of Fluid-Displacement Urethane Button Ice Pressure Panels", **OMAE '91**, Vol. 4, pp. 71-74.

Spencer, P.A., Masterson, D.M., and Metge, M., 1993, "The Flow Properties of Crushed Ice: Crushing Plus Extrusion Tests", **OMAE '93**, Vol. 4, pp 45-51.

Spencer, P.A., Masterson, D.M., Lucas, J., and Jordaan, I.J., 1992, "The Flow Properties of Crushed Ice: Experimental Observations and Apparatus", Proceedings, 11th International Symposium on Ice, **IAHR '92**, pp. 258-268.

Strandberg, A., 1986, **Evaluation of Medof Ice Load Sensor in the Arctic Environment**, Report by Fenco, MacLaren, Shawnigan Engineers, Inc.

Timco, G.W. and Jordaan, I.J., 1987, "Time-Series Variations in Ice Crushing", Proceedings, 9th International Conference on Port and Ocean Engineering Under Arctic Conditions, **POAC '87**, Vol. I, pp. 13-20.

Wessels, E., 1989, "First Results of Ice Force Measurements with TIP-Panels at Norstromsgrund Lighthouse", Proceedings, 10th International Conference on Port and Ocean Engineering Under Arctic Conditions, **POAC '89**, pp. 1428-1439.

Xu, J., 1981, "Dynamic Response of a Jacket Platform Subjected to Ice Loads", Proceedings, 6th International Conference on Port and Ocean Engineering Under Arctic Conditions, **POAC '81**, Vol. I, pp. 503-516.

Appendix A

Molikpaq Instrumentation Calculations

I. Peak Force Comparison Between Medof and Strain Gauge Data

Computation of peak pressures for the Medof panels is based upon the percent loaded area (see Section X). Computation of peak pressure for the strain gauges is based upon ice thickness at that location over a width of 1.14m. *All data was provided by Gulf Resources. Subsequent analysis was performed by the author.*

A. Event I: N1

1. Computation of peak forces registered on **strain gauge N1** for Event I. Forces calculated about 1.14m tributary width.

N1 Peak 1

F_{peak} = (260+250+255+240+230με)*1/5 *24kN/με* 1.14m/2.44m

F_{peak} = 2.77MN

P_{peak} = 1.35MPa

N1 Peak 2

F_{peak} = (230+220+230+235+260+240+225+200με)*1/8 * .0112

F_{peak} = 2.58MN

P_{eak} = 1.26MPa

N1 Peak 3

F_{peak} = (210+220+230+200+190+195+185*3+230+220+210+200+190με)*1/14 *.0112

F_{peak} = 2.28MN

P_{peak} = 1.11MPa

2. Peak Forces Experienced by **N1 Medof Panels** (482, 483) during Event I

	Force (MN)	Pressure (MPa)
Panel 482 experiences 3 peaks:	1.13, 1.25, 2.0	1.08, 1.19, 1.91
Panel 483 experiences 3 peaks:	2.6, 2.25, 2.0	2.48, 2.15, 1.91

B. Event I: N2

1. Computation of peak forces registered on **strain gauge N2** for Event I. Forces calculated about 1.14m tributary width.

N2 Peak 1

F_{peak} = (280+3*260+240με)*1/5 * 30kN/με * 1.14m/2.44m

F_{peak} = 3.64MN

P_{peak} = 0.97MPa

N2 Peak 2

F_{peak} = (270με)*.0140

F_{peak} = 3.78MN

P_{peak} = 1.00MPa

N2 Peak 3

F_{peak} = (220+230+225+220+225+2*230με)*1/7 * .0140

F_{peak} = 3.16MN

P_{peak} = 0.84MPa

N2 Peak 4

F_{peak} = (230+2*235+240+2*250+240+235με)*1/8 * .0140

F_{peak} = 3.35MN

P_{peak} = 0.89MPa

2. Peak Forces Experienced by **N2 Medof Panels** (486, 487, and 488) during Event I.

	Force (MN)	Pressure (MPa)
Panel 486 registered 2 peaks:	4.0, 3.0	1.30, 0.97
Panel 487 registered 6 peaks:	4.25, 3.5, 3.0	1.38, 1.14, 0.97
	2.9, 3.3, 2.9	0.97, 0.94, 1.07, 0.94
Panel 488 registered 3 peaks:	0.75, 0.65, 0.50	1.10, 0.96, 0.74

C. Event I: N3

1. Computation of peak forces registered on **strain gauge N3** for Event I. Forces calculated about 1.14m tributary width.

N3 Peak 1

F_{peak} = (340+3*320με)*1/4 * 22kN/με * 1.14m/2.44m

F_{peak} = 3.34MN

P_{peak} = 1.05MPa

N3 Peak 2

F_{peak} = (280+290+285+295+290+280με)*1/6 * .0102

F_{peak} = 2.95MN

P_{peak} = 0.92MPa

N3 Peak 3

F_{peak} = (300+305+2*310+315+310+320+320+2*335+330+2*340+330με)*1/14 * .0102

F_{peak} = 3.30MN

P_{peak} = 1.03MPa

2. Peak Forces Experienced by **N3 Medof Panels** (491 and 492) during Event I

	Force (MN)	Pressure (MPa)
Panel 491 registered 3 peaks:	0.62, 1.0, 0.38	0.20, 0.32, 0.12
Panel 492 registered 3 peaks:	1.62, 3.75, 1.25	0.53, 1.21, 0.41

II. Average Force Comparison of Medof Panel and Strain Gauge Data

A. Event I: Strain Gauge N1, N2, N3

Computation of average forces over entire Event I (3:20) registered on the strain gauges N1, N2, and N3. Forces calculated about 1.14m tributary width.

N1 Strain Gauge

F_{ave} = [1/2*(190+195με) +210+160+170+210+200+160+200+220+200+195+200+ 180+170+160+200+170+210+160+180+155+170+150με)]*1/23

F_{ave}=[192.5 + 4030με]*1/23

F_{ave} =4222.5με*1/23

F_{ave} =183.6με

F_{ave} = 183.6με * (11.2kN/με) = 2.06MN

N2 Strain Gauge

F_{ave} = [1/2*(200+200) + 215+180+210+190+230+200+210+190+230+210+220 +210+220+220+265+255+265+200+190+190+220+200με]*1/23

F_{ave} = (200με + 4720με)*1/23

F_{ave} = 4920με*1/23

F_{ave} = 213.9με

F_{ave} = 213.9με *14.02kN/με = 3.0MN

N3 Strain Gauge

F_{ave} = [1/2(200+260) + 240+210+290+280+230+200+230+200+220+200+240 +230+290με]*1/14

F_{ave} = (230με + 3060με)*1/14

F_{ave} = 3290με * 1/14

F_{ave} = 235με

F_{ave} = 235με * 10.28kN/με = 2.42MN

B. Event II: Strain Gauge N1, N2, N3

Computation of average forces over entire Event II (3:21) registered on the strain gauges N1, N2, and N3. Forces calculated about 1.14m tributary width.

N1 Strain Gauge

F_{ave} = 1/11*[1/2*(200+140)+160+170+160+240+180+230+180+180+150+170]

F_{ave} = (170με + 1820με) *1/11

F_{ave} = 180.9με

F_{ave} = 180.9με * 24kN/με *1.14m/2.44m = 2.028MN

N2 Strain Gauge

F_{ave} = 1/12*[1/2*(240+260)+210+240+220+240+220+270+260+290+240+290+220]

F_{ave} = (250με + 2700με) * 1/12

F_{ave} = 246με

F_{ave} = 246με * 30kN/με * 1.14m/2.44m = 3.45MN

N3 Strain Gauge

F_{ave} = 1/11*[1/2*(250+240)+230+260+210+200+180+220+180+220+190+210]

F_{ave} = (245με + 2100με)* 1/11

F_{ave} = 213με

F_{ave} = 213με * 25kN/με * 1.14m/2.44m = 2.19MN

C. Event I: Medof Panels

Medof Panel Force Averaged over entire interval of Event I (3:20)

Medof 482

F_{ave} = 1/8*[1/2(1.25+0.85)+(0.85+0.85)+(0.85+0.70)+(0.70+1.20)+(1.2+1.0)+
(1.0+1.25)+(1.25+0.75)+(0.75+2.0)]

F_{ave} = 8.225MN * 1/8

F_{ave} = 1.028MN

Medof 483

F_{ave} = 1/11*[1/2*(0.90+0.50)+(0.50+0.70)+(0.70+0.30)+ (0.30+0.70)+(0.70+1.0)
+(1.0+0.8)+(0.8+1.0)+(1.0+2.55)+(2.55+1.25)+(1.25+2.25)+(2.25+1.5)]

F_{ave} =12.25MN * 1/11

F_{ave} = 1.11MN

Medof Panel 486

F_{ave} = 1/6*[1/2*(3.25+2.25)+4.0+1.3+3.0+1.65+1.65]

F_{ave} = 14.35MN * 1/6

F_{ave} = 2.39MN

Medof Panel 487

F_{ave} = 1/12*[1/2*(3.25+2.500)+4.25+3.30+3.50+2.60+3.10+2.10+2.90+2.80+3.35
+2.75+2.90]

F_{ave} = 36.425MN * 1/12

F_{ave} = 3.04MN

Medof Panel 488

F_{ave} = 1/8*[1/2*(0.45+0.50)+0.85+0.25+0.30+0.25+0.65+0.70+0.25]

F_{ave} = 3.73MN * 1/8

F_{ave} = 0.466MN

Medof Panel 491

F_{ave} = 1/6*[1/2*(0.65+0)+0.25+1.0+0.0+0.0+0.40)]

F_{ave} = 1.975MN * 1/6

F_{ave} = 0.329MN

Medof Panel 492

F_{ave} = 1/5*[1/2*(1.75+0.75)+1.5+3.75+0.75+1.25]

F_{ave} = 8.5MN * 1/5

F_{ave} = 1.70MN

D. Event II: Medof Panels

Medof Panel Force Averaged over entire interval of Event II (3:21)

Medof Panel 482

F_{ave} =1/4*[1/2*(2.0+1.13)+1.5+1.13+0.88]

F_{ave} = 5.08MN * 1/4

F_{ave} = 1.27MN

Medof Panel 483

F_{ave} = 1/8*[1/2*(1.5+0.88)+1.4+2.0+0.88+0.75+1.0+0.63+1.25]

F_{ave} = 9.1MN * 1/8

F_{ave} = 1.14MN

Medof Panel 486

F_{ave} = 1/5*[1/2*(2.25+3.0)+2.60+2.0+3.35+2.45]

F_{ave} = 13.025MN * 1/5

F_{ave} = 2.605MN

Medof Panel 487

F_{ave} = 1/7*[1/2*(2.5+4.25)+2.25+4.10+2.60+3.10+2.75+4.70]

F_{ave} = 22.875MN * 1/7

F_{ave} = 3.27MN

Medof Panel 488

F_{ave} = 1/4*[1/2*(0.50+0.50)+0.15+0.75+0.25]

F_{ave} = 1.65MN * 1.4

F_{ave} = .4125MN

Medof Panel 491

F_{ave} = 0

Medof Panel 492

F_{ave} = 1/4*[1/2*(0.75+0.70)+0.60+2.12+0.75]

F_{ave} = 4.195MN * 1/4

F_{ave} = 1.048MN

E. Event I: Medof Group Force

Mean Panel Group Forces Averaged over entire interval of Event I.

Mean N1 (482,483)
F_{mean} = (1.028MN+1.11MN) * 1/2
F_{mean} = 1.069MN

Mean N2 (486, 487)
F_{mean} = (2.39MN+3.04MN) * 1/2
F_{mean} = 2.72MN

Mean N3 (491, 492)
F_{mean} = (0.329MN+1.70MN) * 1/2
F_{mean} = 1.01MN

F. Event II: Medof Group Force

Mean Panel Group Forces Averaged over entire interval of Event II.

Mean N1 (482, 482)
F_{mean} = (1.27MN+1.14MN) * 1/2
F_{mean} = 1.21MN

Mean N2 (486, 487)
F_{mean} = (2.605MN+3.27MN) * 1/2
F_{mean} = 2.94MN

Mean N3 (491, 492)
F_{mean} = (0.0+1.048MN) *1/2
F_{mean} = 0.524MN

III. Error Approximation between Medof Panel and Strain Gauge Data

Error Percentage of Average Force Values for Events I and II as registered by Medof Panels in Comparison to those registered by Strain Gauges

A. Event I

N1 Medof vs. Strain Gauge
Error = (1.069MN-2.06MN) *1/2.06MN *100
Error = 48%

N2 Medof vs. Strain Gauge
Error = (2.72MN-3.0MN) * 1/3.0MN * 100
Error = 9.0%

N3 Medof vs. Strain Gauge
Error = (2.42MN-1.01MN) * 1/2.42MN * 100
Error = 58%

B. Event II

N1 Medof vs. Strain Gauge
Error = (1.21MN-2.03MN) * 1/2.03MN * 100
Error = 40%

N2 Medof vs. Strain Gauge
Error = (2.94MN-3.5MN) * 1/3.5MN *100
Error = 16%

N3 Medof vs. Strain Gauge
Error = (2.2MN - 0.524MN) * 1/2.2MN * 100
Error = 76%

IV. Event Frequency Calculations in Zones of Phaselock for Various Events

Event I (3:20)

Note: Event I provides data on the transition from nonsimultaneous to simultaneous behavior. Phaselocked regions are those during which synchronized loading, with identical frequencies, occurred across the face of the structure. Hence the following frequencies are representative of strain gauges N1, N2, and N3.

Phaselocked Zone I

5 peaks occur over an interval of 3.6seconds
individual wave period = 0.72 seconds
frequency = 1/period = 1/0.72sec
f=1.39Hz

Phaselocked Zone II

9 peaks occur over an interval of 6 seconds
individual wave period = 0.66 seconds
$f = 1/\tau = 1/0.66$sec
f= 1.50Hz

Phaselocked Zone III

14 peaks occur over an interval of 10 seconds
individual wave period = 0.714 seconds
$f = 1/\tau = 1/0.714$sec
f= 1.40Hz

Event II (3:21:00)

Note: Event II exhibits continuous phaselocked behavior. The following frequency is representative of strain gauges N1, N2, and N3.

7 peaks occur over an interval of 5 seconds
individual wave period = 0.714 seconds
$f = 1/\tau = 1/0.714$sec
f= 1.40Hz

Event III (3:25:00)

Note: Event III exhibited continuous phaselocked behavior. Loading frequency decreased between the beginning and end of the event. Two frequencies were calculated at two strain gauge locations, N1 and N2.

Frequency at N1 during the interval 3:25:00-3:25:05.

2 peaks occur over an interval of 5 seconds
individual wave period = 2.5 seconds
$f = 1/\tau = 1/2.5sec$
$f = 0.4Hz$

Frequency at N1 during the interval 3:25:40-3:25:45.

2 peaks occur over an interval of 8.4 seconds
individual wave period = 4.2 seconds
$f = 1/\tau = 1/4.2sec$
$f = .238Hz$

Frequency at N2 during the interval 3:25:00-3:25:05.

2 peaks occur over an interval of 5 seconds
individual wave period = 2.5 seconds
$f = 1/\tau = 1/2.5sec$
$f = 0.4Hz$

Frequency at N2 during the interval 3:25:38-3:25:47.

2 peaks occur over an interval of 11 seconds
individual wave period = 5.5 seconds
$f = 1/\tau = 1/5.5sec$
$f = .18Hz$

Summary of Frequency Ranges

Event I: 1.39Hz, 1.5Hz, 1.40Hz
Event II: 1.40Hz
Event III: 0.4Hz, .238Hz, 0.18Hz

Outside Range: 1.4Hz - 0.18Hz

VI. Calculation of Loading Rates Used in the Kelvin Model Creep Representation

Medof Panel 491

Medof panel 491 was selected for a stress rate substitution into the Kelvin model. Panel 491 was loaded over the full area of $3.08m^2$. The detailed Medof plot of N3 exhibits a relatively linear increase in load from 0-2.5MN over a period of 30 seconds (3:22:53 - 3:23:23).

Pressure = $2.5MN/3.08m^2$
P = 0.812MPa
σ' = 0.812MPa/0.5min
σ' = 1624kPa/min

Strain Gauge N3 at Event II

An increase in strain of 200με to 280με registered on strain gauge N3 during Event II over a 0.5 second interval.

F = 200με * 22kN/με * 1.14m/2.44m
F = 2.056MN
P = $2.056MN/3.08m^2$
P = 0.667MPa

F = 280με * 22kN/με * 1.14m/2.44m
F = 2.878MN
P = $2.878MN/3.08m^2$
P = .9344MPa

ΔP = 0.9344MPa - 0.667MPa
ΔP = 0.2674MPa

σ' = 0.2674MPa/0.5seconds * 60seconds/min
σ' = 32090 kPa/min

Strain Gauge N3, Event III

An increase in strain of 280με to 480με registered on strain gauge N3 during Event III over an interval of 3 seconds.

$\Delta\varepsilon = 480\mu\varepsilon - 280\mu\varepsilon$
$\Delta\varepsilon = 200\mu\varepsilon$
$F = 200\mu\varepsilon * 22kN/\mu\varepsilon * 1.14m/2.44m$
$F = 2.056MN$
$P = 2.056MN/3.08m^2$

$P = 0.667MPa$

$\sigma' = 0.667MPa/3sec * 60sec/min$
$\sigma' = 13340kPa/min$

VIII. Equations Governing the Kelvin Model Parameters

Time Factor Equations

$N1 = 0.015 * T_{cr} * K1$
$N2 = 0.070 * T_{cr} * K2$
$N3 = 0.640 * T_{cr} * K3$
$N4 = 9.600 * T_{cr} * K4$
$N5 = 0.100 * T_{cr} * K5$

Stiffness Equations

$K1 = K_{cr}/0.290$
$K2 = K_{cr}/0.144$
$K3 = K_{cr}/0.204$
$K4 = K_{cr}/0.360$
K5 = instantaneous stiffness*

*Note: see Table A.1 for details

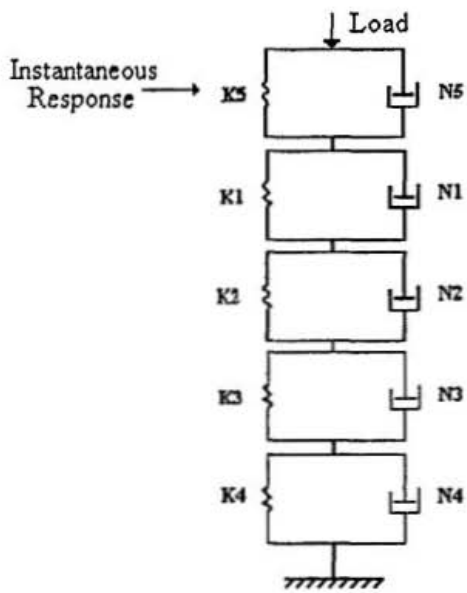

VIII. Illustration of Kelvin Model Creep Equation: Medof Panel 491

For an n-element Kelvin Model the displacement at the front face of the panel is given by:

$$x = \frac{\sigma_o}{k_1} + \sum_{i=2}^{n} \frac{\sigma_o}{k_i} [1 - \exp (\frac{-k_i t}{\eta_i})]$$

$$\text{creep (t)} = \sum_{i=1}^{4} \frac{\dot{\sigma}}{k_i} [t + \exp \frac{\eta_i}{ki} (\frac{-k_i t}{\eta_i}) - 1)]$$

$$\text{creep (t)} = \sum_{i=1}^{n} (\text{Kelvin units I -V})$$

$$\text{Kelvin unit I} = \frac{\dot{\sigma}}{21.035} \{t + \frac{9.466}{21.035} [\exp (\frac{-21.035\ t}{9.466}) - 1]\}$$

$$\text{Kelvin unit II} = \frac{\dot{\sigma}}{42.632} \{t + \frac{88.96}{42.632} [\exp (\frac{-42.632\ t}{88.96}) - 1]\}$$

$$\text{Kelvin unit III} = \frac{\dot{\sigma}}{29.903} \{t + \frac{547.13}{29.903} [\exp (\frac{-29.903\ t}{547.13}) - 1]\}$$

$$\text{Kelvin unit IV} = \frac{\dot{\sigma}}{16.945} \{t + \frac{4880.1}{16.945} [\exp (\frac{-16.945\ t}{4880.1}) - 1]\}$$

$$\text{Kelvin unit V} = \frac{\dot{\sigma}}{4.59} \{t + \frac{.459}{4.59} [\exp (\frac{-4.59\ t}{.459}) - 1]\}$$

Confirmation of the creep equation may be obtained by substituting the stress rate employed by Fenco Engineers, Ltd. during testing of the Medof panel response to an applied load of 960 kPa over 3 minutes. The Table A.2 yields 52.078 mm of creep in panel 491 over the loading duration of 3 minutes. Evaluation of individual Kelvin unit parameters indicates that Units I and II account for 96-98% of total panel creep.

$$\text{Unit I} = \frac{320}{21.035}\{3+\frac{9.466}{21.035}\ [\exp(\frac{-21.035 * 3}{9.466}) - 1\ ]\}$$

Unit I = 38.80 mm

Similarly...
Unit II = 10.57 mm
Unit III = 2.49 mm
Unit IV = .294 mm
Unit V = 202.18 mm

creep (3 minutes) = 52.154*

*Note: Excluding instantaneous response of Kelvin unit V

IX. Conversion Factors for Strain Gauge Data

Bulkhead	Gauge Factor*	Relative Response**
N1	24kN/με	1.0
N2	30kN/με	0.8
N3	22kN/με	1.12

Notes:

* Assumed gauge factor in kN per 2.44m tributary width per με response. Valid for ice thicknesses between 1-5m.

** Lower response indicates stiffer, less responsive bulkhead

X. Ice Thicknesses at Various Locations across the North Face

Using visual observations recorded during the May 12 event and the number of activated Medof panels as an indication of ice thickness.

Location	**Ice Thickness**	**Estimated from active panel #**
N1:	1.8m	Panels 482: 34% area loaded Panel 483: 34% area loaded
N2:	3.5m	Panels 486: 100% area loaded Panel 487: 100% area loaded Panel 488: 22% area loaded
N3:	2.8m	Panels 491: 100% area loaded Panel 492: 100% area loaded

Division of Medof Panel Plots during the 10-15 minute interval into Force Categories*

A =0.0-0.5MN D= 1.5-2.0MN G= 3.0-3.5MN J= 4.5-5.0MN

B=0.5-1.0MN E= 2.0-2.5MN H= 3.5-4.0MN

C= 1.0-1.5MN F= 2.5-3.0MN I= 4.0-4.5MN

Panel 488	Force	Panel 487	Force	Panel 486	Force	Panel 483	Force	Panel 482	Force	Panel 492	Force	Panel 491	Force
10.-10.25	C	10.-10.05	F	10.0-10.25	E	10.0-10.05	E	10.0-10.30	F	10.0-10.10	C	10.0-10.08	E
10.25-10.37	B	10.05-10.10	E	10.25-10.35	F	10.05-10.15	D	10.30-10.35	E	10.10-10.25	D	10.08-10.25	F
10.37-10.5	A	10.1-10.3	D	10.35-10.50	G	10.15-10.35	E	10.35-10.45	D	10.25-10.28	C	10.25-10.45	E
10.5-10.75	B	10.3-10.35	E	10.5-10.6	H	10.35-10.42	F	10.45-10.55	C	10.28-10.34	B	10.45-10.90	D
10.75-11.0	A	10.35-10.45	F	10.6-10.62	G	10.42-10.44	E	10.55-10.85	B	10.34-10.45	A	10.90-10.92	E
11.0-11.25	B	10.45-10.50	G	10.62-10.65	F	10.44-10.45	D	10.85-11.20	C	10.45-10.55	B	10.92-10.95	F
11.25-12.0	A	10.50-10.54	H	10.65-10.70	E	10.45-10.48	C	11.20-11.35	B	10.55-10.70	A	10.95-10.97	G
12.0-12.25	B	10.54-10.60	I	10.70-10.80	D	10.48-11.05	B	11.35-11.45	C	10.70-10.95	B	10.97-11.05	H
12.25-12.50	A	10.60-10.65	H	10.80-10.90	C	11.05-11.10	C	11.45-11.70	D	10.95-12.75	A	11.05-11.08	G
12.5-12.60	B	10.65-10.78	G	10.90-10.95	D	11.10-11.12	D	11.70-11.95	C	12.75-12.90	B	11.08-11.10	F
12.60-13.0	A	10.78-10.95	F	10.95-10.98	E	11.12-11.15	E	11.95-12.25	B	12.90-13.5	A	11.10-11.12	E
13.0-13.10	B	10.95-11.10	E	10.98-11.15	F	11.15-11.18	F	12.25-12.55	C	13.5-13.65	B	11.12-11.15	D
13.10-13.20	C	11.10-11.25	F	11.15-11.18	E	11.18-11.24	E	12.55-12.68	D	13.65-13.68	C	11.15-11.18	C
13.20-13.25	D	11.25-11.35	G	11.18-11.43	D	11.24-11.28	D	12.68-12.96	E	13.68-13.77	D	11.18-11.35	B
13.25-13.70	C	11.35-11.50	F	11.43-11.45	E	11.28-11.32	C	12.96-13.04	D	13.77-13.85	E	11.35-11.42	C
13.70-13.80	D	11.50-11.60	E	11.45-11.75	F	11.32-11.35	D	13.04-13.50	C	13.85-14.0	F	11.42-11.70	B
13.80-13.95	E	11.60-11.70	F	11.75-12.0	E	11.35-11.45	E	13.50-13.90	D	14.0-14.05	E	11.70-11.75	C
13.95-14.05	D	11.70-11.75	G	12.0-12.15	F	11.45-11.70	D	13.90-14.0	E	14.05-14.10	D	11.75-11.90	D
14.05-14.10	C	11.75-11.80	H	12.15-12.35	G	11.70-11.75	C	14.0-14.2	F	14.10-14.15	C	11.90-12.05	E
14.10-14.25	D	11.80-11.85	I	12.35-12.75	F	11.75-12.30	B	14.2-14.45	E	14.15-14.30	B	12.05-12.25	D
14.25-14.35	C	11.85-11.90	H	12.75-12.78	G	12.30-12.40	C	14.45-14.75	D	14.30-14.35	C	12.25-12.65	C
14.35-14.70	D	11.90-11.95	G	12.78-12.84	H	12.40-12.60	B	14.75-15.0	C	14.35-14.38	D	12.65-12.70	B
14.70-15.0	C	11.95-12.10	F	12.84-12.85	G	12.60-12.64	C			14.38-14.65	E	12.70-12.74	C

Panel 488 (cont.)	Force	Panel 487 (cont.)	Force	Panel 486 (cont.)	Force	Panel 483 (cont.)	Force	Panel 482 (cont.)	Force	Panel 492 (cont.)	Force	Panel 491 (cont.)	Force
		12.10-12.20	G	12.85-12.90	F	12.64-12.78	D			14.65-14.68	D	12.74-12.82	D
		12.20-12.30	F	12.90-12.95	E	12.78-12.84	C			14.68-14.70	C	12.82-12.85	E
		12.30-12.35	G	12.95-13.13	D	12.84-12.92	B			14.70-14.80	B	12.85-12.95	D
		12.35-12.38	H	13.13-13.30	C	12.92-13.15	C			14.80-15.0	A	12.95-13.32	C
		12.38-12.42	I	13.30-13.40	D	13.15-13.30	B					13.32-13.38	B
		12.42-12.50	J	13.40-13.50	D	13.30-13.45	A					13.38-13.50	C
		12.50-12.55	I	13.50-13.55	E	13.45-13.65	B					13.50-13.54	D
		12.55-12.65	H	13.55-13.75	F	13.65-13.70	A					13.54-13.58	E
		12.65-12.80	G	13.75-13.85	E	13.70-13.80	B					13.58-13.67	F
		12.80-12.85	F	13.85-13.90	F	13.80-14.0	C					13.67-13.80	G
		12.85-12.90	E	13.90-13.95	G	14.0-14.08	D					13.80-13.95	F
		12.90-13.05	F	13.95-13.00	H	14.08-14.18	C					13.95-14.10	E
		13.05-13.10	E	14.0-14.05	I	14.18-15.0	B					14.10-14.15	D
		13.10-13.15	D	14.05-14.10	J							14.15-14.30	C
		13.15-13.35	C	14.10-14.15	I							14.30-14.32	B
		13.35-13.65	D	14.15-14.16	H							14.32-14.36	C
		13.65-13.70	E	14.16-14.20	G							14.36-14.65	D
		13.70-13.80	F	14.20-14.24	F							14.65-14.68	E
		13.[illegible]90	G	14.24-14.29	E							14.68-14.70	D
		13.90-14.0	F	14.29-14.65	D							14.70-14.75	C
		14.0-14.05	G	14.65-15.0	C							14.75-15.0	B
		14.05-14.10	H										A

Creep within Individual Kelvin Units for a creep rate of 1624 KPa/min

time (seconds)	(minutes)	Kelvin I	Kelvin II	Kelvin III	Kelvin IV	Kelvin V	Sum Kelvin I-IV
0.00	0.00E+00	0.00E+00	0.00E+00	0.00E+00	0.00E+00	0.00E+00	0.00E+00
0.01	1.67E-04	2.38E-06	2.54E-07	4.12E-08	4.62E-09	4.91E-05	2.68E-06
0.02	3.33E-04	9.53E-06	1.01E-06	1.65E-07	1.85E-08	1.96E-04	1.07E-05
0.03	5.00E-04	2.14E-05	2.28E-06	3.71E-07	4.16E-08	4.42E-04	2.41E-05
0.04	6.67E-04	3.81E-05	4.06E-06	6.60E-07	7.39E-08	7.85E-04	4.29E-05
0.05	8.33E-04	5.95E-05	6.34E-06	1.03E-06	1.16E-07	1.23E-03	6.70E-05
0.06	1.00E-03	8.57E-05	9.13E-06	1.48E-06	1.66E-07	1.76E-03	9.65E-05
0.07	1.17E-03	1.17E-04	1.24E-05	2.02E-06	2.26E-07	2.40E-03	1.31E-04
0.08	1.33E-03	1.52E-04	1.62E-05	2.64E-06	2.96E-07	3.13E-03	1.72E-04
0.09	1.50E-03	1.93E-04	2.05E-05	3.34E-06	3.74E-07	3.96E-03	2.17E-04
1.00	1.67E-02	2.35E-02	2.53E-03	4.12E-04	4.62E-05	4.65E-01	2.65E-02
2.00	3.33E-02	9.30E-02	1.01E-02	1.65E-03	1.85E-04	1.76E+00	1.05E-01
3.00	5.00E-02	2.07E-01	2.26E-02	3.71E-03	4.16E-04	3.77E+00	2.33E-01
4.00	6.67E-02	3.63E-01	4.01E-02	6.59E-03	7.39E-04	6.37E+00	4.11E-01
5.00	8.33E-02	5.61E-01	6.26E-02	1.03E-02	1.16E-03	9.48E+00	6.35E-01
6.00	1.00E-01	7.98E-01	8.98E-02	1.48E-02	1.66E-03	1.30E+01	9.04E-01
7.00	1.17E-01	1.07E+00	1.22E-01	2.02E-02	2.26E-03	1.69E+01	1.22E+00
8.00	1.33E-01	1.38E+00	1.59E-01	2.63E-02	2.96E-03	2.11E+01	1.57E+00
10.00	1.67E-01	2.11E+00	2.47E-01	4.11E-02	4.62E-03	3.03E+01	2.41E+00

Table A.1 Kelvin Model Parameters

Panel Time Factor = Tcr
Panel Creep Stiffness = Kcr

Medof Panel	Tcr (min)	Kcr (KPa/mm)	K1 (KPa/mm)	N1 (KPa min/mm)	K2	N2	K3	N3	K4	N4	K5	N5
482	5.2	5.456	18.812	1.467	37.886	13.79	26.743	89	15.154	756.5	3.719	0.372
483	11.0	5.307	18.301	3.02	36.857	28.38	26.017	183.16	14.743	1556.8	3.33	0.333
486	25.0	5.227	18.023	6.759	36.296	63.518	25.621	409.93	14.518	3484.4	1.977	0.198
487	4.7	6.35	12.586	0.887	25.347	8.339	17.892	53.82	10.139	457.47	1.878	0.188
488	6.4	2.861	9.864	0.947	19.866	8.9	14.023	57.437	7.946	488.22	0.961	0.096
491	30.0	6.1	21.035	9.466	42.362	88.96	29.903	547.13	16.945	4880.1	4.59	0.459
492	17.7	3.265	11.259	2.989	22.674	28.093	16.005	181.3	9.069	1541.1	1.644	0.164
496*												
495*												
497*												

* none given

Example Creep Calculations for Medof Panel 491 with a completely loaded area of 3.08 sqm

time (seconds)	(minutes)	creep (displacement in mm) 1624 KPa/min	32090 KPa/min	13340 KPa/min
0.00	0.00E+00	0.00E+00	0.00E+00	0.00E+00
0.01	1.67E-04	2.68E-06	5.30E-05	2.20E-05
0.02	3.33E-04	1.07E-05	2.12E-04	8.81E-05
0.03	5.00E-04	2.41E-05	4.77E-04	1.98E-04
0.04	6.67E-04	4.29E-05	8.48E-04	3.52E-04
0.05	8.33E-04	6.70E-05	1.32E-03	5.50E-04
0.06	1.00E-03	9.65E-05	1.91E-03	7.93E-04
0.07	1.17E-03	1.31E-04	2.59E-03	1.08E-03
0.08	1.33E-03	1.72E-04	3.39E-03	1.41E-03
0.09	1.50E-03	2.17E-04	4.29E-03	1.78E-03
1.00	1.67E-02	2.65E-02	5.24E-01	2.18E-01
2.00	3.33E-02	1.05E-01	2.07E+00	8.62E-01
3.00	5.00E-02	2.33E-01	4.61E+00	1.92E+00
4.00	6.67E-02	4.11E-01	8.11E+00	3.37E+00
5.00	8.33E-02	6.35E-01	1.25E+01	5.21E+00
6.00	1.00E-01	9.04E-01	1.79E+01	7.43E+00
7.00	1.17E-01	1.22E+00	2.41E+01	1.00E+01
8.00	1.33E-01	1.57E+00	3.11E+01	1.29E+01
10.00	1.67E-01	2.41E+00	4.76E+01	1.98E+01
20.00	3.33E-01	8.70E+00	1.72E+02	7.15E+01
30.00	5.00E-01	1.78E+01	3.52E+02	1.46E+02
40.00	6.67E-01	2.90E+01	5.73E+02	2.38E+02
50.00	8.33E-01	4.18E+01	8.25E+02	3.43E+02
60.00	1.00E+00	5.57E+01	1.10E+03	4.57E+02

Appendix B

Equations for the Plasticity Analysis of the Medof Panels

NOTE: *The following equations used in the plasticity analysis were obtained from Ferregut and Daley (1988). Subsequent plasticity analysis for the Molikpaq was performed by the author.*

I. Initiation of Plastic Yield

$$P_y = \frac{2\sigma_y}{(1-\nu^2)}\left(\frac{t}{b}\right)^2$$

where

σ_y = yield strength of the steel (355MPa)
ν = Poisson's ratio in the elastic range (0.3)
t = thickness of the plate (32 mm)
b = length of the plate (400mm)

II. Initiation Plastic Hinges

$$P_{eh} = \frac{3\sigma_y}{(1-\nu^2)}\left(\frac{t}{b}\right)^2$$

III. Initiation of Center Hinge

$$P_{eh3} = \frac{4\sigma_y}{(1-\nu_p^2)}\left(\frac{t}{b}\right)^2$$

where ν_p = Poisson's ratio in the inelastic range (0.5)

IV. Initiation of Permanent Set

$$P_{set} = \frac{0.74\sigma_y}{(1-\nu_p^2)} \frac{t}{b}$$

IV. Ultimate Strength of the Plate (Upper and Lower Bounds)

A. Upper bound ($\nu_p = 0.5$)

$$P_{ult\ (u)} = \frac{1.11\sigma_y}{(1-\nu_p^2)} \frac{t}{b}$$

B. Lower Bound ($\nu = 0.3$)

$$P_{ult\ (l)} = \frac{1.11\sigma_y}{(1-\nu^2)} \frac{t}{b}$$

Appendix C

Rate of Arrival of Incidents for May 12 Event

A. Medof Panel estimation for the rate of arrival of peaks during a five minute interval of the May 12, 1986 event.

total number of peaks during the 10-15 minute interval of the May 12 event for panel

486	16 peaks in 5 minutes
487	16 peaks in 5 minutes

rate of arrival of incidents (λ) = 3.2 peaks per minute

B. Strain Gauge estimation for the rate of arrival of peaks during phaselock burst file 3:21

total number of peaks during the 60 second interval of burst file 3:21: 74peaks

rate of arrival of incidents (λ) = 74 peaks per minute

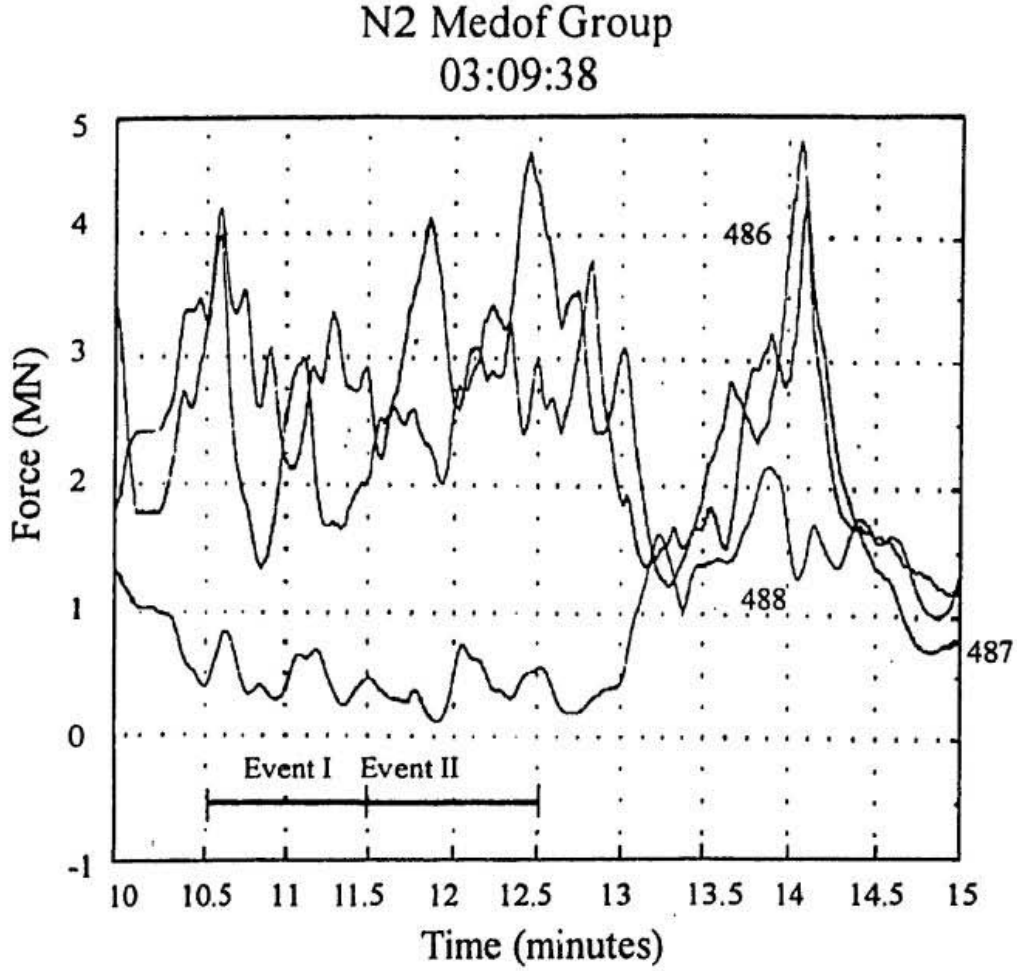

Medof Panel Pressures during the Most Active Interval of Loading (10-15 minute interval)

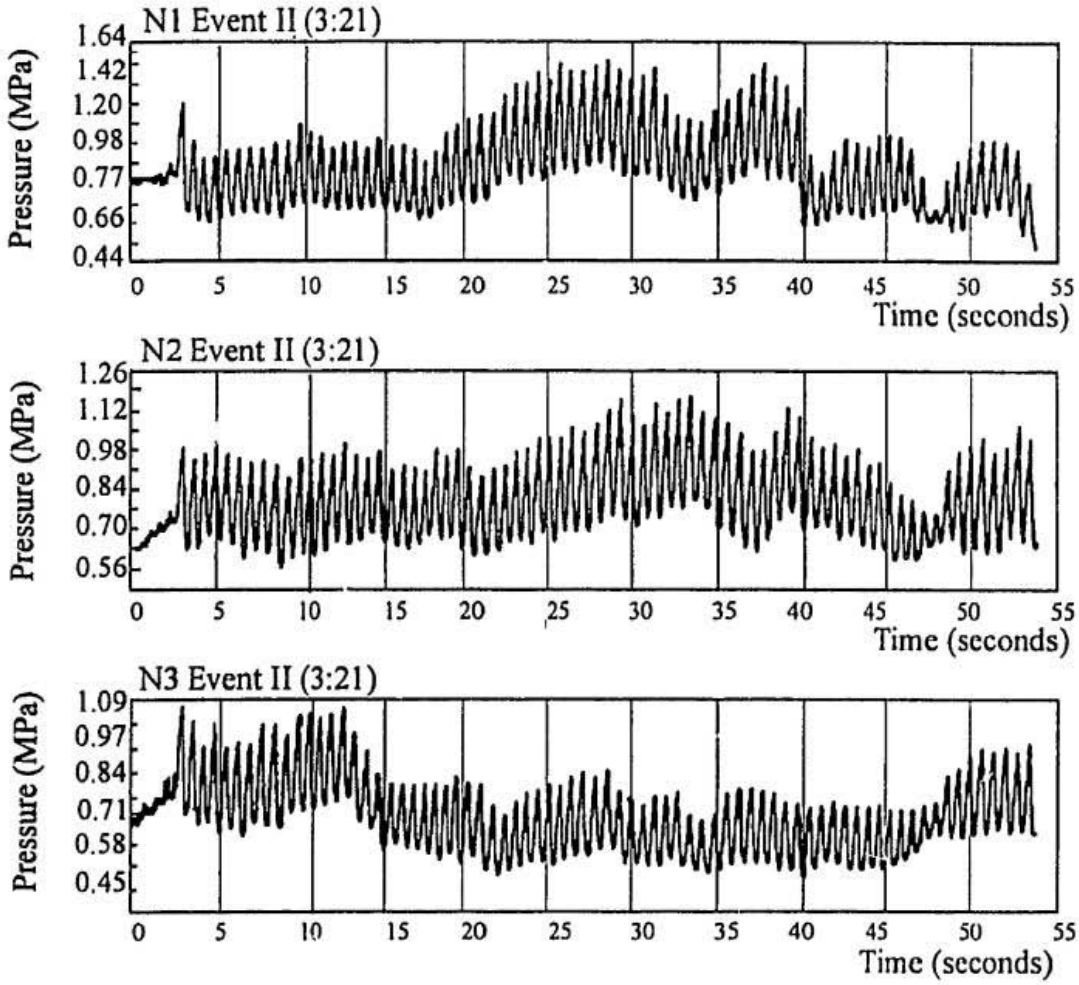

Strain Gauge Trace of the May 12 Event (Burst File 3:21)